



**TECHNISCHE
UNIVERSITÄT
WIEN**
Vienna University of Technology

Diese Dissertation haben begutachtet:

Prof. Dr. K. Held

Prof. Dr. C. Honerkamp

DISSERTATION

Diagrammatic methods beyond DMFT

ausgeführt zum Zwecke der Erlangung des akademischen Grades eines
Doktors der Naturwissenschaften unter der Leitung von

Prof. Dr. Karsten Held

Prof. Dr. Alessandro Toschi (betreuender Assistent)

E 138 - Institut für Festkörperphysik
eingereicht an der Technischen Universität Wien
Fakultät für Physik

von

M.Sc. Ciro Taranto

Matrikelnummer: 1029075
Theresianumgasse 12/2/5, 1040 Wien

Wien, am 12. Mai 2014

Contents

Introduction	2
1 Different methods for different correlations: GW, fRG, and DMFT	9
1.1 Electronic correlations	11
1.2 LDA: mapping onto independent particles	12
1.3 <i>GW</i> : Hedin's equations and the <i>GW</i> approximation	16
1.3.1 <i>GW</i> diagrammatics	19
1.3.2 <i>GW</i> approximation	27
1.3.3 Actual implementations of <i>GW</i> : quasiparticle <i>GW</i>	30
1.4 Functional renormalization group	33
1.4.1 Derivation and diagrammatic elements of fRG	36
1.4.2 Diagrammatic content of fRG	45
1.5 Dynamical mean-field theory	64
1.5.1 Dynamical mean field	64
1.5.2 Functional perspective on DMFT	74
1.5.3 DMFT description of the Mott transition	87
2 Merging <i>GW</i> and dynamical mean field theory: the <i>GW</i>+DMFT method	91
2.1 Advantages of <i>GW</i> +DMFT	91
2.1.1 <i>GW</i> + DMFT: a brief functional perspective	92
2.1.2 <i>GW</i> +DMFT self consistency from a diagrammatic point of view	94
2.1.3 qp <i>GW</i> implementation in VASP	101
2.1.4 Comparison to photoemission spectroscopy	108
2.2 Conclusion	111
3 Combining dynamical mean field theory and functional renormalization group: The DMF²RG	113
3.0.1 Introduction and motivation	114
3.0.2 Extensions of DMFT	117
3.0.3 From infinite to finite dimensions	125
3.0.4 Diagrammatic content	132
3.1 Application to the 2 <i>D</i> Hubbard model	136

3.2 Summary, open questions ad outlook	152
Conclusions & Outlook	159
4 Conclusions	159
Bibliography	161
Acknowledgments	175

List of publications

Peer reviewed

- C. Taranto, S. Andergassen, J. Bauer, K. Held, A. Katanin, W. Metzner, G. Rohringer, and A. Toschi
From infinite to two dimensions through the functional renormalization group
Phys. Rev. Letters **112**, 196402 (2014).
- C. Taranto, M. Kaltak, N. Parragh, G. Sangiovanni, G. Kresse, A. Toschi, and K. Held
Comparing quasiparticle GW+DMFT and LDA+DMFT for the test bed material SrVO₃
Physical Review B **88**, 165119 (2013).
- Y. Nomura, M. Kaltak, K. Nakamura, C. Taranto, S. Sakai, A. Toschi, R. Arita, K. Held, G. Kresse, and M. Imada
Effective on-site interaction for dynamical mean-field theory
Physical Review B **86**, 085117 (2013).
- C. Taranto, G. Sangiovanni, K. Held, M. Capone, A. Georges, and A. Toschi
Signature of antiferromagnetic long-range order in the optical spectrum of strongly correlated electron systems
Physical Review B **85**, 085124 (2012). [Selected as editor's suggestion]

Under review

- Z. Zhong, M. Wallerberger, J. M. Tomczak, C. Taranto, N. Parragh, A. Toschi, G. Sangiovanni, and K. Held
Electronics with correlated oxides: SrVO₃/SrTiO₃ as a Mott transistor
arXiv:1312.5989

Other publications

- K. Held, C. Taranto, G. Rohringer, and A. Toschi
Hedin Equations, GW, GW+DMFT, and All That
Lecture Notes of the Autumn School 2011 Hands-on LDA+DMFT, Forschungszentrum Juelich GmbH (publisher).

Deutsche Kurzfassung

Das Verständnis von elektronischen Korrelationsphänomenen stellt eine der größten Herausforderungen der Festkörperphysik dar. In den letzten 25 Jahren hat sich die dynamische Molekularfeldtheorie (DMFT) als die "Standardmethode" für korrelierte fermionische Systeme etabliert, welche weit über eine störungstheoretische Behandlung hinausgeht und auch heute noch Grundlage von theoretischen Weiterentwicklungen ist. Dank DMFT lassen sich heutzutage nicht nur viele Phänomene gut verstehen, etwa der berühmte Mott-Isolator Übergang, sondern es eröffnen sich sogar Möglichkeiten der Vorhersage elektronischer Eigenschaften für Materialien in denen ein effektives Einteilchenbild unzureichend ist.

Allerdings hat auch die DMFT ihre Grenzen: Zum einen beruht sie auf der Annahme, dass elektronische Korrelationen rein lokal sind. Zum anderen handelt es sich historisch gesehen um eine Methode, welche zuvorderst niederenergetische Freiheitsgrade zu beschreiben versucht. In der Tat existieren Systeme und physikalische Eigenschaften für welche diese Beschränkungen nicht möglich ist.

In der vorliegenden Arbeit versuche ich diese beiden Probleme, welche Gegenstand intensiver Bemühungen in der aktuellen Forschung sind, anzugehen und Wege aufzuzeigen, welche eine bessere Beschreibung korrelierter Materialien ermöglichen. Dazu stelle ich die Kombination von DMFT mit zwei etablierten Methoden vor, die beide auf der Feynmanschen Diagrammatik basieren: Die Hedinsche GW Näherung (G : Greensche Funktion; W : abgeschirmte Wechselwirkung) und die funktionale Renormierungsgruppe (fRG). Während man mit GW höherenergetische Freiheitsgrade erfassen kann, ist fRG in der Lage auch niedrigdimensionale Systeme, in welchen Korrelationen manifest nichtlokal sind, zu beschreiben.

In **Kapitel 1** werden diese drei Methoden (DMFT, GW und fRG) eingeführt. Der erste Teil des Kapitel behandelt GW und diskutiert weitere Näherungen, die oft nötig sind, um GW in realistischen Berechnungen zu verwenden. Im zweiten Teil wird die fRG eingeführt und ihre diagrammatischen Grundlagen erklärt. Schlussendlich wird auch die DMFT und als Anwendungsbeispiel der Mott-Übergang besprochen.

In **Kapitel 2** wird die Kombination von GW und DMFT, welche auch $GW+DMFT$ genannt wird, eingeführt. Die Methode wurde bereits vor einem Jahrzehnt vorgeschlagen und hat viele konzeptuelle Vorteile gegenüber z.B. lokale Dichtapproximation (LDA)+DMFT, einer anderen, sehr erfolgreichen realistischen Erweiterung von DMFT. Leider ist jedoch die Implementierung der $GW+DMFT$ Methode für realistische Berechnungen technisch äußerst aufwendig, weshalb es bisher nur wenige Beispiele tatsächlicher Anwendungen gibt. Deshalb wird hier

die Implementierung einer *Quasiteilchen Näherung* für $GW+DMFT$ vorgeschlagen, deren numerischer Aufwand vergleichbar ist mit jenem von $LDA+DMFT$. Am Beispiel des korrelierten Metalls $SrVO_3$ zeigen wir die Vorteile unserer Methode und vergleichen sie mit experimentellen Photoemissionsspektren, sowie mit Resultaten der etablierten $LDA+DMFT$ Methode.

Schließlich wird in **Kapitel 3** die ‘‘DMF²RG’’ eingeführt, eine neuartige Kombination zwischen $DMFT$ und fRG . Der große Vorteil dieser neuen Methode ist, dass der fRG -Fluss hier bereits von Anfang an die nicht-perturbative Physik der $DMFT$ beinhaltet. Zudem werden nicht-lokale Fluktuationen durch den Fluss unverfälscht in allen Kanälen berechnet. Als erstes Beispiel für die Anwendungsmöglichkeiten der DMF^2RG Methode wird das zweidimensionale Hubbard-Modell bei halber Füllung betrachtet, insbesondere werden die elektronische Selbstenergie sowie einige Zweiteilcheneigenschaften (die statische Spinsuszeptibilität und die 4-Punkt Vertexfunktion) berechnet. Die vielversprechenden Ergebnisse und der Vergleich mit anderen Methoden, wie etwa der ‘‘dynamical cluster approximation’’ (DCA) und Quanten-Monte-Carlo-Methoden zeigt die großen Perspektiven, diese neuen DMF^2RG Methode zu verwenden.

Introduction

Our ability to understand, predict and control the properties of the materials around us is at the basis of many technological applications that are shaping the world as we know it. Most of these applications are based on our deeper comprehension of the quantum properties of matter. Even so, the *quantum realm* is still far from being completely explored, and represents one of the most important frontiers for our physical understanding. There are still several interesting phenomena that remain elusive to us, like the high temperature superconductivity (HTC) or quantum criticality, and many more phenomena that still wait to be unveiled.

Remarkably, the common thread of many of these phenomena is constituted by the relevant role played by the electronic *correlations*. This represents a striking difference from the more conventional situation, where, thanks to the screening of the interaction and to Landau's Fermi liquid theory, we can think of the motion of each electron as if it was independent from the one of the others

On the contrary, in "*strongly correlated*" systems the individual motion of each electron is deeply influenced by the presence of all the others. The theoretical description of this situation is much more challenging, which has stimulated and is still stimulating us to think out of the box. In fact, in the presence of correlations, often we cannot reason in terms of a simple collection of single electrons anymore. Instead collective modes arise which involve all, or many, (valence) electrons, such as, e.g., a string of misaligned electronic spins in the case of spin polarons, also studied in this thesis. Understanding what this behavior is, and how it affects the macroscopic properties of the systems represents one of the major challenges in the field of modern condensed matter.

There are three main strongly interconnected paths to achieve this goal: The experimental exploration, the purely theoretical analysis, and the computational (numerical) approach. In this thesis we are focused on the two latter aspects, and on the connections between them, i.e., how a mathematical theory can be implemented numerically to obtain results, when, as it is almost always the case, an analytical solution is not feasible.

One of the main starting points of this thesis' work, is the dynamical mean-field theory (DMFT). This approach is based on the mapping of a lattice problem onto a single impurity site. The physics captured by DMFT can be understood considering the limit where it becomes exact: the limit of infinite dimensions. In this limit the spatial fluctuations average out and the physics becomes purely local, from which the name "mean-field", while on the other hand, the fluctuations in time are fully retained, and hence the name "dynamic". Although this limit

might sound exotic, DMFT has proven to be an extremely successful tool in the description of strong electronic correlations, succeeding where all the perturbative methods are bound to fail, such as for the description of the Mott metal insulator transition. This is possible because, in DMFT the local physics is treated non perturbatively. For these reasons the last fifteen years have seen the rise of DMFT, in combination with density functional theory (DFT+DMFT), as the tool-of-choice to study strongly correlated materials.

Unfortunately, however, the "mean-field" nature of DMFT manifests itself in a number of physical situation of interest: This is when the nonlocal correlations, neglected by DMFT, play a major role, as, e.g., in low-dimensional systems, or for systems close to a quantum phase transition. A second drawback of DMFT is that, due to the high computational cost of the solution of its many-body problem, it can treat only a restricted number of degrees of freedom. Hence, it is necessary to downfold the high energy degrees of freedom of the original Hamiltonian, for which the strong electronic correlations are less important, onto a low-energy Hamiltonian, which is then treated in DMFT. The downfolding procedure, however, is not uniquely defined and, in practice, it requires the introduction non *ab-initio* parameters, in particular to represent the screened Coulomb interaction in the low-energy Hamiltonian. This represents a major drawback for the predictive power of DMFT-based methods.

To overcome these drawbacks we need to make a further effort and *go beyond* DMFT. To this end, the strategy that we will follow consists in combining the strengths of DMFT with those of two other methods which, taken singularly due to their perturbative nature, are not suited for the description of materials in the strongly correlated regime. These methods are the *GW* which is capable to deal directly with the full expression of the Coulomb interaction, and the functional renormalization group, which, is ideally suited to study in an unbiased way the competing instabilities of a system. However, combining two theories, is a nontrivial task: This can only work if the two methods act in synergy. Therefore one of our major efforts consisted in bridging DMFT with *GW* first, and fRG then in the most effective way.

The combination of *GW* and DMFT was already proposed more than one decade ago in a seminal paper [24] by Biermann and coworkers. While the derivation on paper of the new method, named *GW*+DMFT, is particularly elegant, its practical implementation has been hitherto difficult and it was achieved only in a few cases. This specific, but very important, aspect represents the focus of our work: We have implemented a simplified scheme, which combines some of the strengths of *GW* with the ones of DMFT for the case of a prototypical material, the strongly correlated metal SrVO₃. In order to obtain an implementation feasible at a relative cheap computational cost, we have traded some of the elegance of the original theory in favor of a further "quasiparticle" approximation in *GW*, obtaining a method which is doable at an effort similar to the one required by more the more standard DFT+DMFT algorithms. The application of this method to the case of SrVO₃ allowed us to show an improved agreement of our results with the experiments as compared to the DFT+DMFT results. Furthermore, a comparison of our results with those of rigorous (and cumbersome) *GW*+DMFT implementations shows that the main features of the latter are correctly reproduced.

With the combination of DMFT with fRG, instead, we aimed at a different issue: The treat-

ment of correlations over all length scales for systems with competing instabilities in the regime of intermediate to strong electronic coupling. One of the most famous examples in this respect is given by the two-dimensional Hubbard model used to describe the copper-oxide layers supposed to be one of the most crucial ingredients for the basic understanding of high-temperature superconductivity in the cuprates. Already at weak coupling, due to the reduced dimensionality and hence to the properties of the Fermi surface, a very rich phase diagrams arises, ranging from superconductivity, antiferromagnetism, ferromagnetism, and different types of charge order. This reflects the emergence of several comparable energy scales in the systems, a problem ideally suited for fRG, that can deal unbiasedly with the emergent instabilities. However, the weak coupling limitation of the fRG only allows for indicating what the situation in the strong coupling regime, relevant for HTC, might be. At the same time, due to the reduced dimensionality and to the importance of nonlocal correlations DMFT alone also fails in describing these phenomena. We show, however, that a combined approach of fRG and DMFT, can be derived exactly and is applicable to this class of situations. The nonperturbative description of the local correlations in DMFT is combined with the unbiased treatment of competing instabilities of fRG. From the theoretical point of view we have shown by means of a Feynman diagrammatic analysis, that, even in its first most simple implementation, is the fRG formalism to avoid any double counting of diagrams, and we have also compared the diagrammatic content of DMF²RG to that of other diagrammatic extensions of DMFT. On the practical point of view we have performed the first implementation of the method, and applied to the test case of a two-dimensional Hubbard model, obtaining promising results. Motivated by this, we are confident that the work presented in this thesis can represent a ground zero for several further developments and high impact applications in the field of quantum many-body theory.

Outline

One of the main challenges that we have experienced during the work of this thesis has been represented by the complex communication between people with different scientific backgrounds. This aspect is reflected in the style of this thesis, because some concepts that may sound obvious to people experienced, for example, in fRG can be more difficult to assimilate for someone more trained in DMFT, and *vice versa*. For this reason we decided to be pedagogical in several parts of the thesis, especially when the different approaches used are introduced. At the same time, as we aim at the combination of different theories, we devoted quite some effort trying to clarify the physical content of each of them, their range of applicability and their representation in terms of Feynman diagrams.

The main structure of the thesis is organized as follows. The **first chapter**, is devoted to the presentation to the three existing approaches to electronic correlations that we are going to use afterwards, arranged in an ideal order of complexity of the corresponding Feynman diagrams: First the GW , based on ladder diagrams, then the fRG, based on parquet diagrams, and, finally, DMFT which includes all possible local diagrams. More in detail, after briefly describing density functional theories, we will focus on the GW equations. First we will derive the exact set of Hedin's equation and then the GW approximation to them.

The second part of this chapter is devoted to fRG. This will be analyzed in the language of Feynman diagrams: first the exact hierarchy of flow equations will be derived, then the truncation to it, necessary for making the problem tractable, will be discussed, and eventually the corresponding diagrammatic content will be shown. The section is concluded by an overview of the most common choices for the cutoff functions.

Finally we will turn our attention to DMFT. This will be first derived in a more standard way. Then we will also propose a more unusual derivation, based on functional integral methods. The chapter is concluded by a brief discussion about the DMFT description of the Mott transition.

The **second chapter** is devoted to $GW+DMFT$. The method will first be introduced, emphasizing how GW and DMFT can be integrated in a single, formally elegant, method and the possible advantages of doing this. The practical implementation, however presents several technical complication, and, in a second part of the chapter, we will propose a simplified scheme, which relies on a quasiparticle approximation to the GW self-energy. We will discuss then how, with this approximation, we can perform quasiparticle $GW+DMFT$ calculations keeping substantially unaltered the DFT+DMFT main steps.

In the last part of this chapter, we present the results obtained testing our quasiparticle $GW+DMFT$ implementation in VASP for the correlated metal $SrVO_3$. The improvement over conventional DFT+DMFT is shown by a comparison with experimental data. Finally our results are compared with those obtained within a much more demanding $GW+DMFT$ calculation, exhibiting

good agreement for the main features.

In the **third chapter** we present DMF²RG, our novel approach, obtained by combining DMFT and fRG, to study electronic correlations on all length scales. In the first part of the chapter we present the state-of-the-art methods to treat strong electronic correlations beyond DMFT. This way we emphasize how our new method, exploiting the strengths of fRG, can be competitive with already established approaches. Specifically, we will then demonstrate how the flexible structure of fRG allows us to include in an algorithmically simple way the local nonperturbative physics of DMFT as a starting point for the flow equations. We will then use the results obtained in the first chapter to understand the diagrammatic content of DMF²RG.

After that, we will demonstrate the applicability of the new scheme, by presenting our first practical implementation of DMF²RG. As a test case, we applied it to the two-dimensional Hubbard model, obtaining results for the self-energy, the spin susceptibility, and the one particle irreducible vertex. The former are shown to be in qualitative agreement with results obtained by cluster extension of DMFT and lattice quantum Monte Carlo respectively. A complete understanding of the results for the vertex has not yet been fully gained, but its importance for future studies as well for the interpretation of already obtained results, encourages us to further, more accurate, analysis. This directly leads us to our conclusions and to a rich outlook of further possible improvements, in-depth analysis and possible applications of our newborn approach.

The thesis is completed by the conclusion chapter in which we briefly recapitulate the content of the thesis and the main achievements obtained in it, and the future perspectives of our research work.

Chapter 1

Different methods for different correlations: GW, fRG, and DMFT

In this chapter we prepare the ground for the discussion of the main results of this thesis, presented in the other two chapters. To this end we introduce here the three existing approaches to electronic correlations that we are going to use afterwards, arranged in an ideal order of complexity of the corresponding Feynman diagrammatics: First, the GW based on ladder diagrams for the charge screening, then the fRG, based on parquet diagrams, and, finally, DMFT which includes all possible local diagrams. More in detail, after briefly describing density functional theories, we focus on the GW equations: First we derive the exact set of Hedin's equations and then the GW approximation to them. The second part of the chapter is devoted to fRG. This is analyzed in the language of Feynman diagrams: first the exact hierarchy of flow equations will be derived, then the truncation to it, necessary for making the problem tractable, will be discussed, and eventually the corresponding diagrammatic content will be shown. The section is concluded by an overview of the most common choices for the cutoff schemes. Finally, we will turn our attention to DMFT. This will be first derived in a rather standard way. However we will also propose a less common derivation, based on functional integral methods, which is closer to the spirit of the new developments described in the other chapters. The chapter is concluded by a short discussion about the DMFT description of the Mott transition. We have arranged the chapter so that each section is independent from the others, being self-contained and, unless when strictly necessary, we have tried to avoid technicalities, rather focusing on the physical content of the methods, to facilitate the reading of those who are familiar with one of the methods and are experts of the others.

The present thesis is focused on the electronic properties of condensed matter at low temperatures. With low temperatures we mean the temperature interval up to $\mathcal{O}(10^3)$ K, or equivalently up to $\mathcal{O}(0.1)$ eV. The limiting energy scale is essentially set by the melting temperature of the crystal: For higher temperatures the motion of the ions cannot be considered to be re-

stricted to small vibrations around the position of the lattice sites, and the Born-Oppenheimer approximation [28], that we are going to discuss in the following, does not hold anymore.

On the other hand, when lowering the temperature we encounter several other energy scales, connected with collective excitations or with spontaneous symmetry breaking. For example ferromagnetic or antiferromagnetic transitions usually occur for temperatures below $T_N \sim \mathcal{O}(10^2 - 10^3)\text{K}$, while superconductivity is hitherto restricted to temperatures below $T_C \approx 137\text{K}$.

Consequently, we want to describe the systems of interest using a Hamiltonian which captures the physical properties at these energy scales, while, for simplicity, it may neglect, or treat in a simplified way those effects which supposedly do only play a marginal role, like for example the ionic motion. Considering this, the Hamiltonian that we will use to describe the electronic properties reads:

$$\mathcal{H}_e = \underbrace{\sum_i \left[-\frac{\hbar^2 \Delta_i}{2m} + \sum_l -\frac{e^2}{4\pi\epsilon_0} \frac{Z_l}{|\mathbf{r}_i - \mathbf{R}_l|} \right]}_{\mathcal{H}_0} + \underbrace{\frac{1}{2} \sum_{i \neq j} \frac{e^2}{4\pi\epsilon_0} \frac{1}{|\mathbf{r}_i - \mathbf{r}_j|}}_{\mathcal{H}_{ee}}, \quad (1.1)$$

where Δ_i is the Laplacian operator, m represents the electron mass, \mathbf{r}_i is the position of electron i , with charge $-e$ and spin σ_i , and \mathbf{R}_l is the position of the nucleus l , with charge $Z_l e$, \hbar is the reduced Planck constant and ϵ_0 is the vacuum dielectric constant. The Hamiltonian (1.1) already involves two important approximations:

- The neglecting of relativistic corrections (and of any interaction besides the Coulomb one);
- The so-called Born-Oppenheimer approximation [28]: The degrees of freedom associated with the motion of the nuclei have been decoupled from the ones of the electrons.

The latter is possible due to the fact that the nuclei moves much slower than the electrons, due to the high ratio between the masses of protons and neutrons and the one of electrons. Therefore, in the present approximation, the set of positions $\{\mathbf{R}_l\}$ is considered fixed, i.e. they are the equilibrium position of the nuclei in the periodic lattice. The Coulomb interaction between the nuclei and the electrons then effectively acts as an external potential. However, the determination of the set $\{\mathbf{R}_l\}$ for a real material is itself not an easy task, and sometimes it is determined experimentally instead of being computed from first principles.

It is often desirable to go beyond the Born-Oppenheimer approximation, and treat the motion of the nuclei at least perturbatively around the equilibrium position. This can be done by including a term in the Hamiltonian accounting for the so-called *electron-phonon* coupling: The vibrations of the lattice are treated as quanta, called *phonons*, interacting with the electrons [43]. In some cases the electron-phonon coupling can be very important, e.g., it is at the origin of conventional low-temperature superconductivity.

Let us focus on the terms constituting the Hamiltonian (1.1). The first term accounts for the standard kinetic energy of the electrons; The second term for the Coulomb interaction between

the electrons and the nuclei. As mentioned, this term can also be seen as an external potential term $v_{\text{ext}}(\mathbf{r})$. Such a potential often (and in all the cases we will consider) possesses translational invariance under displacement of a lattice vector \mathbf{R} :

$$v_{\text{ext}}(\mathbf{r} + \mathbf{R}) = v_{\text{ext}}(\mathbf{r}). \quad (1.2)$$

This symmetry has very important consequences, due to the *Bloch theorem* [14], and guarantees the conservation of the total momentum. Finally, the third term accounts for the Coulomb interaction between the electrons and is the most difficult to treat.

1.1 Electronic correlations

The Coulomb interaction between the electrons makes them *correlated*, i.e. the motion of one electron is influenced by the motion of all the others. Formally, due to the interaction term \hat{v}_{ee} , the Hamiltonian (1.1) is non-separable. Indeed, if the Coulomb interactions were so small that one could safely neglect them, it would be possible to write the N particle electronic wave function solution of the Schrödinger equation defined by \mathcal{H} as the Slater determinant of the one electron wave functions $\psi_{n\mathbf{k}\sigma}(\mathbf{r})$. These $\psi_{n\mathbf{k}\sigma}(\mathbf{r})$ would be the solutions of the single particle eigenvalue equation:

$$\mathcal{H}_0\psi_{n\mathbf{k}\sigma} = \left(-\frac{\hbar^2\Delta_i}{2m} + v_{\text{ext}}(\mathbf{r}) \right) \psi_{n\mathbf{k}\sigma} = \epsilon_{n\mathbf{k}}\psi_{n\mathbf{k}\sigma}, \quad (1.3)$$

with eigenenergies $\epsilon_{n\mathbf{k}}$ being the *band energies* of the n th band. Furthermore, due to the above-mentioned periodicity of the external potential, the one-particle functions $\psi_{n\mathbf{k}\sigma}$ are Bloch functions [14]:

$$\psi_{n\mathbf{k}\sigma}(\mathbf{r}) = e^{-i\mathbf{k}\cdot\mathbf{r}}u_{n\mathbf{k}}(\mathbf{r}), \quad (1.4)$$

with $u(\mathbf{r} + \mathbf{R}) = u(\mathbf{r})$, for \mathbf{R} being a lattice vector.

In realistic situations, however, the Coulomb energy can hardly be neglected: The ratio between kinetic and potential energy from \mathcal{H}_{ee} is *not* small. To estimate the ratio let us proceed as follows: First let us assume that N particles occupy a volume Nr_0^3 . Then the minimum kinetic energy per particle will be, due to the uncertainty principle, $\mathcal{O}(\hbar^2/mr_0^2)$. The Coulomb energy per particle, instead, can be estimated as $\mathcal{O}(e^2/\epsilon_0r_0)$, under the assumption that every particle interacts mainly with its nearest neighbors [4]. The ratio between potential and kinetic energy will therefore be roughly proportional to $r_0/a_0 \equiv r_s$, $a_0 = 0.529\text{\AA}$ being the Bohr radius. Neglecting the electron-electron interaction would be reasonable in the limit of high density, corresponding to $r_s \ll 1$. This is not true in conventional metals where r_s is usually of order $\mathcal{O}(1)$, and therefore potential and kinetic energy are of the same order. Hence one needs to deal with the full complexity of the Hamiltonian (1.1).

The exact numerical solution is, however, not feasible already for an extremely small $\mathcal{O}(10)$ number of particles. Besides, the knowledge of the full wave function is, by large extent, also not particularly useful, since one is only interested in the thermodynamic properties of the

system, rather than in the motion of the individual electrons. To overcome these difficulties several techniques have been developed so far to tackle the many electron problem in condensed matter physics during the last century,. Among them, a very successful one is the **local density approximation** (LDA) of density functional theory (DFT), which will be described in the next paragraph. The success of LDA in computing the electronic properties of most materials and in particular of metals is an extremely surprising information: in spite of the large Coulomb energy a description in terms of *effectively* independent particles, called **quasiparticles**, in several (but not all) cases works very well. The electron-electron interaction is accounted for by an *effective potential* acting on the quasiparticles.

A posteriori it is possible to say that this is a consequence of the *Fermi liquid theory*: due to the *adiabatic continuity* [8], in the absence of electronic phase transitions, one can continuously connect the excitation of the system in which the electron-electron interaction is ideally turned off with the (single-particle) excitations of the interacting system. When this picture becomes questionable, and therefore LDA fails to describe the properties of the system, one talks about *strongly correlated materials*. These require a more sophisticated treatment of the electronic interactions.

1.2 LDA: mapping onto independent particles

A quite widespread, though unsatisfactory, definition in the strongly correlated community states that *a strongly correlated material is a material for which LDA fails*. Then, as pointed out by Robert O. Jones [90] it is of great importance to have a feeling of what LDA can do and in which cases it is successful. This is what we are going to discuss in this paragraph.

LDA is a ground state theory: it is designed for the calculation of the ground state energy:

$$\langle \Psi | \mathcal{H}_e | \Psi \rangle = \int d^4x_1 \dots \int d^4x_N \Psi^*(\mathbf{x}_1, \dots, \mathbf{x}_N) \mathcal{H}_e \Psi(\mathbf{x}_1, \dots, \mathbf{x}_N), \quad (1.5)$$

where \mathbf{x}_i is a shorthand for \mathbf{r}_i, σ_i , and $\int d^4x_i \equiv \sum_{\sigma_i} \int d^3r_i$, and N is the number of particles.

To gain some physical insight we introduce the reduced density matrix:

$$\rho^{(1)}(\mathbf{x}, \mathbf{x}') \equiv N \int d^4x_2 \dots \int d^4x_N \Psi(\mathbf{x}, \mathbf{x}_2, \dots, \mathbf{x}_N) \Psi^*(\mathbf{x}', \mathbf{x}_2, \dots, \mathbf{x}_N); \quad (1.6)$$

and the one- and two-particle densities, with $\mathbf{x} = (\mathbf{r}, \sigma)$ and $\mathbf{x}' = (\mathbf{r}', \sigma')$:

$$n^{(1)}(\mathbf{r}) = \sum_{\sigma} \rho^{(1)}(\mathbf{x}, \mathbf{x}) = N \sum_{\sigma} \int d^4x_2 \dots \int d^4x_N |\Psi(\mathbf{x}, \mathbf{x}_2, \dots, \mathbf{x}_N)|^2, \quad (1.7)$$

$$n^{(2)}(\mathbf{r}, \mathbf{r}') = N(N-1) \sum_{\sigma, \sigma'} \int d^4x_3 \dots \int d^4x_N |\Psi(\mathbf{x}, \mathbf{x}', \mathbf{x}_3, \dots, \mathbf{x}_N)|^2. \quad (1.8)$$

With this we rewrite the total energy as:

$$E = \int d^4x' \int d^4x \delta(\mathbf{x} - \mathbf{x}') \left(\frac{-\hbar^2}{2m} \Delta + v_{\text{ext}}(\mathbf{r}) \right) \rho^{(1)}(\mathbf{x}, \mathbf{x}') + \frac{1}{2} \int d^3r \int d^3r' \frac{e^2 n^{(2)}(\mathbf{r}, \mathbf{r}')}{4\pi\epsilon_0 |\mathbf{r} - \mathbf{r}'|}. \quad (1.9)$$

On physical grounds, let us split the two particle density in two terms, introducing the so-called correlation hole function $h(\mathbf{r}, \mathbf{r}')$:

$$n^{(2)}(\mathbf{r}, \mathbf{r}') = n^{(1)}(\mathbf{r}) [n^{(1)}(\mathbf{r}') + h(\mathbf{r}, \mathbf{r}')]. \quad (1.10)$$

The first term in the above equation is nothing more than the probability of finding an electron in the position \mathbf{r} and a second one in the position \mathbf{r}' assuming that there is no correlation between the two electrons (not even the one arising from the Pauli principle).

All the complication has simply been shifted to the hole function. The latter accounts for the fact that the conditional probability of having one electron at the position \mathbf{r}' given that another electron is at the position \mathbf{r} is *not* the product of the two one-particle densities. In fact to know the density of the second electron, one has to take into account the negative density (correlation hole) that the first electron leaves behind in the rest of the space and that depends on its position \mathbf{r} .

A big step forward to find the ground state energy is due to Kohn and Sham [103]. Their idea relies on the Hohenberg-Kohn theorem [67], which states that the ground state properties of a full many body problem can be found by solving an effective single particle problem associated with an effective potential $V^{\text{eff}}[n(\mathbf{r})]$, which is a functional of the ground state density $n(\mathbf{r})$ only. Given this effective potential the ground state energy can be determined using a Ritz-variational scheme, as the functional minimum of the energy functional with respect to the density.

At first sight the gain is not apparent: We have traded an N -particle problem, that we are not able to solve, for a single-particle problem defined by a potential that we do not know. However, the most important information of the Hohenberg-Kohn theorem is that the ground state energy is a functional of the density alone, and not of the wave function. This formalizes an idea that dates back to Dirac, who already in the 1930s wrote [38]:

[...] the whole state of the atom is completely determined by this electric density; it is not necessary to specify the individual three-dimensional wave functions that make up the total electric density. [...]

Following Kohn and Sham, we next write the total energy functional as:

$$E[n^{(1)}] = T_0[n^{(1)}] + \int d^3r v_{\text{ext}}(\mathbf{r}) n^{(1)}(\mathbf{r}) + \frac{1}{2} \int d^3r \int d^3r' \frac{e^2 n^{(1)}(\mathbf{r}) n^{(1)}(\mathbf{r}')}{4\pi\epsilon_0 |\mathbf{r} - \mathbf{r}'|} + E_{\text{xc}}[n^{(1)}] \quad (1.11)$$

Where T_0 is the kinetic energy of a system of **non-interacting electrons** with density $n^{(1)}$, which are taken as a reference system. The second term accounts for the interaction of the

electrons with the lattice ions. The third term is the Coulomb energy that a system of electrons with density $n^{(1)}$ would have if they were classical particles. It is easy to see that this arises by including the first term of Eq. (1.10) in the last one of Eq. (1.9). Finally the last term E_{xc} is called **exchange and correlation energy** and includes all the unknown terms that have been neglected so far.

It consists of two contributions: (i) a potential and (ii) a kinetic energy one.

The former (i) describes the decrease of the Coulomb repulsion between electrons in the same spin state due to the Pauli principle and pure correlation effects due to the fact that electrons do not move independently from each other. This term, sometimes called exchange and correlation term, reads:

$$U_{xc} = \int d^3r n^{(1)}(\mathbf{r}) \frac{1}{2} \int d^3r' \frac{e^2 h(\mathbf{r}, \mathbf{r}')}{4\pi\epsilon_0 |\mathbf{r} - \mathbf{r}'|}. \quad (1.12)$$

The second contribution (ii), also included in E_{xc} , accounts for the difference between the true kinetic energy T of the interacting system and the kinetic energy T_0 of a reference non-interacting system with the same density: $T[n^{(1)}] - T_0[n^{(1)}]$. This term originates from the fact that in the presence of the Coulomb interaction the wave function of the system is deformed, compared to the one of the noninteracting system, even if the two systems share the same electron density. In other words the interacting system will minimize its total energy and therefore adjust its wave function to reduce the potential energy at the price of having a higher kinetic energy compared to the noninteracting system.

Up to now no approximation has been made. The energy has just been expressed as a functional of the electron density alone, and then has been split in a known part and in an unknown part, in which all the difficulties are hidden. On the other hand such a splitting is very convenient, because all the quantities but E_{xc} in Eq. (1.11) can be evaluated exactly, and therefore we only need an approximation for the exchange and correlation energy.

However, before discussing the possible approximation schemes for E_{xc} , let us discuss now how to obtain a single particle Schrödinger equation from the energy functional, Eq. (1.11). First, let us write the density in terms of one-electron wave functions ϕ_i :

$$n^{(1)}(\mathbf{r}) = \sum_{\sigma} \sum_i^N |\phi_i(\mathbf{x})|^2. \quad (1.13)$$

Now the functional (1.11) is minimized with respect to the ϕ_i 's, yielding:

$$\left[-\frac{\hbar^2 \Delta}{2m} + V^{\text{eff}}(\mathbf{r}) - \epsilon_i \right] \phi_i(\mathbf{x}) = 0. \quad (1.14)$$

Here the effective one-particle potential (depending on the particle density) has been identified with:

$$V^{\text{eff}}(\mathbf{r}) = v_{\text{ext}}(\mathbf{r}) + \int d^3r' \frac{e^2 n^{(1)}(\mathbf{r}')}{4\pi\epsilon_0 |\mathbf{r} - \mathbf{r}'|} + \frac{\delta E_{xc}[n^{(1)}]}{\delta n^{(1)}(\mathbf{r})}, \quad (1.15)$$

and the ϵ_i 's appearing in Eq. (1.14) are the Lagrange multipliers used to impose the orthogonality of the one-electron wave functions. Let us stress that all this construction is aimed at

the calculation of the ground state energy. This means that there is no theoretical argument to attribute a physical meaning to the Lagrange multipliers ϵ_i 's and to the one-particle wave functions ϕ_i 's. One is, in principle, only allowed to see them as the eigenvalues and eigenvectors of a simplified one-particle problem that can be used as a tool for the calculation of the ground state energy of a many-body problem.

However, the great success obtained by the LDA is also due to the empirical observation that very often the Lagrange multipliers ϵ_i can be identified with the **real excitations** of the many-body system. Therefore these are used to compute the bandstructure. In this sense LDA does not give only *ground state properties* of a system, but also the *excitation spectra*.

Approximations for the exchange and correlation energy

The last step that we need to actually employ the density functional theory described above is the definition of an approximation for E_{xc} . It is only at this level that some approximation will be introduced: up to now we have only exactly rewritten the problem in a form more suited for developing an approximate scheme.

The name *local density approximation*, in a strict sense, refers to the original approximation proposed by Kohn and Sham, who assumed:

$$E_{xc} = \sum_{\sigma} \int d^3r n^{(1)}(\mathbf{r}) \epsilon_{xc}[n^{(1)}(\mathbf{r})], \quad (1.16)$$

where $\epsilon_{xc}[n^{(1)}]$ is the exchange and correlation energy per particle of a *homogeneous electron gas* with density $n^{(1)}$, that can be obtained, for example by means of quantum Monte Carlo calculations [32]. The name explicitly refers to the fact that the integrand in Eq. (1.16) only depends on the *local* value of the electron density. So in this approximation the homogeneous electron gas is used as reference system.

What one hopes for is that the error made in the estimation of the exchange and correlation potential is small enough to give reasonable results, but in general the approximation is well justified only in the limits of slowly varying densities and very high densities [89]. The simplest generalization of LDA is the *local spin density approximation* (LSDA), which generalizes $\epsilon_{xc}[n_{\uparrow}^{(1)}(\mathbf{r}), n_{\downarrow}^{(1)}(\mathbf{r})]$ to the exchange and correlation energy per particle of a homogeneous electron which is allowed to undergo a spin polarization.

Besides LDA, several other approximations have been developed to improve the description of the exchange and correlation energy, also including non local terms in the functional. This led to several other approximated schemes, including for example the generalized gradient approximation (GGA), hybrid functionals and LDA+U. All these methods, based on the mapping of the interacting problem onto an effective single-particle problem go under the name of density functional theory. However, with a little abuse of notation we will often refer to them simply as LDA.

To summarize, in all DFT methods some system, most usually the homogeneous electron gas, is taken as reference for developing an approximation for the exchange and correlation

energy of the real system. Surprisingly this approximation very often yields very good results not only for the **ground state** properties of the system but also for the **excitation spectra**, i.e. the bandstructure.

Solution of the one-particle Schrödinger equation

To complete the discussion about the LDA methods, we only need to discuss the numerical solution of Eq. (1.14). This can be done in a self-consistent way following the protocol below:

- i. Choose a set of starting one-particle wave functions $\phi_i(\mathbf{r})$, e.g., atomic ones, and calculate the density $n^{(1)}$, by Eq. (1.13).
- ii. Calculate the effective potential $V^{\text{eff}}(\mathbf{r})$ associated with the density $n^{(1)}(\mathbf{r})$.
- iii. Solve the Kohn Sham equations. (1.14) yielding the new wave functions ϕ_i^{new} .
- iv. Compute the new density from the new wave functions using Eq. (1.13).
- v. Compare the old and the new density, and iterate (continuing with ii) until the difference is smaller than some threshold value ϵ_{thres} .
- vi. Once self consistency is reached identify the density $n^{(1)}(\mathbf{r})$ with the ground state density $n(\mathbf{r})$.

From this self-consistent density one can finally compute the ground state energy, and, as mentioned, also the bandstructure.

The approach described above is implemented in several codes available to the scientific community, which mainly differ in the choice of the basis, functions, and it is now the standard for calculating properties of solids. In the following we will describe a different approach, the *GW* approximation, which allows to go beyond LDA (or DFT), still keeping into account the full complexity of the Hamiltonian, and which, on the long term, is a good candidate for becoming the new standard for the computation of properties of solids.

1.3 *GW*: Hedin's equations and the *GW* approximation

Even though the LDA has proven to be a very powerful tool, there is a number of cases for which LDA and related methods fail. An important example are semiconductors, for which the spectral gap is systematically underestimated compared to the experimental values, up to a factor 50% in the case of germanium.

The reason for this discrepancy has been attributed to the presence of extended sp^3 states, whose exchange and correlation interaction is approximated in a quite poor way by the local exchange of LDA. Apart from this, as we will discuss later, LDA also fails for the description of the transition metal oxides (TMO), even at a qualitative level. For example it does not give the insulating behavior of many TMO's.

Also from the theoretical point of view it would be desirable to have a method that goes beyond LDA, at least in two respects. These are, first, the fact that a deep reason for the identification of the spectra with the eigenvalues of the auxiliary one-particle problem is missing, and, second, the fact that LDA is based on the estimation of the exchange and correlation energy from a calculation (often numerically) done for the homogeneous gas. This, as we will discuss in the third chapter, makes the combination of LDA with a diagrammatic method, such as DMFT, more difficult.

For all these reasons, it is strongly desirable to devise methods that go beyond LDA, allowing for a better treatment of the correlations. A first possibility that people have explored is the improvement of the functional E_{xc} . However the approaches developed so far in this direction, like GGA or LDA+ U , were not able to solve the main problems in a systematic way. In the case of GGA, for example the improvement compared to LDA was mainly quantitative, rather than qualitative, and not universally better. On the other hand LDA+ U , besides introducing undesirable fitting parameters, often does not predict the correct ground state. It predicts a too strong tendency towards polarized states, and it opens a gap in the density of states too easily.

An alternative approach consists in using techniques based on quantum field theory. In this context the quantity of main interest is the (one-particle) Green's function, defined as:

$$G(x_1, x_2) = -\langle T[\hat{\psi}(x_1)\hat{\psi}^\dagger(x_2)] \rangle, \quad (1.17)$$

where x_i is a shorthand notation for position in (imaginary) time and space, a spin index and eventually also other quantum numbers (e.g. band index): $x_1 = (\mathbf{r}_1, \tau_1, \sigma_1)$. The operators $\hat{\psi}$ are in the Heisenberg notation, and T stands for a time ordered product. Knowing the Green's function one is able to compute:

- the ground state energy;
- the expectation value of any one-particle operator (and correspondingly from the knowledge of an n -particle Green's function the ground state of any n particle operator, e.g. the spin or charge susceptibility);
- the one-electron excitation spectrum, that in principle can be directly compared with photoemission experiments.

A very important quantity is the self-energy $\Sigma_{\mathbf{k}}(\omega)$.

$$G_{\mathbf{k}}(\omega) = \frac{1}{\omega - \epsilon_{\mathbf{k}} + \mu - \Sigma_{\mathbf{k}}(\omega)}, \quad (1.18)$$

where the Green's function has been Fourier transformed in a frequency/momentum representation, μ is the chemical potential, and $\epsilon_{\mathbf{k}}$ is the eigenenergy of a quasiparticle of momentum \mathbf{k} in the noninteracting system (momentum and frequency conservation has been implicitly assumed by taking a Green's function that depends only on one frequency and momentum argument; for simplicity we disregard a possible spin and orbital dependence here.).

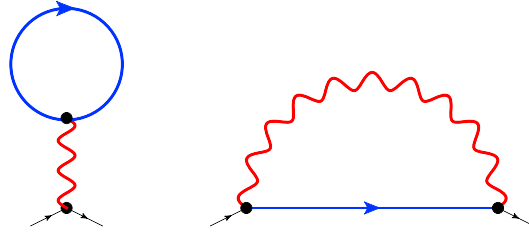


Figure 1.1: The Hartree diagram (on the left) accounts for the interaction of one electron with the background electronic density. The Fock diagram (on the right) is the lowest order diagram encoding exchange effects.

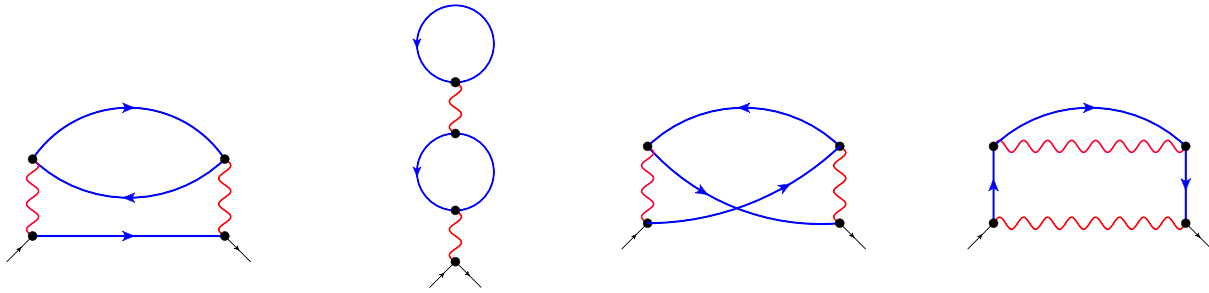


Figure 1.2: Selected self-energy diagrams at second order perturbation theory in the interaction. A straight line represents a noninteracting Green's function, a wavy line represents an interaction vertex.

The self-energy accounts for all the interaction effects in the Green's function. In the absence of interaction, the Green's function can be trivially computed diagonalizing the noninteracting Hamiltonian and the self-energy is zero. In the presence of an interaction V , i.e., the vertex associated with the interaction part of the Hamiltonian \mathcal{H}_{ee} expressed in second quantization, this does not hold anymore and computing the self-energy becomes involved. The first thing that one can think of, to compute the self-energy, is a perturbative expansion in the interaction. In doing so the first two terms contributing to $\Sigma_{\mathbf{k}}(\omega)$ at the lowest order in the interaction V are the ones depicted in Fig. (1.1), the so called Hartree and Fock term¹.

The approximation obtained by truncating the perturbative expansion for the self-energy to the two diagrams in Fig. 1.1 is called the Hartree-Fock approximation (HFA). It is now well known that while the HFA works reasonably well only for atoms, already for insulating solids the HFA predicts a far too large gap, due to the neglect of *screening effects* that reduce the Coulomb repulsion. The description of metals is even worse: HFA predicts qualitatively wrong results, like a zero density of states at the Fermi level.

If one wants to improve on HFA while still maintaining a perturbative approach a naive

¹Details about the Feynman diagrams can be found in the standard literature, see e.g. [1,43,119]. Unless stated otherwise, in the graphic representations of the Feynman diagrams, a single line depicts a *noninteracting* Green's function, a double line an *interacting* Green's function and a wiggled line an interaction vertex V , and frequency momentum and spin must be conserved at every vertex. The thinner black lines represent the "external legs" of the diagrams, they are reminders for the direction of the incoming or outgoing particles, but do not represent a Green's function.

way of proceeding would be the inclusion of higher order diagrams, like those (shown in Fig. 1.2). However this approach is bound to fail. Indeed at the densities of relevance for metals ($r_s > 1$) the perturbation series does not converge at any finite order and one has to devise better approximation techniques.

In this respect the seminal work of Lars Hedin was very important [59]. He, already in 1965,

- rewrote and reorganized a set of equation "well known to the Green's function people" in a way that is particularly suited for devising approximations. These equations are now called *Hedin's equations*.
- suggested a simple approximation to take into account screening effects (for the Coulomb interaction). This is made possible by the resummation at *infinite order* of a certain class of diagrams, motivated by physical reasons. This approximation goes under the name of *GW* approximation.

We will discuss Hedin's equations and the *GW* approximation to them in the next paragraph.

1.3.1 *GW* diagrammatics

In this paragraph we will derive Hedin's equations. Compared to the original derivation [59], which is based on the functional integral, we will use here a different language based on Feynman diagrams.

The first of Hedin's equations relates the one-particle Green's function with the self-energy.

Let us consider the expansion of the Green's function in terms of Feynman diagrams. The diagrams generated at the lowest orders are shown in Fig. 1.3. One can identify two classes of diagrams contributing to the Green's function: Diagrams that can be cut in two halves by cutting one fermionic line, and therefore called **one-particle reducible**, and diagrams that cannot be divided by cutting one fermionic line, called **one-particle irreducible** (IPI).

It is quite natural to collect all the one-particle irreducible diagram into a single structural unity usually called **self-energy operator** (or simply self-energy) and denoted by $\Sigma(\mathbf{r}, \mathbf{r}', \tau)$, or equivalently, in frequency and momentum space², as $\Sigma_{\mathbf{k}}(i\omega_n)$.

By doing so, we can rewrite all the diagrams contributing to the Green's function as it is shown in Fig. 1.4, where the self-energy has been represented by a shaded circle: every irreducible diagrammatic contribution is included in the self-energy, while every reducible contribution can be obtained by forming a chain of noninteracting Green's function and self-energy insertions.

²We are always assuming that we have translational and time invariance therefore the Green's function depends only on one argument in momentum and frequency space. The time and frequency dependence can be expressed either in real time t and frequency ω or in terms of imaginary time τ and Matsubara frequencies $\omega_n = \pi/\beta(2n+1)$, with $\beta = \frac{1}{k_B T}$ the inverse temperature.

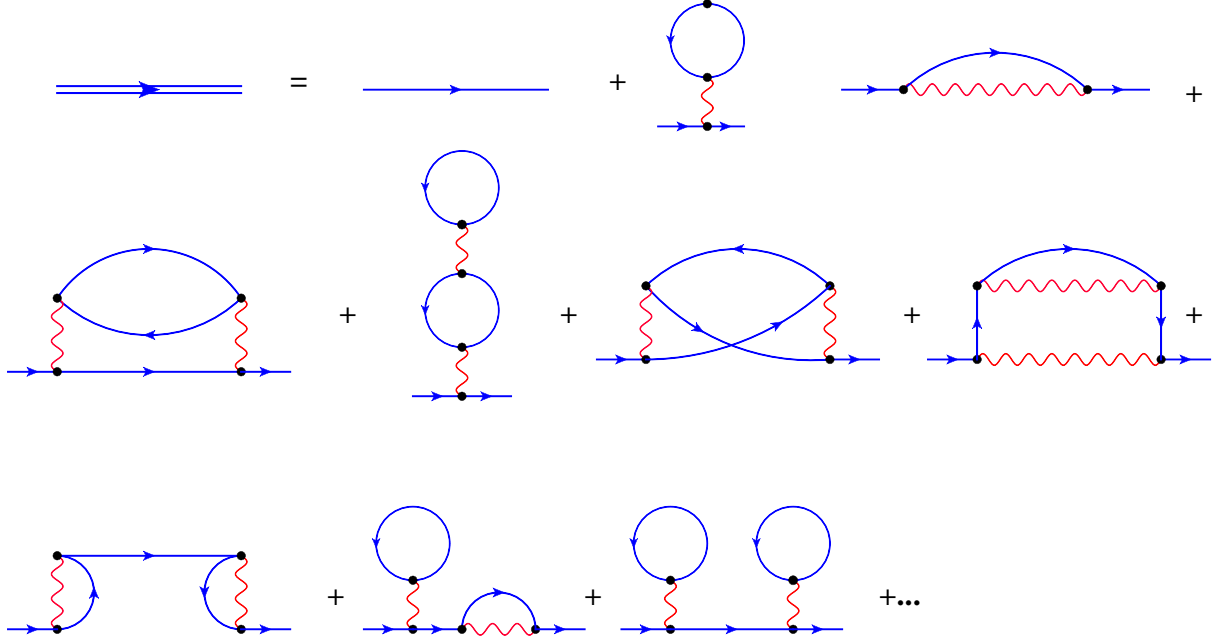


Figure 1.3: Selected diagrams contributing to the Green's function up to the second order in the interaction. The diagrams on the second line are one-particle irreducible, i.e., they contribute to the self-energy. The diagrams on the third line, instead, are one-particle reducible, i.e., they do not contribute to the self-energy, and can be generated as a chain of self-energy insertions.

The diagrammatic equation in Fig. 1.4 is the known as Dyson equation, and its mathematical expression, in real and momentum space reads:

$$G(11') = G^0(11') + \int d2d2' G^0(12)\Sigma(22')G^0(2'1') + \quad (1.19)$$

$$\int d2d2'd3d3' G^0(13)\Sigma(33')G^0(3'2)\Sigma(22')G^0(2'1') + \dots$$

$$= G^0(11') + \int d2d2' G(12)\Sigma(22')G^0(2'1');$$

$$G_{\mathbf{k}}(i\omega_n) = G_{\mathbf{k}}^0(i\omega_n) + G_{\mathbf{k}}^0(i\omega_n)\Sigma_{\mathbf{k}}(i\omega_n)G_{\mathbf{k}}^0(i\omega_n) + \quad (1.20)$$

$$G_{\mathbf{k}}^0\Sigma_{\mathbf{k}}(i\omega_n)G_{\mathbf{k}}^0(i\omega_n)\Sigma_{\mathbf{k}}(i\omega_n)G_{\mathbf{k}}^0(i\omega_n) + \dots$$

$$= G_{\mathbf{k}}^0(i\omega_n) + G_{\mathbf{k}}^0(i\omega_n)\Sigma_{\mathbf{k}}(i\omega_n)G_{\mathbf{k}}^0(i\omega_n).$$

To compactify the expression, we are denoting with a number in the argument a set of space and time coordinates as well as a spin index.

The solution of the equations above can be written as:

$$G(11') = \left([G_0^{-1} - \Sigma]^{-1} \right)_{(11')}; \quad (1.21)$$

$$G_{\mathbf{k}}(i\omega_n) = [(G_{\mathbf{k}}^0(i\omega_n)^{-1} - \Sigma_{\mathbf{k}}(i\omega_n))]^{-1}; \quad (1.22)$$

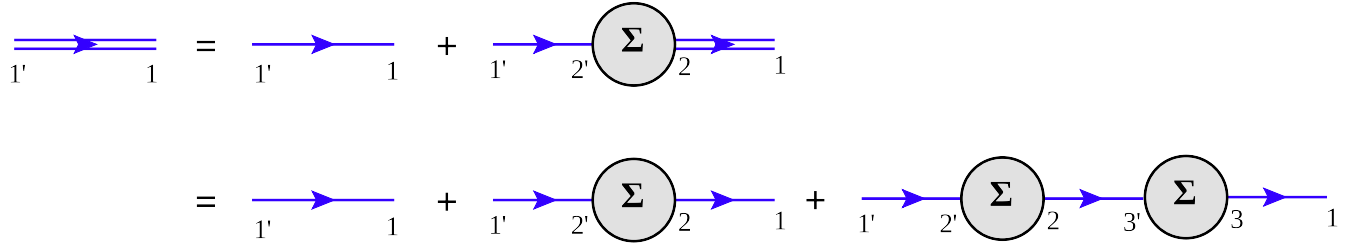


Figure 1.4: Diagrammatic representation of Dyson equation.

where the matrix inversion in the first equation involves an inversion in spatial and temporal coordinates.

Eq. (1.21), or equivalently (1.22), are the desired equations which connect self-energy and Green's function. We will refer to them as **first Hedin's equation** (either in real or momentum space).

In our line of thought we have started from the diagrammatic expansion of the Green's function, used the property of one-particle irreducibility to define the self-energy, from which we have derived the Dyson equation. Equivalently, from a functional integral point of view we can define the self-energy as the difference between the one-particle irreducible (1PI) one-particle vertex for the interacting system $\Gamma^{(1)}(1, 1') = [G]_{(1,1')}^{-1}$ and the 1PI one-particle vertex for the non-interacting system $\Gamma_0^{(1)}(1, 1') = [G_0]_{(1,1')}^{-1}$:

$$[G_0]_{(1,1')}^{-1} - [G]_{(1,1')}^{-1} = \Sigma(1, 1'). \quad (1.23)$$

This equation is just a different way of writing Eq. (1.21), however it can be seen as a definition for the self-energy, from which one can derive Eq. (1.19). The advantage of this perspective is that it highlights the relation between the self-energy and the 1PI one-particle vertex function, which in turn can be obtained from functional derivation³, via the so-called **effective action** $\Gamma[\phi, \bar{\phi}]$ (a quantity related to this functional will be discussed in the next sections). Taking Eq. (1.23) as a definition for the self-energy, one can indeed show that the diagrammatic contributions to it are the one-particle irreducible diagrams described above. More details about this approach can be found in reference [134].

To derive the next of Hedin's equations we introduce the concept of **irreducibility in the interaction**. We represent an interaction vertex V by a wiggled line. For our purposes $V(11'; 22')$ is the Coulomb interaction vertex appearing in the interaction part of the Hamiltonian written in second quantization. A diagram will be called *reducible in the interaction* if it can be separated into two halves by cutting one interaction line, otherwise it will be *irreducible in the interaction*. This concept is introduced in analogy with the (more standard) one-particle irreducibility to introduce two new diagrammatic elements: The screened interaction W and the polarization operator P , shown in Fig. 1.5. The screened interaction is defined as the sum of all Feynman diagrams which connect the left and right side by interactions V . As the self-energy is account-

³In an almost equivalent way the self-energy can also be derived from the derivative of other functionals, like, e.g., the *effective interaction* functional [156].

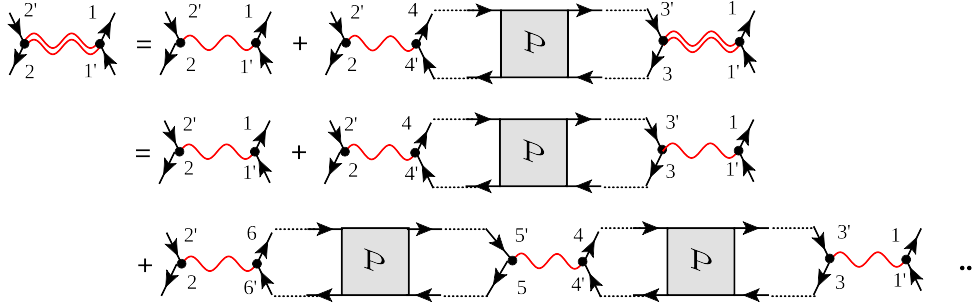


Figure 1.5: Relation between the screened interaction W , represented by a double wiggled line, and the polarization operator P , denoted by a square.

ing for the fact that the electrons interact among themselves in their motion, the polarization accounts for the fact that the Coulomb interaction in a medium is screened. Indeed, the interaction of the electrons is different in a medium than in vacuum: Each electron will polarize the background charges, scatter other electrons, and take part in collective excitations.

These effects are considered in the polarization, that plays a role analogous to the one of the self-energy for the electron propagator: it collects in a structural unit all the irreducible diagrams that correct the bare interaction. It is easy to see then that all the diagrams contributing to W can be obtained by forming a chain of polarization P and bare interaction V , like in Fig. 1.5. The only formal difference compared to Eq. (1.19) consists in the fact that, while the (single-particle) Green's function and the self-energy have only two indices, the interaction, the polarization and the screened interaction are four points objects, depending on four indices. Indeed the polarization is related to the two-particles Green's function. Translated into formulas the equation of Fig. 1.5 reads:

$$W(11'; 22') = V(11'; 22') + \int d3d3' V(11'; 33') P(3'3; 4'4) W(44'; 22'). \quad (1.24)$$

The four indices of the screened interaction label the particle and the hole that are created at the two ends of the diagram. As it is defined the polarization is still a complicated object, that can be still separated in two structurally different parts: a connected part and a disconnected one, as shown in Fig. 1.6, or equivalently by the relation:

$$P(11'; 22') = G(12') G(21') + \int d3d3' G(13) G(3'1') \Gamma^*(33'; 44') G(4'2') G(24). \quad (1.25)$$

Eq. (1.25) is **Hedin's third equation**: The disconnected part is simply the product of two Green's functions, while the connected one contains a **vertex function** Γ^* that corrects the independent propagation of the particles, and includes the many body effects at the two-particle level. It explicitly accounts for the scattering between the particles. The vertex that we have denoted with Γ^* is the *one-particle irreducible vertex* which is, as the superscript "*" shall indicate, also irreducible in the interaction.⁴

⁴The vertex irreducible in the interaction must not be confused with the more standard [134] *one-particle irreducible vertex*, that we will discuss mainly in the section about fRG, cf. Sec. 1.4.

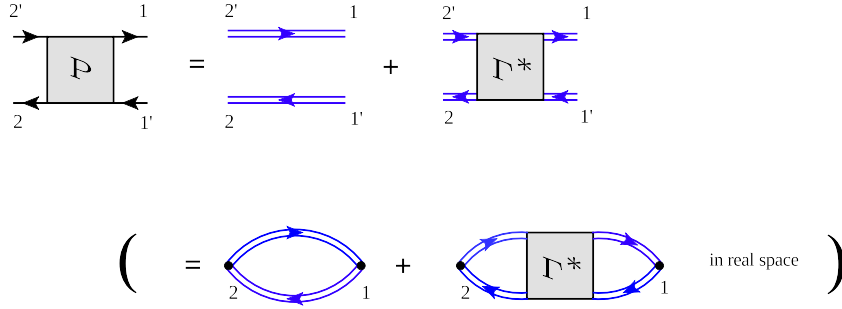


Figure 1.6: Diagrammatic expression of the relation between the polarization operator P , the separated Green's functions (bubble term) and the vertex correction Γ^* . Since the polarization cannot include interaction-reducible diagrams instead of using the vertex Γ we have to express the equation in term of Γ^* (more details are given in the text).

Second line: In terms of real space or momentum (but not in an orbital representation) two indexes can be contracted to a single one.

Hedin's fourth equation is obtained by relating the vertex Γ^* to the *particle-hole irreducible vertex irreducible in the interaction* Γ_{ph}^* . This relation is given by the standard Bethe-Salpeter equation, i.e. the equivalent of the Dyson equation for the vertex. Indeed, the vertex Γ^* will contain some Feynman diagrams that can be separated in two halves by cutting one incoming and one outgoing Green's function line. Such diagrams will be called *particle-hole reducible*, while all the particle-hole irreducible diagrams can be collected in another structural unity, called *particle-hole irreducible vertex irreducible in the interaction* Γ_{ph}^* .

All the diagrams contributing to Γ^* can be generated by summing Γ_{ph}^* and a geometric series of repetitions of Γ_{ph}^* connected by two Green's function, (Fig. 1.8):

$$\Gamma^*(11'; 22') = \Gamma_{\text{ph}}^*(11'; 22') + \int d3d3'd4d4'\Gamma^*(11'; 33')G(3'4)G(4'3)\Gamma_{\text{ph}}^*(44'; 22'). \quad (1.26)$$

Some remarks are necessary here: To avoid that some diagrams are counted twice in Eq. (1.24), we should not include in Γ^* all the diagrams that can be generated as a ladder of interaction and pairs of particle hole Green's functions, otherwise such diagrams would be counted twice when calculating W via Eq. (1.24). This can be easily done by imposing that Γ_{ph}^* does not contain the diagram consisting of the bare interaction V alone, therefore we get:

$$\Gamma_{\text{ph}}^*(11', 22') = \Gamma_{\text{ph}}(11, 22') - V(11', 22'), \quad (1.27)$$

where $\Gamma_{\text{ph}}(11, 22')$ is the "standard" particle-hole irreducible vertex. In the original formulation of his equations, Hedin [59] related the derivative of the self-energy with respect to the Green's function with the particle-hole irreducible vertex:

$$\Gamma_{\text{ph}} = \frac{\delta\Sigma(11')}{\delta G(2'2)}. \quad (1.28)$$

This is a standard field theoretical relation. In terms of Feynman diagrams this relation follows from the observation that differentiation with respect to the Green's function means removing one Green's function line, see Fig. 1.7 and Ref. [22].

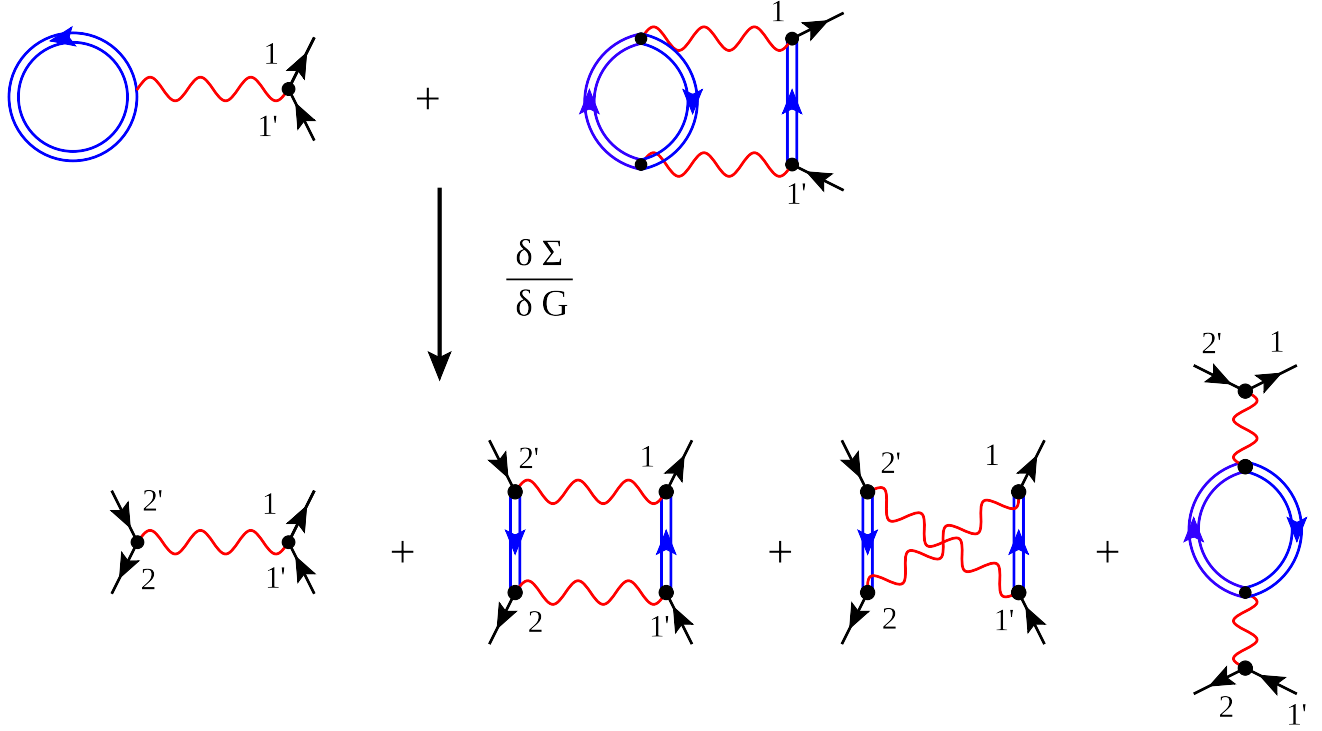


Figure 1.7: By means of selected Feynman diagrams we illustrate that differentiation of Σ with respect to G yields the particle-hole irreducible vertex.

However, in considering the work of Hedin, we should keep in mind that, since he worked out his equations for the case of the uniform electron gas, he could incorporate from the very beginning the Hartree term in the noninteracting Hamiltonian, canceling the energy contribution due to the positive ions. For this reason in our formulation Eq. (1.28) reads:

$$\Gamma_{\text{ph}}^* = \frac{\delta(\Sigma(11') - \Sigma_{\text{Hartree}})}{\delta G(2'2)}. \quad (1.29)$$

Before we can move to the derivation of the last Hedin's equation, we have now to investigate the relation between the two-particle Green's function $G^{(2)}$ and the polarization operator P , and correspondingly between Γ and Γ^* . The *two-particle Green's function* is defined as:

$$G^{(2)}(11'; 22') = \langle T[\hat{\psi}(1')\hat{\psi}(2')\hat{\psi}^\dagger(1)\hat{\psi}^\dagger(2)] \rangle. \quad (1.30)$$

It describes the correlated propagation of two particles. It can be split in a connected part and a disconnected one. The latter is given by the product of two single particle Green's functions:

$$G^{(2)}(11'; 22') = G(11')G(22') + G(12')G(21') + G_C^{(2)}(11'; 22'). \quad (1.31)$$

Following Ref. [134] we relate the two particle-connected Green's function with the one-particle irreducible vertex function Γ :

$$G_C^{(2)}(11'; 22') = \int d3d3' G(13)G(3'1')\Gamma(33'; 44')G(4'2')G(24). \quad (1.32)$$

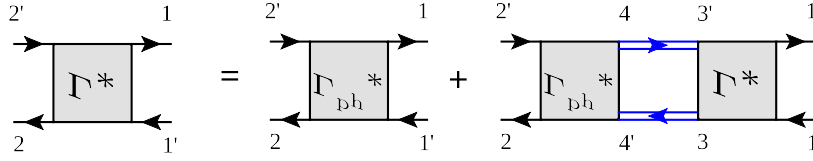


Figure 1.8: Diagrammatic representation of the Bethe-Salpeter equation between the irreducible vertex in the particle-hole channel Γ_{ph}^* and the particle-hole reducible Γ^* . The particle-hole irreducible vertex Γ_{ph}^* collects the Feynman diagrams which cannot be separated into left and right part by cutting two Green's function lines. All diagrams are then generated by the Bethe-Salpeter equation.

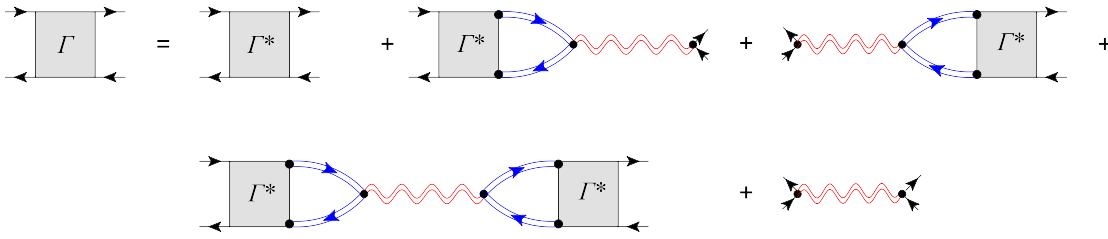


Figure 1.9: Diagrammatic representation of the relation between Γ and Γ^* . This relation can be obtained by an iterative procedure, inserting Eq. (1.27) in Eq. (1.33), and finding an iterative solution for Γ . Using the polarization operator P and the screened interaction W one can collect the generated diagrams in the form shown in the figure.

Comparing this with Eq. (1.25), we see how the connected part of the polarization and the connected part of the two-particle Green's function are related. As in Eq. (1.26), the one-particle irreducible vertex can be expressed in terms of the particle-hole irreducible vertex Γ_{ph} , using a Bethe-Salpeter equation:

$$\Gamma(11'; 22') = \Gamma_{ph}(11'; 22') + \int d3d3'd4d4'\Gamma(11'; 33')G(3'4)G(4'3)\Gamma_{ph}(44'; 22'). \quad (1.33)$$

For later use let us express Γ in terms of Γ^* . To do this we insert Eq. (1.27) in Eq. (1.33). Diagrammatically one can understand the contributions that arise by performing an iterative solution for Γ . By doing so, and collecting the generated diagrams in terms of polarization and screened interaction, using equations. (1.25) and (1.24), one can easily convince himself that all the generated diagrams can be expressed⁵ in the form shown in Fig. 1.9.

Mathematically Fig. 1.9 translates (omitting the arguments of each function and the integration signs) to:

$$\Gamma = \Gamma^* + \Gamma^*GGW + WGG\Gamma^* + \Gamma^*W\Gamma^* + W. \quad (1.34)$$

We are now in the position to consider the last Hedin's equation, that connects the self-energy with the vertex Γ^* . We will proceed as follows: First we will use the Heisenberg equation of motion to relate the self-energy and the two-particle Green's function. Then we will use the relations derived above to express the two-particle Green's function in terms of Γ^* , and to obtain the desired equation.

⁵For a more formal derivation see Ref. [63].

Let us start from the derivation of the equation of motion. The time evolution of an operator in the Heisenberg representation can be expressed in terms of its commutator with the Hamiltonian:

$$i \frac{\partial \hat{\psi}(1)}{\partial \tau_1} = [\hat{\psi}(1), \mathcal{H}_e]. \quad (1.35)$$

From the equation above we derive an equation of motion for the Green's function:

$$- \left[\int d2' \frac{\partial}{\partial \tau_1} \delta(2' - 1) + h_0(12') \right] G(2'1') + \int d3' d2 d2' V(13', 2'2) \langle T \hat{\psi}(3') \hat{\psi}^\dagger(2) \hat{\psi}(2') \hat{\psi}^\dagger(1') \rangle = \delta(1 - 1'). \quad (1.36)$$

The expectation value of four field operators is the two-particle Green's function. From Eq. (1.36) for a non-interacting system ($V(11', 22') = 0$) one can express the noninteracting Green's function as:

$$G_0(1, 1') = - \left[\frac{\partial}{\partial \tau} + h_0 \right]_{(1,1')}^{-1}. \quad (1.37)$$

Substituting Eq. (1.37) back in Eq. (1.36) gives:

$$\int d2' G_0^{-1}(1, 2') G(2', 1') + \int d3' d2 d2' V(13', 2'2) G^{(2)}(3'1'; 21') = \delta(1 - 1'), \quad (1.38)$$

multiplying all terms times $G^{-1}(1', 4)$ and integrating over $1'$ yields:

$$G_0^{-1}(1, 4) - G^{-1}(1', 4) = \int d3 d2 d2' d1' V(13'; 2'2) G^{(2)}(3'2'; 21') G^{-1}(1', 4). \quad (1.39)$$

Inserting Eq. (1.32) and (1.31) for the two-particle Green's function, and comparing with Eq. (1.23) yields:

$$\begin{aligned} \Sigma(1, 4) = & - \int d3 d2 d2' d5' d6 d6' V(13', 2'2) \Gamma(5'6', 46) G(3', 5') G(2', 6') G(6, 2) \\ & - \int d3' d2' V(13'; 2'4) G(3', 2) - \int d2 d2' V(14; 2'2) G(2'2). \end{aligned} \quad (1.40)$$

The diagrammatic representation of the equation above is in the first line of Fig. 1.10.

To close the set of Hedin's equations, we only need now to express Eq. (1.40) in terms of Γ^* . We show how this is possible in a diagrammatic way. First we insert the diagrams shown in Fig. 1.9 or equivalently expressed in Eq. (1.34) in Eq. (1.40). In this way the self-energy can be expressed in terms of the diagrams shown in Fig. 1.11. The diagrams A1, A2 and A3 in Fig. 1.11 can be collected together and form the second diagram of the second line of Fig. 1.10. After some inspection, one can see that the diagrams labeled B1, B2, B3 can be grouped in the diagram shown in the first line of Fig. 1.12 by introducing the block labeled A and shown in the second line of Fig. 1.12. Again, in the first two diagrams of the block A (Fig. 1.12, second line) one can recognize the diagrams forming the polarization multiplied times the

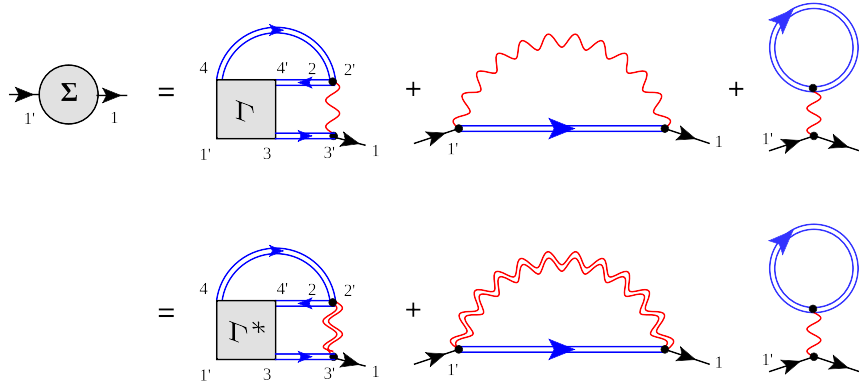


Figure 1.10: Equation of motion for the self-energy, expressed in terms of Γ (first line) and Γ^* (second line)

screened interaction. Finally, expressing Eq. (1.24) in the equivalent form $P = V^{-1} - W^{-1}$, and substituting for the polarization in the block A one gets the first diagram in second line of Fig. 1.10. Expressing such result in mathematical terms gives the desired result, namely **Hedin's fifth equation**:

$$\begin{aligned} \Sigma(1, 4) = & \int d3d2d2'd5'd6d6'W(13', 2'2)\Gamma(5'6', 46)G(3', 5')G(2', 6')G(6, 2) \\ & - \int d3'd2'V(13'; 2'4)G(3', 2') - \int d2d2'W(14; 2'2)G(2'2). \end{aligned} \quad (1.41)$$

In summary, we have re derived the set of five Hedin's equations (1.21), (1.24), (1.25), (1.26) and (1.41), corresponding⁶ to equations (A13), (A20), (A24), (A22) and (A23) respectively in the original paper [59]. This set of equations is exact and is only a rearrangement of standard equation of quantum field theory: solving them exactly is as difficult as solving the original problem. However, they offer a better starting point for developing perturbative approximations.

1.3.2 GW approximation

As it was known already in 1965 [59], expanding the self-energy in terms of the bare interaction V does not take into account a very important process for metals: The screening of the interaction. In fact, whenever an external "test" charge is added to a metallic system the existing charge will rearrange to minimize the Coulomb potential energy. As a consequence each electron will not see the "bare" test charge, but a "screened" charge that also accounts for the polarization of the medium. The most striking consequence of this is the fact that the interaction, instead of being long ranged, i.e., $\propto 1/r$, in a medium becomes effectively short ranged,

⁶We stress once more that in his derivation Hedin followed an equivalent but different route: he incorporated the Hartree potential in the noninteracting Hamiltonian. For the case considered by Hedin, of an uniform electron gas, incorporating the Hartree potential in the noninteracting Hamiltonian is straightforward. He could then derive all his set of equation by appropriate functional derivation. Following this approach is possible also for nonuniform systems, like in Ref. [12].

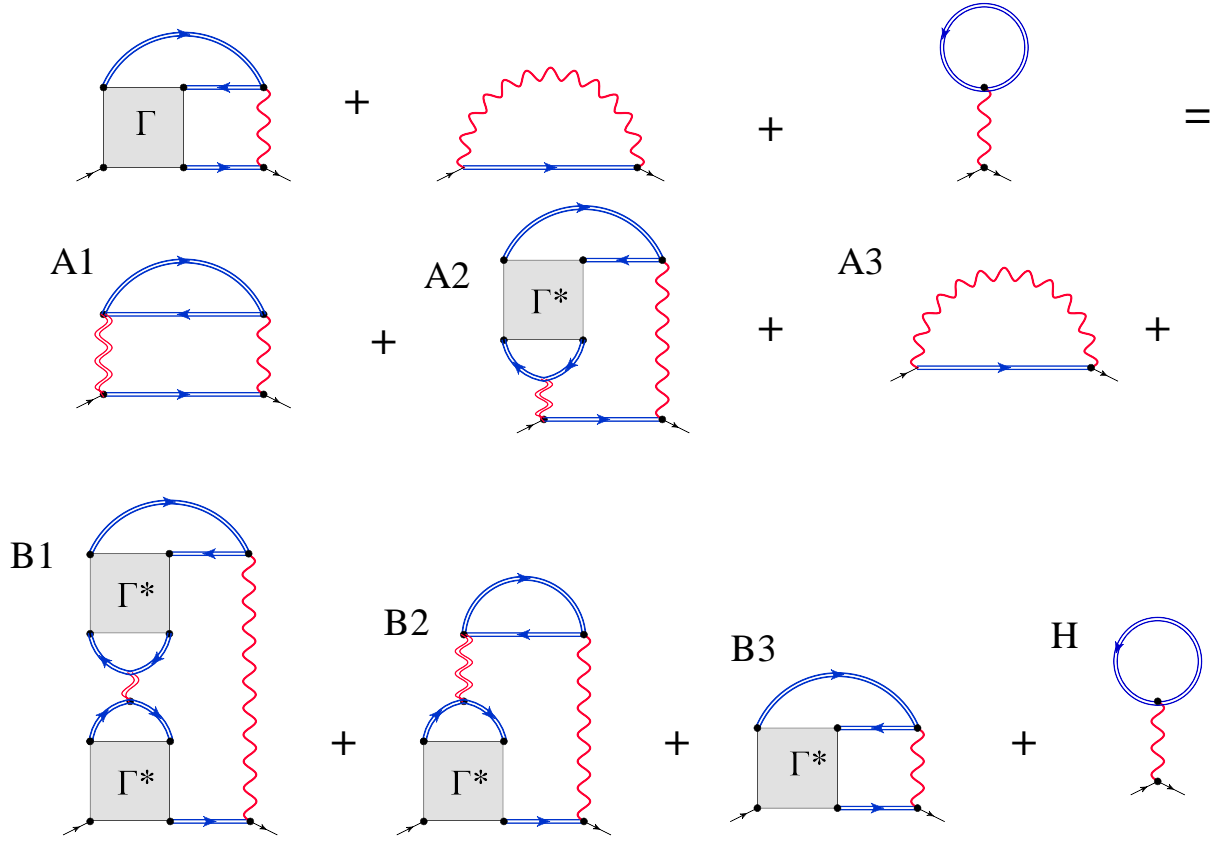


Figure 1.11: Expansion of the Heisenberg equation of motion in terms of Γ^* .

i.e., $\propto e^{-\tau k_{\text{TF}}/r}$, as correctly predicted by Thomas-Fermi theory, with k_{TF} being the Thomas-Fermi momentum, which depends on the details of the medium considered. In this paragraph we will discuss how, starting from the Hedin's equations, we can obtain a perturbation theory that keeps screening into account. In the next section we will discuss physically the meaning of the contributions taken into account.

The approximation is obtained by neglecting completely the vertex corrections, i.e. setting $\Gamma_{\text{ph}}^* = 0$. Then the Bethe-Salpeter Eq. (1.25) gives:

$$\Gamma^* = 0. \quad (1.42)$$

Doing so we only consider the disconnected part of the polarization operator P . Correspondingly the propagation of an electron-hole excitation, described by P , is simplified by the independent propagation of the electron and the hole (each one, however described by a full interacting Green's function). The polarization then reduces to the so-called Lindhardt bubble [119]:

$$P^{\text{GWA}}(11'; 22') = G(12')G(21'). \quad (1.43)$$

Substituting Eq. (1.43) in Eq. (1.24) yields the simplest form of screened interaction:

$$W^{\text{GWA}}(11'; 22') = V(11'; 22') + W(11'; 33')P^{\text{GWA}}(3'3; 4; 4)V(44'; 22'), \quad (1.44)$$

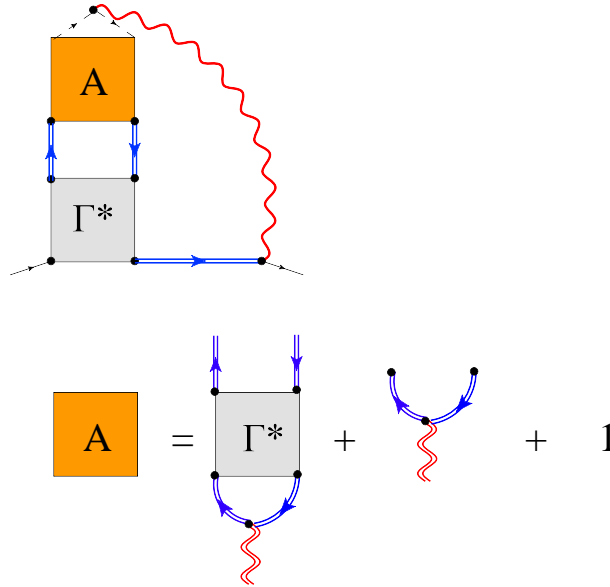


Figure 1.12: The block A includes the diagrams $B1, B2$ and $B3$ defined in Fig. 1.11.

and using the equation of motion (1.41) the self-energy becomes:

$$\Sigma^{\text{GWA}}(11') = -i \int d2d2' G(2'2) W(12'; 21'), \quad (1.45)$$

to which one should add the Hartree term $\Sigma^{\text{Hartree}}(11')$. From this, the Green's function can be obtained using Eq. (1.21):

$$G(11') = G_0(11') + \int d2d2' G(12) [\Sigma^{\text{GW}}(22') + \Sigma^{\text{Hartree}}(22')] G_0(2'1'). \quad (1.46)$$

The new closed set of equations should be solved self consistently.

A first approximation consists in taking G_0 for G in Eq. (1.43) for the polarization, as was done for the first time by Hedin [59], who applied his equations to the uniform electron gas, obtaining⁷ the first results of the *GW* approximation. The results obtained by Hedin were very promising in spite of the seemingly crude approximation. In fact, it turns out that the success of the approximation depends on the fact that it allows for the inclusion of a class of diagrams for the screened interaction, i.e., those diagrams obtained by summing an infinite series of bare interaction and Green's function particle-hole bubbles, that are crucial [119], in the description of screening. In the literature, for historical reasons, one often refers to the approximation that takes into account only the bubble diagrams in the screening of the interaction as the random phase approximation (RPA). Clearly, in *GW*, the screened interaction W contains the information of the RPA screening. Importantly, it can be seen that, in the case of the homogeneous electron gas [119], the RPA screened interaction shows the same exponential decay correctly predicted by the Thomas-Fermi screening $\propto e^{-r k_{\text{TF}}}/r$, and is therefore effectively short ranged.

⁷Besides this, Hedin has also shown that it is possible to generate other Ward conserving approximation [59].

However, RPA is capable to capture more than this exponential decay. In fact, unlike what happens in Thomas-Fermi approximation, which is a purely static approximation, the screening of the interaction in RPA, and therefore in GW , is **dynamic**: The screened interaction W acquires a nontrivial frequency and momentum dependence. Going beyond the RPA approximation is very complicated, and not much is known about the effect of vertex corrections to the polarization. Some attempts have been done to include at the lowest orders perturbative diagrams neglected by RPA [119]. This is however less trivial than it might appear. Furthermore for strongly correlated electron system one should not expect that this brings substantial improvements. Another possibility consists in including in the screening of the interaction not only the ladder diagrams in the particle-hole (direct) channel as considered by RPA, but rather the one-loop parquet diagrams⁸ including also the other two channels, namely particle-particle and particle-hole crossed. In fact, in general, there are no strong reasons to justify *a priori* the fact that the RPA diagrams alone are sufficient to capture all the most important processes contributing to the interaction. These issues are addressed in a slightly different context⁹ in Ref. [71] making use of fRG methods. Nevertheless, as we shall see in the next paragraph, also neglecting completely the vertex corrections, the GW approximation has been successfully applied, in the last few decades, to the study of real material system, providing results in good agreement with LDA for weakly correlated metals, where both methods work well, and results in better agreement with the experiments than the LDA one, in the case of insulators and semiconductors, and more recently also transition metal oxides or pnictides superconductors, like, e.g., in Ref. [175].

1.3.3 Actual implementations of GW : quasiparticle GW

The self-consistent solution of the Hedin's equation above, even in the GW approximation form, is still an extremely complicated task for real materials¹⁰.

For this reason in recent years several (further) approximations to tackle the GW equations have been developed. This gave rise to a full new class of methods. This makes it sometimes not so easy to understand the main approximations employed in each specific implementation. In other words today a series of different methods go under the generic name “ GW ”

More in detail there are two points that require particular care:

- the level of self-consistency;

⁸The parquet diagrams, and the one-loop approximation will be discussed in the section about the fRG diagrammatics, cf. Sec. 1.4.2.

⁹The author of Ref. [71], rather than on RPA focuses on constrained RPA (cRPA) [13, 131]. The cRPA is used to downfold the interaction of a full Hamiltonian on a low-energy one, and therefore the low-energy degrees of freedom are not allowed to take part in the screening of the interaction. The screening from the high energy degrees of freedom, however, is performed in cRPA considering ladder diagrams in the particle-hole direct channel. In Ref. [71] it is shown how to include, at the model level, also parquet diagrams using the fRG formalism. The result is a much more rich frequency structure for the interaction than the one obtained in cRPA.

¹⁰Let us note that the full self-consistent solution of the GW equations is doable for small systems, like molecules. On the other hand the calculation for solids requires the treatment of a larger number of k -points, which strongly increases the computational effort.

- the treatment of the self-energy.

Let us see what are the methods that arise from dealing in different ways with these two points.

Level of self-consistency Most *GW* calculations start from a preliminary LDA bandstructure calculation. The next step is the computation of the polarization. This is done starting from the knowledge of the eigenvalues and eigenfunctions of LDA. The Lindhardt bubble is expressed using the Lehman representation of the Green's function [144]:

$$P_{\mathbf{q}}(\mathbf{G}, \mathbf{G}', \omega) = \frac{1}{\Omega} \sum_{nn'\mathbf{k}} 2w_{\mathbf{k}}(f_{n'\mathbf{k}-\mathbf{q}} - f_{n\mathbf{k}}) \frac{\langle \psi_{n'\mathbf{k}-\mathbf{q}} | e^{-i(\mathbf{q}+\mathbf{G})\mathbf{r}} | \psi_{n\mathbf{k}} \rangle \langle \psi_{n\mathbf{k}} | e^{-i(\mathbf{q}+\mathbf{G}')\mathbf{r}'} | \psi_{n'\mathbf{k}-\mathbf{q}} \rangle}{\omega + \epsilon_{n'\mathbf{k}-\mathbf{q}} - \epsilon_{n\mathbf{k}} + i\eta \text{sgn}[\epsilon_{n'\mathbf{k}-\mathbf{q}} - \epsilon_{n\mathbf{k}}]}, \quad (1.47)$$

where $w_{\mathbf{k}}$ is the k -point weight, $f_{n\mathbf{k}}$ is the one electron occupancy of the state $n\mathbf{k}$, η is an infinitesimal complex shift, \mathbf{q} and \mathbf{k} are wave vectors in the Brillouin zone. \mathbf{G} and \mathbf{G}' are reciprocal vectors of the lattice. In the equation above the spin sum has been substituted with the factor two in front of the expression, while the spin indices have been suppressed. This is sometimes referred to as *test charge* approximation, as it would correspond to the response of the system to a spineless (test) charge in RPA.

Using the LDA wave function and the polarization above one can compute the screened Coulomb interaction W_0 , and, after convolution with the LDA Green's function, the *GW* self-energy: $\Sigma = iG_0W_0$. In this approximation Green's function, polarization and self-energy are computed in a non-self-consistent way, and the approximation is referred to as G_0W_0 approximation.

This approximation already yields improved results compared to LDA, but still depends crucially on the LDA underlying calculation. To further improve on this, however, it is desirable to go beyond a single shot G_0W_0 calculation on top of LDA, going in the direction of a self-consistent *GW*. This is not a trivial task and there are several ways to proceed that have been explored.

On the one hand, one possibility consists in realizing a full update of the Green's function *and* of the screened potential. This approach has been followed for the free electron gas [68] as well as for metals and semiconductors [162]. The results obtained in this way, however, did not turn out to be satisfactory. This is explained considering that the shift of spectral weight from the quasiparticle peaks into satellites causes a substantial reduction of the screening. This results in an overestimation of the bandwidth and of the bandgaps, as severe as the underestimation in LDA. For this reason it is still not completely clear how reliable fully self-consistent *GW* approximation *without vertex corrections* are [166]. Furthermore this approach is technically extremely demanding.

For these reasons different partially self-consistent approaches have been developed, in which one updates the quasiparticle eigenvalues in the Green's function and/or in the dielectric function, while the one-electron wave functions are kept fixed to the LDA solution. The advantage of these partially self-consistent approaches compared to the fully self consistent one is twofold: on the one hand the problem of the shift of spectral weight to the satellites is less

severe, and on the other hand the computational burden is less heavy. However, to proceed in this direction some further simplification to the self-energy is required. This is described in the next paragraph.

Treatment of the self-energy: the quasiparticle approximation

In the partially self-consistent approaches to GW one is interested in the calculation of the quasiparticle energies $\epsilon_{n\mathbf{k}}$. If one assumes that the wave functions are kept fixed at the LDA value, the quasiparticle energies can be computed self-consistently solving the diagonal matrix elements of the quasiparticle (QP) equation [80, 165]:

$$\epsilon_{n\mathbf{k}} = \text{Re}[\langle \psi_{n\mathbf{k}} | T + v_{\text{ion}} + v_{\text{Hartree}} + \Sigma(\epsilon_{n\mathbf{k}}) | \psi_{n\mathbf{k}} \rangle], \quad (1.48)$$

where v_{Hartree} is the Hartree potential, and $\Sigma(\epsilon_{n\mathbf{k}})$ is the self-energy operator computed at frequency $\omega = \epsilon_{n\mathbf{k}}$. To obtain a solution of the above equation one can proceed iteratively, obtaining the quasiparticle energy $\epsilon_{n\mathbf{k}}^{N+1}$ at the iteration $N + 1$ linearizing the self-energy around $\epsilon_{n\mathbf{k}}^N$:

$$\epsilon_{n\mathbf{k}}^{N+1} = \epsilon_{n\mathbf{k}}^N + Z_{n\mathbf{k}} \text{Re}[\langle \psi_{n\mathbf{k}} | T + v_{\text{ion}} + v_{\text{Hartree}} + \Sigma(\epsilon_{n\mathbf{k}}^N) | \psi_{n\mathbf{k}} \rangle - \epsilon_{n\mathbf{k}}^N], \quad (1.49)$$

with $Z_{n\mathbf{k}}$ being the renormalization factor:

$$Z_{n\mathbf{k}} = \left(1 - \text{Re} \langle \psi_{n\mathbf{k}} | \frac{\partial}{\partial \omega} \Sigma(\omega) \Big|_{\omega=\epsilon_{n\mathbf{k}}^N} | \psi_{n\mathbf{k}} \rangle \right)^{-1}. \quad (1.50)$$

If one relies on a single-shot G_0W_0 on top of LDA one simply gets, after one iteration only of equation (1.49):

$$\epsilon_{n\mathbf{k}}^{G_0W_0} = \epsilon_{n\mathbf{k}}^{\text{LDA}} + Z_{n\mathbf{k}} \text{Re}[\langle \psi_{n\mathbf{k}} | T + v_{\text{ion}} + v_{\text{Hartree}} + \Sigma(\epsilon_{n\mathbf{k}}^{\text{LDA}}) | \psi_{n\mathbf{k}} \rangle - \epsilon_{n\mathbf{k}}^{\text{LDA}}]. \quad (1.51)$$

The solution of this set of equations is a new set of quasiparticle energies. For every k point the self-energy is computed at a single frequency¹¹ and all the quasiparticle weight is transferred from the original LDA quasiparticle energy $\epsilon_{n\mathbf{k}}^{\text{LDA}}$ to the GW quasiparticle energy. Since the frequency dependence as well as the imaginary part of the self-energy have been neglected, there is no incoherent spectral weight at frequencies different from the quasiparticle energy and the excitations of the system are given by infinitely long lived quasiparticles at the new set of energies. The effect of the interaction, included via the GW self-energy, is therefore a shift of the excitation energy in exactly as in a one-particle picture. For these reasons we will refer to this approximation as quasiparticle GW (qp GW).

We also notice that these methods, whatever the degree of self consistency applied, still depend on the wave functions, computed in LDA, and therefore may have problems in the treatment of systems for which the LDA gives unreliable results [166].

¹¹Actually, since the numerical derivative of the self-energy is required, the self-energy is computed also at frequency values $\epsilon_{n\mathbf{k}} + \delta\omega$ and $\epsilon_{n\mathbf{k}} - \delta\omega$.

Comparison of different schemes

As there is a number of similar possible approximations that change only by the degree of self consistency, it is not clear which approximation is better justified *a priori* and only the comparison with experiments can *a posteriori* answer this question, at least partially. Traditionally the quantity that is used to test the quality of a GW calculation is the quasiparticle band gap. Indeed it is known, that it is not correctly computed by LDA based approximations¹², which usually yield a bandgap way too small compared to the experimental one. In Ref. [166] three quasiparticle GW method are tested against the experimentally measured bandgap for a number of materials. Namely the authors consider:

- one shot qpG_0W_0 ;
- partially self-consistent $qpGW_0$;
- self-consistent(at the quasiparticle level) $qpGW$.

The main result is summarized in Fig. 1.13. One can see that the qpG_0W_0 bandgaps are already much closer than LDA to the experimental values, but are still a bit too small for all the considered materials except carbon. A partial self-consistency substantially improves the results, and apart for ZnO, the computed bandgap is always less than 10% off the experimental one. It is also shown that there is a linear correlation between the error in the predicted bandgap and the error in the dielectric constant computed at the RPA level. This proves that an accurate prediction of the screening properties of a given material is necessary for an accurate calculation of its bandgap. This is also important when considering the results obtained with the self-consistent $qpGW$ approximation: While $qpGW_0$ usually underestimates the bandgap it is slightly overestimated by $qpGW$. The reason for this is that, if one neglects the vertex corrections, the RPA screening is not sufficient to give a good estimate of the dielectric constant.

From such a systematic analysis the authors could conclude that the method that best predicts the bandgap is the $qpGW_0$, even if this is probably caused by a fortunate cancellation of errors. The predicted band gap is usually only around 3%-5% smaller than the experimental one. The most important deviations from the experimentally predicted smaller bandgap occurs for materials having shallow d states. For these a treatment at the perturbative level, like in GW based methods, can hardly be sufficient.

1.4 Functional renormalization group

In the previous section about GW we have seen how the inclusion of a subclass of diagrams could substantially improve the results of plain perturbation theory, and we have also given an argument to justify the selection of such diagrams, considering the important role that they play in the screening of the Coulomb interaction.

¹²In LDA the bandgap can be computed interpreting the eigenvalues of the Kohn-Sham equation as the quasiparticle energy. This is not fully justified: The bandgap is not a ground state property.

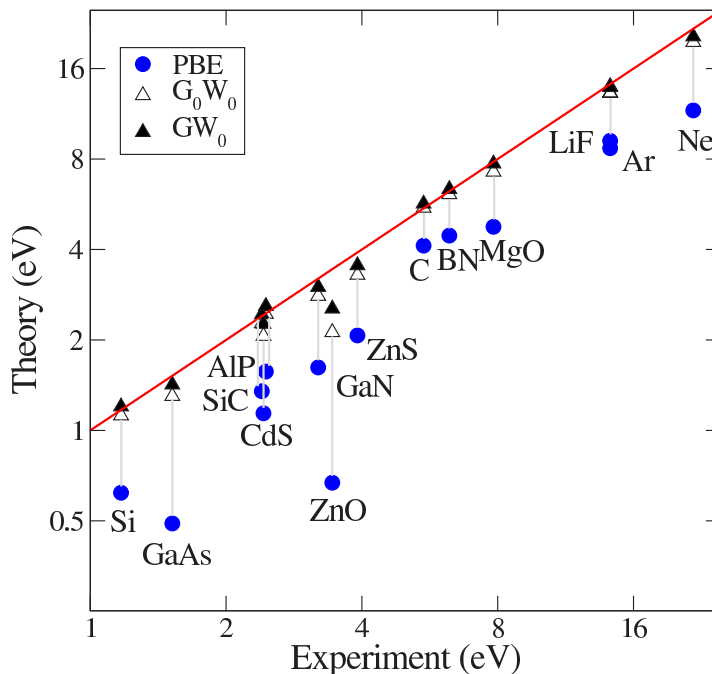


Figure 1.13: Quasiparticle band gaps computed in LDA (marked as PBE, blue dots), qpG_0W_0 , and $qpGW_0$, plotted against the experimental ones, for several materials. On both axis a logarithmic scale has been used. One can see a substantial improvement of qpG_0W_0 and $qpGW_0$ as opposed to LDA, that tends to underestimate the band gap. The figure is reproduced from Ref. [166].

There are important cases, however, where this procedure is not sufficient to take the most important physics into account. This typically happens if

- the physical properties of the system are influenced by different **competing instabilities**;
- correlation effects become too strong.

In these cases more involved many-body approaches are required. Furthermore, due to the complexity of the many-body approaches, one often has to abandon the ambition of treating all the degrees of freedom on the same footing, and rather restrict oneself to a *low-energy* Hamiltonian, on which the other degrees of freedom are downfolded. In a renormalization group sense this corresponds to formally integrating out all the high energy degrees of freedom, for which the correlation effects are less relevant. The low-energy Hamiltonian is then approached with the most appropriate many-body method to treat the physical aspects that are expected to be

more relevant. The downfolding procedure itself, however, is often very complicated, and in practice, one has to define a *model* Hamiltonian, like, e.g., the Hubbard Hamiltonian [77], to describe the problem. The model Hamiltonian is a further approximation to the low-energy one, that can be required either to avoid the complication of the downfolding or because the downfolded Hamiltonian might still be too difficult to solve (for a given many-body method) or contain too much information than required to capture the essential physics of the problem.

While we will discuss the theoretical tools to be used to treat the strong correlations later on (cf. Sec. 1.5), in the present chapter we focus on the first situation, i.e., the one of competing instabilities, which can arise also in a weak-coupling regime in presence of nontrivial nesting properties, or in general, when, at lower energy scales, a treatment that includes the charge-channel only, like *GW*, is not sufficient.

As a paradigmatic example of this we can consider the Hubbard model in two spatial dimensions: In the case of half-filling and with nearest neighbors hopping t only, the noninteracting Fermi surface of the system will be perfectly nested. This means that the low-temperature particle-hole fluctuations corresponding to the nesting vector [here $\mathbf{Q} = (\pi, \pi)$], will be large and eventually logarithmically divergent as the temperature is lowered to zero. From these divergent fluctuations one expects an instability of the ground state towards antiferromagnetism. At the same time, if one increases the ratio t'/t of the next neighbors hopping t' over the nearest neighbors hopping t or changes the filling, the perfect nesting property of the Fermi surface will be lost, and other kinds of instabilities will emerge. In particular, the checkerboard commensurate antiferromagnetic fluctuations, with wavevector (π, π) , will now compete with incommensurate antiferromagnetism, d -wave superconductivity and even ferromagnetism for t'/t sufficiently large. From a diagrammatic perspective this can be understood as follows: In the first case due to the perfect nesting there is one susceptibility (i.e. the one associated with the nesting vector) that dominates over the others and a specific analysis restricted to diagrams in the corresponding channel, for example an appropriate RPA ladder resummation, is often an accurate approximation. In the second case however no dominating channel can be clearly identified. Hence for a correct description of the system (and of its instabilities) one should include diagrams in all channels as well as the coupling among them. This task is much more difficult: While it is rather easy to express the ladder diagrams in a given channel in terms of a geometric series (for example like it is done for the screened interaction W in the previous section), there is no simple way of computing infinite resummations of diagrams in which the channels mix among each other. The diagrams in which the channel mix are those needed to accurately describe the competing instabilities.

A very efficient way that emerged in the last fifteen years to deal with this kind of problems makes use of the **functional Renormalization Group** (fRG) [129, 141], which is the main topic of the present section. From a very pragmatic point of view, this is for us the main motivation to introduce fRG: It allows us to sum parquet diagrams in a systematic and unbiased way. On the other hand, we should recall here that fRG is a powerful technique that goes beyond this, being also connected, as the name suggests, with Wilson's idea of the renormalization group [185], as well with Shankar's modern renormalization group techniques [164].

The main idea behind fRG is to rewrite a problem which we are not able to solve exactly in terms of a set of coupled differential equations, whose integration would provide the *exact* solution of the problem. For practical purposes, however, the integration of the full set of differential equations cannot be performed in general, as it corresponds to compute exactly the flow of a *functional*, which is typically not feasible for a nontrivial case. The way to circumvent this is to formally expand the functional in terms of its derivative with respect to the fields and study their flow. The expansion of the functional flow, however, would generate a set of coupled differential equations involving functions of arbitrary high degrees of freedom. Obviously to make possible a numerical treatment of these equations one should *truncate* the set of flow equations at a certain level. It is only at this point that an approximation, in an otherwise exact set of equations, is introduced. In this respect fRG can be seen as an excellent starting point for devising new approximations, numerically affordable and superior to standard lowest order perturbation theory or resummation of ladder diagrams of a selected channel in RPA.

In the next subsection the fRG equations will be derived and discussed in more detail. Thereafter we will show the relation between the diagrammatic content of fRG with the one of the so-called parquet approximation [22], which is, in usual cases, very complicated to solve even numerically [187]. In this context the main approximations used in fRG, as well as the main *cutoff schemes* will be introduced. Finally, we will discuss the major achievements of fRG over the last fifteen years, focusing in particular on the results for the two dimensional Hubbard model.

1.4.1 Derivation and diagrammatic elements of fRG

The name *functional* renormalization group stems from the fact that the flow equations can be obtained directly for a generating¹³ functional [134], and eventually expanded into the fields. This also stresses one important difference compared to Wilson's renormalization group: The flowing quantity is a functional, and *not* some coupling in the Hamiltonian. In the literature several review papers [5, 129, 141, 157] and textbooks [104, 156] are now available in which the aforementioned derivation is elucidated in detail. Here, following Jakobs and coworkers [83, 84] we prefer to present first a derivation of the flow equations which focuses more on the diagrammatic aspects of fRG, and which is specific for the one particle irreducible (1PI) vertex functions. Such a diagrammatic derivation will be also helpful in the discussion of the diagrammatic content of fRG.

Let us start from the action describing a spin-1/2 fermionic system, which we write as:

$$\mathcal{S}[\bar{\psi}, \psi] = \mathcal{S}_0[\bar{\psi}, \psi] + \mathcal{S}_{\text{int}}[\bar{\psi}, \psi], \quad (1.52)$$

with ψ being Grassman's variables [134]. The first term represents the Gaussian part of the action:

$$\mathcal{S}_0 = -T \sum_{n\sigma} \int d^d k \bar{\psi}_{\mathbf{k},\sigma}(i\omega_n) \mathcal{G}_0(\mathbf{k}, i\omega_n)^{-1} \psi_{\mathbf{k}\sigma}(i\omega_n). \quad (1.53)$$

¹³Usually are obtained for the generating functional of the connected Green's function, of the one particle irreducible vertex functions or of the amputated connected Green's functions (effective interaction).

where $\bar{\psi}_{\mathbf{k},\sigma}(i\omega_n)$ and $\psi_{\mathbf{k},\sigma}(i\omega_n)$ are the Grassman's variables associated with the creation and annihilation operators in a Hamiltonian formulation. For a noninteracting system with band dispersion $\epsilon_{\mathbf{k}}$ and chemical potential μ the propagator $\mathcal{G}_0(\mathbf{k}, i\omega_n)$ reads:

$$\mathcal{G}_0(\mathbf{k}, i\omega_n) = -\langle \psi_{\mathbf{k}\sigma}(i\omega_n) \bar{\psi}_{\mathbf{k}\sigma}(i\omega_n) \rangle_0 = \frac{1}{i\omega_n - \mu - \epsilon_{\mathbf{k}}}, \quad (1.54)$$

and the symbol $\langle \dots \rangle_0$ denotes the expectation value within the system defined by the action \mathcal{S}_0 :

$$\langle \dots \rangle_0 = \frac{\int \mathcal{D}[\bar{\psi}, \psi] \dots e^{-\mathcal{S}_0[\bar{\psi}, \psi]}}{\int \mathcal{D}[\bar{\psi}, \psi] e^{-\mathcal{S}_0[\bar{\psi}, \psi]}}. \quad (1.55)$$

This functional integral can be computed exactly, due to the Gaussian form of \mathcal{S}_0 . In the more general case all the complications are originated by the interaction term, that for the case of an instantaneous two-body interaction we assume to be of the following form:

$$\mathcal{S}_{\text{int}} = \frac{T^3}{2\mathcal{V}} \int d^d k d^d k' d^d q \sum_{n,n',m} \sum_{\sigma,\sigma'} V_{\mathbf{k}\mathbf{k}'\mathbf{q}} \bar{\psi}_{\mathbf{k}\sigma}(i\omega_n) \bar{\psi}_{\mathbf{k}'+\mathbf{q}\sigma'}(i\omega_{n'}+i\Omega_m) \psi_{\mathbf{k}'\sigma'}(i\omega_{n'}) \psi_{\mathbf{k}+\mathbf{q}\sigma}(i\omega_n+i\Omega_m), \quad (1.56)$$

with Ω_m being a bosonic Matsubara frequency: $\Omega_m = T\pi(2m)$ and $\omega_n = T\pi(2n+1)$ being a fermionic Matsubara one. The form of the interaction is specified by $V_{\mathbf{k}\mathbf{k}'\mathbf{q}}$. Here we have assumed SU(2) spin-rotational and translational invariance, which allows us to restrict the momentum summation to three independent sums, due to momentum conservation. If additional (e.g. orbital) degrees of freedom are involved the fields would acquire a further index and a summation over four indexes would become necessary.

We focus, in the following, on two models in particular, i.e. the Anderson impurity model (AIM) and the two-dimensional Hubbard model with onsite interaction. In the former the sums over the momentum indexes are suppressed everywhere, since it corresponds to a single impurity model without spatial dependence. In this case the action (in absence of a magnetic field) is completely defined by (i) the Gaussian propagator:

$$\mathcal{G}_{\text{AIM}}(i\omega_n) = \frac{1}{i\omega_n - \mu - \Delta(\omega_n)}, \quad (1.57)$$

with $\Delta(\omega_n)$ being the hybridization function, and (ii) by the coupling U of the quartic part of the action. On the other hand, in the Hubbard model with onsite interaction the momentum dependence of the Gaussian part is retained, while the matrix element of the interaction is structureless in momentum space: $V_{\mathbf{k}\mathbf{k}'\mathbf{q}} = U$, which corresponds, in a lattice model in real space to an interaction only between fermions sitting on the same lattice site. From this moment on, to simplify the notation, we will often refer to the interaction simply as U , even if the locality of the interaction is not necessary for the derivation of the fRG equations.

The basic idea of fRG is to obtain a one-parameter family of effective actions, by making the Gaussian propagator \mathcal{G}_0 explicitly dependent on an additional parameter Λ :

$$\mathcal{G}_0(\mathbf{k}, i\omega_n) \rightarrow \mathcal{G}_0^\Lambda(\mathbf{k}, i\omega_n) = \mathcal{G}_0(\mathbf{k}, i\omega_n) f^\Lambda(\mathbf{k}, i\omega_n). \quad (1.58)$$

The explicit form of the *regulating function* f^Λ does not need to be specified at the moment, and several possible alternative choices will be presented later on (cf. Subsec. 1.4.2).

Upon this substitution also the effective action acquires a Λ -dependence: $\mathcal{S} \rightarrow \mathcal{S}^\Lambda$. The nontrivial, interacting part of the action is left *unchanged* by this substitution; however all the functional integrals like the one for the grand canonical partition function:

$$Z = \int \mathcal{D}[\bar{\psi}, \psi] e^{-\mathcal{S}[\bar{\psi}, \psi]}, \quad (1.59)$$

or the one for the imaginary time ordered n -particle Green's function:

$$G^{(n)}(\mathbf{k}_1 i\omega_1, \dots, \mathbf{k}_n i\omega_n | \mathbf{k}'_1 i\omega'_1, \dots, \mathbf{k}'_n i\omega'_n) = -\frac{1}{Z} \int \mathcal{D}[\bar{\psi}, \psi] e^{-\mathcal{S}[\bar{\psi}, \psi]} \psi_{\mathbf{k}_1}(i\omega_1) \dots \psi_{\mathbf{k}_n}(i\omega_n) \bar{\psi}_{\mathbf{k}'_n}(\omega'_n) \dots \bar{\psi}_{\mathbf{k}'_1}(i\omega'_1), \quad (1.60)$$

acquire a Λ -dependence. The advantage of the procedure that we are going to describe is that if the Λ -dependence of the Gaussian propagator is smooth and differentiable we are able to compute also the Λ -derivative of quantities which can be in principle obtained performing functional integrals (involving non Gaussian term), like, e.g., the one in Eq. (1.60). Assuming that we know the result of the functional integration, say for a generic quantity \mathcal{F}^Λ , at some value Λ_0 and that we are able to compute its Λ -derivative for all the values of Λ in the interval $[\Lambda_0, \Lambda']$, then we can obtain the value of the functional integral \mathcal{F}^Λ for any value of Λ in the interval by integrating a (standard) differential equation:

$$\mathcal{F}^{\Lambda'} = \int_{\Lambda_0}^{\Lambda'} d\Lambda \partial_\Lambda \mathcal{F}^\Lambda. \quad (1.61)$$

Usually, one refers to an equation in the form of Eq. (1.61) as **flow equation** for the quantity \mathcal{F} . In particular, the relevant quantities for the physical system we are interested in will be recovered for Λ_{fin} , when $f^{\Lambda_{\text{fin}}} = 1$. In this way a functional integration, which we are not able to perform, is traded for a standard integration of a differential equation.

Up to now this procedure is exact, but of little use unless we make it more concrete and specify some physical quantities for which we want to obtain the flow equations. It turns out that a convenient choice are the n -particle vertex functions *one*-particle irreducible (1PI) Γ_n . These are defined as the sum of all the connected Feynman diagrams with n incoming and n outgoing legs, which do not fall apart cutting *one* fermionic internal line. Let us stress that this is just one among several possible choices. In fact, one could also focus on other quantities, like, e.g. the connected Green's functions. This would correspond to other fRG schemes [129, 189].

Let us remember that an equivalent definition of the 1PI vertex functions can be given in terms of expansions in the fields of a 1PI generating functional $\Gamma[\bar{\psi}, \psi]$ [134]. It is possible to obtain a flow equation directly for the 1PI generating functional, as it is usually done in most of the functional derivations mentioned above, [5, 104, 129, 141, 156, 157]. This way, one obtains an equation for a functional, which turns out to be manageable only after an expansion in the fields: the final result is the hierarchy of equations for the 1PI vertex functions, which we will derive below following a different (diagrammatic) path.

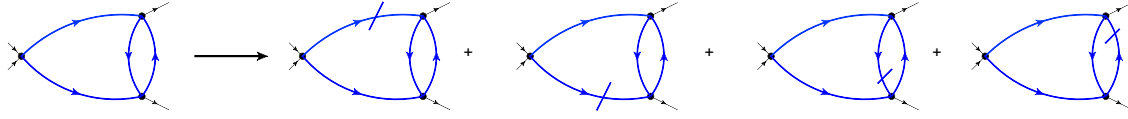


Figure 1.14: Diagrammatic representation of the Λ -derivative of a third order diagram contributing to the two particle 1PI vertex.

Let us start by writing the expansion for the 1PI n -particle vertex Γ_n^Λ at a given scale Λ as:

$$\Gamma_n^\Lambda = \sum_{d_{n,m}^\Lambda \in \text{1PI}_n} d_{n,m}^\Lambda. \quad (1.62)$$

1PI_n denotes the set of *all* diagrams, of all orders, contributing to Γ_n^Λ the n -particle 1PI vertex; $d_{n,m}^\Lambda$ is a selected diagram belonging to this set of perturbative order m in the interaction (but, obviously, having n incoming and outgoing legs). As such, it can be expressed as the integral of a product of $2m - n$ Green's functions \mathcal{G}_0^Λ , fulfilling momentum and frequency conservation at each interaction vertex, times a factor accounting for the interaction at each vertex. In the integral, the only terms that depend on Λ are the Green's function, since we have explicitly assumed that the interaction part of the action is Λ -independent. Therefore, the Λ -derivative of Γ_n^Λ can be written as the sum of terms in each of which one of the Green's function is derived with respect to Λ :

$$\partial_\Lambda \Gamma_n^\Lambda = \sum_{d_{n,m}^\Lambda \in \text{1PI}_n} \sum_{j=1, 2m-n} \int d^d k_j \sum_{i\omega_j} d_{n,m}^{\prime\Lambda}(j) \partial_\Lambda \mathcal{G}_0^\Lambda(\mathbf{k}_j, i\omega_j), \quad (1.63)$$

where $d_{n,m}^{\prime\Lambda}(j)$ corresponds to the diagram $d_{n,m}^\Lambda$ with the only difference that the j -th Green's function (and the relative integration) is removed. Mathematically:

$$d_{n,m}^\Lambda = \sum_{i\omega_j} \int d^d k_j d_{m,n}^{\prime\Lambda}(j) \mathcal{G}_0(\mathbf{k}_j, i\omega_j). \quad (1.64)$$

Introducing a new diagrammatic element for $\partial_\Lambda \mathcal{G}_0^\Lambda(\mathbf{k}_j, i\omega_j)$, which we denote by a single slashed line, we can represent diagrammatically the contributions to the derivative of the vertex function, as it is done in Fig.1.14 for a specific third order diagram. Let us observe that the Λ -derivative does not change the topology of the diagrams, i.e., the diagrams contributing to $\partial_\Lambda \Gamma_n^\Lambda$ are the same contributing to Γ_n^Λ , but with each Green's function line substituted once by a slashed line.

Let us now focus on the diagrams $d_{n,m}^{\prime\Lambda}$ contributing to the Λ -derivative of the 1PI vertexes. We will show that these diagrams can be expressed as a closed chain of one-particle irreducible blocks connected by Green's functions lines and a single slashed line. To see this we notice that $d_{n,m}^\Lambda$ is by definition one-particle irreducible, hence each diagram obtained removing a Green's function line can be written as a chain of irreducible sub-blocks connected by Green's function lines (see for example Fig. 1.15). Being in the form of a *chain* as soon as the diagram with

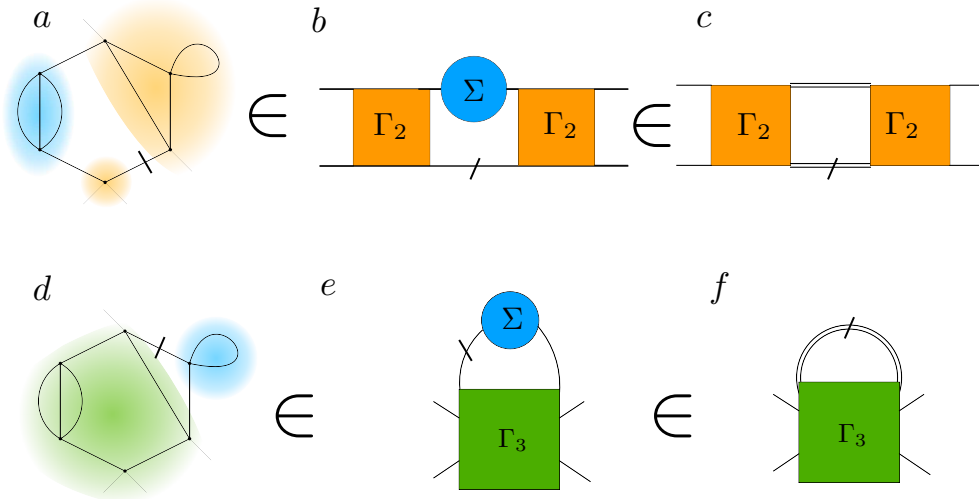


Figure 1.15: Schematic illustration of the ring shaped diagrams contributing to the derivative of a Feynman diagram in fRG. Diagrams a and d are topologically the same, but the slashed line, corresponding to the derivative of a Green's function is located in two different positions. Removing the slashed lines one obtains one-particle *reducible* diagrams. For example in diagram d it would be possible to separate the self-energy insertion (in sky blue) by cutting one Green's function line. Upon reinserting the slashed line the diagrams must form a ring structure, that guarantees one-particle *irreducibility*. Changing the position of the slashed line one obtains different vertex structure (compare diagrams b and e). In diagrams c and f the self-energy insertion has been reabsorbed in the *dressed* Green's function lines, represented by the double lines.

a Green's function removed contains more than one block it is one-particle *reducible*. Upon reinserting the missing Green's function, the diagram $d_{m,n}^\Lambda$ must be 1PI. This is the case only if the chain closes into a ring shaped structure once the Green's function line is restored. We refer to diagrams of this form as *ring*-diagrams, in which each vertex is connected to the neighboring one by a single Green's function line. The consideration above does not hold only for the diagram $d_{m,n}^\Lambda$, but also for its derivative $d_{m,n}^{\Lambda'}$. The only difference is that in the latter case in place of the missing Green's function is reinserted its Λ -derivative, i.e. a slashed line takes the place of a non slashed one, as shown in Fig. 1.15.

After having understood the shape of the diagrams contributing to $\partial_\Lambda \Gamma_n^\Lambda$ we have to sum them up. This is done in two steps: First, (i) we sum up all the diagrams sharing the same ring structure, but different sub blocks. Next, (ii) we sum up all those diagrams which have the same

vertex structure, but different self-energy insertions. As an example we can imagine that we are interested in those diagrams contributing to $\partial_\Lambda \Gamma_2^\Lambda$, in which one of the sub-blocks has only two legs and two sub-blocks have four legs (see Fig. 1.15a). It is easy to imagine that summing these diagrams including all the possible diagrams contributing to each sub-block will give us a diagram in which the sub-blocks are respectively substituted by the one-particle (1PI) vertex function, i.e. the self-energy¹⁴ Σ^Λ , and by the two-particle 1PI vertex function, i.e. Γ_2^Λ (see Fig. 1.15b). Let us then suppose that we want to sum all the self-energy insertions on the Green's function line connecting two given vertex functions. We have two possibilities: The slashed line, corresponding to $\partial_\Lambda \mathcal{G}_0^\Lambda$ may or may not be between the two considered vertexes. In the latter case the two vertexes can be connected by a dressed Green's function:

$$G^\Lambda = \mathcal{G}_0^\Lambda + \mathcal{G}_0^\Lambda \Sigma^\Lambda \mathcal{G}_0^\Lambda + \dots, \quad (1.65)$$

which accounts for all the diagrams with different self-energy insertions, and is represented by a double line. Instead all the diagrams in which the slashed line is located between the two vertexes can be summarized in a diagram introducing the so-called *singles scale* propagator:

$$\begin{aligned} S^\Lambda &= (1 + \mathcal{G}_0^\Lambda \Sigma^\Lambda + \dots) \partial_\Lambda \mathcal{G}_0^\Lambda (1 + \Sigma^\Lambda \mathcal{G}_0^\Lambda + \dots) \\ &= G^\Lambda (\mathcal{G}_0^\Lambda)^{-1} \partial_\Lambda \mathcal{G}_0^\Lambda (\mathcal{G}_0^\Lambda)^{-1} G^\Lambda = -G^\Lambda \frac{\partial (\mathcal{G}_0^\Lambda)^{-1}}{\partial \Lambda} G^\Lambda = \frac{\partial G^\Lambda}{\partial \Lambda} \Big|_{\Sigma^\Lambda = \text{const.}}, \end{aligned} \quad (1.66)$$

as shown diagrammatically in Fig. 1.15 by a slashed double line.

Considering the discussion above, the Λ -derivative of the vertex function Γ_n^Λ is obtained as follows: First draw all the rings including 1PI vertex functions Γ_m^Λ with $1 < m \leq n + 1$ and with incoming external indexes $\mathbf{k}_1, \omega_1, \dots, \mathbf{k}_n, \omega_n$ and outgoing external indexes $\mathbf{k}'_1, \omega'_1, \dots, \mathbf{k}'_n, \omega'_n$. One of the lines connecting the vertex functions must be a single-scale propagator S^Λ , while all the others are full propagators G^Λ . Then evaluate the ring diagrams performing the internal summation and following the standard diagrammatic rules.

The derivative of each n -particle 1PI vertex function, and therefore its flow equation, involves all the 1PI vertex functions with up to $2(n + 1)$ amputated legs. In fact, it is easy to see that closing two of the legs of an $n + 1$ -particle 1PI vertex with a single-scale propagator one obtains a diagram in the allowed ring structure with $2n$ amputated legs, i.e., this diagram contributes to the Λ -derivative of the n -particle vertex Γ_n^Λ . On the other hand it is not possible to generate diagrams of ring structure with $2n$ legs using vertexes of more than $n + 1$ particles: This structure allows to saturate only two of the external legs of a vertex. As a consequence of the fact that $\partial_\Lambda \Gamma_n^\Lambda$ depends also on Γ_{n+1}^Λ , we obtain an infinite hierarchy of flow equations.

For practical purposes, the treatment of vertexes with more than four legs is not feasible and therefore one usually **truncates** the flow equations by taking all the 1PI vertex functions Γ_n^Λ of order $n > 2$ equals to zero. This approximation is motivated by the fact that the original interaction in Eq. (1.56) is a two-particle interaction. Therefore, if (as is done in most fRG flows, see below) we start from $\mathcal{G}_0^{\Lambda_0} = 0$ the vertex functions with more than two legs vanish at the

¹⁴Strictly speaking the self-energy is not exactly the one-particle 1PI vertex function [134], but they differ by a noninteracting Green's function line.

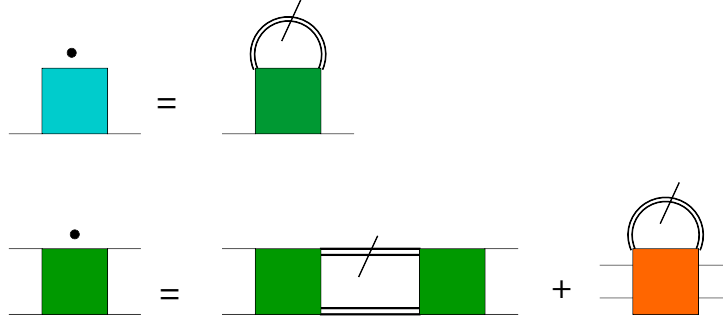


Figure 1.16: Flow equations for the self-energy Σ^Λ (light blue block), and the one-particle 1PI vertex Γ_2^Λ (green block). The last term of the derivative of Γ_2^Λ contains the three-particle 1PI vertex Γ_3^Λ (orange block), which in a truncated scheme is usually neglected. In order to translate these diagrams into equations one needs to attribute a direction and a spin to each of the internal lines.

beginning of the flow, but can grow bigger during the flow. By neglecting these vertex functions our flow equations are *not* exact anymore, but they can still be used to get approximate results for the self-energy and the two particle vertex functions. In fact it is reasonable to believe that at weak or moderate-coupling the n -particle vertex functions will not become too big and the approximation is justified. More formal arguments about the correctness of this approximation are given, for example, in Ref. [157].

In this respect fRG can be seen as a *renormalization group based* way of doing perturbation theory, and in a subsequent paragraph we will investigate more in detail the relation between diagrams of perturbation theory and diagrams of fRG.

The flow equations for the self-energy and the one-particle 1PI vertex can be written applying the standard [1, 134] diagrammatic rules¹⁵ to the diagrams shown in Fig. 1.16. In a very compact notation the flow equations, after truncating the three-particle 1PI vertex, i.e., $\Gamma_3^\Lambda = 0$, read:

$$\partial_\Lambda \Sigma^\Lambda = \Gamma_2^\Lambda \circ S^\Lambda, \quad (1.67)$$

$$\partial_\Lambda \Gamma_2^\Lambda = \Gamma_2^\Lambda \circ (S^\Lambda \circ G^\Lambda) \circ \Gamma_2^\Lambda. \quad (1.68)$$

Here the symbol ‘ \circ ’ stands for the standard summation over all internal variables, i.e., momentum integration as well as spin and Matsubara frequency summation. In most situations one has to truncate the flow equations by imposing that $\Gamma_3^\Lambda = 0$, i.e., the flow equations are truncated at the three-particle level. In this case the flow equation for the two-particle 1PI vertex includes a diagram, in the form of a *fermionic loop*, i.e., two fermionic lines connect two vertexes. The topological structure of this diagram (or diagrams, if we explicitly specify the direction and the spin of the internal lines) is topologically the same as the diagrams obtained in the context of (Shankar’s) modern renormalization group [164], in a cumulant expansion of the interaction

¹⁵In the diagrams in Fig. 1.16, and in general whenever we do not attribute a specific direction to the internal lines, vertex blocks represent the fully antisymmetrized vertexes, as explained, e.g., in Ref. [1] cf. Sec. 9.1.

part of the action at the quadratic order. In modern renormalization group framework these diagrams are called **one-loop** diagrams, a term that we will also use here to refer to the diagrams obtained at this truncation level.

Including 1PI vertexes Γ_n^Λ of higher n in the flow equations allows us to include in the flow equation for the two-particle 1PI vertex, also diagrams with more fermionic loops. For example it is easy to see, as we will show, how including (even partially) the contribution of the three-particle vertex generates *two-loop* diagrams. This will be discussed in the following, where we discuss also how retaining the most significant contribution of the three-particle vertex in the flow equation of the two-particle vertex allows for important improvements, in the diagrammatic content produced and in the fulfillment of the Ward identities.

Three-particle vertex and two-loop truncation Let us anticipate a very typical choice for the initial conditions of the flow and assume that $\mathcal{G}_0^{\Lambda_0} = 0$ for all momenta and frequencies. This corresponds, in RG language, to suppressing all the fluctuations, on all energy scales, at the beginning of the flow, . In this case $\Gamma_2^{\Lambda_0} = U$ and $\Gamma_{n>2}^{\Lambda_0} = 0$, i.e., at the beginning of the flow the n -particle vertex functions with $n > 2$ vanish. Therefore the three diagrams¹⁶ contributing to $\partial\Gamma_3^\Lambda$ in Fig. 1.17 are respectively of order $\mathcal{O}(U^4)$, $\mathcal{O}(U^4)$ and $\mathcal{O}(U^3)$. If we want to retain only the lowest order contributions arising from Γ_3^Λ in the flow for Σ^Λ and Γ_2^Λ , we can restrict ourselves to the lowest order diagram, which, in a compact notation¹⁷, reads:

$$\partial_\Lambda \Gamma_3^\Lambda = \Gamma_2^\Lambda G^\Lambda \Gamma_2^\Lambda G^\Lambda \Gamma_2^\Lambda S^\Lambda + \Gamma_2^\Lambda G^\Lambda \Gamma_2^\Lambda S^\Lambda \Gamma_2^\Lambda G^\Lambda + \Gamma_2^\Lambda S^\Lambda \Gamma_2^\Lambda G^\Lambda \Gamma_2^\Lambda G^\Lambda + \mathcal{O}(U^4). \quad (1.69)$$

To obtain the lowest order contribution of Γ_3^Λ to the flow of Γ_2^Λ , we should integrate Eq. (1.69). To this extent let us first substitute the single-scale propagator $S^\Lambda = \partial_\Lambda G^\Lambda|_{\Sigma=\text{const.}}$ with the derivative of the full Green's function with respect to Λ . Within a perturbation theory analysis, this is allowed at the third order in U since the error that we make in the substitution is $\propto (\partial_\Lambda \Sigma^\Lambda) \Gamma_2^\Lambda \Gamma_2^\Lambda \Gamma_2^\Lambda \sim \mathcal{O}(U^4)$. Then we rewrite Eq. (1.69) as a total derivative, by letting the Λ -derivative act also on the vertexes Γ_2^Λ , and again notice that the error that we make in doing so is $\propto (\partial_\Lambda \Gamma_2^\Lambda) \Gamma_2^\Lambda \Gamma_2^\Lambda \sim \mathcal{O}(U^4)$. In this way we obtain:

$$\Gamma_3^\Lambda = \int_0^\Lambda \partial_\Lambda (\Gamma_2^\Lambda G^\Lambda \Gamma_2^\Lambda G^\Lambda \Gamma_2^\Lambda G^\Lambda) + \mathcal{O}(U^4) = \Gamma_2^\Lambda G^\Lambda \Gamma_2^\Lambda G^\Lambda \Gamma_2^\Lambda G^\Lambda, \quad (1.70)$$

where in the last equation we have retained only the terms up to third order in U . Reinserting Eq. (1.70) for Γ_3^Λ in the flow equation for the two-particle 1PI vertex we obtain the diagrams shown in Fig. 1.18. In particular, diagrams *b* and *c* in Fig. 1.18 contain *two fermionic loops*, hence the name *two-loop approximation* [41, 96]. The diagram in Fig. 1.18*b* has a much easier structure than the third one. In fact in 1.18*b* the extra loop containing the single-scale propagator topologically has the form of a self-energy insertion. On the other hand, diagram 1.18*c* has the typical form of a parquet diagram. This can be seen considering that one can group the loop

¹⁶By looking at the diagrammatic structure of $\partial\Gamma_n^\Lambda$ one can see that the lowest order diagram is the one consisting of a ring in which the sub-block Γ_2^Λ is repeated n times.

¹⁷Here to avoid lengthy expression we suppress all the indexes and integrals.

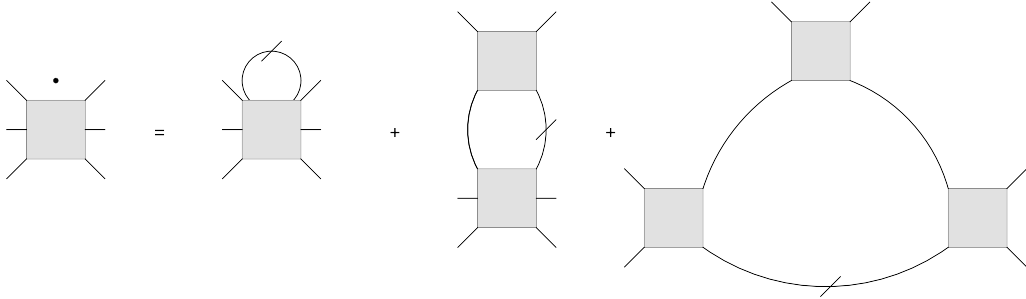


Figure 1.17: Λ -derivative of Γ_3^Λ .

on the right in a single vertex block. We refer to this loop as *internal*, since the loop variables of the *external* loop enter in its argument. This can also be seen in terms of **two-particle reducibility**: The third diagram in Fig. 1.18 falls apart in two pieces by cutting the loop lines of the *external* loop, and only afterwards also the *internal* loop can be split in two pieces by cutting two fermionic lines.

Conservation of Ward identities and Katanin substitution One possible way of estimating the improvement of the two-loop approximation compared to the one-loop one is by analyzing the violation of the Ward identity for the charge conservation [95]. The Ward identities [1, 181] are a set of relations that the vertex functions must fulfill in order that the conservation of physical quantities is respected. However in approximate solutions of a given problem the Ward identities may be violated. This is also the case for fRG, whenever we truncate the flow equations at a given order. Following Katanin [95] it is possible to derive a Ward identity, relative to charge conservation, which connects the self-energy and the two-particle 1PI vertex. By further deriving the Ward identity with respect to Λ one can see that the violation to the Ward identities, when truncating the flow equations, involves terms which are of $\mathcal{O}(U^3)$, i.e. the Ward identity is fulfilled only within the accuracy $\mathcal{O}(U^3)$. Repeating the same steps for the two-loop approximation one can further see that, in this case, the Ward identity is fulfilled with accuracy $\mathcal{O}(U^4)$. This shows the advantage of using a more complicated two-loop approximation rather than a one-loop one. Technically, the inclusion of the two-loop diagram in Fig. 1.18b) is not complicated: By inspection of such diagram one can recognize the derivative of the self-energy, and hence the following substitution, often called *Katanin substitution*:

$$S^\Lambda \rightarrow S^\Lambda - G^\Lambda \frac{\partial \Sigma^\Lambda}{\partial \Lambda} G^\Lambda = \frac{\partial G^\Lambda}{\partial \Lambda}, \quad (1.71)$$

accounts for the diagram in Fig. 1.18b). The inclusion of the diagram in Fig. 1.18c) is instead more involved [41].

In practice, it has been observed that using the Katanin substitution improves the convergence properties of the flow equations, and therefore it has been often applied, even without the inclusion of the overlapping two-loop diagrams in the flow. Only more recently it has been possible to implement a full two-loop approximation, with promising results [41, 98].

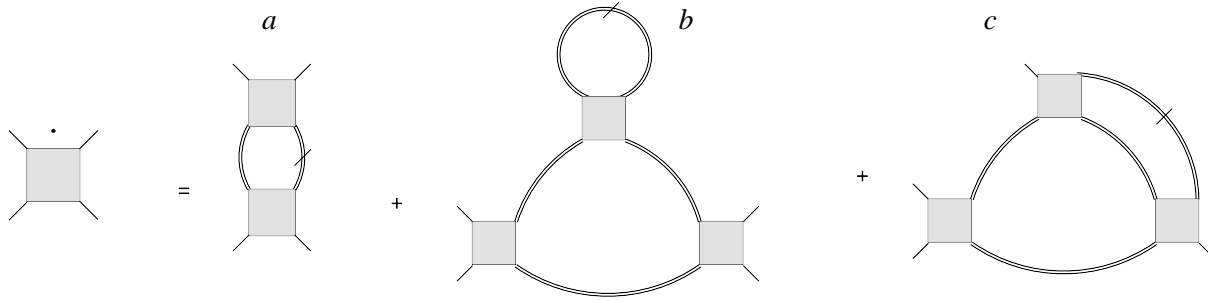


Figure 1.18: Contributions to $\partial_\Lambda \Gamma_2^\Lambda$ at the two-loop truncation level

1.4.2 Diagrammatic content of fRG

While it is clear that the fRG can be regarded as a *diagrammatic theory* (i.e., its equations can be expressed in terms of Feynman diagrams), it is not so obvious understanding how its diagrammatic content can be explicitly related to the specific subset of diagrams of other diagrammatic approximations, like e.g., n -th order perturbation theory, fluctuation exchange (FLEX), or parquet approximation. This is due to the fact that in the fRG a new diagrammatic element, the single-scale propagator, comes into the play, and the corresponding 1PI vertexes can be obtained only after integrating a set of differential equation, which is not present in the other diagrammatic theories. Without truncation, the integration could be done exactly and the diagrams would coincide with the exact ones. However, since truncation is unavoidable, the differential equations cannot be integrated exactly. In this situation the question about which (or how) diagrams are resummed, by integrating the flow equations, becomes highly nontrivial.

In the following we address this specific issue proceeding in two steps: First we will rewrite the flow equations in a less compact way and highlight their *channel* structure; then we will *formally* integrate them by iteration in order to compare them to other approximations.

As a first step let us rewrite explicitly the one-loop flow equations for the self-energy and the 1PI two-particle vertex. To this extent we just have to apply the diagrammatic rules and specify the direction of the internal propagators and label the external lines in the flow equations of Fig. 1.19.

$$\partial_\Lambda \Sigma^\Lambda(1'|1) = \int d2 S^\Lambda(2) \Gamma_2^\Lambda(2, 1'|2, 1); \quad (1.72)$$

$$\partial_\Lambda \Gamma_2^\Lambda(1'2'|12) = \mathcal{T}_{\text{pp}}^\Lambda(1'2'|12) + \mathcal{T}_{\text{ph-d}}^\Lambda(1'2'|12) + \mathcal{T}_{\text{ph-c}}^\Lambda(1'2'|12). \quad (1.73)$$

Here the label $1 \equiv (i\omega_1, \mathbf{k}_1, \sigma_1)$ denotes the set of Matsubara frequency, momentum and spin¹⁸. Accordingly, the integral $\int d1$ is a shorthand for $T \sum_{i\omega_1} \sum_{\sigma_1} \int d^d k$. The quantities \mathcal{T}_x , with $x = \text{pp}, \text{ph-d}, \text{ph-c}$, correspond respectively to the contribution of the first diagram, middle three diagrams, and last diagram on the right hand side of Fig. 1.19 respectively, and the subscript denotes the particle-particle, particle-hole direct and particle-hole crossed channels. In Fig. 1.19 the dashed lines inside the two-particle vertexes denote spin conservation and the

¹⁸And possibly also other degrees of freedom, e.g. an orbital index.

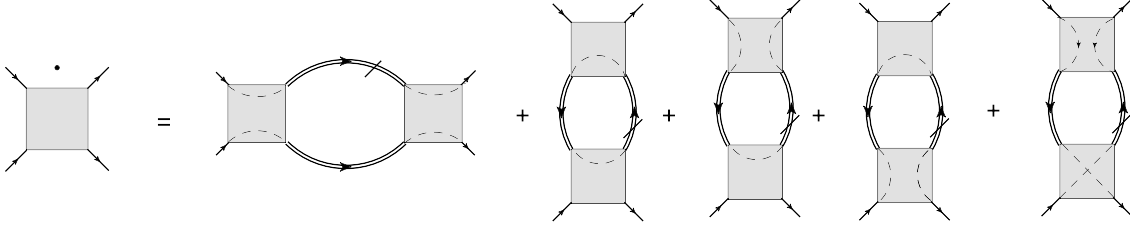


Figure 1.19: Explicit flow equations in the one-loop approximation to the flow equation for the two particle 1PI vertex Γ_2^Λ . The first diagram on the right hand side corresponds to the particle-particle channel, the second, third and fourth correspond to the particle-hole direct (or sometimes particle-hole bubble) channel, and the fifth corresponds to the particle-hole crossed channel (or sometimes particle-hole exchange).

ordering of the creation and annihilation operators associated with the vertexes. The reason for such a classification will be apparent in a moment. We can use the fact that for a translationally invariant system the arguments of the vertex functions are not independent:

$$\Sigma^\Lambda(1|1') \propto \delta(1 - 1'), \quad (1.74)$$

$$\Gamma^\Lambda(1'2'|12) \propto \delta(1' + 2' - 1 - 2), \quad (1.75)$$

to fix one of the two internal indices in the loops of Fig. 1.19. Doing so the contribution of each channel reads:

$$\begin{aligned} \mathcal{T}_{\text{pp}}(1'2'|12) &= \int d3 \quad (1.76) \\ \Gamma_2^\Lambda(1'2'|3(1' + 2' - 3)) &[S^\Lambda(3)G^\Lambda(1' + 2' - 3) + G^\Lambda(3)S^\Lambda(1' + 2' - 3)]\Gamma_2^\Lambda(3(1' + 2' - 3)|12), \end{aligned}$$

$$\begin{aligned} \mathcal{T}_{\text{ph-d}}(1'2'|12) &= \int d3 \quad (1.77) \\ \Gamma_2^\Lambda(1'3|1(3 + 1' - 1)) &[S^\Lambda(3)G^\Lambda(1' - 1 + 3) + G^\Lambda(3)S^\Lambda(1' - 1 + 3)]\Gamma_2^\Lambda((3 + 1' - 1)2'|32) + \\ \Gamma_2^\Lambda(1'3|1(3 + 1' - 1)) &[S^\Lambda(3)G^\Lambda(1' - 1 + 3) + G^\Lambda(3)S^\Lambda(1' - 1 + 3)]\Gamma_2^\Lambda((3 + 1' - 1)2'|23) + \\ \Gamma_2^\Lambda(1'3|(3 + 1' - 1)1) &[S^\Lambda(3)G^\Lambda(1' - 1 + 3) + G^\Lambda(3)S^\Lambda(1' - 1 + 3)]\Gamma_2^\Lambda((3 + 1' - 1)2'|32) \end{aligned}$$

$$\begin{aligned} \mathcal{T}_{\text{ph-c}}(1'2'|12) &= \int d3 \quad (1.78) \\ \Gamma_2^\Lambda(1'(3 + 2' - 1)|32) &[S^\Lambda(3)G^\Lambda(2' - 1 + 3) + G^\Lambda(3)S^\Lambda(2' - 1 + 3)]\Gamma_2^\Lambda(32'|1(3 + 2' - 1)) \end{aligned}$$

From the argument of the Green's function and single-scale propagator in the internal loop one can see the reason for the subdivision of $\partial_\Lambda \Gamma_2^\Lambda$ in three channels. In fact the Green's function and the single-scale propagator in each of the three classes of diagrams depends either on the loop argument, i.e., the integration variable 3 in equations (1.76-1.78), and on a single momentum and frequency transfer: $1' + 2'$ for \mathcal{T}_{pp} , $1' - 1$ for $\mathcal{T}_{\text{ph-d}}$ and $2' - 1$ for $\mathcal{T}_{\text{ph-c}}$. This dependence plays a major role: assume that at a given scale Λ the two-particle vertex is a well

behaved function; then the only possible divergence in $\partial_\Lambda \Gamma_2^\Lambda$ can be driven by a singularity in the bubble appearing in the internal loop. This kind of divergence is not surprising: it is closely related to the divergence of the renormalized vertex in RPA. In some studies [36, 191] only those terms for which the internal loops exhibit a singular dependence in each of the three channels were retained in the derivation of the flow equations of the divergent couplings. This approach, dubbed sometimes *g*-ology model, is particularly interesting for systems with clear Fermi surface nesting: It is assumed that the nonsingular terms do not affect qualitatively the physics of the competing instabilities, which is mostly determined by the structure of the Fermi surface, and consequently, by the corresponding singularity in the loop diagrams. This can be particularly relevant, for example, for one dimensional systems, or two dimensional systems with flat Fermi surfaces. However, in contrast with what is done in references [36, 191] the fRG scheme does *not* include in the flow equations only the most divergent contributions, but it allows to take into account also nonsingular diagrams that can give quantitative changes in the final results.

Two-particle vertex parametrization Before proceeding with the discussion let us discuss the most natural parametrization of the arguments of the two-particle 1PI vertex. This will be needed in the third chapter, and is connected with the channel decomposition described above. The two-particle 1PI vertex can be parametrized in terms of three independent frequencies and momenta. A convenient choice is represented by the following bosonic frequencies and momenta transfer:

$$\Pi = 1' + 2', \quad (1.79)$$

$$\Delta = 1' - 1, \quad (1.80)$$

$$X = 2' - 1. \quad (1.81)$$

This choice is strongly physically motivated: It corresponds to the frequency and momentum transfer in the three channels described above, and therefore constitutes, at least at weak-coupling, the "natural" argument for the (full) vertex¹⁹. Indeed, this parametrization captures the frequency dependence of the weak coupling structures of the local 1PI vertex [94, 149]. Conversely, the original (fermionic) Matsubara frequencies and incoming/outgoing momenta can be expressed as:

$$\begin{aligned} 1' &= \frac{1}{2}(\Pi + \Delta - X) \quad , & 2' &= \frac{1}{2}(\Pi - \Delta + X), \\ 1 &= \frac{1}{2}(\Pi - \Delta - X) \quad , & 2 &= \frac{1}{2}(\Pi + \Delta + X). \end{aligned} \quad (1.82)$$

Let us notice in passing that if we define the bosonic Matsubara frequencies as $\Omega_\Pi = 2\pi/\beta n_\Pi$, $\Omega_\Delta = 2\pi/\beta n_\Delta$ and $\Omega_X = 2\pi/\beta n_X$, the only allowed combinations for the three frequencies are

¹⁹At weak-coupling, one can expect that the main structures of the 1PI vertex will be the ones associated with the lowest order diagrams $\mathcal{O}(U^2)$, which have the frequency and momentum dependence described above. We note, incidentally, that these diagrams are *two-particle reducible*, and therefore not present in the *two-particle irreducible* vertex.

those with $n_{\Pi} + n_{\Delta} + n_X$ odd, to preserve the fermionic frequency of the Matsubara frequencies.

Iterative solution of the flow equations

We are finally in the position to show explicitly which diagrams are generated by the flow. To this extent let us maintain the fermionic frequency and momenta parametrization of the vertex and solve the flow equations (1.72) and (1.76-1.78) iteratively. Let us stress from the very beginning that the iterative solution is used only for pedagogical purposes. In principle, one can not attribute a too specific physical meaning to the intermediate result (at a certain integration step), since the iterative solution obviously corresponds to the true solution of the problem only after convergence. Let us denote $\Sigma^{(n)\Lambda}$ and $\Gamma_2^{(n)\Lambda}$ the self-energy and two-particle 1PI vertex function at the iteration n . At the 0-th order in the iteration we assume:

$$\Sigma^{(0)\Lambda} = \Sigma^{\Lambda_0}, \quad (1.83)$$

$$\Gamma_2^{(0)\Lambda} = \Gamma_2^{\Lambda_0}, \quad (1.84)$$

which do not depend on Λ . Therefore the integration of equations (1.72) and (1.73) can be readily performed, and we obtain, for the self-energy after the first iteration:

$$\begin{aligned} \Sigma^{(1)\Lambda}(1) &= \Sigma^{\Lambda_0}(1) + \left[\int d2 \ G^{\Lambda'}(2) \Gamma_2^{\Lambda_0}(12|12) - \Gamma_2^{\Lambda_0}(12|21) \right]_{\Lambda'=\Lambda_0}^{\Lambda'=\Lambda} \\ &= \Sigma^{\Lambda_0}(1) + \Sigma_{\text{HF}}^{\Lambda}(1) - \Sigma_{\text{HF}}^{\Lambda_0}(1). \end{aligned} \quad (1.85)$$

The interpretation of this result is straightforward if we start the flow with a vanishing Gaussian propagator $\mathcal{G}_0^{\Lambda_0} = 0$. In this case the initial conditions are $\Sigma^{\Lambda_0} = 0$ and $\Gamma_2^{\Lambda_0} = U$. By reinserting these in Eq. (1.85) one can easily see that the obtained result is the first order perturbation theory result, i.e., the ‘‘standard’’ Hartree-Fock diagrams.

In general, if we started the flow from a nonvanishing choice of \mathcal{G}_0^{Λ} the corresponding initial condition for the self-energy and the 1PI two-particle vertex would have been different. In this case, the flow equations generate a term $\Sigma_{\text{HF}}^{\Lambda} - \Sigma_{\text{HF}}^{\Lambda_0}$ which corrects an initial condition Σ^{Λ_0} non vanishing from the beginning. The topological form of the term generated by the flow $\Sigma_{\text{HF}}^{\Lambda}$, however, would *not* change compared to the previous case: It still consists of the Hartree and the Fock diagrams, *but* this time with two important differences: (i) the vertexes in the diagrams are not U anymore, but rather $\Gamma_2^{\Lambda_0}$, corresponding to the specific choice of the initial Gaussian propagator, (ii) the Green’s function lines are dressed by the self-energy Σ^{Λ_0} . However, Σ^{Λ_0} is by definition the *exact* self-energy of the problem defined by the action \mathcal{S}^{Λ_0} , hence already includes the Hartree and Fock diagrams of that specific action. To avoid double counting these diagrams need to be subtracted, and this is *automatically* done by the lower boundary of the integral in $d\Lambda$, which gives $-\Sigma_{\text{HF}}^{\Lambda_0}$, and removes the redundant contribution to the self-energy.

For the two-particle vertex we obtain:

$$\begin{aligned}
\Gamma_2^{(1)\Lambda}(1'2'|12) &= \Gamma_2^{\Lambda_0}(1'2'|12) + \left[\int d3 \left\{ \right. \right. & (1.86) \\
&\quad \chi^{\Lambda'}(3, 1' + 2' - 3) \Gamma_2^{\Lambda_0}(1'2'|3(1' + 2' - 3)) \Gamma_2^{\Lambda_0}(3(1' + 2' - 3)|12) \\
&\quad + \chi^{\Lambda'}(3, 1' - 1 + 3) \Gamma_2^{\Lambda_0}(1'3|1(3 + 1' - 1)) \Gamma_2^{\Lambda_0}((3 + 1' - 1)2'|32) \\
&\quad + \chi^{\Lambda'}(3, 1' - 1 + 3) \Gamma_2^{\Lambda_0}(1'3|1(3 + 1' - 1)) \Gamma_2^{\Lambda_0}((3 + 1' - 1)2'|23) \\
&\quad + \chi^{\Lambda'}(3, 1' - 1 + 3) \Gamma_2^{\Lambda_0}(1'3|(3 + 1' - 1)1) \Gamma_2^{\Lambda_0}((3 + 1' - 1)2'|32) \\
&\quad \left. \left. + \chi^{\Lambda'}(3, 2' - 1 + 3) \Gamma_2^{\Lambda_0}(1'(3 + 2' - 1)|32) \Gamma_2^{\Lambda_0}(32'|1(3 + 2' - 1)) \right\} \right]_{\Lambda'=\Lambda_0}^{\Lambda'=\Lambda} \\
&\equiv \Gamma_2^{\Lambda_0}(1'2'|12) + \left[\Gamma^{\Lambda_0} \circ \chi^{\Lambda'} \circ \Gamma^{\Lambda_0}(1'2'|12) \right]_{\Lambda'=\Lambda_0}^{\Lambda'=\Lambda}.
\end{aligned}$$

Where $\chi^\Lambda(1, 2) = G^\Lambda(1)G^\Lambda(2)$. The result of Eq. (1.86), if our initial condition is $\mathcal{G}_0^\Lambda = 0$, is the second-order perturbation theory expression for the vertex [96]. Correspondingly, similarly to what happens for the self-energy, if we start from a different, less trivial, choice for the initial Gaussian propagator, one gets a correction to the initial two-particle 1PI vertex $\Gamma_2^{\Lambda_0}$, including one-loop diagrams built with the Green's function bubble of the problem at the final scale Λ and the initial vertex function. Again the lower boundary of the integral automatically removes the diagrams that would be otherwise counted twice.

Obtaining the next step in the iteration is more involved. Let us focus on the two particle vertex and substitute the result of equation (1.86) for the vertex, and dress the Green's function with the self-energy obtained by (1.85) in the right hand side of the flow equations. To generate diagrams up to the third order in the two-particle vertex, we substitute $\Gamma_2^{(1)\Lambda}$ only for one of the two vertexes on the right hand side of the equation. We can distinguish the following classes of diagrams:

- **one diagram** in which the two vertexes are both Γ^{Λ_0} :

$$\Gamma_2^{(2a)\Lambda}(1'2'|12) = \Gamma_2^{\Lambda_0}(1'2'|12) + \int_{\Lambda_0}^{\Lambda} d\Lambda' \Gamma_2^{\Lambda_0} \circ P^{(2)\Lambda'} \circ \Gamma_2^{\Lambda_0}, \quad (1.87)$$

with $P^{(2)\Lambda}(12) \equiv G^\Lambda(1)S^\Lambda(2) + S^\Lambda(1)G^\Lambda(2)$, with the Green's function lines dressed by the self-energy at the previous iteration $\Sigma^{(1)\Lambda}$. Due to the Λ -dependence of $\Sigma^{(1)\Lambda}$ the integration over Λ can not be performed as easily as in the previous iteration, since P^Λ is not in the form of a total Λ -derivative. On the other hand, if we apply the Katanin substitution Eq. (1.71) to the single-scale propagator, the integral can be performed and gives a correction to the two-particle vertex identical to the one of Eq. (1.86), but with the propagators in the bubble $\chi^{(2)}$ computed with the self-energy of the previous iteration $\Sigma^{(1)\Lambda}$.

- **Ladder type diagrams** like the ones shown in Fig. 1.20. We use the symbol $\circ_{x=pp,\overline{ph},ph}$ to specify the summation over the internal indexes, but including *only* diagrams reducible

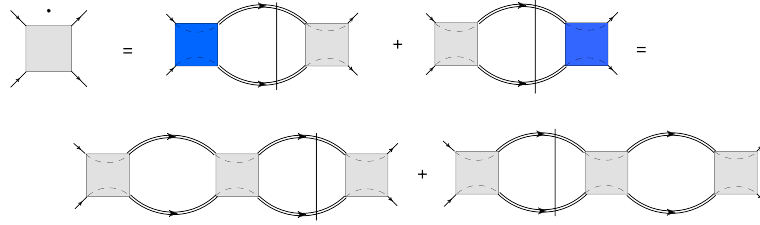


Figure 1.20: Ladder type diagrams generated at the second step in an iterative solution of the flow equations. The blue box represents $\Gamma_2^{(1)\Lambda'}$, while the gray one represents $\Gamma_2^{\Lambda_0}$. Here the long line crossing two Green's functions marks the propagators the loop on which the Λ -derivative acts.

either in the particle-particle, particle-hole direct or particle-hole crossed channel respectively (i.e., *reducible* in the specified channel). Then such a diagram, e.g., in the particle-particle channel reads:

$$\begin{aligned} \Gamma_2^{(2b)\Lambda}(1'2'|12) &= \int_{\Lambda_0}^{\Lambda} d\Lambda' \Gamma_2^{\Lambda_0} \circ_{\text{pp}} \chi^{(1)\Lambda'} \circ_{\text{pp}} \Gamma^{\Lambda_0} \circ_{\text{pp}} P^{(2)\Lambda} \circ_{\text{pp}} \Gamma_2^{\Lambda_0} \quad (1.88) \\ &+ \int_{\Lambda_0}^{\Lambda} d\Lambda' \Gamma_2^{\Lambda_0} \circ_{\text{pp}} P^{(2)\Lambda'} \circ_{\text{pp}} \Gamma^{\Lambda_0} \circ_{\text{pp}} \chi^{(1)\Lambda} \circ_{\text{pp}} \Gamma_2^{\Lambda_0}. \end{aligned}$$

Once again, this integral cannot be performed straightforwardly, even using the Katanin substitution: Forming a total Λ -derivative would be possible only if all the lines in the two terms were dressed with the same self-energy, which is evidently not the case. However this looks, to some extent, suspicious: From the structure of the flow equations it appears that self-energy and vertex are always kept at the same scale Λ . In fact, this problem reflects the arbitrariness in the iterative solution of a system of coupled equations, which does not have a meaning at each iteration step. Hence even limiting ourselves to illustrative purposes, it is desirable to keep all the internal lines dressed with the *same* self-energy. A possible way to obtain this is proceeding as follows: First compute the self-energy from the two-particle vertex at the previous iteration; then, plug the new self-energy and the old two-particle vertex for computing an updated vertex using equations (1.76-1.78). Finally insert again this ‘‘intermediate’’ vertex just obtained in the flow equations (1.76-1.78) to compute the final vertex function. This is reminiscent of the internal loop iteration that is sometimes needed in the iterative solution of the parquet equations [187]. Following the prescription just described for the iterative solution, we have that all the lines in the diagrams like the ones shown in Fig. 1.20 are dressed with the same self-energy. Doing so (and using the Katanin substitution) we are now able to integrate Eq. (1.88) by forming a total Λ -derivative and we obtain a standard ladder diagram with two loops. Such diagrams are generated in all channels separately. These are the diagrams that can be generated by means of RPA.

- **Parquet-type diagrams**, like the one shown in Fig. 1.21. In this class of diagrams a block containing a loop (internal, according to the definition given above) in some given

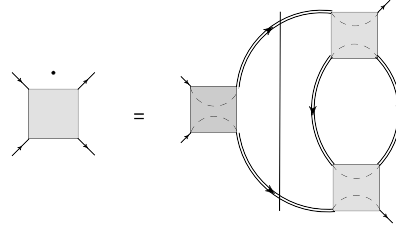


Figure 1.21: Parquet type-diagram generated in the second step of an iterative solution of the flow equations. The blue box represents $\Gamma_2^{(1)\Lambda'}$, while the gray one represents $\Gamma_2^{\Lambda_0}$. In this case the internal loop is particle-hole and the external one particle-particle.

channel, say for example particle-hole direct, substitutes one of the two bare vertexes that build up the external loop in a different channel, say for example particle-particle. Also in this case we can not form a total Λ -derivative: The single-scale propagator acts only on the line of the external loops, there is no diagram in which the derivative acts on the lines of the internal loop, and, hence, even applying the Katanin substitution is not sufficient to form a total derivative. For simplicity, let us restrict ourselves to the third order²⁰ in the two-particle vertex U . At this order we can approximate the single-scale propagator with the total derivative of the Green's function. Doing so, the diagram of Fig. 1.21 evaluates to:

$$\int_{\Lambda_0}^{\Lambda} d\Lambda' \Gamma_2^{\Lambda_0} \circ_{pp} P^{\Lambda'} \circ_{pp} \Gamma_2^{\Lambda_0} \circ_{ph} \chi^{\Lambda'} \circ_{ph} \Gamma^{\Lambda_0} = \quad (1.89)$$

$$\Gamma_2^{\Lambda_0} \circ_{pp} \chi^{\Lambda'} \circ_{pp} \Gamma_2^{\Lambda_0} \circ_{ph} \chi^{\Lambda'} \circ_{ph} \Gamma^{\Lambda_0} -$$

$$\int_{\Lambda_0}^{\Lambda} d\Lambda' \Gamma_2^{\Lambda_0} \circ_{pp} \chi^{\Lambda'} \circ_{pp} \Gamma_2^{\Lambda_0} \circ_{ph} P^{\Lambda'} \circ_{ph} \Gamma^{\Lambda_0}.$$

The last term is identical to the one in Fig. 1.21, but with the line denoting the Λ -derivative switched from the external propagator to the internal one. There is no diagram that cancels this contribution at the truncation level of three-particle vertex. Such a diagram is however present at the two-loop level (see Fig.1.18). A posteriori this is not surprising after all, and we could have seen this in a different way. The derivative of a third order parquet-type diagram is shown in Fig. 1.14. It is made up of four contributions. It is easy to see that upon removing the slashed line the two diagrams on the left can be put in the form of two blocks with four legs connected by a Green's function. These two blocks belong to the two-particle 1PI vertex, and therefore the first two diagrams of Fig. 1.14 are included in the flow with truncation at the level of the three-particle vertex. On the contrary removing the slashed line from the two rightmost diagrams in Fig. 1.14 one obtains a block with *six* legs, i.e., a block included in the *three*-particle vertex. Truncating at the level of the three-particle vertex we do not include these diagrams in our flow equa-

²⁰It would be more appropriate to say that we restrict ourselves to some order in $\Gamma_2^{\Lambda_0}$. However for the time being we take the freedom of assuming that the initial vertex is of the same order of the interaction. Practically this is always the case.

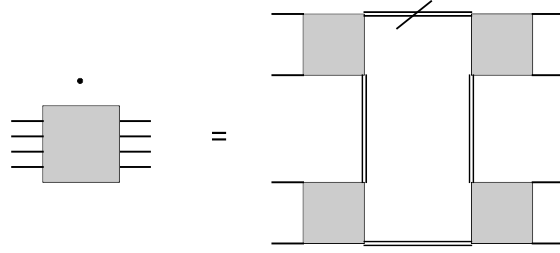


Figure 1.22: Lowest order contribution to the flow of the four-particle 1PI vertex Γ_4^Λ .

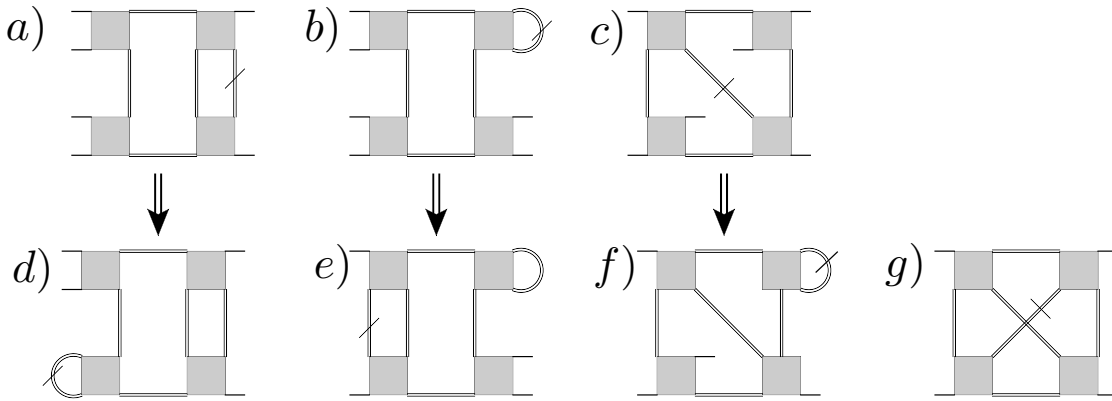


Figure 1.23: Top row: Contributions to Γ_3^Λ at the fourth order in $\Gamma_2^{\Lambda_0}$, arising from the four-particle 1PI. Bottom row: Some selected contributions at the three loop level to be included in the flow of the two-particle 1PI vertex.

tion. These diagrams are exactly the same that we miss to form a total Λ -derivative in the iterative solution, as illustrated before. We will argue later that even if those diagrams are of third order in the interaction, in many cases (in particular for a *regularizing* cutoff) the neglected diagrams (i.e. those in which the single-scale propagator is acting on the internal loop) are less relevant than the ones included (i.e. those in which the single-scale propagator is acting on the external loop).

- **double counting subtraction terms**, generated by the lower boundary of the integral over $d\Lambda$. Structurally these diagrams are the same as the diagrams shown above, but with the internal loop lines being substituted by the Green's functions at the scale Λ_0 . The role of these diagrams is very important, as they guarantee that no new diagram generated by the flow is counted twice. This means, in practice, that all the corresponding diagrams already included in the initial condition, but evaluated with the initial Green's function, are removed. It is important to stress here that within the fRG procedure the removal of double counting diagrams is intrinsically encoded in the formalism, i.e. it is not necessary to subtract them by hand (as for example in LDA+DMFT). In the case of $\mathcal{G}^{\Lambda_0} = 0$ all these diagrams vanish identically.

An intriguing question is the following: by retaining the leading terms at the fourth order in Γ^{Λ_0} , can we obtain something similar to the Katanin substitution for the parquet type diagrams (like those of Fig 1.21)? The answer is indeed positive. First, we would need to take into account the lowest order contribution in the flow equation of Γ_4^Λ . It is clear that this contribution is constituted by a ring of four two-particle 1PI vertexes connected by three Green's function and one single-scale propagator, as shown in Fig.1.22. Inserting this diagram in the flow for the three- and two-particle 1PI vertex generates respectively diagrams with two and three loops, as in Fig. 1.23. In particular, the diagrams d) and f) of Fig.1.23 have the required structure to allow for the substitution $S^\Lambda \rightarrow \partial_\Lambda G^\Lambda$ in the diagram of Fig.1.21. Let us also observe in passing, that the fourth diagram of the bottom row of Fig. 1.23 is the lowest order *two-particle* irreducible diagram, and hence it cannot be generated within a parquet²¹ approximation [22, 149].

From the analysis above we can draw some conclusion about the diagrammatic content of fRG. Truncating the equation hierarchy at the level of the three-particle vertex, the flow equations for the vertex are in the form of equations (1.76-1.78) diagrammatically shown in Fig.1.19, hence also the name one-loop approximation for this truncation level. In an iterative solution, we recover the results of first order perturbation theory for the self-energy, and second order perturbation theory for the vertex after the first iteration. By further iterations of the flow equations, we obtain diagrams which have the topology of parquet-diagrams, but due to the neglect of three- and more particle vertex, are only an *approximation* to them. The reason for this lays in the fact that, structurally, the parquet diagrams consist of a sequence of nested loops. Recasting a diagram in the form of a total derivative with respect to Λ requires that the single-scale propagators acts once on every loop line. Instead, truncating the flow equation at some level, one is able to include only those diagrams in which the single-scale propagator acts on the outermost loops. For example truncating at the level of the three-particle vertex one obtains the one-loop approximation, and the single-scale propagator acts only on the lines of the outer loop.

As a further example let us consider the diagrams in Fig. 1.24. In the top row we show a diagram of fourth order in the interaction with three nested loops. The Λ -derivative of this diagram consists of six diagrams, in which a single-scale propagator substitutes each of the the Green's function lines. Of these six diagrams, the two with the single-scale propagator on the outermost loop can be obtained already truncating the flow equations at the level of the three-particle vertex. This is shown in the middle row of Fig. 1.24: One can substitute the vertex labeled 1 with a block of a loop and two vertexes obtained at the previous iteration; eventually substituting a block containing a loop also for the diagram labeled 2, in the next iteration, one recovers the desired diagram. At the next loop-nesting level, to obtain a diagram in which the single-scale propagator substitutes one of the Green's function lines of the first internal loop, one needs to consider a diagram with two loops, like the one shown in in the left

²¹The ‘‘parquet approximation’’ must not be confused with the parquet equations. The parquet equations are an exact relation between the two-particle reducible vertexes and the two-particle irreducible (2PI) one, while the parquet approximation consists in replacing the 2PI vertex with its lower order contribution to calculate the two-particle reducible vertexes.

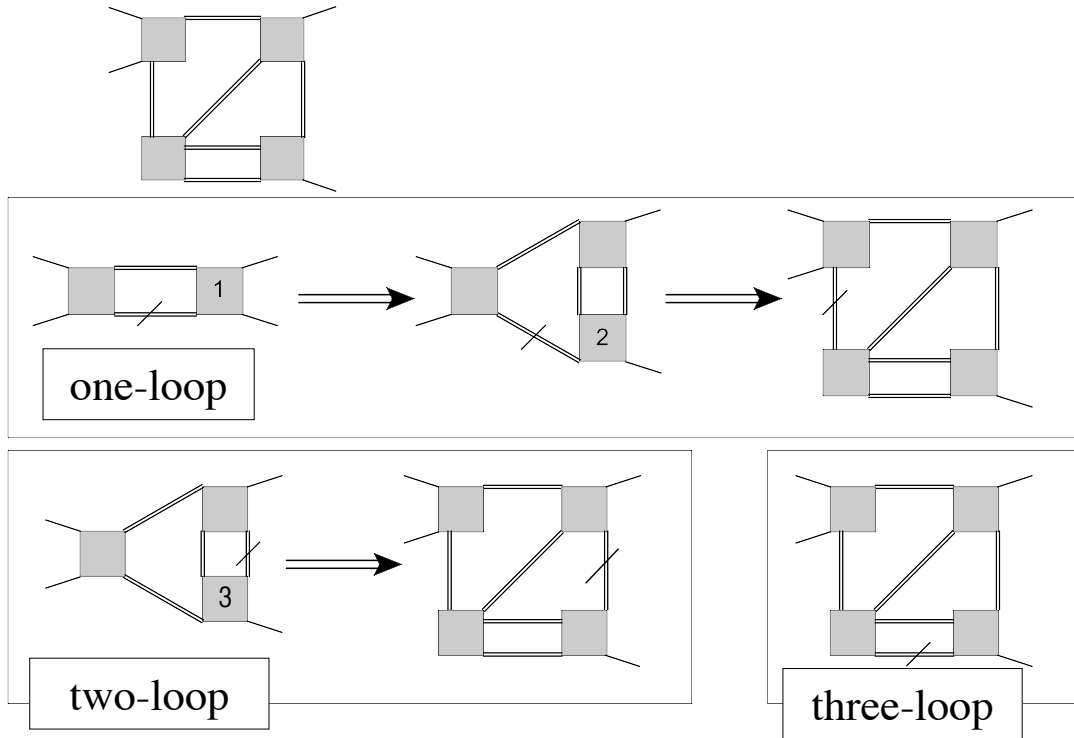


Figure 1.24: Example of how a diagram is generated in the iterative solution of the flow equations.

of bottom row of Fig. 1.24. Then, at the next iteration step, substituting the vertex labeled 3 with a block containing one loop one obtains the desired contribution. Finally, the diagrams in which one of the fermionic lines of the innermost loop is slashed can not be obtained by substituting any of the vertices by a block containing a loop, i.e., it is not obtained at the one-loop level. These diagrams can be obtained only in an approximation that includes from the beginning, in the flow equations for the 1PI two-particle vertex, diagrams with three nested loops, which can be ascribed to the leading order contribution of the four-particle vertex. Only if all these contribution are included one can form the total derivative of the diagram that we are considering.

As mentioned, in a one-loop approximation scheme, therefore, we would obtain the diagrams of second order perturbation theory at the first step of an iterative procedure. Higher order contributions would be generated in the next iterations, but an exact identification with perturbative diagrams is not possible for them. Topologically, the generated diagrams (at this approximation level) are in the form of a sequence of nested loops, and consequently **two-particle reducible**: It will always be possible to split the diagrams in two parts by cutting the lines of the most *external* loop. Hence the structure of the diagrams generated at the one- (and two-) loop truncation level is exactly the same of the diagrams included in the parquet ap-

proximation. Arguably, even if the diagrams of the parquet approximation are not reproduced exactly, due to the truncation, the fRG will, in many cases, capture the main contribution to them. The connection between parquet approximation²² and fRG that we have elucidated using a diagrammatic procedure is shown in Ref. [25, 26] regarding the problem from the opposite perspective, i.e., they started considering the parquet approximation as a perturbative approximation for the vertex and shown that retaining only the leading contributions they lead to the one-loop renormalization group equations. We will come back to the approach of Ref. [26] at the end of this section. Two-particle irreducible diagrams beyond the bare interaction are not included in the parquet approximation. The lowest order ones, however, can be in principle be obtained in fRG in a three-loop truncation scheme, i.e., retaining the leading order contribution from the four-particle vertex allows, in principle, to go beyond the parquet approximation, in an fRG framework.

In general if we retain contribution up to the n -loop (i.e., we keep the leading order contribution from the $n + 1$ -particle 1PI vertex) we reproduce, after the n -th iteration the perturbation theory result up to the order $n + 1$ for the two-particle 1PI vertex. Among the generated diagrams, all the 2PI diagrams, up to the given approximation order, would be included. By further iterating, we will build approximately other *reducible* diagrams, but no more irreducible ones will be generated.

Finally let us conclude with two important remarks: First, as mentioned, the results of an iterative solution must be taken with a grain of salt, and in a *real* solution one can not rigorously isolate the contributions of some perturbation order. Second, we have often implicitly assumed that $\Gamma_2^{\Lambda_0} = U$, which is the typical case, but not strictly necessary. In fact we will see in the following that one can also start from a $\Gamma_2^{\Lambda_0}$ already containing nontrivial correlation effects.

Hitherto, most of the fRG calculations have been performed at the one-loop approximation level, since including an higher number of loops raises the level of the computational challenge significantly: Only a few calculations at the two-loop level have been performed [41, 96] with a still manageable computational cost.

Choice of the cutoff

In this section we will discuss some possible cutoff choices. In particular we will first discuss the most *conventional* choices, in the sense that they are suited for starting the flow from a problem which includes only ‘‘trivial’’ correlations (i.e. $\Gamma_2^{\Lambda_0} = U$), or in other words, a problem in which all the fluctuations, at all energy scales, are suppressed. This is opposed to the cutoffs that already include some nontrivial correlation effects in the beginning of the flow, like the recently introduced hybridization cutoff [102] for an impurity problem, or the cutoff used in DMF²RG, that will be the main topic of the fourth chapter.

Due to the truncation, the final result, of the fRG flow, due to the truncation, will be in-

²²We also mention that some similar relations were obtained also by the russian school, see, e.g., Ref. [191] and reference therein. Here some equations close to the ones of one-loop renormalization group are obtained starting from the perturbative expansion of the vertex using the so-called ‘‘Sudakov trick’’. It is very difficult, however, to find a description of this trick in the western literature.

fluenced by the cutoff used, through the choice of the initial ‘‘solvable’’ action S^{Λ_0} , but also through the details of the Gaussian propagator for each value of Λ . Therefore it is necessary to choose appropriately in order to grasp the relevant. There are two main guidelines to be in principle considered in this choice: the regulator property and the unbiasedness, i.e., the property of treating on the same footing all the channels.

The regulator properties are connected with the way instabilities may arise due to the properties of the Fermi surface. To see this, let us consider the general expression of the susceptibility in the random phase approximation (RPA):

$$\chi^{\text{RPA}} = \frac{\chi^0}{1 - U\chi^0}. \quad (1.90)$$

Here we have omitted the specific momentum and frequency arguments, and denoted with χ some general susceptibility of the system; χ^0 represents the bare Green’s function bubble, whose general expression is of the form [4]:

$$\chi^0(i\Omega, \mathbf{q}) \propto \int d\mathbf{k} \frac{n(\xi_{\mathbf{k}}) - n(\xi_{\mathbf{k}+\mathbf{q}})}{i\Omega - (\epsilon_{\mathbf{k}} - \epsilon_{\mathbf{k}+\mathbf{q}})}, \quad (1.91)$$

with n being the Fermi function, and ξ the energy measured from the Fermi level. A divergence in the expression of Eq. (1.90) for some value of frequency and momentum signals the tendency of the system towards an instability, and requires a different treatment. Especially at low temperature more than one susceptibility may diverge, making it difficult to find out which is the leading one. Let us illustrate how this happens with some examples. Trading the integral over the momenta for an integral over the density of states $N(\epsilon) = \int d\mathbf{k} \delta(\epsilon - \epsilon_{\mathbf{k}})$ we obtain the following expression for $\Omega = 0$ and $\mathbf{q} \rightarrow 0$ at low temperature:

$$\chi^0(i\Omega = 0, \mathbf{q} \rightarrow 0) \propto \int d\epsilon N(\epsilon) \frac{\partial n(\epsilon)}{\partial \epsilon} = N(0). \quad (1.92)$$

In two dimensions, or in general in presence of a Van Hove singularity of the density of states the quantity $N(0)$ is logarithmically divergent.

Another divergence in two dimensions and with nearest neighbors hopping dispersion $\epsilon_{\mathbf{k}} = -[2t(\cos(k_x) + \cos(k_y))]$ happens for $\mathbf{Q} = (\pi, \pi)$, the nesting vector at half-filling (the Fermi surface is perfectly nested²³). In this case:

$$\chi^0(i\Omega = 0, \mathbf{Q}) = \int d\epsilon N(\epsilon) \frac{n(\epsilon - \epsilon_F) - n(-\epsilon - \epsilon_F)}{2\epsilon}. \quad (1.93)$$

In this case the divergence is even stronger as the function to integrate is large for small values of ϵ : the contribution coming from the energy region close to the Fermi surface is the most important. Since the two dimensional Hubbard model at half-filling has also a Van Hove singularity in the density of states, the system has two divergent susceptibilities in the particle-hole

²³In the words of Shankar: ‘‘Each point on the Fermi surface goes to another point on the Fermi surface upon adding a vector \mathbf{Q} . This means that, if we shift the figure by \mathbf{Q} , the shifted figure (in the repeated zone scheme) will fit perfectly with the original like something out of Escher’s drawings’’ [164]

crossed channel. The RPA is able to treat them *singularly*, the ‘renormalization’ of the susceptibility at a wave vector \mathbf{q} depends only on the bare susceptibility at that vector, and is not influenced by the other, possibly divergent, susceptibilities. In this case RPA predicts, for the half filled Hubbard model, an instability of the system towards the symmetry breaking associated with the stronger susceptibility, i.e., the antiferromagnetic one associated with the nesting vector, which is eventually correct. We will see soon how a regularizing cutoff allows us to better tackle this problem.

The other requirement that we want from a regulating function is the unbiasedness. This means that we want our cutoff to allow for a treatment on the same footing of all the channels and of all the momentum and frequency combinations, including both the diverging and the non diverging ones.

Regularizing cutoffs The main contributions to the bubble diagrams come from the region of the momentum space in the immediate vicinity of the Fermi surface, see equations (1.92) and (1.93). Our aim is to sum up these contributions to the integral step by step, by getting gradually closer to the Fermi surface, and eventually recovering the divergence at the very end of the flow.

This is closely related to the original spirit of Wilson renormalization group, in which, starting from high energy, some energy (or distance) scale is gradually integrated out, to obtain, in the end of the flow, the solution of the problem in which all the energy scales are taken into account.

In our framework we can reach this goal by assuming that the Gaussian propagator has the following form:

$$\mathcal{G}_{\mathbf{k}}^{\Lambda}(i\omega) = \mathcal{G}_{\mathbf{k}}(i\omega)\Theta_{\Lambda}(i\omega, \mathbf{k}), \quad (1.94)$$

where Θ_{Λ} is a function equal to one for energy or momentum larger than the cutoff Λ (which dimensionally is an energy) and equal to zero for energy or momentum smaller than Λ , the momentum being measured from the Fermi surface. In this way, starting from some value of Λ much bigger than all the other typical energy scales of the problem, we can gradually include fluctuations of smaller momentum, by decreasing Λ till the original Green’s function is restored. In this way the most divergent terms in the bubble are roughly limited to:

$$\chi \propto \log \left[\frac{D}{\max(i\Omega, T, \Lambda)} \right], \quad (1.95)$$

D being the scale for the kinetic energy of the system. This expression may diverge only for small Λ , i.e. when the fluctuations have been taken into account at all the energy scales.

At some particular scale Λ_c the vertex function $\Gamma_2^{\Lambda_c}$ generated during the flow may become very big compared to the other energy scales of the problem and eventually diverge by further lowering the cutoff. In this case, one has to stop the fRG flow, since in this regime the truncation can not be considered a good approximation any more. If one has to stop at some nonzero scale, the algorithm is (usually) not able to describe a physical action: The low energy degrees of freedom have not been taken into account yet. However, even if it is not assured that the

instabilities that emerge first in the flow are the ones that in the end survive at the end of the flow, we can use the two-particle 1PI vertex at the “stopping scale” as an indication of the emergent instabilities for the real physical system. The “stopping scale” itself can be considered, in certain circumstances and with a grain of salt, as an indication of the critical temperature at which the system would enter in a broken spin phase. We note here that there is some freedom in the explicit choice of the function Θ_Λ . A typical choice goes under the name of **momentum shell cutoff**. This corresponds to taking

$$\mathcal{G}_\mathbf{k}^\Lambda(i\omega) = \mathcal{G}_\mathbf{k}(i\omega)\theta(|\xi_\mathbf{k}| - \Lambda), \quad (1.96)$$

with θ being either the usual Heaviside step function, or some smoothed version of it. In the case of a sharp step function the Λ -derivative of \mathcal{G}^Λ is nonzero only in a momentum shell with $|\xi_\mathbf{k}| - \Lambda$. This is the reason for the name *single-scale propagator*: its support is reduced to momenta with a single energy (measured from the Fermi surface). With this choice of the cutoff we take into account one momentum shell at a time, getting gradually closer to the Fermi surface. This is reminiscent of the gradual treatment of the momenta in Wilson’s [185] renormalization group or in (Shankar’s) [164] modern renormalization group. In particular, we also note that in the loop equations for the two-particle vertex (1.76-1.78) it appears a single-scale propagator and a Green’s function, the single-scale propagator in modern RG terms is “*on-shell*”, while the Λ -dependent Green’s function is not. This situation is closer to the one of the *field theoretical approach* described by Shankar [164], in which one of the internal propagator momenta is at the cutoff and the other has support up to the cutoff value.

This kind of cutoff has been widely used, for example in the study of the two dimensional Hubbard model. Unfortunately, however, the momentum cutoff is regulating but not unbiased: The particle-hole processes with different momenta are not treated in a uniform way [70]. To see this, let us consider the expression of the susceptibility bubble for small values of momentum \mathbf{q} , Eq. (1.92), which has contribution only in the momentum region where $\frac{n(\epsilon)}{\partial\epsilon} \neq 0$. This is true only in a small momentum shell around the Fermi surface of width $\approx T$. Therefore in a momentum shell cutoff scheme, these processes, which may eventually lead to a divergent susceptibility, will be only taken into account for $\Lambda \leq T$. In the presence of other divergence tendencies we may have to stop the flow before we reach the scale $\Lambda \sim T$, and therefore before we are able to include the effect of particle-hole excitations with small momentum transfer. Even if there are no strong tendencies to divergences the processes with a different momentum transfer will be treated at higher cutoff scales, in contrast to the idea of unbiasedness. To better deal with this point also other cutoff schemes have been devised.

By looking at the the expression in Eq. (1.95), we evince that, if we want to avoid the divergence of the susceptibility before the low energy degrees of freedom have been considered, we can also act either on temperature or on the frequency.

Let us first discuss the **frequency cutoff**. In this case we assume the regulating function

$\Theta_\Lambda(i\omega, \mathbf{k})$ to be a function of the frequency only. One possibility is a sharp cutoff²⁴, like [94]:

$$\Theta_\Lambda(i\omega, \mathbf{k}) = \theta(|\omega| - \Lambda). \quad (1.97)$$

Another possibility [79] is to use a smooth function, like in the so called Ω -scheme. In this case the regulating function would be:

$$\Theta_\Lambda(\omega, \mathbf{k}) = \frac{\omega^2}{\omega^2 + \Lambda^2}. \quad (1.98)$$

A possible drawback of the momentum shell cutoff and of the frequency cutoff is that if we have to stop the flow at the stopping scale Λ_C , the system defined by the action \mathcal{S}^{Λ_C} , which contains only fluctuations of energies higher than the stopping scale, does not strictly correspond to the physical system we are interested in, for which fluctuations of all energies are allowed. However, if we consider the frequency cutoff, the Gaussian propagator \mathcal{G}^{Λ_C} has support only at high frequencies, and the corresponding action can be loosely interpreted as a physical action at a higher temperature.

For these reasons, it is sometimes useful to adopt a physical cutoff. Eq. (1.95) suggests that such a possibility can be given by using the temperature itself as a cutoff. This is the spirit of the **temperature flow** scheme [73, 74]. In this scheme the fields are rescaled by the temperature in a way that does not affect the interaction part of the action. Therefore, in order to cancel the temperature dependence of S_{int} in Eq. (1.56) we rescale the fields according to:

$$\phi_{\mathbf{k}\sigma}(i\omega) = T^{-\frac{3}{4}}\psi_{\mathbf{k}\sigma}(i\omega), \quad \bar{\phi}_{\mathbf{k}\sigma}(i\omega) = T^{-\frac{3}{4}}\psi_{\mathbf{k}\sigma}^\dagger(i\omega). \quad (1.99)$$

Rewritten in the new fields, the action depends explicitly on the temperature only in its Gaussian part, that is proportional to $T^{-\frac{1}{2}}$ (see also Eq. 1.53). The n -particle 1PI vertex function expressed in the new fields $\tilde{\Gamma}_n$ and the one expressed in the original fields Γ_n , are related by:

$$\Gamma_n = T^{\frac{3n}{2}}\tilde{\Gamma}_n. \quad (1.100)$$

Therefore one can perform the flow starting from high temperature for the ϕ fields, and then obtain the vertex functions for the original problem. The starting point for the flow is at high temperature, in which case $\Gamma_2 = U$. The temperature flow is unbiased. As a consequence, the temperature flow can produce qualitatively different results from the momentum shell cutoff ones, especially if particle-hole processes with small momentum transfer play an important role. This happens, for example, in the two dimensional Hubbard model with next nearest neighbors hopping [74], where a ferromagnetic instability may emerge for some values of the parameters.

Non-regularizing cutoff The ones discussed up to now are the more common cutoff choices which possess regulating properties: i.e. the logarithmic divergence of the bubbles is recovered only in the very end of the flow. However, if we study a system for which we do not expect a

²⁴Or some generalization of it to take into account the fact that the Matsubara frequencies are defined on a discrete grid [94].

particularly strong divergence due to the Fermi surface properties, or in other words if we do not expect divergences for the bare bubble, we can treat all the degrees of freedom at the same time and use the coupling strength as flowing quantity. This is the basic idea of the **interaction cutoff** [72]. To realize this task we have to rescale the fields in a way that, effectively, the ratio between the potential and kinetic energy is changed, but leaving formally untouched the interaction part of the action. To this extent we introduce a multiplicative factor in the Gaussian part of the action:

$$\mathcal{S}_0^\Lambda = T \sum_{n\sigma} \int d^d k c_{\mathbf{k},\sigma}^\dagger(i\omega_n) \Lambda^{-\frac{1}{2}} \mathcal{G}_0(\mathbf{k}, i\omega_n)^{-1} \Lambda^{-\frac{1}{2}} c_{\mathbf{k}\sigma}(i\omega_n), \quad (1.101)$$

with the flow parameter Λ having in this case the dimension of a pure number. The physical system we are interested in is recovered for $\Lambda = 1$. To understand the physical meaning of the interaction cutoff we formally rescale the fields according to:

$$\phi_{\mathbf{k}\sigma}(i\omega) = \Lambda^{-\frac{1}{2}} \psi_{\mathbf{k}\sigma}(i\omega), \quad \bar{\phi}_{\mathbf{k}\sigma}(i\omega) = \Lambda^{-\frac{1}{2}} \bar{\psi}_{\mathbf{k}\sigma}(i\omega). \quad (1.102)$$

In this way the Gaussian part of the action would formally be Λ independent, while the interaction part would become proportional to Λ^2 . We can absorb this factor in an effective interaction $\tilde{U}^\Lambda = \Lambda^2 U$, and interpret the new action as the one of a (physically well defined) system with a \tilde{U}^Λ rescaled interaction for every given value of the cutoff Λ . The flow can then be started at $\Lambda = 0^+$, i.e. from an infinitesimally small interaction, until the original bare interaction U is recovered. As it clear from Eq. (1.101) the Λ -dependent propagators reads:

$$[\mathcal{G}_0^\Lambda(\mathbf{k}, i\omega_n)]^{-1} = \Lambda^{-\frac{1}{2}} \mathcal{G}_0(\mathbf{k}, i\omega_n)^{-1} \Lambda^{-\frac{1}{2}}, \quad (1.103)$$

hence the cutoff acts in the same way on all the modes and therefore it is also referred to as a *flat cutoff*.

Hybridization cutoff Let us close this small overview of cutoff choices with the recently introduced *hybridization cutoff* [102]. We will also come back on this topic at the end of the third chapter. The hybridization cutoff is designed to treat the problem of an impurity embedded in a bath, in particular in view of a possible application as impurity solver for DMFT or its cluster extensions [101]. The idea of the cutoff is assuming as starting point for the flow the exact solution (for the self-energy and the 1PI vertex) of a small exactly solvable portion of the system, such as, e.g., an isolated atom, and in the flow gradually activating the hybridization with the rest of the system. To this end, the bath is discretized and represented as a chain of noninteracting sites attached to the impurity. Next, a small portion of this chain, called "core" and including the interacting site, is singled out and solved exactly. The size of this portion is mainly determined by the maximal system size that one can solve exactly. Finally, the hybridization of the end site of the core with the rest of the chain is restored, and the self-energy and vertex function of the impurity computed through the flow equations. Although this cutoff is not completely successful in reproducing the Kondo physics [102], it's application as impurity

solver for DMFT [101] gives satisfactory results for both weak and strong coupling regime. This highlights the important role played by the self-consistent hybridization function in DMFT and at the same time indicates a possible way to approach a strong coupling correlation regime in fRG. These two points will be discussed more in Sec. 1.5 and 3.2 respectively.

Regularizing cutoffs and neglected terms in the perturbative expansion.

After having discussed some possible cutoffs, we are now in the position to better analyze the diagrams that are neglected in a one-loop approximation to the fRG equations. In particular we focus on diagrams such as the one presented in Fig. 1.21, i.e., the lowest order parquet diagrams. We have already mentioned that integrating by parts the diagram in the figure one gets, besides the parquet diagram without the single-scale propagators, the integral of an identical diagram but in which the single-scale propagator replaces one of the internal loop lines.

This last contribution is unpleasant since (i) it only arises due to the truncation of the flow equations, and (ii) it is of the same perturbative order in the interaction as the retained diagram. Therefore it is desirable to show that the retained diagrams contribution is much larger than the neglected one. A general argument is difficult to find, also because the relative weight of the retained and neglected diagrams (that would be needed to obtain exactly the parquet diagram without single-scale propagators) crucially depends on the cutoff choice. To see this let us compare the situation for a regularizing cutoff (e.g., frequency cutoff), and a non regularizing cutoff (e.g., interaction cutoff).

The latter case is easier: neglecting everywhere the self-energy in the Green's function and considering that $G^\Lambda = \Lambda G$, we obtain $S^\Lambda = \frac{\partial G^\Lambda}{\partial \Lambda} = G$, $\chi^\Lambda = G^\Lambda G^\Lambda = \Lambda^2 G G$, and $P^\Lambda = \partial_\Lambda \chi^\Lambda = 2\Lambda G G$. Therefore it can be easily seen that, since the cutoff function does not operate selectively in frequency or momentum space, the integrals over $d\Lambda$ are independent from the integrals over the momentum and frequency variables, and can be performed separately. Hence, the contribution of every diagram is independent on the position of the single-scale propagator in the loop: The neglected and retained diagrams have the same weight.

The situation is different in the case of cutoffs that operate selectively in momentum or frequency space. In this case since the integral over $d\Lambda$ and those over the internal loop variables do not factorize and an analytic evaluation is more involved. This issue has been addressed by Binz and coworkers in Ref. [26]. In particular in Appendix B of Ref. [26] it is analyzed a parquet diagram consisting of a particle-particle loop embedded in a particle-hole crossed one (which is the same diagram we will analyze numerically in the following, obtaining the same results). The authors of Ref. [26] show that, assuming perfect nesting of the Fermi surface and an infrared cutoff (i.e., a cutoff excluding the low-energy degrees of freedom, like the momentum cutoff), the contribution to the Λ -derivative of the diagram arising from the derivative of the internal loop lines is negligibly small compared to the contribution arising from the derivative of the external loop. Therefore, they conclude that, if a diagram is reducible in a channel (e.g., in this case in the particle-hole crossed channel), the main contribution to its Λ -derivative will be obtained by deriving only the propagators connecting the irreducible blocks and not deriving the

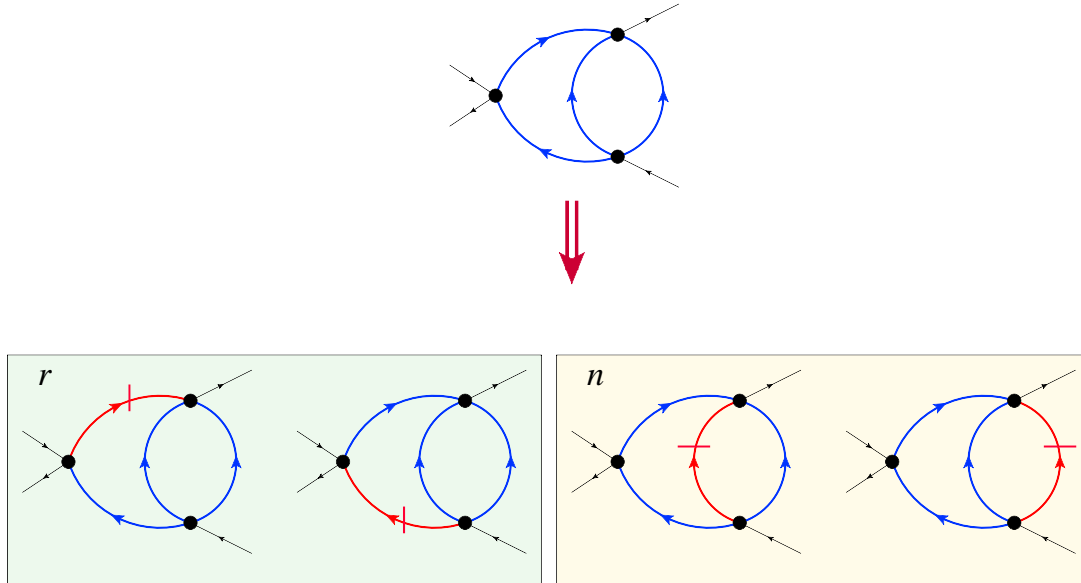


Figure 1.25: Parquet-type diagram studied numerically. In the top line the diagram is shown with all the fermionic lines being Green’s function, corresponding to calculation (i) described in the text. In the bottom line we show the four contribution to the Λ -derivative of the diagram. Integrating all the four contributions over $d\Lambda$ corresponds to calculation (ii) in the text. The contributions have been separated in “ r ”, retained in one-loop fRG, and “ n ” neglected in one-loop fRG.

irreducible blocks themselves [26]. This justifies the one-loop truncation of the flow equations, at least for systems with nested Fermi surfaces. This argument is somewhat analogous to the results obtained by Shankar [164] in the framework modern renormalization group. In Ref. [164], in fact, he argues²⁵ that it is possible to relate the sum over all loops to the one-loop result. The argument is based on an analogy with the small parameter of the $1/N$ expansion, made possible by phase space arguments, which are beyond the scope of this thesis.

On a different perspective, since analytical evaluations are difficult and need to restrict oneself to specific situations (e.g., perfect nesting of the Fermi surface), one can rely on numerical techniques, for example by evaluating numerically the Λ -derivatives of the lowest order parquet diagrams and comparing for these the contributions arising from the derivative of the internal and of the external loop lines. This approach, although less elegant than analytical estimations, has the advantage of being flexible and easily generalizable to different choices of the cutoffs and general Fermi surfaces. In particular, we have analyzed numerically the third order parquet diagram shown in Fig. 1.25, for the dispersion of a two dimensional Hubbard model at half-filling with nearest neighbors hopping only, and onsite interaction U . We neglected everywhere the self-energy and did the numerical calculation at finite temperature T . We have evaluated the diagram in two different ways:

- (i) direct evaluation from standard perturbation theory;

²⁵cf. Sec. VII of Ref. [164]

- (ii) evaluation of the integral over $d\Lambda$ of the four diagrams obtained by substituting one of the Green's function lines with a single-scale propagator (bottom row of Fig. 1.25). As a cutoff we have assumed a frequency cutoff at finite temperature, following Ref. [94]:

$$\Theta(|\omega| - \Lambda) = \begin{cases} 0 & \text{if } -\pi T > |\omega| - \Lambda, \\ \frac{1}{2} + \frac{|\omega| - \Lambda}{2\pi T} & \text{if } -\pi T \leq |\omega| - \Lambda \leq \pi T, \\ 0 & \text{if } |\omega| - \Lambda > \pi T, \end{cases} \quad (1.104)$$

$$\text{and } S^\Lambda(\mathbf{k}, \omega) = G(\mathbf{k}, \omega)\Theta(|\omega| - \Lambda).$$

The numerical evaluation following (i) and (ii) has provided the same result (within the numerical error) as expected. Furthermore, the evaluation (ii) using the fRG procedure allowed us to disentangle the contribution of the retained (Fig.1.25*r*) and of the neglected diagrams (Fig.1.25*n*). This way we have checked that the contribution coming from the integration of Fig.1.25*r* is typically one order of magnitude larger than the one coming from the integration of Fig.1.25*n*, for all the values of momentum²⁶ and temperature considered. Although this numerical analysis does not allow for a definitive assessment about the validity of the one-loop approximation, it provides a further indication that the major role is played by the diagrams retained in the one-loop approximation (for the cutoff considered). However, this should be verified case by case, and supported with physical intuition, and, whenever possible, with analytical or semi-analytical evaluations.

²⁶The diagram, due to energy and momentum conservation, depends on three momentum and frequency variables. The three frequency variables have been assumed to be equal to the lowest Matsubara frequency, while several combinations of momentum variables have been analyzed.

1.5 Dynamical mean-field theory

In the present section we will discuss the **dynamical mean field theory** (DMFT). DMFT has been the first method to give a reliable nonperturbative description of the Mott transition, and is nowadays one of the most powerful tools for the description of strongly correlated systems. Hence it is not surprising that it has been described in a very large number of references, and that it has been derived in several different ways, see, e.g., Refs. [46, 48, 60].

Therefore we will not try to give an exhaustive overview about DMFT, for which we refer to the literature, but we will rather present it in a way to prepare the ground for the combination with *GW* and with fRG, which we will discuss in the following chapters.

To this end we will present two different derivations of DMFT. The first one uses an easier formalism and is intended to show the physical content of DMFT. The second one makes use of a more involved *functional integral* formalism and is intended to show the formal similarities as well the differences with fRG.

In this perspective we will first introduce what is the idea behind DMFT, i.e., the extension of standard mean field theories to quantum problems, by using a **local** approximation to describe the properties of lattice models for solids. Then we will describe in which limits this approximation becomes exact: the limit of **infinite dimensions**, but also in the **noninteracting** and in the **atomic limit**. At this point we will be in the position to tackle a more technical discussion and deal with the derivation of the DMFT self consistency equations, that allow the mapping of a lattice model onto an **Anderson Impurity Model** (AIM). These two points, (i) the description of a lattice problem with a local approximation and (ii) the mapping onto an impurity site, constitute the heart of DMFT.

The limit of infinite dimensions will serve us as a guide to understand what kind of physics we are able to capture by the DMFT approximation. In view of a later use, we will propose two possible complementary pictures to visualize DMFT: On the one hand we can imagine that we are approximating a finite dimensional problem by the AIM which better describes its local physics, or, on the other hand, we can imagine to approximate the local physics of the finite dimensional lattice with the one of an appropriate (*auxiliary*) *infinite dimensional problem*.

To make contact with the fRG techniques we will discuss an alternative derivation of DMFT, following the lines of the discussion presented in Ref. [46]. This derivation is based on the definition of an effective action functional of the local Green's function and is related to the Baym-Kadanoff [19] and Luttinger-Ward [117] approach. As an example of successful application of DMFT we will touch upon the DMFT description of the Mott transition. We will not discuss here, instead, the combination of DFT and DMFT methods aimed to an *ab-initio* treatment of strongly correlated materials.

1.5.1 Dynamical mean field

One of the most essential model Hamiltonians that is able to capture the relevant physics of strongly correlated materials is the Hubbard Hamiltonian [53, 77, 92] (and its generalizations,

e.g., to many bands). In general, this Hamiltonian describes two kinds of processes: The hopping of an electron from one site to another one and the energy cost of doubly occupying a lattice site.

If we focus on one lattice site only (in a one band case), there are four possible configurations: $|0\rangle$, $|\uparrow\rangle$, $|\downarrow\rangle$ and $|\uparrow, \downarrow\rangle$. The configuration of the site can change as the electrons hop back and forth to the neighboring sites: If we look *only at this single site* the lattice plays the role of a bath and guarantees the electrons the chance to hop, therefore changing the configuration of the site, which is still a full quantum problem.

This idea can be formalized in the following way: Instead of considering the lattice problem with all its degrees of freedom, we can approximate it with a single site problem, embedded in an effective bath, drastically reducing the number of degrees of freedom. In this way we keep track of the *local* physics of each site: We do not focus on *where* the electrons are going or coming from, but, *on the given site*, the electrons still feel the interaction among each other.

However, a given electron on the site i will not feel the interaction with a time averaged electron density on the site, but an interaction that will depend on the quantum state of the site i at a specific time τ . In this sense the question *where* (on which site) the other electrons are hopping is not relevant, but the question *when* an electron is coming back still is: In this sense the physics is *dynamic*, i.e., time dependent.

Once we approximate the lattice physics with the one of a single site embedded in an effective bath, we need to perform two main steps to accomplish our task:

- we have to define the equations that connect the lattice problem to the effective bath in a self-consistent way;
- we have to solve the impurity problem (which remains a quantum many body problem).

While the solution of the many body problem can be achieved in several different ways using different techniques (**impurity solvers**), the problem of defining the self-consistent bath is more fundamental and we will focus on it in the following.

Self-consistent AIM

To be specific let us focus on a single band Hubbard model, whose Hamiltonian can be written as:

$$H = \sum_{ij,\sigma} (t_{ij} + \mu\delta_{ij}) c_{i\sigma}^\dagger c_{j\sigma} + U \sum_i \hat{n}_{i\uparrow} \hat{n}_{i\downarrow}. \quad (1.105)$$

Here t_{ij} is the hopping amplitude, U is the Coulomb interaction, μ is the chemical potential, $c_{i\sigma}^\dagger$ ($c_{i\sigma}$) creates (annihilates) an electron of spin σ at the lattice site i . The quantity that describes the dynamical state of the lattice site i is the local Green's function:

$$G_{\text{loc},\sigma}(\tau - \tau') \equiv -\langle T c_{i\sigma}(\tau) c_{i\sigma}^\dagger(\tau') \rangle. \quad (1.106)$$

From $G_{ii,\sigma}$ one can read out the probability that the lattice site is occupied at some given time or that the electron can hop back or forth from the bath: It is the relevant quantity to describe the embedding in an effective medium.

As stated above, our aim is finding the local problem that describes the state of a site of the lattice problem. The Hamiltonian that describes the local problem of an impurity embedded in a bath can be written in the form of the AIM:

$$H_{\text{AIM}} = H_{\text{atom}} + H_{\text{bath}} + H_{\text{coupling}}. \quad (1.107)$$

The first term describes the on-site interaction between spin-up and spin-down fermions:

$$H_{\text{atom}} = U\hat{n}_{\uparrow}\hat{n}_{\downarrow} + \mu(\hat{n}_{\uparrow} + \hat{n}_{\downarrow}), \quad (1.108)$$

where the chemical potential μ is used to fix the occupation on the site, and $\hat{n}_{\sigma} = c_{\sigma}^{\dagger}c_{\sigma}$, with c_{σ}^{\dagger} and c_{σ} the creation and annihilation operators of the impurity site.

The ‘‘form’’ of the effective bath is encoded in the two followings terms:

$$H_{\text{bath}} = \sum_{l\sigma} \tilde{\epsilon}_l a_{l\sigma}^{\dagger} a_{l\sigma} \quad (1.109)$$

$$H_{\text{coupling}} = \sum_{l\sigma} V_l (a_{l\sigma}^{\dagger} c_{\sigma} + c_{\sigma}^{\dagger} a_{l\sigma}), \quad (1.110)$$

the operators $a_{l\sigma}$ define an *auxiliary* set of fermions, with dispersion defined by $\tilde{\epsilon}_l$ and hopping amplitude to the impurity given by V_l . The set of $\tilde{\epsilon}_l$'s and V_l 's will be referred to as ‘‘Anderson parameters’’.

The details of the AIM defined by Eq. (1.107), i.e., its Anderson parameters, have to be determined considering that we want it to describe the local physics of a lattice site, which, in turn, is completely defined by the local Green's function, equation (1.106). Therefore one wants to determine that particular AIM whose interacting Green's function $G_{\sigma}^{\text{AIM}}(\tau - \tau') \equiv -\langle T c_{\sigma}(\tau) c_{\sigma}^{\dagger}(\tau') \rangle_{\text{AIM}}$ is equal to the local one of the lattice:

$$G_{\text{loc}\sigma}(\tau - \tau') \stackrel{!}{=} G_{\sigma}^{\text{AIM}}(\tau - \tau'). \quad (1.111)$$

Whenever this condition is met the one-particle physics on the impurity site and on each lattice site is the same, regardless of what happens respectively to the auxiliary fermions and to each other lattice site. In fact, sharing the same local Green's function, the single impurity and the lattice site will also give the same results for the single one-particle local operators like, e.g., the magnetization or the (local) density of states. To fulfill the requirement (1.111) one has to fix the Anderson parameters defining the auxiliary fermions $\tilde{\epsilon}_l$ and V_l . However, even assuming that our impurity solver allows us to solve exactly the AIM and to compute G_{σ}^{AIM} we still do not know the local Green's function of the lattice $G_{\text{loc}\sigma}$. Therefore solving equation (1.111) is not possible until we define an approximation for the local Green's function. In DMFT we will chose an approximation for G_{loc} that involves the AIM Green's function itself. We will see that this gives rise to the DMFT self consistency cycle: The AIM determines the self-energy that enters in the local Green's function, and the local Green's function obtained this way determines a new AIM. However before discussing how to find the self-consistency equation it is useful to switch to an effective action formalism for the AIM.

This is particularly convenient since the auxiliary fermions in the Hamiltonian (1.107) are noninteracting²⁷, and can be therefore easily integrated out. This yields the following effective action:

$$\mathcal{S}_{\text{AIM}} = -\frac{1}{\beta} \int_0^\beta d\tau \int_0^\beta d\tau' \sum_\sigma \bar{\psi}_\sigma(\tau) \mathcal{G}_0^{-1}(\tau - \tau') \psi_\sigma(\tau') + U \int_0^\beta d\tau n_\uparrow(\tau) n_\downarrow(\tau). \quad (1.112)$$

Here the action is expressed in terms of the Grassman variables ψ and $\bar{\psi}$ associated with the annihilation and creation operators of the impurity. β is the inverse temperature. The Gaussian part in the action (1.112) is specified by the noninteracting Green's function of the AIM (also called Weiss field) \mathcal{G}_0 . It is related with the Anderson parameters of the auxiliary bath fermions by:

$$\mathcal{G}_0^{-1} = i\omega_n + \mu - \Delta(i\omega_n), \quad (1.113)$$

$$\Delta(i\omega_n) = \sum_l \frac{|V_l|^2}{i\omega_n - \tilde{\epsilon}_l}, \quad (1.114)$$

and $\Delta(i\omega_n)$ is usually referred to as the *hybridization function*. The action (1.112) has the appropriate form to describe the single site embedded in a lattice, since it does now depend only on the Grassman variables of the impurity site. The term quadratic in the fields in the action (1.112) describes processes in which a fermion leaves or reaches the impurity site, while the term proportional to U , quartic in the field, is responsible for the local Coulomb repulsion. The fact that the Gaussian propagator \mathcal{G}_0 is time dependent is essential to describe *retarded processes* in which a particle leaves the site at a time τ and comes back on the site at a time τ' after propagating in the bath during the time interval $\tau' - \tau$. Conversely, this can also be analyzed in frequency space: The fact that the Weiss field is frequency dependent implies that the particle that hops to the impurity site or leaves it can have different energies, and fermions of different energies have different probabilities to hop.

\mathcal{G}_0 can be considered the *quantum counterpart* of the effective *mean field* of classical statistical mechanics, since its functional form is used to represent, in an effective way, the relation between a site and the lattice. This is also the origin for the name *Weiss field* attributed to \mathcal{G}_0 . Until now, we did not yet introduce any specific approximation for the local Green's function, but we only stated that if we know the local Green's function of a lattice problem we can also find the AIM whose Green's function equals the local one of the lattice. However this is of little or no use until we define an approximation to find the local lattice Green's function. The guideline that suggests the best approximation comes from the infinite dimensional limit of a lattice model. In this case the mapping onto an AIM is exact, i.e., not only one can find an AIM having the same local Green's function of the lattice model, but it is possible to calculate *exactly* the local Green's function of the lattice from the solution of a self-consistent AIM.

²⁷Here we mean that there is no term in the Hamiltonian (1.107) beyond the quadratic one in the operators of the auxiliary fermions. However, strictly speaking, there is some interaction between the auxiliary fermions due to their linear coupling with the impurity. This can be most easily seen formally integrating out the degrees of freedom of the impurity.

Infinite dimensional limit

The infinite dimensional limit of a lattice (Hubbard) model was pioneered in 1989 by Metzner and Vollhardt [130]. This limit, although sounding exotic, turns out to be very useful. In fact it represents the limit in which the dynamical mean field theory, intended as a mean field theory in space but not in time, becomes exact. This is analogous to the what happens for a classical spin system where, in the infinite dimensional limit, the mean field approximation (in space *and* time) becomes exact [130]. For a quantum model, like the Hubbard model, this is not the case, since a static mean field approximation, such as the Hartree-Fock approximation, does not allow to obtain an exact result, even in the infinite dimensional limit [130]. This is very reasonable: In infinite dimensions the fluctuations in space are averaged out, while there is no suppression for the fluctuations in time, and therefore one needs a **dynamical** mean field.

Before discussing the physics, let us make a short remark about the nomenclature. We refer here to the limit of infinite *dimensions* according to the original paper in which it was proposed. However, rather than the number of dimensions, it is the coordination number, i.e., the number of neighbors to which an electron can hop from a given site, which is really important. In this way the limit can be made also for lattices, like the Bethe lattice, for which the dimension is not well defined. Obviously for a hypercubic lattice in d dimensions with nearest neighbor hopping the coordination number is $z = 2d$.

Following Metzner and Vollhardt [130] we refer to the specific case of a Hubbard Hamiltonian in the form (1.107), where the two sums range over the sites of a d -dimensional lattice. In the case of a hypercubic lattice with nearest neighbors hopping the kinetic term can be diagonalized in momentum space, with eigenvalues:

$$\epsilon_{\mathbf{k}} = -2t \sum_{j=1}^d \cos k_j, \quad (1.115)$$

with t the hopping amplitude and $\mathbf{k} = (k_1, k_2, \dots, k_d)$ the momentum vector. From this one can evaluate the density of states $D(\epsilon) = (2\pi)^{-d/2} \sum_{\mathbf{k}} \delta(\epsilon - \epsilon_{\mathbf{k}})$, which in the infinite dimensional limit, due to the central limit theorem, reads [130]:

$$D(\epsilon) = \frac{1}{2t(\pi d)^{1/2}} \exp \left[- \left(\frac{\epsilon}{2t\sqrt{d}} \right)^2 \right], \quad (1.116)$$

i.e., the density of states is a Gaussian distribution with variance $t\sqrt{2d} \xrightarrow{d \rightarrow \infty} \infty$. The kinetic energy per lattice site of the noninteracting model equals the second moment of the density of states, i.e., the variance for a Gaussian density of states. Therefore the energy scale associated with the kinetic energy diverges in infinite dimensions for fixed t .

On the other hand, the potential energy per lattice site, does not scale with the number of dimensions. In this situation the model (1.105) would be trivial: It would not describe a competition between kinetic and potential energy. To avoid this we assume that the hopping amplitude scales according to the *proper scaling*:

$$t \propto t^*/\sqrt{2d}, \quad (1.117)$$

with $t^*/U \approx \mathcal{O}(1)$. In this way the variance stays finite, and the model still describes the competition between kinetic and potential energy in the limit $d \rightarrow \infty$.

Let us note [46] that this agrees with the scaling of the exchange interaction between nearest neighbors, for statistical mechanics models, that takes the form: $J_{ij} \propto J^*/z$, which is needed to recover the essential physics involved in the magnetic transition of those models. In fact, it can also be seen that in the limit of large U the Hubbard model can be mapped on a $t - J$ model, with superexchange $J_{ij} \propto t_{ij}^2/U$. In this case the proper scaling Eq. (1.117) guarantees that the superexchange scales like $1/z$.²⁸

The proper scaling was derived above in the special case of a hypercubic lattice with nearest neighbors hopping only. This can be generalized to a system with longer range hoppings by introducing the quantity $\mathcal{Z}_{\|i-j\|}$ which counts the number of equivalent sites at the (Manhattan) distance $\|i - j\|$ from the site i [60]. It can be seen that assuming a scaling of the form

$$t_{ij} \propto t_{ij}^*/\sqrt{\mathcal{Z}_{\|i-j\|}}, \quad (1.118)$$

with t_{ij}^* being independent on $\mathcal{Z}_{\|i-j\|}$ guarantees a finite kinetic energy also in the limit $\mathcal{Z}_{\|i-j\|} \rightarrow \infty$.

Let us assume now the proper scaling of the form of Eq. (1.118) and see how it affects the diagrammatics of DMFT.

Locality of the self-energy Let us focus on the self-energy. In this derivation we follow the lines of Ref. [60]. The proper scaling imposed on the hopping amplitude, implies that also the noninteracting Green's function scales in the same way:

$$G_{ij}^0(\omega) \propto \frac{1}{\sqrt{\mathcal{Z}_{\|i-j\|}}}. \quad (1.119)$$

This can be easily seen by the definition of the Green's function in real space [60].

The interacting and noninteracting Green's function are connected via the Dyson equation 1.21. Therefore, unless the self-energy tends to zero more slowly than the hopping amplitude when $\mathcal{Z}_{\|i-j\|} \rightarrow \infty$, the interacting Green's function will scale like the noninteracting one. In the end we will find that the self-energy is purely local, therefore validating this *ansatz*.

Due to the assumed locality of the Coulomb interaction, in a Feynman diagram, the interaction line²⁹ always connects a lattice site i with itself. Let us consider a diagram contributing to the self-energy, like the one shown in Fig. 1.26. The sites i and j are connected by three lines and each of them brings in a factor $\mathcal{Z}_{\|i-j\|}^{-1/2}$, hence the diagram scales with a factor $\mathcal{Z}_{\|i-j\|}^{-3/2}$. This factor implies that, for $i \neq j$, in the limit of $\mathcal{Z}_{\|i-j\|} \rightarrow \infty$ the diagrams vanishes. This is not the case for *local* diagrams, i.e. those with $i = j$ which stay of order $\mathcal{O}(1)$ even in the limit of infinite coordination. Therefore the nonlocal self-energy diagrams in which two different sites

²⁸We also mention that the idea of the proper scaling is, in some sense, related to the one of the $1/N$ expansions, in which one writes a theory in terms of fermions with N components. The difference is that in this case one usually introduces a term $1/N$ to avoid the divergence of the interaction energy, rather than of the kinetic one [164].

²⁹In the Feynman diagrams that we show in this chapter we represent the Coulomb interaction as a wiggled line.

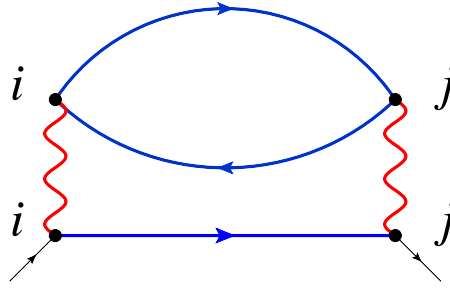


Figure 1.26: Feynman diagram for the self-energy. In the limit of infinite dimensions it contributes *only* if $i = j$.

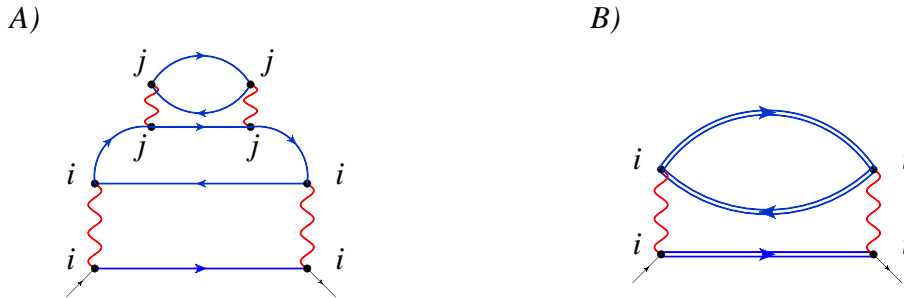


Figure 1.27: A) Non skeleton Feynman diagram for the self-energy. B) Second order Feynman diagram in terms of dressed Green's functions.

are connected by at least three Green's function lines are irrelevant compared to the ones, topologically identical, in which the three Green's function lines connect the same site. Focusing on skeleton diagrams (the ones relevant for the self-energy) one can see that whenever in the diagram there are two sites, i and j these *must* be connected by *at least* three Green's function lines, either directly or through other sites.³⁰ In any case their contribution will scale *at least* like $1/\mathcal{Z}_{\|i-j\|}^{-3/2}$.

Hence all the nonlocal self-energy diagrams are irrelevant, and the only relevant diagrams in the limit of infinite dimensions are the purely local ones: as announced the self-energy in this limit is purely local:

$$\Sigma_{ij}(\omega) = \delta_{ij}\Sigma(\omega), \quad (1.120)$$

$$\Sigma_{\mathbf{k}}(\omega) = \Sigma(\omega). \quad (1.121)$$

This also justifies the initial ansatz on the scaling of the interacting Green's function.

Mapping on the AIM in $d \rightarrow \infty$ We shall now come back to our original problem and discuss how to calculate the local Green's function of an infinite dimensional lattice by pinpoint-

³⁰More precisely one can talk of independent paths that connect the site i to the site j . Each one brings in at least a factor $\mathcal{Z}_{\|i-j\|}^{-1/2}$.

ing and solving the self-consistent AIM. Let us stress that in the limit of infinite dimensions the proper scaling has to be the one described above, to allow for an exact relation. We will then *assume* that the relation (1.121) holds, as an approximation, also in the case of a finite dimensional lattice.

We have just shown that in infinite dimension the only diagrams that contribute to the self-energy are the local skeleton (i.e., built with *interacting* Green's function lines) ones. Topologically, therefore, the diagrams contributing to the self-energy of an infinite dimensional lattice are equal to those that contribute to the self-energy of a *general* AIM, which include only local Green's function lines by definition. If we further assume that also the (local) interaction term is the same for the impurity and for each individual lattice site, then the self-energy diagrams of the two systems, besides being topologically equivalent, will also assume exactly the same value *if* the local *interacting* Green's function lines are the same. In other words, since the diagrams are topologically the same the *functional* that gives the self-energy as a function of the interacting Green's function is the same for the AIM and for the infinite dimensional lattice. Therefore, the knowledge of the AIM that fulfills Eq. (1.111), i.e., that has the same local Green's function as the infinite dimensional Hamiltonian, also *implies* the knowledge of the lattice self-energy, since the two self energies of the two models are the same:

$$\Sigma(\omega) = \Sigma^{\text{AIM}}(\omega). \quad (1.122)$$

We can next make use of the Dyson equation to express the local Green's functions of the lattice and of the AIM in function of the self-energy:

$$G_{\text{loc}\sigma}(\omega) = \int d\epsilon \frac{D(\epsilon)}{i\omega + \mu - \epsilon - \Sigma(\omega)}, \quad (1.123)$$

$$G_{\sigma}^{\text{AIM}}(\omega) = [\mathcal{G}_0^{-1}(\omega) - \Sigma^{\text{AIM}}(\omega)]^{-1}. \quad (1.124)$$

Equation (1.122) can be used to assume that the self energies in equations (1.123) and (1.124) are the same. Reinserting them in Eq. (1.111) we obtain an implicit relation for the Weiss field \mathcal{G}_0 of the AIM that satisfies equation (1.111):

$$(\mathcal{G}_0^{-1}(\omega) - \Sigma(\omega))^{-1} = \int d\epsilon \frac{D(\epsilon)}{i\omega - \epsilon + \mu - \Sigma(\omega)}, \quad (1.125)$$

where the self-energy Σ can be calculated from the solution of the AIM. In general the Weiss field of the AIM that fulfills Eq. (1.111) is not known. Therefore equation (1.125) can be regarded as a **self-consistency** equation: If one is able to find an AIM with an associated Weiss field $\mathcal{G}_0(\omega)$ and self-energy $\Sigma(\omega)$ that fulfill equation (1.125) one also knows *exactly* the self-energy and local Green's function of the infinite dimensional problem specified by the density of states $D(\epsilon)$. In practice the problem of solving equation (1.125) arises from the fact that the self-energy is not known a priori, but one has to solve a many-body problem. The usual way to deal with equation (1.125) is by making use of the following self consistency cycle:

- (i) Start from a reasonable guess, e.g., for the self-energy;

- (ii) compute a new Weiss field \mathcal{G}_0 by inverting Eq. (1.125).
- (iii) Solve the new AIM defined by the new Weiss field. In the solution of the AIM problem several different impurity solvers can be used;
- (iv) iterate, inserting the new self-energy in Eq. (1.125), step (ii).

Self-consistency will be reached when, for a given accuracy, the quantities (e.g. the self-energy or the Weiss field) computed in the new iteration equal the ones of the previous iteration. Whenever self-consistency is reached one knows the *exact* self-energy and local Green's function of an infinite dimensional problem, which would have been extremely difficult to obtain from a direct solution (e.g., using exact diagonalization, quantum Monte Carlo, or any other technique) of the lattice original problem.

Approximation for finite dimensions In finite dimensions, in general, the self-energy is *not* purely local. However, in several situations as we will describe below, we can still assume that relation (1.122) holds as an **approximation** for the self-energy of a finite dimensional problem. This implies that we assume a purely local self-energy also in the finite dimensional case, neglecting its the nonlocal part. Under the assumption of a local self-energy, equation (1.122), the local Green's function can be computed using a Dyson equation of the form (1.123), where the density of states $D(\epsilon)$ refers now to the finite dimensional lattice. The local Green's function obtained this way can be inserted in Eq. (1.111), or equivalently in Eq. (1.125), to form together with equation (1.122) a set of approximate self-consistent equations. This set of equations is at the basis of the **DMFT approximation**.

The self-energy Σ^{DMFT} , obtained at self consistency, is *assumed* to be the DMFT approximation for the self-energy of the finite dimensional problem. Obviously this is not exactly true: We are neglecting the nonlocal part of the self-energy, or, equivalently, its momentum dependence. Through the Dyson equation the momentum dependence of the self-energy also enters in the local Green's function. Therefore also equation (1.111) only holds approximatively, and the AIM describes in an approximate way the local physics on a lattice site (cf. footnote 31). Let us stress, however, that this does not depend on the question whether an impurity problem that describes it exactly exists (at least at the one particle level) but on the fact that we do not know how to find the right AIM, and we have to rely on an approximation to find it. At the same time, while the self-energy momentum dependence is neglected, the interacting Green's function remains momentum dependent, due to the momentum dependence of $G_0(\mathbf{k}, \omega)$.

The physical condition that we have to keep in mind when we want to apply DMFT is that we are going to neglect the nonlocal self-energy. This implies that if we have physical reasons to believe that the nonlocal fluctuations, that translate in a strong momentum dependence of the self-energy, might play a key role, DMFT must be either discarded, or supported with the results from some DMFT extensions or other techniques that allow for the (at least partial) inclusion of nonlocal fluctuations.

Other limits where the DMFT is exact One of the main strengths of DMFT is that it is able to accurately describe the two opposite limits of weak and strong coupling. This is not the case for many other approximations. For example, focusing on the half filled Hubbard model, a good description of its physics can be obtained in the weak coupling regime by means of perturbation theory, e.g., Hartree-Fock (or BCS) like theories. Also the region of (very) strong coupling can be described in a perturbative way, after projecting out the doubly occupied states and mapping on a $t - J$ model at weak coupling ($J \propto t^2/U \ll t$). However these perturbative approaches work only in one of the two limits.

On the other hand DMFT is exact in both limits of **non-interacting bands** and of **isolated atoms**, regardless of the number of dimensions. Let us briefly show why this is the case. The non-interacting limit is (trivially) given by $U = 0$. Then the self-energy of the lattice is k -independent by definition, as it vanishes for every k -point. Equation (1.125) simply gives:

$$\mathcal{G}_0(\omega) = G_{\text{loc}}^0(\omega). \quad (1.126)$$

In this limit (and *only* in this limit) the Gaussian propagator of the AIM associated with the lattice problem by the approximation (1.122) equals the noninteracting local propagator of the lattice.

In the opposite limit, that of isolated atoms, the self-energy is local by definition, as each atom is isolated. Formally this is obtained by removing all the hoppings among the atoms: $t_{ij} = 0$, or equivalently $\epsilon_{\mathbf{k}} = 0$. The density of states reduces to a δ -function: $D(\epsilon) = \delta(\epsilon)$. As a consequence, the self consistency equation (1.125), after expressing $\mathcal{G}_0(\omega)$ in terms of the hybridization function $\Delta(\omega)$, reduces to:

$$(i\omega - \Delta(\omega) - \Sigma(\omega))^{-1} = \frac{1}{i\omega - \Sigma(\omega)}, \quad (1.127)$$

i.e., the hybridization function vanishes for all the values of its argument $\Delta(\omega) = 0$.

Remarkably DMFT is exact in both limits, and provides an interpolation between them for intermediate coupling regimes. This is important because it allows to describe not only the two regimes of strong and weak coupling but also the (more complicated) intermediate regime *on the same footing*. In the interpolation between the two physical situations a key role is played by the evolution of the hybridization function $\Delta(\omega)$. Let us stress here, that in spite of appearing in the noninteracting part of the auxiliary AIM, the hybridization function, in a DMFT calculation, already carries crucial information about the correlations of the lattice model, i.e., through equations (1.111) and (1.125) it depends on the interaction. In fact this quantity can be interpreted as a ‘‘quantum’’ generalization of a classical mean field [49]. More specifically we have seen $\Delta(\omega)$ vanishes in the atomic limit, Eq. (1.127). Moreover the low frequency behavior of the hybridization function plays the crucial role in the Mott transition: $\Delta(\omega \rightarrow 0) = 0$ corresponds to a Mott insulating solution. Besides this, also *before* the Mott transition is approached, the hybridization function encodes very important features about the new energy scales arising in the lattice problem [62], for example a three peak structure of $\Delta(\omega)$ is associated with the emergence of a kink in the self-energy. The connection can be made more explicit analyzing the Mott transition in a Landau theory framework, as done in [106, 107, 150].

Auxiliary model In view of the upcoming discussion about DMF²RG let us elaborate further about the concept of the auxiliary model in DMFT. As discussed above, in DMFT we approximate the self-energy of a lattice model with the one, local by definition, of an AIM. We have often referred to the latter as an *auxiliary* model. We try now to better investigate the connection of the auxiliary model with the lattice one, making the distinction between finite and infinite dimensions.

In infinite dimensions the proper scaling and the locality of the self-energy guarantee that the lattice self-energy can be computed *exactly* from the one of the auxiliary model: In this limit DMFT is not an approximation but a *mapping*. This is not the case in finite dimensions. In this case the *physical* meaning of the auxiliary model is less well defined. Indeed the auxiliary model can be thought of as that model that best approximates the local quantities of the lattice one under the approximation that the lattice self-energy is local³¹.

However, in view of the combination with fRG, it might be instructive to envision the auxiliary model in an equivalent way. Let us notice explicitly that in Eq. (1.125) the lattice enters *only* through the noninteracting density of states $D(\epsilon)$. This means that, as long as we focus on the paramagnetic phase [48, 133], we can find several different lattices which share the same density of states and are therefore described by the same AIM in DMFT. More specifically, we can define an *auxiliary infinite dimensional lattice*, with hopping \tilde{t}_{ij} , which has the same density of states $D(\epsilon)$ of the finite dimensional lattice we are interested in. The infinite dimensional lattice defined by the infinite dimensional hoppings \tilde{t}_{ij} will share with the auxiliary AIM the same self-energy and local Green's function, which in infinite dimensions are exact. Therefore one can equivalently think of DMFT as having *approximated* the self-energy and local Green's function of a finite dimensional lattice with the ones of the *infinite dimensional* auxiliary lattice which has the same density of states. This consideration will turn useful in defining an fRG-like flow equation in the context of DMF²RG.

1.5.2 Functional perspective on DMFT

In the following we would like to present a different derivation of DMFT, based on the definition of an **effective action** $\Gamma[G]$, which is a **functional** of the local Green's function. This second derivation will not add information about the physical content of DMFT, already discussed in the previous paragraphs using a formalism way less involved. Instead here we wish “to kill two birds with one stone”³²: On the one hand, we want to show that the local Green's function in DMFT can be obtained by **functional minimization** of an effective action functional. On the other hand we want to explicitly show some *formal* similarities between the functional that we will use to derive DMFT and the generating function for the one-particle irreducible functions studied in fRG (see footnote 38). The common idea is that both in fRG

³¹The *exact* local Green's function of the lattice model $G_{loc\sigma}(\omega) = [\sum(G_{k\sigma}^0(\omega)^{-1} - \Sigma_k(\omega))]^{-1}$, is, in general, different from the DMFT one. Strictly speaking the AIM that best describes the local properties of the lattice model is the one whose interacting Green's function is $G_{loc\sigma}(\omega)$, which does not necessarily coincide with the AIM of DMFT at self consistency.

³²This sentence has been already used in a scientific work, see Ref. [164].

and in DMFT one can start from a simpler form of the functional, that one knows how to treat *exactly*, and then “*flow*” to the more complicated functional in which one is interested in. In DMFT: We will start from a functional corresponding to a problem in which the hopping is completely suppressed, i.e. we will start from an *atomic problem* and then switch on the hoppings. There are however important differences. Indeed to obtain the physical quantities of interest in the generating functionals one has to evaluate their functional derivatives, and this is done in two different ways in fRG and in DMFT, therefore yielding two different answers. These answers are complementary in the sense that in fRG one drops the higher order vertex functions (with the truncation of the flow equations) but keeps a complex momentum and frequency dependence, while in DMFT one rather gives up the momentum dependence, while retaining a nonperturbative description.

The presentation below is based on the one given in Ref. [46]. Related approaches are presented in [86] and [34, 35]. In Ref. [34] the connection between the functional derivation of DMFT and the common Green’s function methods early developed by Baym and Kadanoff (BK) [19] and Luttinger and Ward (LG) [117] is also stressed. In both cases one builds a functional of the Green’s function so that its stationary point gives the physical value of the Green’s functions. The main difference consists in the fact that, while the BK and LW functionals depend on the *local* and *nonlocal* Green’s functions, the DMFT functional depends only on the local one. Obviously, also in the case of the BK and LG theories the functionals cannot be computed exactly and one has to rely on approximations.

The rest of this section is organized as follows. First we will construct the effective action, i.e., the functional of the local Green’s function $\Gamma[G]$ which is stationary for the physical value of the local Greens function G_{loc} :

$$\frac{\delta\Gamma[G]}{\delta G} = 0 \Rightarrow G = G_{\text{loc}}. \quad (1.128)$$

We stress that this functional can be formally constructed *exactly* [134] using some standard relations in the functional integral formalism. Of course the complication comes when we want to compute the functional, or its derivatives, a task that requires approximations.

Then, before discussing the DMFT approximation to the functional, we will present an “*fRG intermezzo*”: To stress the analogy between the construction of the DMFT functional and the fRG one we will report the fRG flow equation for the 1PI effective action functional $\Gamma_{\text{fRG}}^{\Lambda}$, whose structure is formally similar to the “flow equations” that lead to the construction of the DMFT functional. We hope, with this comparison, to stimulate further analysis or refined approximations.

Then, we will focus again on the DMFT functional, and present the approximation that we will use to compute it explicitly, i.e., we will see how the counterpart of Eq. (1.122) arises in the functional derivation framework. Once we have defined a way to compute approximately the functional we still have to *minimize* it. In doing that we will recover the *self-consistency* condition, Eq. (1.125). Finally we will discuss the differences between the DMFT approximation and the fRG one. The main steps that we will follow in this procedure are sketched in Fig. 1.28.

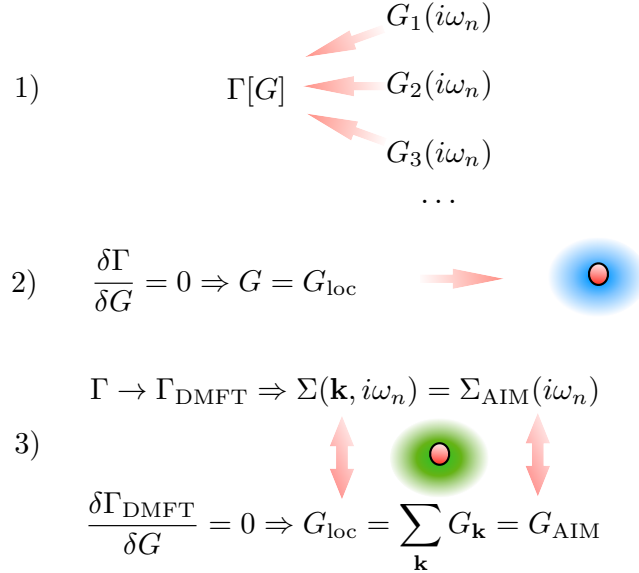


Figure 1.28: Schematic representation of the derivation of the DMFT self consistency equations using an approximate functional of the local Green's function $\Gamma_{\text{DMFT}}[G]$. The first step consists in the construction of the exact effective action functional of the local Green's function. The argument of the functional is an arbitrary function of frequency or time G . The effective action functional is constructed in a way that it is stationary for the physical value of the local Green's function (step 2). Hence, by minimizing $\Gamma[G]$ one obtains the physical value G_{loc} of the local Green's function. The knowledge of the local Green's function of the lattice is sufficient to determine an AIM which has the same local physics of each lattice site, i.e., the same Green's function. The steps 1) and 2) can be formally achieved but require the integration of functional integrals which, in general, are not doable. Therefore in step 3) we approximate the effective action functional: $\Gamma \rightarrow \Gamma_{\text{DMFT}}$. To this end, we assume that the self-energy of the lattice is approximated by the one of a (self-consistent) AIM. The minimization of the approximated functional, then, corresponds to the requirement that the impurity Green's function equals the local one of the lattice (with the approximated self energy). This way, the DMFT self-consistency cycle is defined: The local Green's function is determined by the AIM through the self-energy, and, at the same time, the choice of the specific AIM is defined by the minimal condition for the functional, through the requirement $G_{\text{loc}} = G_{\text{AIM}}$.

Construction of the effective action

Before starting with the derivation of the effective action, let us state the obvious and focus on the definition of the object we are going to construct: The effective action $\Gamma[G]$. Γ is a *functional*, i.e., its argument is a *function* $G(\omega)$ of a *single* time argument, which can be specified in imaginary frequency ω or time τ . G is *not* necessarily the local Green's function of the system we are considering. However, we are going to *construct* the effective action in a way that its

argument *at its stationary point*³³ is the physical local Green's function of the system, that we call G_{loc} . G_{loc} has the physical meaning of local Green's function, while, in general, we cannot attribute a specific physical meaning to G , and we have to regard it just as the argument of the functional. In this section, unless we specify the momentum argument, the symbol G is used for a function of the time or frequency only, and one should not confuse it with the Green's function of the system.

To write the effective action in a manageable form, we start by considering a one band Hubbard Hamiltonian, explicitly dependent on a parameter Λ [46]:

$$H^\Lambda = \Lambda \sum_{ij,\sigma} t_{ij} c_{i\sigma}^\dagger c_{j\sigma} + U \sum_i n_{i\uparrow} n_{i\downarrow} \quad (1.129)$$

$$= \Lambda \int d^3k \sum_\sigma \epsilon_{\mathbf{k}} c_{\mathbf{k}\sigma}^\dagger c_{\mathbf{k}\sigma} + U \sum_i n_{i\uparrow} n_{i\downarrow}. \quad (1.130)$$

For $\Lambda = 0$ the Hamiltonian (1.130) is purely local (atomic problem), while for $\Lambda = 1$ it corresponds to the lattice Hamiltonian we are interested in. Let us explicitly notice that Λ multiplies only the part of the Hamiltonian that is *quadratic in the creation and annihilation operators*. To make an analogy with fRG, we can define from Eq. (1.130) the Λ dependent noninteracting Green's function associated with H^Λ :

$$G_0^\Lambda(i\omega_n, \mathbf{k}) = [Q_0^\Lambda(i\omega_n, \mathbf{k})]^{-1} = (i\omega_n + \mu - \Lambda\epsilon_{\mathbf{k}})^{-1}. \quad (1.131)$$

This quantity³⁴ is the coefficient of the quadratic term in the fields in a functional integral formulation. The latter is based on the action S^Λ associated with the Hamiltonian H^Λ , that reads:

$$\mathcal{S}^\Lambda[\psi, \bar{\psi}] = -\frac{1}{\beta} \sum_{\omega_n, \sigma} \int d^3k \bar{\psi}_{\mathbf{k}\sigma}(i\omega_n) [G_0^\Lambda(i\omega_n, \mathbf{k})]^{-1} \psi_{\mathbf{k}\sigma}(i\omega_n) + U \sum_i n_{i\uparrow} n_{i\downarrow}, \quad (1.132)$$

with $n_{i\sigma}(\tau) = \bar{\psi}_{i\sigma}(\tau) \psi_{i\sigma}(\tau)$. Let us notice that the action S^Λ depends on Λ only through the propagator of the Gaussian part G_0^Λ . The first functional that we construct is the **generating functional for the local connected Green's function** of the Hamiltonian H^Λ . To do this in the functional integral formalism, we couple a term **bilinear** in the fields to a **local source term**³⁵

³³We are not going to discuss two important points here: (i) the *representability* condition and (ii) the *stability* of the functional. The representability condition corresponds, in this context, to the question whether one can always find an AIM whose Green's function equals the local one of the lattice. The stability issue corresponds to the question whether the vanishing of the functional derivative yields a true minimum, or a saddle point. This problem is still open in DMFT and is discussed in Ref. [35], and it is possibly also connected with the recently exposed divergences of the vertex [85, 160]. For a (brief) discussion of these two points, as well of the connection with the BK and LW functionals, we address the reader to Ref. [46].

³⁴The quantity Q_0^Λ is introduced here to make contact with the notation of Ref. [129] generally used in the fRG literature.

³⁵We will refer equivalently to the source term Δ either in time or frequency domain. For a more general description of the generating functional for the connected Green's functions, of the source terms, and of the Legendre transformation in functional integral context we refer to Ref. [134], specifically Sec. 2.4.

$\Delta(\tau)$:

$$\begin{aligned} \mathcal{G}^\Lambda[\Delta(\omega)] &= -\ln \int D\psi D\bar{\psi} \exp\{-\mathcal{S}^\Lambda[\psi, \bar{\psi}] \\ &\quad - \int_0^\beta d\tau \int_0^\beta \sum_\sigma \Delta(\tau) \bar{\psi}_{i\sigma}(\tau) \psi_{i\sigma}(0)\}. \end{aligned} \quad (1.133)$$

Or, expressing explicitly the action \mathcal{S}^Λ , Eq. (1.132):

$$\begin{aligned} \mathcal{G}^\Lambda[\Delta(\omega)] &= -\ln \int D\psi D\bar{\psi} \exp\left\{ \int_0^\beta d\tau [-H^\Lambda[\psi, \bar{\psi}] + \sum_{i\sigma} \bar{\psi}_{i\sigma}(\tau) (-\partial_\tau + \mu) \psi_{i\sigma}(\tau)] \right. \\ &\quad \left. - \int_0^\beta d\tau \sum_{i\sigma} \Delta(\tau) \bar{\psi}_{i\sigma}(\tau) \psi_{i\sigma}(0) \right\}. \end{aligned} \quad (1.134)$$

The reason why we chose to couple the bilinear term $\bar{\psi}_{i\sigma}(\tau) \psi_{i\sigma}(\tau')$ to the local source will be apparent in a moment.

The *interacting* local Green's function of H^Λ (or equivalently of \mathcal{S}^Λ) is defined as³⁶ the following expectation value:

$$G_{\text{loc}}^\Lambda(\tau) = \frac{\int D\bar{\psi} D\psi \bar{\psi}_{i\sigma}(\tau) \psi_{i\sigma}(0) e^{-\mathcal{S}^\Lambda[\psi, \bar{\psi}]}}{\int D\bar{\psi} D\psi e^{-\mathcal{S}^\Lambda[\psi, \bar{\psi}]}}. \quad (1.135)$$

This quantity can be expressed particularly easily [134] using the generating functional (1.133), as we can see by differentiating³⁷ with respect to the source, for vanishing value of the source field:

$$\left. \frac{\delta \mathcal{G}^\Lambda[\Delta]}{\delta \Delta(i\omega_n)} \right|_{\Delta=0} = G_{\text{loc}}^\Lambda(i\omega_n). \quad (1.136)$$

In complete analogy with equation (1.136), we can define the following quantity:

$$G^\Lambda[i\omega_n; \Delta] \equiv \frac{\delta \mathcal{G}^\Lambda[\Delta]}{\delta \Delta(i\omega_n)}. \quad (1.137)$$

This quantity is the equivalent of a local Green's function for an action that *includes* the coupling to the source Δ . The quantity $G^\Lambda[i\omega_n; \Delta]$ depends on its time and frequency argument, but *also* on (i) the source field $\Delta(\omega)$ and (ii) on the parameter Λ .

The generating functional (1.134) that we have defined is a functional of the source $\Delta(\tau)$, which, being the argument of the functional, is an arbitrary function, while the local Green's function of the action \mathcal{S}^Λ can be computed by functional derivation with respect to the source *only for vanishing value of the source*. However the functional $\mathcal{G}_c^\Lambda[\Delta]$ is not the one we are

³⁶We assume that no spin symmetry breaking happens, and therefore the local Green's function does not depend on the spin.

³⁷One has to consider that in Ref. [134] the source is coupled to the field, while here we have coupled the source to a bilinear in the field, that is why a physical quantity, like the Green's function, is given by a *first* derivative of the generating functional with respect to the source, and not by a *second* derivative.

looking for, as can be seen considering equation (1.136), i.e. the physical local Green's function is not obtained by functional minimization. The problem is that the generating functional $\mathcal{G}_c^\Lambda[\Delta]$ is not a functional of the local Green's function, but of the source. To write a functional of the Green's function we can use equation (1.137): Instead of using as argument of the functional the source Δ itself we can use the local Green's function that can be obtained in the presence of Δ . We stress that this local Green's function is also, in principle, an arbitrary function: To every different function corresponds a different source field, while of course the *physical* value of the Green's function is uniquely determined (for every value of Λ) by the condition that the source vanishes. To finally obtain a functional with the required properties we need to perform a **Legendre transformation**. This is done in two steps:

- (i) First we formally invert Eq. (1.137), and look at Δ as a function of G : $\Delta = \Delta^\Lambda[G]$ is the function that inserted in Eq. (1.137) gives $G^\Lambda[\Delta^\Lambda[G]] = G$. Here G and Δ are functions of a frequency or time argument only. The quantities with a Λ subscript, instead, are quantities that involve a functional integration, like equation (1.137) for G^Λ and its inversion for Δ^Λ . They depend on their frequency or time argument, on another function (i.e., the source Δ for G^Λ and the function G for Δ^Λ) and on Λ and therefore, implicitly on the Hamiltonian H^Λ .
- (ii) Then we define the following functional of G :

$$\Gamma^\Lambda[G] = \mathcal{G}^\Lambda[\Delta^\Lambda(G)] - \int_0^\beta d\tau \Delta^\Lambda[\tau; G] G(\tau). \quad (1.138)$$

The functional (1.138) is the **effective action** of the local Green's function. By construction it obeys the following relation [134]:

$$\frac{\delta \Gamma^\Lambda[G]}{\delta G} = -\Delta^\Lambda[G]. \quad (1.139)$$

From Eq. (1.136) one can see that the physical local Green's function corresponds to $\Delta[G_{\text{loc}}^\Lambda] = 0$, and therefore Eq. (1.139) tells us that the effective action is stationary for $G = G_{\text{loc}}^\Lambda$. Hence the functional just defined is the one we are looking for: The physical value of the local Green's function is stationary for the effective action (1.138). The functional just defined is similar, in its construction, to the one used in (the 1PI version of) fRG [129]³⁸. We refer to the functional (1.138) as the effective action of the local Green's function.

The construction of the effective action (1.138) is quite standard, but we have obtained just a *formal* expression for it. What we want to do now is finding a way to compute it, at least in an approximate way. To this end the Λ dependence of the Hamiltonian (1.130) that we have required from the beginning will turn out useful. In fact, we start with noting that we are able to compute the value of the functional Γ^Λ for $\Lambda = 0$. This can be done exactly

³⁸ In fRG using the 1PI generating functional, or effective action corresponds to a specific choice of the functional [129]. However there are also other possible functionals, for example the effective interaction.

since the Hamiltonian $H^{\Lambda=0}$ is purely local. In this situation the argument of the exponential in the generating functional (1.134) for the Hamiltonian $H^{\Lambda=0}$, for every value of the source Δ , is equal to the **action of an AIM** in which the source Δ plays the role of the hybridization function:

$$\mathcal{S}_{\text{AIM}}[\Delta] = -\frac{1}{\beta} \sum_{\omega_n, \sigma} \bar{\psi}_{i\sigma}(i\omega_n) [i\omega_n + \mu - \Delta(i\omega_n)] \psi(i\omega_n) + U \int_0^\beta d\tau n_\uparrow(\tau) n_\downarrow(\tau'), \quad (1.140)$$

and therefore the generating functional (1.134) itself for the lattice at $\Lambda = 0$ equals the free energy of the AIM F_{AIM} :

$$F_{\text{AIM}}[\Delta] = \mathcal{G}^{\Lambda=0}[\Delta]. \quad (1.141)$$

In equations (1.140) and (1.141) we have stressed in the arguments of the action and of the free energy of the AIM that they have to be seen as functions of the source, in the language of the generating functional of the lattice, or as functionals of the hybridization in the language of the action of the AIM. Therefore computing the Green's function $G^{\Lambda=0}$ in presence of the source Δ corresponds to the solution of the AIM with hybridization function $\Delta(\omega_n)$. This is for sure possible: Thanks to the development in impurity solvers we can compute the Green's function $G^\Lambda[i\omega; \Delta]$ for every value of the hybridization function $\Delta(i\omega)$. Conversely we can, in principle, invert the relation to find the hybridization function $\Delta^{\Lambda=0}[i\omega, G]$ of the AIM whose Green's function is $G(i\omega)$. To this end we write the effective action $\Gamma^{\Lambda=0}$ expressing the free action in terms of $\Delta^0[G]$:

$$\Gamma^0[G] = F_{\text{AIM}}[\Delta^0[G]] - \int_0^\beta d\tau G(\tau) \Delta^0[\tau; G]. \quad (1.142)$$

Similarly to section 1.4 for fRG, we know the effective action at $\Lambda = 0$, and we want to compute it at $\Lambda = 1$. This is possible if we can evaluate the Λ -derivative of the effective action $d\Gamma^\Lambda/d\Lambda$, and then integrate over $d\Lambda$:

$$\Gamma^{\Lambda=1}[G] = \Gamma^{\Lambda=0}[G] + \int_0^1 d\Lambda \frac{d\Gamma^\Lambda[G]}{d\Lambda}. \quad (1.143)$$

It is worth noting that this decomposition for the effective functional of the lattice problem at $\Lambda = 1$ in terms of a contribution at $\Lambda = 0$, i.e., for the simpler case without hopping taken as ‘reference system’, plus an integral that describes a gradual switching on of the hopping, is still exact. The gain from this decomposition is that the approximation that will be made involves only the term in the integral in Eq. (1.143). This is also similar to what is done in LDA, where the reference system is the noninteracting electron gas (the analogy is better explained in Ref. [46]).

To compute $\Gamma^{\Lambda=1}$ using equation (1.143) we have to start by computing the Λ derivative of Γ^Λ . This can be done by deriving Eq. (1.138) with respect to Λ :

$$\begin{aligned} \frac{d\Gamma^\Lambda[G]}{d\Lambda} &= \left. \frac{d\mathcal{G}^\Lambda}{d\Lambda} \right|_{\Delta=\Delta^\Lambda[G]} + \int_0^\beta d\tau d\tau' \left\{ \left. \frac{d\Delta^\Lambda[\tau; G]}{d\Lambda} \frac{\delta\mathcal{G}^\Lambda[\Delta]}{\delta\Delta(\tau)} \right|_{\Delta=\Delta^\Lambda[G]} \right. \\ &\quad \left. - \frac{d\Delta^\Lambda[\tau; G]}{d\Lambda} G(\tau) \right\}, \end{aligned} \quad (1.144)$$

where the first term in the integral comes from the application to the chain rule to $\mathcal{G}^\Lambda[\Delta^\Lambda[G]]$. Due to Eq. (1.137) the argument of the integral vanishes and the derivative of the effective action equals the derivative of \mathcal{G}^Λ at fixed value of the source $\Delta^\Lambda[G]$:

$$\frac{d\Gamma^\Lambda[G]}{d\Lambda} = \frac{d\mathcal{G}^\Lambda}{d\Lambda}\Big|_{\Delta=\Delta^\Lambda[G]}. \quad (1.145)$$

By noting that \mathcal{G}^Λ depends on Λ only through the sources and through the inverse propagator Q_Λ^0 (1.131) of the Gaussian part of the action (1.132) we obtain:

$$\frac{d\Gamma^\Lambda[G]}{d\Lambda} = \frac{1}{\beta} \sum_{\omega_n, \sigma} \int d^3k \dot{Q}_0^\Lambda \langle \bar{\psi}_{\mathbf{k}\sigma}(i\omega_n) \psi_{\mathbf{k}\sigma}(i\omega_n) \rangle \Big|_G. \quad (1.146)$$

where $\langle \dots \rangle|_G$ denotes the expectation value *in the presence of the source* $\Delta^\Lambda[G]$:

$$\langle \dots \rangle|_G \equiv \frac{\int D\psi D\bar{\psi} \dots e^{-S^\Lambda[\psi, \bar{\psi}] - \int_0^\beta d\tau \Delta^\Lambda(\tau) \bar{\psi}(\tau) \psi(0)}}{\int D\psi D\bar{\psi} e^{-S^\Lambda[\psi, \bar{\psi}] - \int_0^\beta d\tau \Delta^\Lambda(\tau) \bar{\psi}(\tau) \psi(0)}}, \quad (1.147)$$

and a dot denotes a Λ -derivative: $\dot{Q}_0^\Lambda = \partial Q_0^\Lambda / \partial \Lambda$. Finally, noting that $\dot{Q}_0^\Lambda(i\omega_n, \mathbf{k}) = \epsilon_{\mathbf{k}}$ we can express the derivative of the effective action in terms of the Green's functions computed in the presence of the source:

$$\frac{d\Gamma^\Lambda[G]}{d\Lambda} = \frac{1}{\beta} \sum_{\omega_n, \sigma} \int d\mathbf{k} \epsilon_{\mathbf{k}} G^\Lambda(i\omega_n, \mathbf{k}) \Big|_G. \quad (1.148)$$

The right hand side of this equation can be identified with the kinetic energy computed in the presence of the source. Eq. (1.148) inserted in Eq. (1.143), gives the exact expression for the effective action functional.

This is the last exact expression for the effective action that we are able to obtain. From now on, to proceed further, we have to rely on some approximation, which in this case is the DMFT approximation. Before switching to that step, however, in the next subsection we will show that equations (1.145) and (1.146) are formally similar to the equations that define the fRG flow equations for the 1PI generating functional.

Comparison with fRG flow equations

In order to make a comparison with fRG, we write the flow equations for a functional similar to the effective action of the local Green's function $\Gamma^\Lambda[G]$. There are two main differences however. The first one is that in fRG one does not look only at local quantities, and the second one is that one usually works with functionals expressed in terms of *the expectation value of the fields themselves*, and not in terms of expectation values of bilinear forms of the fields.

	DMFT	fRG
Functionals	$\mathcal{G}^\Lambda[\Delta], \Gamma^\Lambda[G]$	$\mathcal{G}_{\text{fRG}}^\Lambda[\eta, \bar{\eta}], \Gamma_{\text{fRG}}^\Lambda[\phi, \bar{\phi}]$
Source(s)	$\Delta(\tau)$	$\eta(x), \bar{\eta}(x)$
Coupling	$\bar{\psi}_{i\sigma}(\tau)\psi_{i\sigma}(0)\Delta(\tau)$	$(\bar{\eta}, \psi) + (\bar{\psi}, \eta)$
Expectation values	$G^\Lambda = \frac{\delta \mathcal{G}^\Lambda}{\delta \Delta}$	$\phi^\Lambda = -\frac{\delta \mathcal{G}_{\text{fRG}}^\Lambda}{\delta \bar{\eta}}, \bar{\phi}^\Lambda = -\frac{\delta \mathcal{G}_{\text{fRG}}^\Lambda}{\delta \eta}$
"Flow" equations	Eqs. (1.146), (1.148)	Eqs. (1.157), (1.158)
Approximation	<i>Local self-energy</i>	<i>Truncation of the hierarchy of flow equations</i>

Table 1.1: Illustration of the main quantities involved in the functional derivation of DMFT and relative comparison with fRG quantities.

This means that in defining the counterpart of the generating functional (1.134) the sources are coupled to the fields, and not to a term bilinear in them. The Legendre transformations defined consequently.

Let us also note explicitly that the choice of the Hamiltonians H^Λ (1.130) defines a one parameter family of Gaussian propagators G_0^Λ (1.131), which is well suited to fully determine an fRG flow, and one could keep, in principle, the same Λ dependent actions \mathcal{S}^Λ for an fRG flow or for a DMFT integration of the (nonlocal) effective action. We will use from now on the subscript fRG to emphasize that the functionals $\mathcal{G}_{\text{fRG}}^\Lambda[\eta, \bar{\eta}]$ and $\Gamma_{\text{fRG}}^\Lambda[\phi, \bar{\phi}]$ are not the same as the functionals defined above, although they play a similar role. Let us start by defining the generating functional of the connected Green's function [129, 134] as:

$$\mathcal{G}_{\text{fRG}}^\Lambda[\eta, \bar{\eta}] = -\ln \int D\psi D\bar{\psi} e^{-\mathcal{S}^\Lambda[\psi, \bar{\psi}] + (\bar{\eta}, \psi) + (\bar{\psi}, \eta)}. \quad (1.149)$$

Here the sources $\eta(x), \bar{\eta}(x)$ are not local and depend on a full set of quantum numbers x which collects, e.g., position (momentum), imaginary time (frequency) and spin, and the round brackets denote a scalar product: $(f, g) \equiv \int dx f(x)g(x)$. The "expectation values" of the fields can be defined from the functional derivatives of equation (1.149) with respect to the sources:

$$\phi^\Lambda[\eta, \bar{\eta}] = -\frac{\delta \mathcal{G}_{\text{fRG}}^\Lambda}{\delta \bar{\eta}}, \quad (1.150)$$

$$\bar{\phi}^\Lambda[\eta, \bar{\eta}] = -\frac{\delta \mathcal{G}_{\text{fRG}}^\Lambda}{\delta \eta}. \quad (1.151)$$

These relations can be formally inverted to express the sources η in terms of the expectation values of the fields:

$$\phi^\Lambda[\eta^\Lambda[\phi, \bar{\phi}], \bar{\eta}^\Lambda[\phi, \bar{\phi}]] = \phi, \quad (1.152)$$

$$\bar{\phi}^\Lambda[\eta^\Lambda[\phi, \bar{\phi}], \bar{\eta}^\Lambda[\phi, \bar{\phi}]] = \bar{\phi}. \quad (1.153)$$

With these definitions the effective action is obtained performing the following Legendre transformation [129]:

$$\Gamma_{\text{fRG}}^\Lambda[\phi, \bar{\phi}] = (\bar{\eta}^\Lambda[\phi, \bar{\phi}], \phi) + (\bar{\phi}, \eta^\Lambda[\phi, \bar{\phi}]) + \mathcal{G}_{\text{fRG}}^\Lambda[\eta^\Lambda[\phi, \bar{\phi}], \bar{\eta}^\Lambda[\phi, \bar{\phi}]]. \quad (1.154)$$

Let us follow the notation of Ref. [129] and define the matrix of the second derivatives of $\Gamma_{\text{fRG}}^\Lambda[\phi, \bar{\phi}]$ with respect to the fields as:

$$\Gamma^{(2)\Lambda}[\phi, \bar{\phi}] = \begin{pmatrix} \frac{\partial^2 \Gamma_{\text{fRG}}^\Lambda}{\partial \bar{\phi}(x') \partial \phi(x)} & \frac{\partial^2 \Gamma_{\text{fRG}}^\Lambda}{\partial \bar{\phi}(x') \partial \bar{\phi}(x)} \\ \frac{\partial^2 \Gamma_{\text{fRG}}^\Lambda}{\partial \phi(x') \partial \phi(x)} & \frac{\partial^2 \Gamma_{\text{fRG}}^\Lambda}{\partial \phi(x') \partial \bar{\phi}(x)} \end{pmatrix}. \quad (1.155)$$

It can be seen [129, 134] that the inverse of the quantity defined in Eq. (1.155) can be directly connected with the Green's function computed in presence of the sources. Let us define the matrix \dot{Q}_0^Λ by:

$$\dot{Q}_0^\Lambda(x, x') = \begin{pmatrix} \dot{Q}_0^\Lambda(x, x') & 0 \\ 0 & -\dot{Q}_0^\Lambda(x', x) \end{pmatrix}, \quad (1.156)$$

Using these definitions we can write [129] the Λ -derivative of the effective action, i.e., the fRG flow equation for the 1PI functional as:

$$\frac{d\Gamma_{\text{fRG}}^\Lambda[\psi, \bar{\psi}]}{d\Lambda} = \frac{d\mathcal{G}_{\text{fRG}}^\Lambda[\eta, \bar{\eta}]}{d\Lambda} \Big|_{(\eta, \bar{\eta})=(\eta^\Lambda[\psi, \bar{\psi}], \bar{\eta}^\Lambda[\psi, \bar{\psi}])} \quad (1.157)$$

$$= -(\bar{\psi}, \dot{Q}_0^\Lambda \psi) - \frac{1}{2} \text{tr} \{ \dot{Q}_0^\Lambda (\Gamma^{(2)\Lambda}[\psi, \bar{\psi}])^{-1} \}. \quad (1.158)$$

Equations (1.145) and (1.157) are similar: The derivative of an effective action can be expressed in terms of the derivative of the respective generating functional at fixed value of the sources.

The formal analogy between equations (1.146) and (1.158) is more obscure, but one can see it³⁹ considering that the second derivative of the effective functional $\Gamma_{\text{fRG}}^\Lambda$ is basically the inverse of a Green's functions, see Refs. [129, 134].

In spite of the formal analogies, the approximations used to explicitly compute the derivative of the (otherwise exact) functionals $d\Gamma^\Lambda/d\Lambda$ and $d\Gamma_{\text{fRG}}^\Lambda/d\Lambda$ are very different in DMFT and fRG, therefore yielding results that are valid in different regimes. In the fRG framework, the problem is dealing with $\Gamma^{(2)\Lambda}[\phi, \bar{\phi}]$, which is still a functional of the fields ϕ and $\bar{\phi}$. As we have seen in section 1.4, this problem is usually tackled by an expansion around zero in $\bar{\phi}, \phi$, which generates a hierarchy of differential equations for the one-particle irreducible vertex functions. A subsequent truncation of the hierarchy is then needed to obtain a finite set of equations. Due to the truncation, the approximation is reliable for weak to moderate values of the coupling, while the frequency and momentum dependence of the vertices can be maintained. In the next paragraph we will see that in DMFT one uses a completely different approximation.

³⁹One can also check that the term $-(\bar{\psi}, \dot{Q}_0^\Lambda \psi)$ appearing in Eq. (1.158) but not in Eq. (1.146) is due to the fact that the sources are coupled to the fields in the former case and to a bilinear of the fields in the latter, and therefore the Green's function is obtained by a second derivative of the generating functional $\mathcal{G}_{\text{fRG}}^\Lambda$ w.r.t. to $\eta, \bar{\eta}$, and by a first derivative of \mathcal{G}^Λ w.r.t. Δ . This can be seen most easily by explicitly writing the Λ derivative of the \mathcal{G}_{fRG} and comparing it to the second derivative w.r.t. the sources.

DMFT approximation to the effective action

Until now we have just defined a functional $\Gamma^\Lambda[G]$, so that $\Gamma^{\Lambda=1}[G]$ is the effective action for the system we are interested in. We stress that this functional is *exact*: No approximation is involved. However we could have formally written the exact effective action functional from the beginning, without making use of the Λ integration of the kinetic energy described above. The reason why we have introduced the Λ dependence is that it allows to rewrite the effective action in the form (1.143), which is convenient for what we are doing next, i.e., finding an approximation to practically use the effective action functional. Indeed, also in the form of Eq. (1.143) to compute the effective action functional $\Gamma^\Lambda[G]$ we have to evaluate $\sum_{\omega_n, \sigma} \int d^3k \epsilon_{\mathbf{k}} G^\Lambda(\mathbf{k}, i\omega_n)|_G$, i.e., the kinetic energy in the presence of the source $\Delta^\Lambda[G]$. Computing exactly this quantity is, in general, not possible. In the presence of this source we constraint the value of the local Green's function: $\langle \bar{\psi}_{i\sigma}(\omega) \psi_{i\sigma}(\omega) \rangle|_G = G$, but even in this case we still do not know the value of the *nonlocal Green's function*: In general the constraint on the local Green's function alone is not sufficient to determine the kinetic energy⁴⁰.

Therefore to proceed further we define the self-energy associated with the Λ dependent Hubbard model, in presence of the source $\Delta^\Lambda(i\omega_n)$:

$$G^\Lambda(\mathbf{k}, i\omega_n) = \frac{1}{i\omega_n + \mu - \Delta^\Lambda(i\omega_n) - \Lambda \epsilon_{\mathbf{k}} - \Sigma^\Lambda[\mathbf{k}, i\omega_n; \Delta^\Lambda]}. \quad (1.159)$$

Let us underline that, as specified by the Λ superscript, Δ^Λ is the source that guarantees that the interacting local Green's function of the Hamiltonian H^Λ assumes the value G (which in general *does not need* to be the *physical* value of the local Green's function). The problem of determining $\Delta^\Lambda(\omega)$ is not possible in general, since the Hamiltonian H^Λ for non zero values of Λ is a lattice Hamiltonian with non vanishing hopping amplitudes. This is different for $\Lambda = 0$, in which case one has to solve an AIM rather than a lattice model, then one can invert Eq. (1.137) to find the source term $\Delta^0[G]$ that gives G as local Green's function. This source, seen as hybridization function, defines an AIM, with self-energy Σ^0 and Green's function G . Let us remark here that in principle the self-energy Σ^0 depends on the hybridization function that defines the AIM, which in turns is a functional of G . The **DMFT approximation** that we are going to follow from now on consists in replacing the self-energy Σ^Λ with the self-energy at the beginning of the flow $\Sigma^{\Lambda=0}$, i.e., the self-energy of the AIM whose local Green's function is G , at least for the purpose of the calculation of the kinetic energy in equation (1.148). This approximation is *equivalent* to the one defined by equation (1.122). Performing the substitution equation (1.159) yields for the local Green's function:

$$G^\Lambda(i\omega_n) = \int d\epsilon \frac{D(\epsilon)}{i\omega_n + \mu - \Delta^\Lambda(i\omega_n) - \Lambda \epsilon - \Sigma^0(i\omega_n)}. \quad (1.160)$$

Defining the Hilbert transform associated with the density of states $D(\epsilon)$ as $\tilde{D}(z) = \int d\epsilon D(\epsilon) \frac{1}{z-\epsilon}$ Eq. (1.160) reads:

$$G^\Lambda(i\omega_n) = \frac{1}{\Lambda} \tilde{D}\left(\frac{\zeta^\Lambda}{\Lambda}\right), \quad (1.161)$$

⁴⁰A notable exception is the Bethe lattice with infinite connectivity [46].

with

$$\zeta^\Lambda = i\omega_n + \mu - \Delta^\Lambda(i\omega_n) - \Sigma^0(i\omega_n), \quad (1.162)$$

Following [46], we write the self-energy Σ^0 in terms of the local Green's G function and of the hybridization function Δ^0 , inverting the Dyson equation:

$$\Sigma^0(\omega_n) = i\omega_n + \mu - \Delta^0(\omega_n) - G(\omega_n)^{-1}. \quad (1.163)$$

Substituting it in Eq. (1.162) we obtain:

$$\zeta^\Lambda = \Delta^0(i\omega_n) - \Delta^\Lambda(i\omega_n) + G(i\omega_n)^{-1}. \quad (1.164)$$

To obtain an expression for $\Delta^\Lambda(i\omega_n)$ in terms of $\Delta^0(i\omega_n)$ let us introduce the inverse of the Hilbert transform R with $\tilde{D}[R(g)] = g$ which, combined with equations (1.161) and (1.164) gives:

$$\Delta^\Lambda[i\omega_n; G(i\omega_n)] = G(i\omega_n)^{-1} + \Delta^0[G(i\omega_n)] - \Lambda R[\Lambda G(i\omega_n)]. \quad (1.165)$$

Inserting the relation just obtained in the equation for the kinetic energy⁴¹, equation (1.148), in the DMFT approximation of a local self-energy, equation (1.160), we obtain:

$$\frac{d\Gamma_{\text{DMFT}}^\Lambda[G]}{d\Lambda} = \frac{1}{\beta} \sum_{\omega_n, \sigma} \frac{1}{\Lambda} \int d\epsilon \frac{\epsilon D(\epsilon)}{R(\Lambda G(i\omega_n)) - \epsilon} \quad (1.166)$$

$$= \frac{1}{\beta} \sum_{\omega_n, \sigma} \left\{ -\frac{1}{\Lambda} + \frac{1}{\beta} G(i\omega_n) R[\Lambda G(i\omega_n)] \right\}. \quad (1.167)$$

The integral over $d\epsilon$ has been performed by summing and subtracting $R(\Lambda G(\omega_n))$ in the numerator. The subscript DMFT is used to emphasize that the functional that we are using is *not exact* anymore, but is obtained with the DMFT approximation (1.160). Finally, combining (1.167) and (1.143) we obtain the effective functional of the local Green's function in the DMFT approximation:

$$\begin{aligned} \Gamma_{\text{DMFT}}^{\Lambda=1}[G] &= F_{\text{AIM}}[\Delta^0[G]] - \frac{1}{\beta} \sum_{\omega_n} G(i\omega_n) \Delta^0(i\omega_n) + \\ &\int_0^1 d\Lambda \frac{1}{\beta} \sum_{\omega_n} G(i\omega_n) R[\Lambda G(i\omega_n)]. \end{aligned} \quad (1.168)$$

Here we have dropped the term $1/\Lambda$ since it does not depend on G , and therefore does not contribute to functional derivatives. Eq. (1.168) is a closed expression for the effective functional of the local Green's function of the lattice in the DMFT approximation: Under this approximation we are able, in principle, to compute the effective functional also for non vanishing values of Λ . Eq. (1.168) still involves the solution of a many body problem through the implicit relation that connects G with the source $\Delta^0[G]$.

⁴¹Strictly speaking, the sum over ω_n must be performed with a convergence factor $e^{i\omega_n 0^+}$.

Minimization of the functional Our task is not yet accomplished: We have found a way to compute the functional, but we are interested in the *minimum of its functional derivative* with respect to G . Therefore what we are going to do now is **minimize** the functional $\Gamma_{\text{DMFT}}^\Lambda$. The physical value of the local Green's function $G_{\text{loc}}(i\omega_n)$ (in the DMFT approximation) is the one that minimizes the effective action:

$$\frac{\delta\Gamma_{\text{DMFT}}[G]}{\delta G} = 0 \Rightarrow G = G_{\text{loc}}. \quad (1.169)$$

Using the fact that $\delta\Gamma^0/\delta G = -\Delta^0$ this reduces to:

$$\Delta^0[i\omega_n] = \frac{\delta}{\delta G(i\omega_n)} \int_0^1 d\Lambda \frac{1}{\beta} \sum_{\omega_n} G(i\omega_n) R[\Lambda G(i\omega_n)]. \quad (1.170)$$

Using the relation⁴² $R[\Lambda G] + \Lambda G \partial_\Lambda R[\Lambda G] = \partial_\Lambda [\Lambda R[\Lambda G]]$, Eq. (1.170) becomes:

$$\Delta_{\text{DMFT}}^0[i\omega_n; G] = R[G(i\omega_n)] - \frac{1}{G(i\omega_n)}. \quad (1.171)$$

In this equation we appended the subscript DMFT to the source Δ^0 to emphasize that this is the specific value of the source that minimizes the effective action $\Gamma_{\text{DMFT}}^{\Lambda=1}$ *in the DMFT approximation*. In other words, Δ_{DMFT}^0 is the hybridization function of the AIM whose Green's function is the *physical* local Green's function G_{loc} of the Hamiltonian $H^{\Lambda=1}$, under the DMFT approximation. Equation (1.170) assumes a familiar form expressing the hybridization function Δ^0 in terms of the self-energy, Eq. (1.163), rearranging the terms and taking the Hilbert transform of both sides:

$$G_{\text{loc}}(i\omega_n) = \int d\epsilon \frac{D(\epsilon)}{i\omega_n + \mu - \epsilon - \Sigma_{\text{DMFT}}(i\omega_n)}, \quad (1.172)$$

which is nothing more than the usual DMFT self consistency equation (1.125). In the functional framework the self consistency relation guarantees that the effective action functional (in the DMFT approximation) is minimal for the self-consistent Green's function. The same self-consistency equation also corresponds to $\Delta^{\Lambda=1}[G] = 0$, which is to be expected considering that $\delta\Gamma^{\Lambda=1}/\delta G = \Delta^{\Lambda=1}$, and this quantity must vanish when the derivative is evaluated for the physical local Green's function.

Let us stress that we did not rely on any expansion in the fields, and therefore we did not need to truncate a hierarchy of flow equations, as was done in fRG. This is the cornerstone for the success of DMFT in strong coupling problems: The only approximation that we have made is assuming a specific (local) form of the self-energy in the derivation of an effective functional. Whether this approximation works or not is nontrivially related with the strength of the coupling U/t (i.e., since there is no perturbative expansions and this parameter does not need to be small), and we have seen that both the limits of vanishing and atomic limit are exactly reproduced. The quality of the approximation is more directly related on how well the self-energy is approximated by a local one. If this is not the case our estimation for the kinetic

⁴²To evaluate the lower boundary of the integral also note that $\lim_{x \rightarrow 0} R[x] = 1/x$.

energy contribution to the effective action will be quite poor. Those are the cases in which we will have to work out approximations aimed at the inclusion of nonlocal correction to the DMFT self-energy.

1.5.3 DMFT description of the Mott transition

One of the main successes of DMFT is the qualitative and quantitative description of the Mott metal insulator transition. Here we will briefly review the main points of the DMFT description of the Mott transition. The aim is to show what are the strengths of DMFT and to highlight the role played by the AIM.

The Mott transition is the paradigmatic phenomenon that causes a material predicted to be conducting by bandstructure theory to become insulating due to strong electronic correlations. The physical mechanism behind the Mott transition was understood already several decades ago: In an half filled system and in absence of strong Coulomb repulsion the electrons have available states for the hopping and the system is metallic. However, when the Coulomb repulsion is stronger a double occupation on a lattice site is energetically costly. As a consequence, in the limit where U is much bigger than the hopping amplitude t , every site is occupied exactly by one electron and the electrons can not move anymore, i.e., they become localized.

While the two limits of weak and strong Coulomb interaction were understood long ago, a qualitative and quantitative description of the transition region has been elusive until it was studied by DMFT. In fact, unlike in the two other limits, in the transition region the problem is nonperturbative, since a really small parameter is missing, and a correct description of it should take into account several different energy scales: The interplay of potential and kinetic energy gives rise to a new energy scale (reminiscent of the Kondo temperature in isolated impurities) which is often orders of magnitude smaller than the hopping amplitude or the Coulomb repulsion. We refer to the literature for a more thorough discussion, in particular to Ref. [45,81] for a ‘‘material perspective’’ and to [46,48] for a DMFT point of view. Let us focus on the DMFT description of an Hubbard model in infinite dimensions and discuss one by one the main features. In the main points of this discussion we follow Ref. [46].

Fermi liquid. The original energy scales are roughly given by the kinetic energy $\propto D$ (D being half the bandwidth) and the potential energy $\propto U$. For low temperatures T and in the metallic state the system will be in a Fermi liquid state, characterized by a *quasiparticle weight* Z , which in DMFT is \mathbf{k} independent: The fraction of spectral weight in every quasiparticle peak is the same for each $\epsilon_{\mathbf{k}}$. For higher temperatures the assumptions of Fermi liquid theory [1] do not hold any longer. This temperature is referred to as *coherence temperature* ϵ_F^* . At very low temperatures the quasiparticle weight evolves continuously from $Z = 1$ for the noninteracting case to $Z \rightarrow 0$ as U approaches a *finite* critical value for the Mott transition.

Hubbard bands. While the Fermi liquid theory is a low energy theory which does not describe the high energy incoherent excitations, DMFT gives also access to them. In fact, the fraction $1 - Z$ of spectral weight that does not constitute the quasiparticle peak needs to be transferred to some other incoherent excitations. Considering the \mathbf{k} -summed spectra, the inco-

herent spectral weight forms the so-called upper and lower Hubbard bands, roughly centered at $-U/2$ and $U/2$. This unveils the connection with the underlying local problem: The spectrum of an isolated atom at half-filling consists of two delta peaks at $-U/2$ and $U/2$. In the lattice case these peaks broaden to form the Hubbard bands, with an energy cost of moving one electron from the lower to the upper Hubbard band being proportional to the energy necessary to form a double occupation, i.e., $\propto U$. Hence, in DMFT, we obtain a *three peaks spectrum* composed of two Hubbard bands and a quasiparticle peak of half-bandwidth ZD , which collects the quasiparticle excitations.

Kondo physics. The reduction of the quasiparticle weight Z when increasing U and the formation of a three peak structure is not surprising: It is closely resembling the evolution of the spectral function in the Kondo problem (at half filling) [66]. To some extent this is to be expected: In both cases the self-energy is given by the solution of an AIM. However a closer look reveals a dramatic difference: In the case of the Kondo problem the quasiparticle weight decreases like: $Z \propto e^{\frac{1}{\nu}}$ (in the limit of large U), therefore vanishing only when U approaches infinity, while the critical value for the Mott transition is finite. The reason for this difference has to be looked for in the difference in the form of the hybridization function. Indeed in the description of the Kondo problem the hybridization function is kept constant as U is changed, while in the lattice problem the hybridization function depends on U through Eq. (1.125). In particular, in DMFT, the hybridization function acquires a nontrivial frequency structure, while a common, but not unique, assumption to describe the Kondo problem is $\Delta(\omega) = -i\Gamma \text{sign}(\omega)$. The hybridization function in DMFT indeed is not only a computational tool but has a physical meaning by itself. In the metallic phase, close to the Mott transition, it shows a three peak structure, which is connected to the formation of new energy scales associated with the so-called ‘‘kinks’’ in the self-energy [62]. On the other hand the vanishing of the hybridization function for $\omega \rightarrow 0$ is related to the Mott transition in an insulating state [106]. As a bottom line there is a lot that can still be learnt from the understanding of the Kondo physics, applied to the specific AIM that fulfills the self consistency equations for some given lattice in DMFT.

Insulating phase. When U exceeds some critical value, DMFT gives an insulating solution. This is associated with the vanishing of the quasiparticle weight Z and with the formation of unscreened local moments, as can be inferred from the temperature dependence of the local susceptibility $\chi_{\text{loc}} \propto 1/T$, which follows the Curie law⁴³. Importantly, due to the presence of the local moments, the entropy of the insulating phase is *higher* than the one to the metallic phase.

First order phase transition. The Mott transition in DMFT is a first order phase transition. This is confirmed by the fact that in a region of the phase diagram it is possible to stabilize two different solutions, an insulating and a metallic one. The area where this is possible is delimited by two lines $U_{c1}(T)$ and $U_{c2}(T)$ [27, 48], that represent respectively the minimal value of U for which one can obtain an insulating solution and the maximal value of U for which it is possible to obtain a metallic solution. The two lines meet at a critical endpoint. The real first

⁴³We have assumed a paramagnetic solution, if we would have allowed for it [48], in absence of frustration, we would have obtained an antiferromagnetically ordered solution.

order transition line can be found by minimizing the free energy (therefore the entropy plays an important role).

The discussion above shows that DMFT is able to capture three different regimes using a single framework: The weak and the strong coupling regimes, that can be described also with other techniques, and the more challenging intermediate regime that includes the Mott transition region. For U values slightly smaller than the critical U_{c1} DMFT reveals important physical analogies between the lattice systems and a Kondo systems at strong coupling, and accounts for the appearance of new energy scales. Finally let us stress that, remarkably, the DMFT description of the Mott transition, rigorously exact *only* in infinite dimensions, agrees very well with the experimental observations collected for several materials [46, 48], e.g., for SrVO_3 [163].

DMFT in the symmetry broken phase An application of DMFT in the broken phase, obtained in the work of this thesis, can be found in Ref. [171], where the antiferromagnetic regime of the Hubbard model in infinite dimensions is studied at weak and strong coupling. In particular it is discussed that the mechanisms that stabilize the onset of long range order, in the two coupling regimes, are different. Surprisingly, this also have consequences for the optical conductivity, which usually is supposed to depend only weakly on the spin degrees of freedom. Finally, it is also argued that the theoretical prediction has already been observed in the optical conductivity of LaSrMnO_4 . For more details we address the reader to the original paper [171].

Chapter 2

Merging GW and dynamical mean field theory: the $GW+DMFT$ method

This chapter is devoted to the combination of GW and $DMFT$. The method is first introduced, emphasizing how GW and $DMFT$ can be integrated in a single, formally elegant, method and the possible advantages of doing this. The practical implementation, however, presents several technical complication, and, in the central part of the chapter, we propose a simplified scheme, which relies on a quasiparticle approximation to the GW self-energy. Hence we discuss how, with this approximation, one can perform quasiparticle $GW+DMFT$ calculations keeping substantially unaltered the $DFT+DMFT$ main outline. In the last part of this chapter, we present the results obtained testing our quasiparticle $GW+DMFT$ implementation in $VASP$ for the correlated metal $SrVO_3$. The improvement over conventional $DFT+DMFT$ is shown by a comparison with experimental data. Eventually our results are compared with those obtained within a much more demanding, full $GW+DMFT$ calculation, exhibiting good agreement for the main features.

This chapter is partially based on Ref. [170], [Taranto *et al.*, Phys. Rev. B **88**, 165119 (2013)], but considerably extends it.

2.1 Advantages of $GW+DMFT$

The local density approximation (LDA) plus dynamical mean field theory (DMFT) approach [10, 60, 61, 108, 113] has been a significant step forward for calculating materials with strong electronic correlations. This is because -on top of the LDA- DMFT includes a major part of the electronic correlations: the local ones. In recent years, LDA+DMFT has been applied successfully to many materials and correlated electron phenomena, ranging from transition metals and their oxides to rare earth and their alloys, for reviews see Refs. [60, 108].

For truly parameter-free *ab initio* calculations, however, two severe shortcomings persist: (i) the screened Coulomb interaction is usually treated as an adjustable parameter in LDA+DMFT

and (ii) the so-called double counting problem, i.e., it is difficult to determine the electronic correlations already accounted for at the local density approximation (LDA) level. These shortcomings are intimately connected with the fact that the non-linear dependence on the electronic density of density functional theory does not match with the many-body, Feynman-diagrammatic, structure of DMFT. These problems can be mitigated, but not solved, by constrained LDA (cLDA) calculations [37, 52, 126], which can be exploited to extract two independent parameters: interaction and double counting correction. [126, 127]

A conceptually preferable and better defined many-body approach is achieved if one substitutes LDA by the GW approximation, [12, 59] described in Sec. 1.3. This approach, named $GW+DMFT$, was formalized for the first time by Biermann, Aryasetiawan and Georges, in 2003 [24], who also applied a simplified version of it in a realistic calculation for Ni. Compared to standard LDA+DMFT, $GW+DMFT$ presents important conceptual advantages both regarding (i) the choice of the Coulomb parameter and (ii) the double counting problems. However this is only possible at a much higher computational price.

2.1.1 $GW + DMFT$: a brief functional perspective

As it is stressed in Ref. [173], to overcome the difficulties of the LDA+DMFT based methods, it is desirable to have a theory that:

1. is formulated in the Green's function language;
2. deals directly with the long-range Coulomb interaction;
3. retains the nonperturbative character of the dynamical mean field theory.

The $GW+DMFT$ approach that we are going to discuss fulfills these requirements. This can be explicitly seen by constructing a specific Baym-Kadanoff functional [24, 173] appropriate to derive the $GW+DMFT$ approximation. Once the approximation to the functional is done the physical quantities of interest can be computed by calculating the stationary points of the Baym-Kadanoff functional, as mentioned in Sec. 1.5.2. More in particular, the functional of Ref. [24] directly follows from the ones introduced by Refs. [3, 35], and its main feature (as well its main difference from the functional of Sec. 1.5.2), is that it is *not* only a functional of the interacting Green's ¹ function G , but it is *also* a functional of the **screened Coulomb interaction** W . Therefore, by finding the stationary points of the functional with respect to its arguments one obtains the values of the Green's function and of the screened Coulomb interaction [24]. The

¹Let us note that here G does not denote the *local* component only of the Green's function (as in Sec. 1.5.2), but also the nonlocal part.

explicit form of the exact functional that we consider ² is:

$$\Gamma[G, W] = \text{Tr} \ln G + \text{Tr}[(\mathcal{G}_H^{-1} - G^{-1})G] - \frac{1}{2} \text{Tr} \ln W + \frac{1}{2} \text{Tr}[(V^{-1} - W^{-1})W] + \Psi[G, W]. \quad (2.1)$$

$V(\mathbf{r} - \mathbf{r}')$ is the Coulomb potential, $\mathcal{G}_H^{-1} = i\omega + \mu - v_c - v_H$ is the bare Green's function of the solid, with v_c being the crystal potential and $v_H(\mathbf{r}) \equiv \int d^3r' V(\mathbf{r} - \mathbf{r}')n(\mathbf{r}')$ the Hartree potential. All the complication is contained in the many body correction [173] $\Psi[G, W]$, which is the part of the functional that we will have to approximate. An appropriate choice of the approximation applied to the functional leads directly to the $GW+DMFT$ equations. Some light on the diagrammatic content of Ψ can be shed by performing a functional derivation of it for stationary points of Γ yielding [24, 173] the self-energy Σ and the polarization operator P :

$$\frac{\delta\Gamma}{\delta G} = 0 \Rightarrow G^{-1} = \mathcal{G}_H^{-1} - \Sigma, \quad \Sigma = \frac{\delta\Psi}{\delta G}, \quad (2.2)$$

$$\frac{\delta\Gamma}{\delta W} = 0 \Rightarrow W^{-1} = V^{-1} - P, \quad P = -2 \frac{\delta\Psi}{\delta W}, \quad (2.3)$$

i.e., diagrammatically Ψ is the sum of all skeleton diagrams that are irreducible with respect to both the one-electron propagator and the interaction lines. The self-energy Σ defined here does not include the Hartree diagram, which is explicitly included into the bare Green's function \mathcal{G}_H . The equations above, show that the interacting Green's function and the screened Coulomb interaction enter in a very similar fashion in the effective action (2.1). At the same time one can see the analogy between the role of the bare Green's function \mathcal{G}_H and the one of the bare Coulomb interaction V , as well between the self-energy Σ and the polarization operator P .³

Let us stress that until now we have just rewritten the effective action in the form (2.1), which is *exact* by definition. The advantage of the expression (2.1) is that it is well suited for making approximation on the many-part of the functional $\Psi[G, W]$. With the appropriate approximation one can obtain the effective action $\Gamma_{GW+DMFT}$, which leads to the $GW+DMFT$ approach. Specifically the approximation consists in replacing the nonlocal part⁴ of the Ψ -functional [3] with the GW approximation: $\Psi_{GW} = -\frac{1}{2} \text{Tr} G W G$, and adding to it the Ψ -functional of a *self-consistent* Anderson impurity model (AIM) $\Psi_{\text{AIM}}[G^{\text{RR}}, W^{\text{RR}}]$, where \mathbf{R}

²To obtain the functional of the Green's function *and* the screened Coulomb interaction one can [35] start from the free energy functional of the solid and use an Hubbard-Stratonovich transformation to decouple the quartic term in the fermionic fields ψ . This introduces a set of bosonic fields ϕ . The action written in terms of the bosonic and fermionic fields assumes a particularly symmetric form, from which the functional follows straightforwardly. This action, see Ref. [35] Eq. (24), consists of a quadratic term in the fermionic fields, with propagator \mathcal{G}_H , a quadratic term in the bosonic fields with propagator V , and a coupling of the form $\phi\bar{\psi}\psi$ between bosonic and fermionic fields. This also shows the similar role played in this context by the bare Green's function \mathcal{G}_H and the bare Coulomb interaction. The functional $\Gamma[G, W]$ written in equation (2.1) is then obtained in the standard way coupling the field to appropriate sources, performing a Legendre transformation and expressing explicitly the sources in term of G and W [24, 35].

³To further emphasize the analogy between G , the propagator of the fermionic field, and W we stress that [173] W can also be defined as the correlation function of bosonic excitations corresponding to density fluctuations, i.e., the propagator of the Hubbard-Stratonovich field decoupling the Coulomb interaction term.

⁴We do not enter in the details here, for which we refer to [24], but we just note that in order to perform this operation one needs to specify a basis set, like the maximally localized Wannier functions [125] or linearized muffin tin orbitals [6]: locality refers to sites indexes \mathbf{R} not to position in space \mathbf{r} .

denotes a lattice position. Hence the nonlocal part of the Ψ -functional is treated by keeping only the leading order in W , while the local part requires a nonperturbative treatment and can be calculated from an impurity model as in DMFT. This can be justified *a posteriori* by the observation [190] that (at least for systems whose physics is not too low dimensional [15, 173]) the self-energy diagrams of higher order in W give mainly a local contribution which advocates the use of DMFT, while for the nonlocal diagrams a leading order approximation, like the GW one is sufficient.

The specific form attributed to the functional $\Gamma^{GW+DMFT}[G, W]$ encodes two essential points of the method:

- (i) The minimization of the functional $\Gamma_{GW+DMFT}$ involves the functional derivatives of both Ψ_{GW} and Ψ_{AIM} . This implies that $GW+DMFT$ should be implemented using a self-consistency cycle (see below) that involves both GW and DMFT, i.e., the separated self-consistency of DMFT and GW alone, like one would have in a one-shot calculation, is, in principle, not sufficient. However, as we will see, very good results can be obtained also within non self-consistent calculations.
- (ii) Importantly, Ψ_{AIM} depends on both the Green's function and the screened Coulomb interaction. This implies that one does not only have to find a self-consistent Weiss field \mathcal{G}_{AIM} , see, e.g., Sec. 1.5, but also a self-consistent interaction \mathcal{U} that together with it defines the AIM. In other words, in $GW+DMFT$ the self-consistency requirement is extended also to a two-particle quantity, i.e., the local projection of the screened interaction, which is required to equal the impurity screened interaction [173].

Let us explicitly observe that for the AIM the "auxiliary interaction" \mathcal{U} and the auxiliary Weiss field \mathcal{G}_{AIM} play a similar role. As the Weiss field \mathcal{G}_{AIM} , also the auxiliary interaction \mathcal{U} will acquire a nontrivial frequency dependence due to the screening of the interaction operated by other electrons⁵. This is also at the origin of the absence of free parameters in the method: Once we have specified the bare Green's function and the bare (long range) Coulomb interaction V in real space the parameters to associate to the AIM are obtained self consistently.

2.1.2 $GW+DMFT$ self consistency from a diagrammatic point of view

We now turn our attention to the $GW+DMFT$ self-consistency cycle. Instead of following the functional approach we will rather focus on the Feynman diagrams, and the result will be the same if we take the right combination of diagrams for the self-energy and the polarization operator. Specifically, DMFT will give a nonperturbative solution for the *local* part of the self-energy and of the polarization, hence the best that one can do is to combine the local DMFT

⁵Possibly, not all the bands will be taken into account into the DMFT part of the calculations, since solving an AIM with $\mathcal{O}(10)$ bands is already technically very demanding. If it is the case only the bands close to the Fermi level will be described by DMFT, while all the others will be treated only at the GW level. In this case the frequency dependence of the interaction will account also for the screening of all the bands not treated in DMFT. [173]

self-energy and polarization (obtained solving an AIM), and the nonlocal GW self-energy and polarization. Doing so, the connection with the functional formalism [24] is clear considering the approximation described above for $\Psi_{GW+DMFT}$ and the diagrams that one can obtain by its derivation, equations (2.2) and (2.3). In the rest of the paragraph, we will mainly follow the lines of Ref. [63]. Let us also note here that, while the functional written in terms of \mathcal{G}_H , which incorporates the Hartree potential v_H , acquires a more symmetric form, in the following we find more clear treating explicitly the Hartree term. Before proceeding with the self-consistency scheme, it is necessary to specify a local basis set. Once this is specified, the quantities with which one has to deal, like, e.g., the Green's function or the Coulomb interaction, are matrices in orbital space and depend either on a set of discrete lattice vectors \mathbf{R} (or on a momentum vector \mathbf{k}). Their local projection, therefore, is well defined, e.g., the local component of the Green's function will be denoted by: $\mathbf{G}^{\mathbf{R}\mathbf{R}}$. The $GW+DMFT$ self-consistency cycle then consists of the following steps:

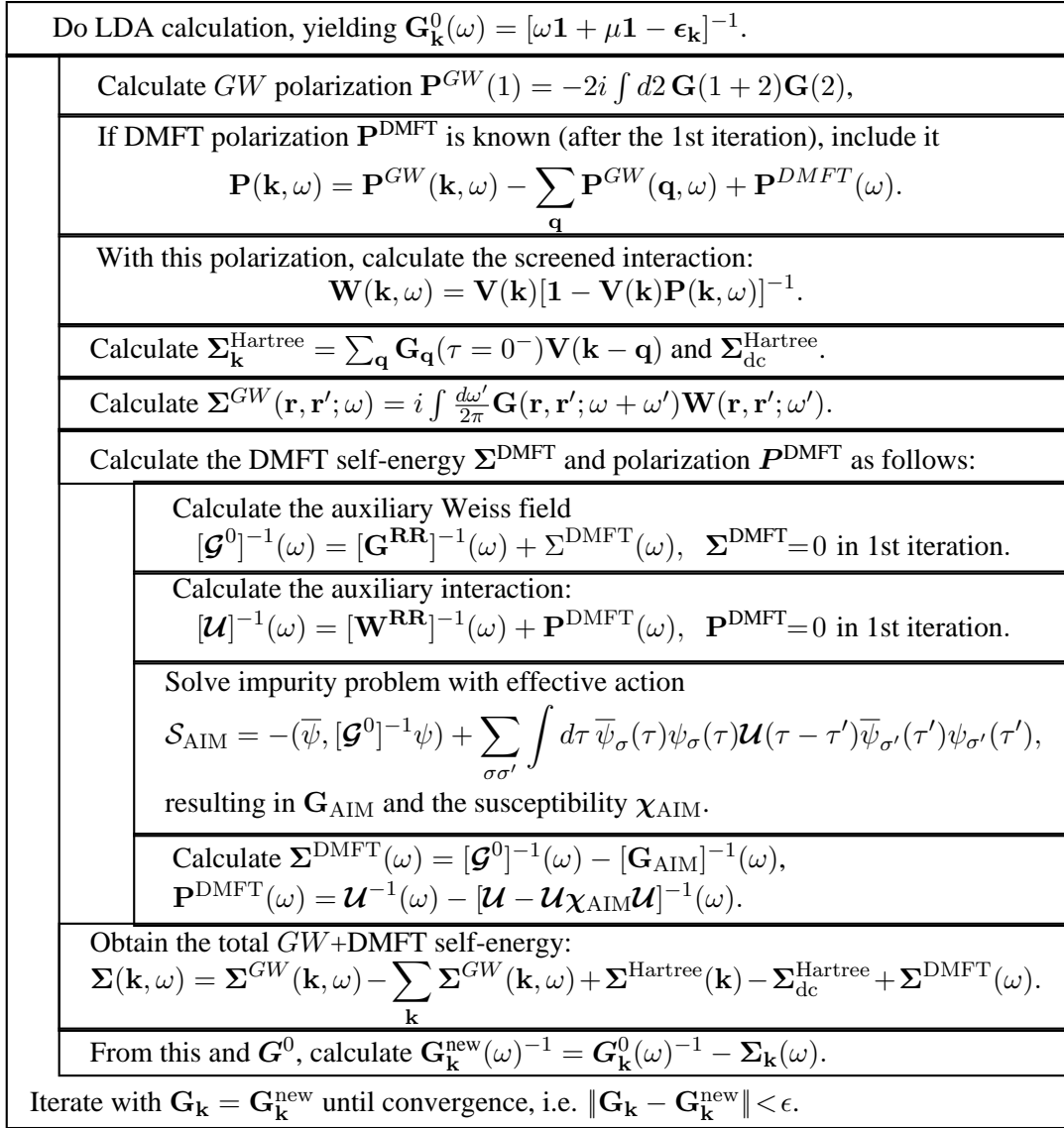


Figure 2.1: Flow diagram of the $GW+DMFT$ algorithm (adapted from [63]).

- (i) In most GW calculations, the starting point is a conventional density functional theory calculation, for example LDA, that yields a set of one-electron orbitals $|\phi_{\mathbf{k}}\rangle$ (bold symbols denote matrices in orbital space) and one-electron⁶ energies $\epsilon_{\mathbf{k}}$. Accordingly the Green's function can be computed as:

$$[\mathbf{G}^0]^{\text{RR}'}(\omega) = \frac{1}{N_k} \sum_{\mathbf{k}} e^{i\mathbf{k}(\mathbf{R}-\mathbf{R}')} [\omega\mathbf{1} + \mu\mathbf{1} - \epsilon_{\mathbf{k}}]^{-1}, \quad (2.4)$$

with μ being the chemical potential, and N_k the number of \mathbf{k} -points used for the sum. In the first step, when no self-energy from $GW+DMFT$ is known, this LDA Green's function

⁶We remind that the interpretation of the eigenvalues of the Kohn-Sham equation as one-particle energies does not have a strong theoretical justification, see Sec. 1.2.

is directly used in step (ii) as interacting Green's function.

- (ii) Knowing the Green's function, one can calculate the GW polarization:

$$\mathbf{P}^{GW}(1) = -2i \int d2 \mathbf{G}(1+2)\mathbf{G}(2). \quad (2.5)$$

Here, as in Sec. 1.3, to simplify the notation we use $1 \equiv (\mathbf{k}_1, \omega)$ and the integral is intended over a frequency and momentum variable. The factor two in the equation above corresponds to the spin summation.

- (iii) From the polarization operator, in turn, the local polarization has to be subtracted since this can (and has to) be calculated more precisely within DMFT, including also a local vertex correction. Mathematically this reads:

$$\mathbf{P}(\mathbf{k}, \omega) = \mathbf{P}^{GW}(\mathbf{k}, \omega) - \sum_{\mathbf{q}} \mathbf{P}^{GW}(\mathbf{q}, \omega) + \mathbf{P}^{DMFT}(\omega). \quad (2.6)$$

- (iv) Next, the screened interaction \mathbf{W} is calculated from the bare Coulomb interaction and the overall polarization operator:

$$\mathbf{W}(\mathbf{k}, \omega) = \frac{\mathbf{V}(\mathbf{k})}{\mathbf{1} - \mathbf{V}(\mathbf{k})\mathbf{P}(\mathbf{k}, \omega)}. \quad (2.7)$$

$\mathbf{V}(\mathbf{k})$ and $\mathbf{W}(\mathbf{k}, \omega)$ are the bare and screened Coulomb interaction projected onto the local basis. For example the bare interaction matrix reads:

$$\mathbf{V}_{ijkl}^{\mathbf{R}\mathbf{R}'} \equiv \langle \phi_i^{\mathbf{R}} \phi_j^{\mathbf{R}'} | V | \phi_k^{\mathbf{R}} \phi_l^{\mathbf{R}'} \rangle, \quad (2.8)$$

with i, j, k and l being the orbital indexes. The frequency dependence of the screened interaction thus arises from the one of the polarization.

- (v) Now, we are in the position to calculate the GW self-energy. The first term is the Hartree diagram,⁷ which can be calculated straightforwardly in imaginary time τ , yielding Σ^{Hartree} :

$$\Sigma_{\mathbf{k}}^{\text{Hartree}} = \sum_{\mathbf{q}} \mathbf{G}_{\mathbf{q}}(\tau = 0^-) \mathbf{V}(\mathbf{k} - \mathbf{q}), \quad (2.9)$$

and the corresponding local contribution $\Sigma_{\text{dc}}^{\text{Hartree}}$, which we need to subtract later to avoid a double counting as it is also contained in the DMFT.

- (vi) The second term of the GW self-energy corresponds to the exchange diagram⁸ (with full Green's function and screened interaction):

$$\Sigma^{GW}(\mathbf{r}, \mathbf{r}'; \omega) = i \int \frac{d\omega'}{2\pi} \mathbf{G}(\mathbf{r}, \mathbf{r}'; \omega + \omega') \mathbf{W}(\mathbf{r}, \mathbf{r}'; \omega'). \quad (2.10)$$

⁷Let us note explicitly that in several cases the Hartree term is directly included in the bare Green's function, like, e.g., in Ref. [24].

⁸For illustrative reasons, we give here the expression of the self-energy as a function of the position vectors \mathbf{r} and \mathbf{r}' . However to make use of this self-energy in a $GW+DMFT$ scheme, one needs to project this self-energy on some basis set. For more details we refer to the literature, e.g., Ref. [165] Eq. (10) for a complete expression of the self-energy on a specific basis set, and Ref. [12] for a more thorough discussion about the basis sets in numerical implementations of GW .

- (vii) The *GW* self-energy and polarization operator obtained this way have to be supplemented by the corresponding DMFT local ones calculated from an appropriate auxiliary AIM. The latter is defined by an auxiliary propagator (Weiss field) $\mathcal{G}^0(\omega)$, as well by an auxiliary interaction $\mathcal{U}(\omega)$. With these two quantities, the action of the auxiliary AIM reads:

$$\mathcal{S}_{\text{AIM}} = -\frac{1}{\beta} \sum_{\omega_n \sigma} \bar{\psi}_\sigma(i\omega_n) [\mathcal{G}_\sigma^0]^{-1}(i\omega_n) \psi_\sigma(\omega) + \sum_{\sigma \sigma'} \int d\tau \bar{\psi}_\sigma(\tau) \psi_\sigma(\tau) \mathcal{U}(\tau - \tau') \bar{\psi}_{\sigma'}(\tau') \psi_{\sigma'}(\tau'), \quad (2.11)$$

where we have omitted a summation over the band indexes.

- (viii) The Weiss field \mathcal{G}^0 can be obtained by asking that, at self-consistency, the local Green's function of the lattice equals the Green's function of the AIM:

$$[\mathcal{G}^0]^{-1}(\omega) = [\mathbf{G}^{\text{RR}}]^{-1}(\omega) + \Sigma^{\text{DMFT}}(\omega). \quad (2.12)$$

In the first iteration, when no previous self-energy from the solution of an AIM is available one can assume $\Sigma^{\text{DMFT}} = 0$. This equation is almost identical to the one that gives the Weiss field in DMFT, Eq. (1.125). However it should be noted that in Eq. (2.12) the local Green's function of the lattice is dressed by a *k-dependent self-energy*, see step (xii), and not by the local one of the AIM alone, as in DMFT.

- (ix) In a completely parallel fashion one can obtain the auxiliary interaction $\mathcal{U}(\omega)$:

$$[\mathcal{U}]^{-1}(\omega) = [\mathbf{W}^{\text{RR}}]^{-1}(\omega) + \mathbf{P}^{\text{DMFT}}(\omega). \quad (2.13)$$

Here the local screening is removed from the interaction since it will be again included by DMFT. In Eq. (2.13) the polarization of the auxiliary AIM clearly plays the same role as the self-energy Σ^{DMFT} in the equation for the bare Green's function \mathcal{G}^0 , Eq. (2.12).

- (x) Once the action of the AIM (2.11) has been completely defined it has to be solved for its interacting Green's function \mathbf{G}_{AIM} and two-particle charge susceptibility χ_{AIM} . This step, performed with an impurity solver, is probably one of the most demanding from the computational point of view, together with⁹ the calculation of the frequency dependent polarization and self-energy in *GW*.

- (xi) From \mathbf{G}_{AIM} and χ_{AIM} one can compute the new self-energy and polarization operator respectively:

$$\Sigma^{\text{DMFT}}(\omega) = [\mathcal{G}^0]^{-1}(\omega) - [\mathbf{G}_{\text{AIM}}]^{-1}(\omega), \quad (2.14)$$

$$\mathbf{P}^{\text{DMFT}}(\omega) = \mathcal{U}^{-1}(\omega) - [\mathcal{U} - \mathcal{U} \chi_{\text{AIM}} \mathcal{U}]^{-1}(\omega). \quad (2.15)$$

The steps from (vii) to (xi) are the ones that explicitly involve an impurity action, and therefore form the "DMFT block" of the self-consistency cycle.

⁹At the model level the solution of the AIM is for sure more involved than the *GW* part. In real material, instead, since for convergency reasons one can not restrict oneself to a few bands in the *GW*, its computational cost is comparable with that of the impurity solver.

- (xii) After having obtained the new self-energy of the AIM we are in the position to sum all the terms contributing to the $GW+DMFT$ self-energy: The local one from the AIM, and the nonlocal Hartree and exchange:

$$\Sigma^{GW+DMFT}(\mathbf{k}, \omega) = \Sigma^{GW}(\mathbf{k}, \omega) - \sum_{\mathbf{k}} \Sigma^{GW}(\mathbf{k}, \omega) + \Sigma^{\text{Hartree}}(\mathbf{k}) - \Sigma_{\text{dc}}^{\text{Hartree}} + \Sigma^{\text{DMFT}}(\omega). \quad (2.16)$$

- (xiii) The new Green's function to be used in the next step is calculated using the Dyson equation with the self-energy just obtained:

$$[\mathbf{G}_{\mathbf{k}}^{\text{new}}]^{-1}(\omega) = [\mathbf{G}_{\mathbf{k}}^0]^{-1}(\omega) - \Sigma^{GW+DMFT}(\mathbf{k}, \omega). \quad (2.17)$$

- (xiv) The new Green's function is used to start a new iteration of the self-consistency cycle, starting from step (ii). The self consistency is eventually reached when the Green's function from the new iteration equals the one from the previous iteration.

A critical point is the physical meaning of the auxiliary interaction of the AIM. In particular, it can be considered a "*bare interaction*" with respect to the AIM, in complete analogy with the definition of the bare Green's \mathcal{G}^0 : If the interaction was decoupled via an Hubbard-Stratonovich transformation, \mathcal{U} would appear as the bare propagator for the bosons that decouple the interaction. However, exactly as the Weiss field carries information about the hopping from and to neighboring sites, the interaction \mathcal{U} contains information about the *nonlocal* screening to the interaction, as can be seen considering equations (2.6), (2.7) and (2.13). The point here is made even more subtle considering that there can be bands which take part to the screening of the Coulomb interaction that are usually neglected in the DMFT part of the calculation, in a so-called *orbital-separated scheme* [173]. Therefore the screening from these bands¹⁰ needs to be taken into account in \mathcal{U} , which, hence, from the point of view of the lattice is far from being bare. Altogether equations (2.12) and (2.13) can be viewed [24] as a **representability** assumption, i.e., one is asking that the local components of \mathbf{G} and \mathbf{W} are equal to the ones obtained by the auxiliary action (2.11) once a suitable choice for the auxiliary Weiss field \mathcal{G}^0 and auxiliary interaction \mathcal{U} is made. This choice is not known a priori and one has to resort to the self-consistency cycle to find the right auxiliary AIM. The flow diagram in Fig. 2.1 already shows that the $GW+DMFT$ approach is much more involved¹¹ than LDA+DMFT. However, it has the advantage that, at self consistency, there is no double counting problem, since the LDA enters only in the first step, and also the Coulomb interaction is calculated *ab initio* in a well defined and controlled way. Hence, no *ad hoc* formulas or parameters need to be introduced or adjusted.

It has to be noted that in the flow diagram that we have presented we did not discuss the important point of the appropriate choice of the basis set. This is nontrivial: The DMFT, as

¹⁰This screening is done at the RPA level: The polarization coming from bands neglected in DMFT is computed by Eq. (2.6) and takes part to the screening of \mathbf{W} . For more details about this point see Ref. [173], Sec. II C.

¹¹For a comparison of the flow diagrams of the two approaches compare, e.g., Fig. 11 and Fig. 15 of Ref. [60].

mentioned above, requires a *local* basis set that describes the narrow d or f orbitals, which are expected to be the most strongly correlated orbitals. On the other hand the GW is naturally formulated in real or k space and is presently implemented, e.g., in LMTO [12] or projector augmented wave (PAW) basis [165]. The switching between these two representations is non trivial. It can be done by a downfolding [7] or by a projection onto Wannier orbitals, e.g., using maximally localized Wannier orbitals [111, 125] or a simpler projection onto the d (or f) part of the wave function within the atomic spheres [2, 9]. On the DMFT side, the biggest open challenges are to actually perform the DMFT calculations with a frequency dependent Coulomb interaction $\mathcal{U}(\omega)$ and to calculate the DMFT charge susceptibility or polarization operator. In particular DMFT calculations with a frequency dependent \mathcal{U} interaction have been only recently tested at the model level [15, 16, 54, 76], and on top of an LDA calculation for BaFe_2As_2 [182] and SrVO_3 [31] (other calculations with a frequency dependent interaction, but in a $GW+DMFT$ context are listed below).

A measure of the difficulty of the implementation of the $GW+DMFT$ method can be given comparing the number of realistic calculations for materials performed using this method with the number of material calculations in LDA+DMFT: While the latter, during the last ten years, is of the order of a few hundreds, only a few materials calculations are reported within $GW+DMFT$, in particular one for Ni [24], some for SrVO_3 [155, 170, 173, 174], and one for adatom systems [58], in none of which a full self consistency has been achieved. Following these consideration, if one wants to make further progress in realistic calculations for materials using $GW+DMFT$ at a reasonable computational cost it is necessary to proceed with further approximations.

In the following paragraph we present one possible approximation that allows to combine some aspects of GW with the DMFT at a computational cost comparable with the one of LDA+DMFT. This approach makes use of a **quasiparticle** approximation (qp) to the self-energy, see Sec. 1.3.3, and is therefore named qp $GW+DMFT$. The quality of the approximation will be demonstrated for the correlated metal SrVO_3 , and compared to the results obtained in LDA+DMFT [116, 135, 136, 140, 163] as well to those of photoemission spectroscopy [163]. We find the qp $GW+DMFT$ spectra to be quite similar to the LDA+DMFT ones due to a partial cancellation of two effects: The reduced GW bandwidth in comparison to LDA and the weaker screened Coulomb interaction. An important difference, however, is in the position of the lower Hubbard band, which in qp $GW+DMFT$ agrees better with the experiments. Importantly, the quasiparticle approximation to the self-energy neglects the effects of frequency dependence of the self-energy, and therefore a consistent approximation to the Coulomb interaction has to be assumed, i.e., we take a *static* approximation also for the Coulomb interaction. This is also clear by performing a calculation including a \mathcal{Z}_B factor, introduced by Casula *et al.* in Ref. [30], to mimic the frequency dependence of the calculation. The results obtained this way are quite different from the ones of qp $GW+DMFT$ without \mathcal{Z}_B factor, and are in worse agreement with the spectroscopy experiments. To further understand this and the role of the frequency dependence of the interaction (and self-energy) we will compare our results to the ones obtained with the computationally more expensive $GW+DMFT$ implementation of Refs. [173, 174], in which the

frequency dependent of the self-energy and of the interaction is fully taken into account.

2.1.3 $qpGW$ implementation in VASP

Let us briefly outline the relevant methodological aspects. The starting point of our calculation is the GW implementation within (VASP) [165]. Specifically, we first performed Kohn Sham density functional theory calculations using the local density approximation for $SrVO_3$ at the LDA lattice constant of $a = 3.78 \text{ \AA}$ and determined the Kohn Sham one-electron orbitals $|\phi_{n\mathbf{k}}\rangle$ and one-electron energies $\epsilon_{n\mathbf{k}}$. The position of the GW quasiparticle peaks $E_{n\mathbf{k}}^{QP}$ were calculated by solving the linear equation

$$E_{n\mathbf{k}}^{QP} = \epsilon_{n\mathbf{k}} + Z_{n\mathbf{k}} \times \text{Re}[\langle \phi_{n\mathbf{k}} | T + v_c + v_H + \Sigma^{GW}(\mathbf{k}, \omega = \epsilon_{n\mathbf{k}}) | \phi_{n\mathbf{k}} \rangle - \epsilon_{n\mathbf{k}}], \quad (2.18)$$

where T is the one-electron kinetic energy operator and v_c and v_H are the crystal potential and the Hartree-potential, respectively. Σ^{GW} is the G_0W_0 self-energy, and $Z_{n\mathbf{k}}$ is the renormalization factor evaluated at the Kohn-Sham eigenvalues [80, 165], see below. The original Kohn Sham orbitals are maintained at this step.

Equation (2.18) can be obtained after a linearization of the self-energy around the LDA single particle energies:

$$\Sigma^{GW}(\mathbf{k}, E_{n\mathbf{k}}^{QP}) \approx \Sigma^{GW}(\mathbf{k}, \omega = \epsilon_{n\mathbf{k}}) + \underbrace{\frac{\partial \Sigma^{GW}(\mathbf{k}, \omega)}{\partial \omega} \Big|_{\omega = \epsilon_{n\mathbf{k}}}}_{\equiv \xi_{n\mathbf{k}}} (E_{n\mathbf{k}}^{QP} - \epsilon_{n\mathbf{k}}). \quad (2.19)$$

Since the off-diagonal components of the self-energy are small, we concentrate on the diagonal components only. This yields the following equation for the quasiparticle poles:

$$E_{n\mathbf{k}}^{QP} \langle \phi_{n\mathbf{k}} | 1 - \xi_{n\mathbf{k}} | \phi_{n\mathbf{k}} \rangle = \langle \phi_{n\mathbf{k}} | T + v_c + v_H + \Sigma(\mathbf{k}, \epsilon_{n\mathbf{k}}) - \xi_{n\mathbf{k}} \epsilon_{n\mathbf{k}} | \phi_{n\mathbf{k}} \rangle, \quad (2.20)$$

which is exactly equation (2.18) once the quasiparticle renormalization factor $Z_{n\mathbf{k}}$ is expressed in terms of the derivative of the self-energy:

$$Z_{n\mathbf{k}} = (1 - \xi_{n\mathbf{k}})^{-1}. \quad (2.21)$$

The Kohn Sham orbitals expressed in the projector augmented wave (PAW) basis are then projected onto maximally localized Wannier functions [125] using the Wannier90 code [132]. To construct an effective low-energy Hamiltonian for the t_{2g} vanadium orbitals, we follow Faleev, van Schilfgaarde and Kotani and approximate the frequency dependent G_0W_0 self-energy by an Hermitian operator \bar{H} that reproduces the position of the quasiparticle peaks of the original self-energy exactly [33, 42]:

$$\bar{H}_{mn,\mathbf{k}} = \frac{1}{2} [\langle \phi_{m\mathbf{k}} | \Sigma^*(\mathbf{k}, E_{m\mathbf{k}}^{QP}) + \Sigma(\mathbf{k}, E_{n\mathbf{k}}^{QP}) | \phi_{n\mathbf{k}} \rangle]. \quad (2.22)$$

This approximation is commonly used in GW calculations, in particular for self-consistent calculations, since fully frequency dependent calculations are computationally very demanding.

In practice, for the present calculations, we have applied the slightly more involved procedure to derive an Hermitian approximation outlined in Ref. [166], although this yields essentially an almost identical Hermitian operator $\bar{H}_{mn,\mathbf{k}}$. Furthermore, the off diagonal components are found to be negligibly small, also in the Wannier basis, and henceforth disregarded. The final Hermitian and \mathbf{k} -point dependent operator \bar{H} is transformed to the Wannier basis and passed on to the DMFT code, where it is used to construct the \mathbf{k} -dependent self-energy by adding the local DMFT self-energy.

This qp*GW*+DMFT procedure allows to maintain the structure and outline of the common DFT-DMFT scheme and can be easily adopted in any DMFT code. Instead of the LDA one-electron matrix elements, the qp*GW* ones are passed to the DMFT. To avoid a double counting of the local part of the qp*GW* Hermitian operator we have to subtract it. In the case of the degenerate t_{2g} orbitals the double counting correction basically yields only a constant shift. The double counting correction can be performed in the following way. What we have to do is subtracting the local part of all qp*GW* self-energy contributions. i.e., the local part of the (i) $\Sigma(\mathbf{k}, \epsilon_{n\mathbf{k}})$, (ii) $\xi_{n\mathbf{k}}$ and (iii) $\xi_{n\mathbf{k}}\epsilon_{n\mathbf{k}}$ terms in equation (2.20). We define their local part as the one-center $\mathbf{R} = 0$ component of the Wannier representation:

$$\bar{A}_{ij} = \frac{1}{N_k} \sum_{n\mathbf{k}} U_{ni}^{*(\mathbf{k})} A_n(\mathbf{k}) U_{jn}^{(\mathbf{k})}. \quad (2.23)$$

where N_k is the number of \mathbf{k} -points and $U_{ni}^{(\mathbf{k})}$ the unitary matrix for the transformation of Bloch vectors $|\phi_{n\mathbf{k}}\rangle$ to Wannier states $|w_{i0}\rangle$. For $A_n(\mathbf{k}) = \Sigma(\mathbf{k}, \epsilon_{n\mathbf{k}})$, $\xi_{n\mathbf{k}}$, and $\xi_{n\mathbf{k}}\epsilon_{n\mathbf{k}}$ these averages are computed, transformed back to the Bloch basis using again $U_{ni}^{(\mathbf{k})}$ and subtracted in Eq. (2.20). With the local part subtracted, Eq. (2.20) becomes

$$E_{n\mathbf{k}}^{\text{qp-nl}} \langle \phi_{n\mathbf{k}} | 1 - \xi_{n\mathbf{k}} + \bar{\xi}_n | \phi_{n\mathbf{k}} \rangle = \langle \phi_{n\mathbf{k}} | T + v_c + v_H + \Sigma(\mathbf{k}, \epsilon_{n\mathbf{k}}) - \bar{\Sigma}_n - \xi_{n\mathbf{k}}\epsilon_{n\mathbf{k}} + \bar{\xi}_n \epsilon_n | \phi_{n\mathbf{k}} \rangle. \quad (2.24)$$

This yields the bandstructure without local quasiparticle self-energy contributions. The Hamiltonian corresponding to this bandstructure is subsequently transformed again to the Wannier basis and passed to the DMFT. Let us emphasize that this local part of the *quasiparticle GW* self-energy is very different from the local part of a frequency-dependent full *GW* self-energy. In the latter case, we naturally obtain also a frequency-dependent local part $\Sigma_{\text{loc}}^{\text{GW}} = \sum_{\mathbf{k}} \Sigma(\mathbf{k}, \omega)$. In our case of the quasiparticle linearization of the *GW* self-energy [Eq. (2.20)], we obtain three frequency-independent terms stemming from the constant $[\bar{\Sigma}_n]$ and linear terms $[\bar{\xi}_n]$ and $[\bar{\xi}_n \epsilon_n^0]$ in Eq. (2.20), respectively. This is consistent with the qp*GW* approximation. Let us note though that doing (i) the qp approximation and (ii) subtracting the local part does not commute. For a comparison with the double-counting correction in approximations that maintain the frequency dependence of the self-energy see Refs. [173, 174].

This procedure neglects lifetime broadening and any frequency dependence of the *GW* self-energy beyond its linear part. Let us also note that hitherto we did not perform self-consistency on the *GW* part. *The GW part of the calculation has been performed by Merzuk Kaltak, in the group of Georg Kresse at the University of Vienna.*

Fig. 2.3 shows the obtained G_0W_0 bandstructure, which for the t_{2g} vanadium target bands is about 0.7 eV narrower than for the LDA. The oxygen p band (below -2 eV) is shifted downwards by 0.5 eV compared to the LDA, whereas the vanadium e_g bands (located about 1.5 eV above the Fermi-level) are slightly shifted upwards by 0.2 eV. In the LDA, the top most vanadium t_{2g} band at the M point is slightly above the lowest e_g band at the Γ point, whereas the G_0W_0 correction opens a gap between the t_{2g} and e_g states.

Within this Wannier basis, we also calculate the screened Coulomb interaction using the random phase approximation (RPA). As described in Ref. [137], for an accurate estimate of the interaction value to be used in DMFT (U^{DMFT}), only the local screening processes of the t_{2g} target bands of SrVO_3 are disregarded since only these are considered later on in DMFT. This approach [137] is similar to the constrained RPA (cRPA), with the difference being that in cRPA also *non-local* screening processes of the t_{2g} target bands are disregarded which are not included in DMFT. Depending on the material and doping level, there might be a difference between U^{DMFT} and U^{cRPA} . However, for the case of SrVO_3 , this difference is very minor, and we hence only consider U^{DMFT} in the following.

Here some remarks are in order. First, we explicitly note that the value U^{DMFT} corresponds to the **static** value of the interaction: $U^{\text{DMFT}} = U^{\text{DMFT}}(\omega = 0)$, i.e., the frequency dependence of the interaction, arising from the RPA polarization, is neglected. This assumption is justified considering that we are also neglecting the frequency dependence of the GW self-energy, as we are also going to show mimicking the frequency dependence of the interaction using the \mathcal{Z}_B factor. Second, we observe that quite counterintuitively U^{DMFT} turns out to be slightly larger than U^{cRPA} , in spite of the fact that the nonlocal contribution to the polarization is allowed to screen the interaction in U^{DMFT} and not in U^{cRPA} . This effect has been attributed [137] to Friedel oscillations of the nonlocal polarization, which also strongly depends on the filling of the system: While for lower fillings (of the t_{2g} manifold) the nonlocal screening effects is *negative*, i.e., it increases the value of the interaction instead of decreasing it, for higher filling the nonlocal screening effect becomes *positive*.

In Fig. 2.2 we show¹² the frequency dependence of the cRPA interaction U (in our notation U^{cRPA}) compared to the local part of the fully RPA screened interaction W . The latter is computed allowing *all* bands (including the t_{2g} ones) to screen the interaction through the RPA polarization (it corresponds to the W defined in the paragraphs above if we assume $\mathbf{P} = \mathbf{P}^{GW}$ for the local and nonlocal part). We can distinguish three different regimes for the frequency dependence of U (and W): (i) a first regime for $\omega \lesssim 15\text{eV}$, (ii) a second regime for $15\text{eV} \lesssim \omega \lesssim 35\text{eV}$, and a third regime for ω larger than 35eV. In the first region (i) the interaction U^{cRPA} stays more or less constant. From a comparison with W it is clear that U^{cRPA} is flat because the particle-hole excitations in the t_{2g} bands have been suppressed. In the second region (ii) W and U^{cRPA} are very close, and show a dramatic frequency dependence around $\omega \sim 15\text{eV}$, corresponding to the plasma frequency of the system [4, 119]. In the third region (iii) the screening is rather ineffective and the value of the screened interactions is close to the

¹²The data are provided by J. M. Tomczak, see also [173].

bare one. If there was no region (i) in which the interaction stays more or less constant it would appear hard to justify at all a calculation with a static $\omega = 0$ calculation.

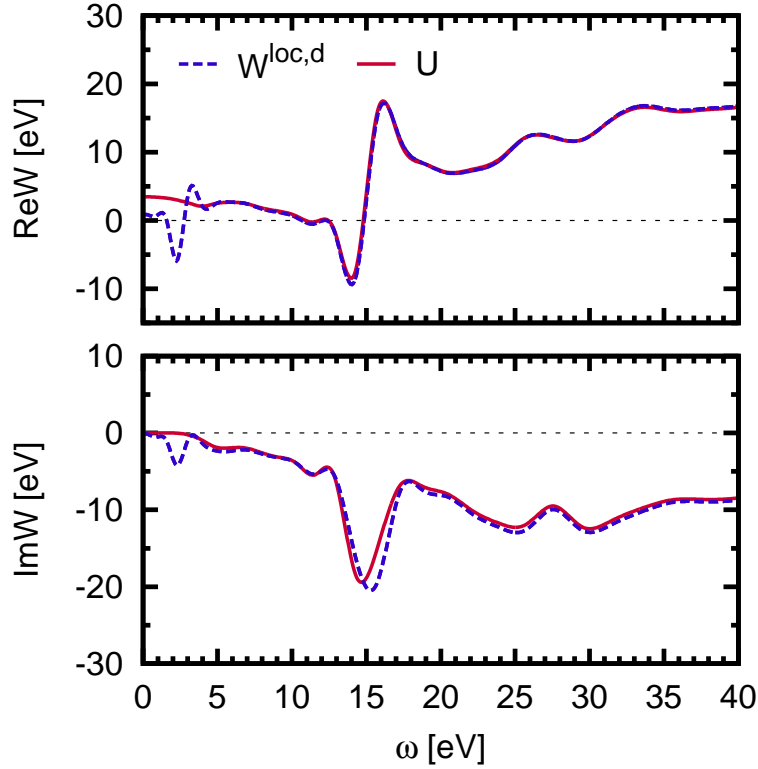


Figure 2.2: Frequency dependence of the real and imaginary part of the fully screened RPA interaction $W(\omega)$ and of the cRPA interaction $U(\omega)$ for SrVO_3 . For the latter, the t_{2g} bands are not contributing to the screening. One can see that at low frequencies W exhibits a nontrivial frequency dependence, attributed to particle-hole processes taking place in the vicinity of the Fermi level. On the other hand U stays more or less flat up to $\omega \approx 15\text{eV}$, corresponding to the plasmon frequency of the system. For larger frequencies the screening is not effective anymore, and the two interaction converge to the unscreened value $V \approx \mathcal{O}(20\text{eV})$. The data have been provided by J. M. Tomczak [174].

With our calculations, we carefully compare qp*GW*+DMFT with LDA+DMFT and experimental results. In both cases, we use (frequency-independent) interactions obtained from this locally unscreened RPA and cLDA. The Kanamori interaction parameters as derived from the locally unscreened RPA are: intra-orbital Coulomb repulsion $U^{\text{DMFT}} = 3.44\text{eV}$; inter-orbital Coulomb repulsion $\bar{U}^{\text{DMFT}} = 2.49\text{eV}$; Hund's exchange and pair hopping amplitude $J^{\text{DMFT}} = 0.46\text{eV}$. These values are, for SrVO_3 , almost identical¹³ to the cRPA [137]. In

¹³Note that the values differ slightly from the VASP values published in Ref. [137] since with additional data, we have further improved the extrapolation.

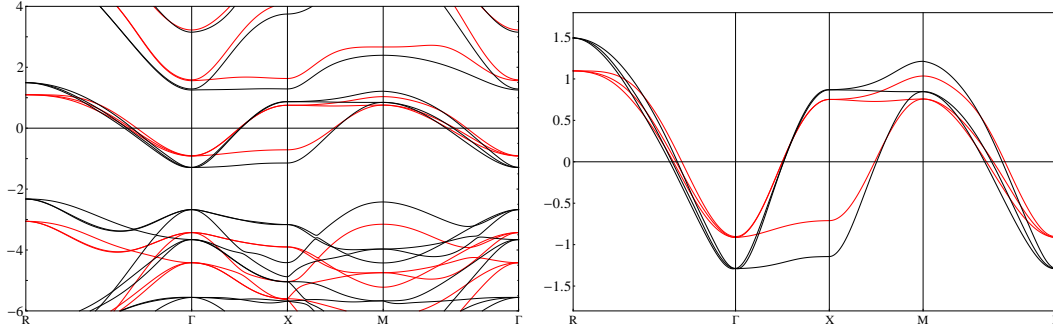


Figure 2.3: (Color online) Upper panel: G_0W_0 quasiparticle bands (red, grey) in comparison to LDA (black). The Fermi level sets our zero of energy and is marked as a line. Lower panel: Wannier projected t_{2g} bandstructure from G_0W_0 (red, grey) and LDA (black). The t_{2g} target bands bandwidth is reduced by ~ 0.7 eV in GW .

cLDA, on the other hand, somewhat larger interaction parameters were obtained and are employed by us¹⁴ for the corresponding calculations: $U^{\text{cLDA}} = 5.05$ eV, $\bar{U}^{\text{cLDA}} = 3.55$ eV, $J^{\text{cLDA}} = 0.75$ eV [163].

For the subsequent DMFT calculation, we employ the Würzburg-Wien w2dynamics code [139], based on the hybridization-expansion variant [183] of the continuous-time quantum Monte Carlo method (CT-QMC) [153]. This algorithm is particularly fast since it employs additional quantum numbers for a rotationally-invariant Kanamori interaction [139]. The maximum entropy method is employed for the analytical continuation of the imaginary time and (Matsubara) frequency CT-QMC data to real frequencies [88].

All our calculations are without self-consistency, which is to some extent justified for SrVO_3 : Since the three t_{2g} bands of SrVO_3 are degenerate, DMFT does not change the charge density of the low-energy t_{2g} manifold and hence self-consistency effects are expected to be small within LDA+DMFT. This is, in principle, different for $GW+DMFT$. Here, the frequency dependence of the DMFT self-energy might yield some feedback already for a simplified Faleev, van Schilfgaarde and Kotani quasiparticle self-consistency [33, 42]. Finally, as anticipated above, we also test the \mathcal{Z}_B -factor renormalized GW bandwidth with $\mathcal{Z}_B = 0.7$ obtained in [30] for mimicking the frequency dependence of the cRPA interaction.

Results for SrVO_3

For analyzing the differences between qp $GW+DMFT$ and LDA+DMFT we analyze and compare five different calculations in the following:

1. LDA+DMFT@ \bar{U}^{cLDA} (conventional LDA+DMFT calculation with the cLDA interaction $\bar{U}^{\text{cLDA}} = 3.55$ eV),

¹⁴Note, that cLDA tends to overestimate the Hund's exchange J , see [60], so that in subsequent LDA+DMFT calculations smaller values of J have been employed [186] For the d^1 system SrVO_3 this smaller value of J mainly influences the upper Hubbard band.

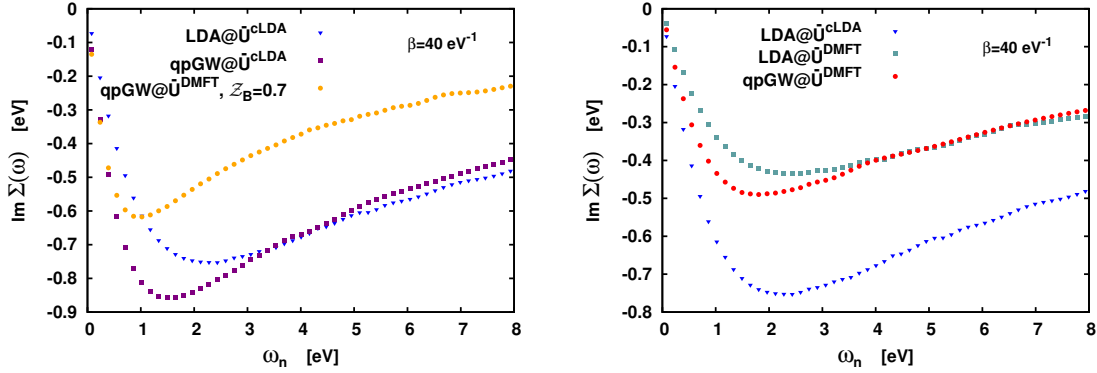


Figure 2.4: Comparison of the imaginary part of the DMFT t_{2g} self energies Σ vs. (Matsubara) frequency ω for SrVO₃ at inverse temperature $\beta = 40 \text{ eV}^{-1}$ as computed in five different ways: employing qp*GW* and LDA Wannier bands, the locally unscreened RPA interaction $\bar{U}^{\text{DMFT}} = 2.49 \text{ eV}$ and the cLDA $\bar{U}^{\text{cLDA}} = 3.55 \text{ eV}$, as well as the $Z_B = 0.7$ renormalization [30].

2. LDA+DMFT@ \bar{U}^{DMFT} (LDA+DMFT calculation but with the locally unscreened RPA interaction $\bar{U}^{\text{DMFT}} = 2.49 \text{ eV}$),
3. qp*GW*+DMFT@ \bar{U}^{DMFT} (qp*GW*+DMFT calculation with $\bar{U}^{\text{DMFT}} = 2.49 \text{ eV}$),
4. qp*GW*+DMFT@ \bar{U}^{cLDA} (qp*GW*+DMFT calculation but with $\bar{U}^{\text{cLDA}} = 3.55 \text{ eV}$),
5. qp*GW*+DMFT@ \bar{U}^{DMFT} , $Z_B = 0.7$ (as 3. but with a Bose renormalization factor Z_B).

Let us first turn to the imaginary part of the local self-energy which is shown as a function of (Matsubara) frequency in Fig. 2.4. The self-energy yields a first impression of how strong the electronic correlations are in the various calculations. This, in Matsubara frequency space, can be inferred from the imaginary part of the self-energy for the first few Matsubara frequencies, which (for a metallic solution) carries the information about the renormalization factor and the quasiparticle lifetime, and therefore contain the most relevant information about the electronic correlations. The high frequency tail of the self-energy, on the other hand, decays like $\lim_{\omega_n \rightarrow \infty} \Sigma(i\omega_n) = -U^2(n-1)n/\omega_n$, where n is the occupation of each band, which, in the case of SrVO₃, due to the degeneracy of the t_{2g} bands, is fixed. Therefore the high energy tails of the self-energy carry only the trivial information about the value of the interaction used in the calculations, and only very little message about the correlations, hence comparing the self-energy of the different calculations one should mainly focus on the low frequency part, and in particular its slope. The LDA+DMFT@ \bar{U}^{DMFT} self-energy is the least correlated one, somewhat less correlated than LDA+DMFT@ \bar{U}^{cLDA} due to the smaller locally unscreened Coulomb interaction ($\bar{U}^{\text{DMFT}} = 2.49 \text{ eV} < 3.55 \text{ eV} = \bar{U}^{\text{cLDA}}$). For the same reason also the qp*GW*+DMFT@ \bar{U}^{DMFT} self-energy is less correlated than that of a qp*GW*+DMFT@ \bar{U}^{cLDA} calculation.

Scheme	Z	d_{intra}	$d_{\text{inter}}^{\uparrow\uparrow}$	$d_{\text{inter}}^{\uparrow\downarrow}$
LDA+DMFT@ \bar{U}^{cLDA}	0.51	0.004	0.013	0.009
LDA+DMFT@ \bar{U}^{DMFT}	0.67	0.007	0.016	0.013
qp $GW+DMFT$ @ \bar{U}^{DMFT}	0.57	0.005	0.014	0.010
qp $GW+DMFT$ @ \bar{U}^{cLDA}	0.39	0.003	0.010	0.007
qp $GW+DMFT$ @ $\bar{U}^{\text{DMFT}}, \mathcal{Z}_B=0.7$	0.36	0.003	0.009	0.006
experiment [124, 163, 168]	$\sim 0.5-0.6$			

Table 2.1: DMFT quasiparticle renormalization factors Z from the five different calculations at inverse temperature $\beta = 40 \text{ eV}^{-1}$. Also shown are the pairwise double occupations within the same orbital d_{intra} and between different orbitals with the same $d_{\text{inter}}^{\uparrow\uparrow}$ and opposite spin $d_{\text{inter}}^{\uparrow\downarrow}$. The ‘‘standard’’ LDA+DMFT@ \bar{U}^{cLDA} and qp $GW+DMFT$ @ \bar{U}^{DMFT} calculations are similarly correlated and well agree with experiment. Using the cLDA interaction (\bar{U}^{cLDA}) for qp $GW+DMFT$ or the locally unscreened RPA (\bar{U}^{DMFT}) for LDA+DMFT yields a too strongly and too weakly correlated solution in comparison to experiment, respectively. Note that qp $GW+DMFT$ becomes even more strongly correlated, if the Bose renormalization factor is included.

If we compare LDA+DMFT and qp $GW+DMFT$ on the other hand, the LDA+DMFT self-energy is less correlated than the qp $GW+DMFT$ one, if the Coulomb interaction is kept the same. This is due to the 0.7 eV smaller GW t_{2g} -bandwidth in comparison to LDA. This observation also reflects in the DMFT quasiparticle renormalization factors Z , which were obtained from a fourth-order fit to the lowest four Matsubara frequencies, see Table 2.1. In other words, GW self-energy, including part of the correlations, provides a further renormalization factor reducing the bandwidth in comparison to LDA.

However, the effect of the smaller GW bandwidth is partially compensated by the smaller \bar{U}^{DMFT} interaction strength. Altogether this yields rather similar self energies of the standard approaches: LDA+DMFT@ \bar{U}^{cLDA} and qp $GW+DMFT$ @ \bar{U}^{DMFT} , see lower panel of Fig. 2.4. This also reflects in very similar renormalization factors in Table 2.1, $Z = 0.51$ vs. $Z = 0.57$, which both agree well with experimental estimates of 0.5-0.6 [124, 163].

Since one important difference is the strength of the interaction, it is worthwhile recalling that \bar{U}^{DMFT} is defined as the local interaction strength at low frequencies. While this value is almost constant within the range of the t_{2g} -bandwidth, it approaches the bare Coulomb interaction at larger energies, exceeding 15 eV, as we discussed above, see Fig. 2.2. It has been recently argued and shown in model¹⁵ calculations [30] that the stronger frequency-dependence of the screened Coulomb interaction at high energies is of relevance and can be mimicked by a \mathcal{Z}_B -renormalization factor for the bandwidth. The latter can be determined from the frequency

¹⁵See also Ref. [54], for a further comparison with a full frequency-dependent calculation.

dependence of the interaction using the relation [30]: $\mathcal{Z}_B = \exp\left(\frac{1}{\pi} \int d\omega \frac{U(\text{Im}\omega)}{\omega^2}\right)$, and its evaluation in the case of SrVO_3 [30] yields $\mathcal{Z}_B = 0.7$.

We have tried to take this into account in the $\text{qp}GW+DMFT@U^{\text{DMFT}}$, $\mathcal{Z}_B = 0.7$ calculation. Due to the additional bandwidth renormalization, this calculation is very different from all others and yields the largest quasiparticle renormalization, i.e., $Z = 0.36$ is smallest.

This too small quasiparticle weight can be understood as follows: in the calculation of the DMFT self-energy, the \mathcal{Z}_B factor mimics the effect of the frequency-dependence of cRPA screened Coulomb interaction, which is much larger at high frequencies. In a fully frequency dependent GW calculation, this is properly matched by a correspondingly large GW self-energy at large frequencies. However, within the quasiparticle treatment of the GW self-energy (which represents a linear approximation around the LDA quasiparticle energy to its frequency dependence) such high frequency contributions of the GW self-energy are not included. As our results show, in this case, it is hence more consistent not to include the frequency dependence for the Coulomb interaction only, which the \mathcal{Z}_B factor emulates.

Next, we compare the k -integrated spectrum in Fig. 2.5. At low-frequency we find the same trends as for the self-energy results: the $\text{qp}GW+DMFT$ and $LDA+DMFT$ at U^{DMFT} and U^{cLDA} , respectively, yield a rather similar spectrum. In particular, the quasiparticle peak has a similar weight and shape. However, a difference is found at larger frequencies: the $\text{qp}GW+DMFT$ Hubbard bands are closer to the Fermi level in comparison to $LDA+DMFT$ (see Sec. 2.1.4). If we perform $\text{qp}GW+DMFT$ and $LDA+DMFT$ at the ‘‘wrong’’ interaction strength (i.e., U^{cLDA} and U^{DMFT} , respectively), we obtain a noticeably stronger and weaker correlated solution, respectively. This trend is also reflected in the double occupations presented in Table 2.1. Finally, as in the case of the self-energy, the $\text{qp}GW+DMFT@U^{\text{DMFT}}$, $\mathcal{Z}_B = 0.7$ solution is much more strongly correlated.

2.1.4 Comparison to photoemission spectroscopy

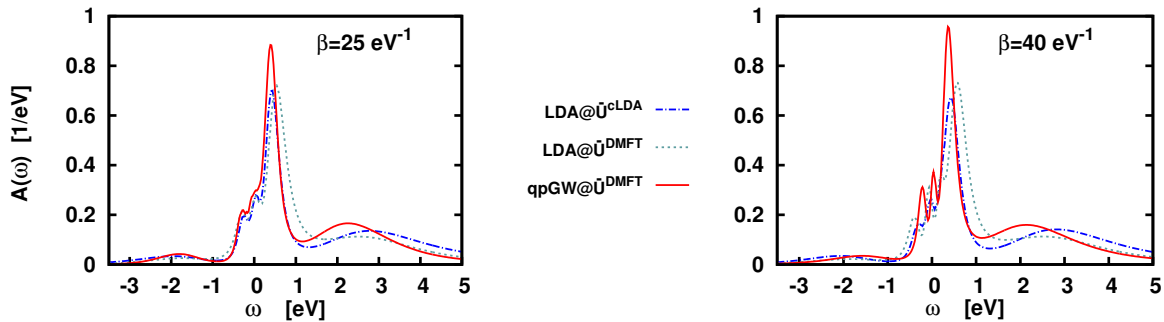


Figure 2.5: Spectral function for SrVO_3 (t_{2g} orbitals only) computed in five different ways as in Fig. 2.4. At lower temperatures the central peak gets only slightly sharper and higher, albeit the temperature effects from $\beta = 25$ to 40 eV^{-1} are small.

An obvious question is whether $LDA+DMFT$ or $qpGW+DMFT$ yields “better” results. This question is difficult to answer and for the time being we resort to a comparison with experimental photoemission spectroscopy (PES) [163]. However, one should be well aware of the limitations of such a comparison. On the theory side, the involved approximations common to the calculations, as, e.g., neglecting non-local correlations beyond the DMFT and GW level, or further effects, such as the electron-phonon coupling or the photoemission matrix elements, might bias the theoretical result in one way or the other. On the experimental side, care is in place as well, although the PES results have considerably improved in the last years due to better photon sources¹⁶. Furthermore, in Ref. [163] an oxygen p -background has been subtracted, which by construction removes all spectral weight below the region identified as the lower Hubbard band.

Fig. 2.6 compares the proposed $LDA+DMFT$ and $qpGW+DMFT$ (with and without Bose renormalization) with PES experiment. To this end, the theoretical results have been multiplied with the Fermi function at the experimental temperature of 20K and broadened by the experimental resolution of 0.1 eV. The height of the PES spectrum has been fixed so that its integral yields 1, i.e., accommodates one t_{2g} -electron, as in theory.

The $qpGW+DMFT@\bar{U}^{DMFT}$ and $LDA+DMFT@\bar{U}^{cLDA}$ have a quite similar quasiparticle peak, which also well agrees with experiment, as it was already indicated by the quasiparticle renormalization factor. A noteworthy difference is the position of the lower Hubbard band which is at -2 eV for $LDA+DMFT@\bar{U}^{cLDA}$ and ~ -1.6 eV for $qpGW+DMFT@\bar{U}^{DMFT}$. The latter is in agreement with experiment and a result of the reduced GW bandwidth. Let us note that the sharpness and height of the lower Hubbard band very much depends on the maximum entropy method, which tends to overestimate the broadening of the high-energy spectral features. Hence, only the position and weight is a reliable result of the calculation.

As we have already seen, the Bose-factor renormalized $qpGW+DMFT@\bar{U}^{DMFT}$, $\mathcal{Z}_B = 0.7$ calculation is distinct from both, $qpGW+DMFT@\bar{U}^{DMFT}$ and $LDA+DMFT@\bar{U}^{cLDA}$. It is also different from experiment with a much more narrow quasiparticle peak and a lower Hubbard band much closer to the Fermi level. A similar difference between static U on the one side and frequency dependent U was reported in Ref. [30]. A difference of this magnitude is hence to be expected.

Our results also compare well with those obtained within more involved schemes, like those presented in Ref. [173, 174], in which a $GW+DMFT$ calculation is performed for $SrVO_3$. In this works the frequency dependence of the self-energy is taken into account, and a dynamical interaction $\mathcal{U}(\omega)$, obtained by cRPA, is employed. While the GW self-energy and the value of the interaction $\mathcal{U}(\omega)$ are not treated self consistently, a full self consistency is achieved for the Green’s function in DMFT [173]. A careful analysis of the frequency and momentum dependence of the GW self-energy, similar to the one carried out for the first time in Ref. [175], allows the authors of [173] to show that the GW self-energy can be essentially separated in two contributions: (i) a *dynamical* part which is essentially *local*, (ii) and a *static nonlocal*

¹⁶The surface sensitivity in PES has also been discussed very recently for the case of $SrVO_3$, see Ref. [192].

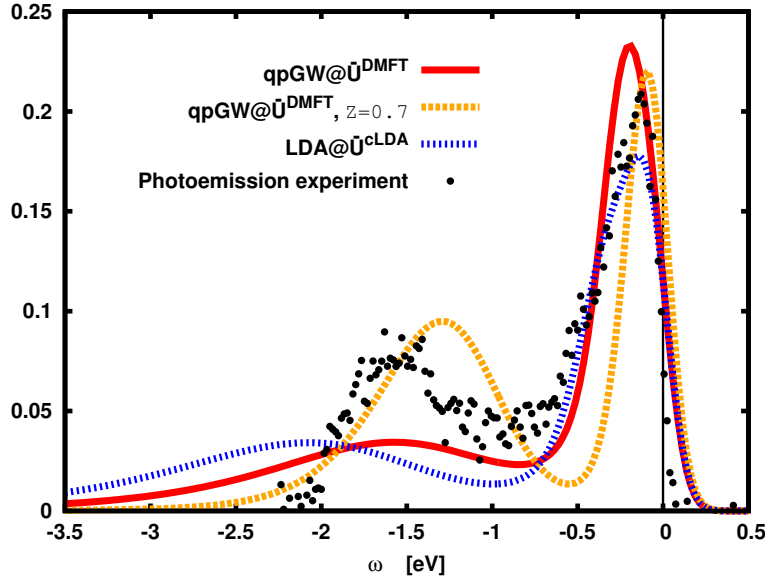


Figure 2.6: Comparison of $LDA+DMFT@U^{cLDA}$, $qpGW+DMFT@U^{DMFT}$ (without and with Bose renormalization $Z_B=0.7$) and experiment. The position of the lower Hubbard band is better reproduced in $qpGW+DMFT$ whereas the central peak is similar in $LDA+DMFT$ and $qpGW+DMFT$. The Bose renormalization $qpGW+DMFT$ differs considerably (photoemission spectra reproduced from Ref. [163]).

part. These two contributions to the self-energy have opposite effect on the LDA bandstructure, which partially cancel each other: The local and dynamic contribution (i) tends to *shrink* the bandstructure (i.e., to shift coherent spectral weight closer to the Fermi level, reducing the coherent quasiparticle energies) while the nonlocal and static contribution (ii) tend to enlarge the bandstructure (i.e., shifting the quasiparticle excitation energies more far away from the Fermi level). In a combination with DMFT only the nonlocal contribution (ii) needs to be retained, resulting in effectively enhanced k -dependence of the bandstructure compared to LDA. However in the GW +DMFT calculations of J. M. Tomczak *et al.* [173, 174], this effect is more than compensated by the frequency dependence of the interaction, which, for larger values of the frequency approaches the bare Coulomb value: in spite of a bandstructure with a larger bandwidth the Z factor is in the right value range, in comparison with the experiment, and hence with our $qpGW+DMFT$ calculation. On the other hand our approximate treatment of the GW self-energy, which neglects the frequency dependence of the GW self-energy that is linearized *before* removing the local contribution¹⁷, yields an effective nonlocal $qpGW$ Hamiltonian with a *reduced* bandwidth compared to LDA. As discussed above, combining this approximation with a frequency dependent Coulomb interaction would yield a too correlated result, while using a consistent static approximation also for the self-energy yields results in agreement with the ones of Ref. [173, 174]. However there are some features that can only be captured by the

¹⁷This is rather different from the qp Hamiltonian obtained in [173], Eq. (48), where the quasiparticle approximation is performed *after having removed the local self-energy contribution*.

more elaborated GW +DMFT scheme of Refs. [173, 174]. In particular, while the agreement in the vicinity of the Fermi level is quite good, and the height and spectral weight of the central peak of the spectrum is well reproduced by our qp GW +DMFT, the transfer of spectral weight to satellites and excitations far away from the Hubbard bands (especially in the unoccupied part of the spectrum) can only be reproduced within a scheme that takes into account the frequency dependence of the Coulomb interaction and of the GW self-energy.

2.2 Conclusion

We have carried out a careful comparison of LDA+DMFT, qp GW +DMFT (specifically, quasiparticle G_0W_0 +DMFT) and experiment for the case of SrVO₃, which is often considered to be a “benchmark” material for new methods for correlated systems. To this end, the LDA or G_0W_0 quasiparticle bandstructure was projected onto maximally localized Wannier orbitals for the t_{2g} bands. For these in turn correlation effects have been calculated on the DMFT level. If we take the locally unscreened RPA interaction (or the similar cRPA one) for the qp GW +DMFT and the cLDA interaction for LDA+DMFT, the two approaches yield rather similar self energies and spectral functions at the Fermi level. These also agree rather well with photoemission spectroscopy. A noteworthy difference between these two calculations is found, however, for the position of the lower Hubbard band, which is better reproduced in qp GW +DMFT. Similar spectra were also obtained by Tomczak *et al.* [173, 174] using a GW +DMFT calculation including the frequency dependence of the interaction.

From a principle point of view also a LDA+DMFT calculation with a locally unscreened or cRPA Coulomb interaction is possible and employed in the literature. In the static limit, these cRPA interactions are typically smaller than cLDA values. At least for SrVO₃, these smaller interaction values yield too weak electronic correlations if used for LDA+DMFT calculations.

Our calculations are performed using the GW implementation of one of the most widespread DFT codes. The implementation that we proposed has the advantage that it substantially keeps the same procedure employed in LDA+DMFT, as well as a comparable computational cost, but with several advantages compared to it. At the theoretical level the interaction value for the DMFT can be determined *ab initio* in a consistent way, and a well defined treatment of the double counting is possible. Besides this, the description of the lower Hubbard band in SrVO₃ is also improved. Therefore, while a self-consistent and fully frequency dependent scheme would be preferable, due to the high difficulty of the method it does not seem realistic that a full GW +DMFT can overtake the standard LDA+DMFT scheme, at least in the foreseeable future, and our qp GW +DMFT scheme might represent a valid alternative to it.

Chapter 3

Combining dynamical mean field theory and functional renormalization group: The DMF²RG

In this chapter we present DMF²RG, our novel approach, obtained by combining DMFT and fRG, with the aim of studying electronic correlations on all length scales and at all coupling strengths. In the first part of the chapter, we present the state-of-the-art methods to treat strong electronic correlations beyond DMFT. This way we emphasize how our new method, exploiting the strengths of fRG, can be competitive with already established approaches. Specifically, we show how the flexible structure of fRG allows us to include in an algorithmically simple way the local nonperturbative physics of DMFT as a starting point for the flow equations. We will then use the results obtained in the first chapter to understand the diagrammatic content of DMF²RG. After that, we demonstrate the applicability of the new scheme, by presenting our first practical implementation of DMF²RG. As a test case, we apply it to the two-dimensional Hubbard model at half filling, obtaining results for the momentum and frequency resolved self-energy, spin susceptibility, and one particle irreducible vertex. The former two are shown to be in qualitative agreement with results obtained by cluster extension of DMFT and lattice quantum Monte Carlo respectively. Finally we conclude the chapter with a outlook of further possible improvements, in-depth analysis and possible applications of our newborn approach, and a brief summary of our findings.

The material presented in this chapter is partially taken from Taranto *et al.*, *Phys. Rev. Lett.* **112**, 196402 (2014), Ref. [169].

The very idea of introducing a new method that combines DMFT and fRG arises from the desire of developing a scheme which is, at the same time, **unbiased** (towards any channel) and **non-perturbative** (in the electronic interaction). For this reason we propose a scheme that inherits the non-perturbative character of DMFT, while adding to its local physics the non-local fluctuations in all the channels by means of fRG.

Explaining how to achieve this goal is the main subject of the first part of this chapter: We will focus first on the physical idea that drives us in developing the new method, and then we will deal with the formal details. However before introducing DMF²RG, we will present some of the state-of-the-art methods that include *non-local correlations* on top of a DMFT treatment of the local ones. This discussion is aimed at motivating why a novel diagrammatic technique, such as DMF²RG, may be helpful, being complementary, and even superior in specific respects, with the ones (**cluster** and **diagrammatic**) already existing.

After this discussion, we will show the feasibility of the method, presenting numerical result for a special case, i.e. the two-dimensional Hubbard model at half filling. The presentation will be first focused on the practical implementation of the method, and on the several further approximations involved, and, subsequently, will be devoted to the analysis of the results, also in comparison with the ones obtained with fRG and DCA. Finally we will also propose an alternative path to improve the present formulation of DMF²RG, introducing an auxiliary problem which might be more suited than the original one for an fRG treatment in the strong-coupling regime.

3.0.1 Introduction and motivation

As we have discussed in the previous chapters, correlated electron systems display undoubtedly some of the most fascinating phenomena of condensed matter physics, including, among the others, superconductivity, which we will discuss more in detail later, and quantum criticality.

Besides these phenomena belonging to the “more traditional” condensed matter area, the accurate study of the strongly correlated regime of lattice models is becoming more important also in the context of cold atoms. In fact the tremendous progress in trapping, cooling, and controlling atoms in an optical lattice is offering the possibility of “simulating” a lattice model in a different context from the one usually studied in connection with real materials. Although the physics involved in cold atoms experiments is arguably more complicated (as it involves, e.g., the specific form of the Feshbach resonances and of the trapping potentials), the cold atomic systems are appealing for their cleanness (absence of phonons) and for their incredibly high tunability. The considerations above have justified the huge effort devolved in the last several years to the study of phenomena involving strong electronic correlations. However, most of the approaches developed so far have not been able to deal *at the same time* with all the aspects of strongly correlated electron problems. Let us use the striking example of the high temperature superconducting cuprates to show where the difficulties arise.

The case of cuprates The technological potential of high temperature superconductors is virtually unlimited, and several applications have already been used in different fields, ranging from frontier research in high energy particle physics (in the magnets that deflect the flux at LHC) to medical devices (for example in the devices used for the nuclear magnetic resonance). Obviously, even more applications would be possible if we were able to find the way of “design-

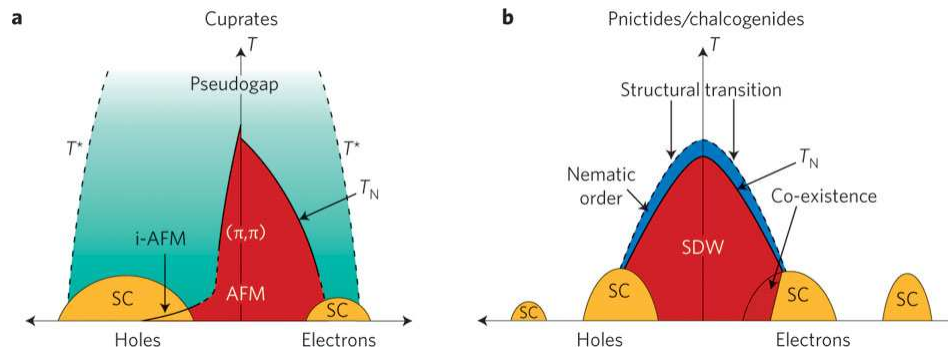


Figure 3.1: Schematic representation of the phase diagram of cuprates (panel a) and pnictides (panel b) for hole and electron doping. Adapted from Ref. [18].

ing’’ material to further increase the critical temperature (at the moment the highest recorded critical temperature at ambient pressure is 134K for the so called Hg-1223 compound). Obviously, before a reliable material design is possible, it is necessary to understand the essence of the mechanism behind the superconductivity in the discovered materials. Even today, more than 25 years after the discovery of cuprate superconductivity by Bednorz and Müller, these task has not been completely achieved. However, almost three decades of intensive research made several points clear:

- The relevant physics happens in the copper oxide planes, which constitute the common elements of all cuprates;
- The parent compounds, that become superconducting upon doping, are usually strongly correlated (Mott) antiferromagnets below their respective Néel temperature;
- Doping the parent compound a nontrivial phase diagram emerges: The Néel temperature quickly drops and a pseudogap opens in the spectral function. All in all the phase diagram is rather rich, as it is shown in Figure 3.1, and includes, besides superconductivity also magnetic ordering and “strange metal” phases;
- The superconducting pairing function has a $d_{x^2-y^2}$ character: It has a nontrivial spatial dependence in the copper-oxide planes;
- For hole doping, in the underdoped region of the phase diagram a pseudogap [159, 172] opens below some temperature T^* . The signature of the pseudogap is the opening of a gap in the spectrum for some directions of the momentum. The nature of the pseudogap and its connection with the superconductivity has been subject to intensive discussion in the literature, see, e.g., [159] and references therein.

From the theoretical point of view, there is no general consensus yet about the minimal model that can be used to describe the cuprates. However, it is believed, and the experience has shown, that most of the features of the cuprate phase diagram, including the pseudogap,

can be understood using a two dimensional **single band two-dimensional Hubbard model**, as early suggested by Anderson [159]. We will adopt this model in the following, even if it is still debated what is the role played by multi-band effects, in particular due to the hybridization with the p -bands of oxygen.

From the points listed above one can see why the description of cuprates is so difficult: On the one hand the strong electronic correlations, due to a poorly screened Coulomb interaction on the copper $3d$ orbitals, prevent the full success of perturbative methods (like fRG) alone. On the other hand, the main non perturbative method which is able to study strong electronic correlations, i.e. DMFT, fails due to the low-dimensionality of the copper oxygen layers, where the main physics is supposed to happen. Due to its spatial mean-field character DMFT alone is not able to deal with the strongly non-local self-energy, which reflects the appearance of the pseudogap, nor with the momentum dependence of the pairing function.

Even if DMFT is not sufficient, a lot of progress has been made using, among other methods, approaches which extend DMFT, like the cluster extensions, such as cellular DMFT (cDMFT) or dynamical cluster approximation (DCA), which are mainly focused on the treatment of (short-range) strong electronic correlations. At the same time, even if fRG is only able to address the weak coupling regime, thanks to the unbiased inclusion of parquet-like diagrams, it has allowed to gain a deep insight about the competing instabilities in the two-dimensional Hubbard model.¹ These two approaches, cluster extensions of DMFT and fRG, focus on different aspects of the problems and have different limitations. Cluster DMFT methods are by construction limited to describe short correlation lengths (see below) and therefore the obtained results do not fully describe the cuprate situation, where long range order is realized. Moreover, the results obtained with cluster methods require a nontrivial extrapolation to the limit of infinitely large cluster. At the same time the perturbative analysis of fRG has to be performed in a parameter range which is far away from the one expected to be relevant for the cuprates: The analysis of the weak coupling instabilities may serve only as an indication for what the situation is at strong coupling.

In fact the discussion above can be considered quite paradigmatic: fRG and DMFT allow to study complementary aspects of a correlated problem. This motivates us in combining the main strength of DMFT (nonperturbative treatment of purely local diagrams) with the one of fRG (unbiased, but perturbative, treatment of competing instabilities) in a single novel approach. This method is coined DMF²RG, and it can be considered either as a diagrammatic extension of DMFT or as a new starting point for an fRG flow. With this, we mean that it aims at the inclusion of non-local diagrams in a perturbative (diagrammatic) way on top of the nonperturbative local diagrams of DMFT. The main difference from the other existing diagrammatic extensions of DMFT is the fact that the way non-local diagrams are computed relies on fRG. To understand the great potential gain of the use of fRG, before presenting the DMF²RG, we will first introduce the standard (cluster and diagrammatic) extensions of DMFT.

¹We note that fRG has been recently also used in the study of pnictides. In this case the electronic correlations are supposed to be less strong while the interplay of several bands, with different topologies of the Fermi surfaces is more important [115].

3.0.2 Extensions of DMFT

As discussed in chapter 1.5, DMFT represent the “quantum” extension of the classical (static) mean-field theory [47]. More formally, it provides the exact solution of a quantum many-body Hamiltonian in the limit of infinite spatial dimensions ($d \rightarrow \infty$) [48]. Hence DMFT allows for an accurate (and non-perturbative) treatment of the *purely local* part of the correlations. At the same time, the mean-field nature with respect to the spatial degrees of freedom implies that all the *non-local* spatial correlation are completely neglected.

Several approaches have been developed in the past two decades to include non-local correlations beyond DMFT. These can mainly be classified into cluster and diagrammatic extensions of DMFT. The philosophy behind these approaches is different and therefore they are suited to analyze different questions and regimes in a complementary way. Let us discuss the cluster extensions first.

Cluster extensions

With the increasing computational power and the progress in the impurity solvers, in recent years it has become possible to solve, numerically exactly and with high efficiency, bigger and bigger cluster of impurities. Since DMFT is based on a mapping of a lattice problem onto a single AIM embedded in a self-consistent bath, the most natural extension of it consists in mapping a small portion of the lattice problem on a cluster consisting of $N_c > 1$ impurity sites embedded in a self-consistent bath. In this way the correlations inside the cluster are treated exactly (or numerically exactly), while the correlations beyond the cluster size are treated at the dynamical mean field level using the self-consistent effective bath. This procedure is the basic idea behind the so-called *cluster extensions* of DMFT.

There are two possibilities to define the cluster: it can be done either in **real space** or in **momentum space**. Defining the cluster in real space is more intuitive, as one simply needs to single out a portion of the lattice and associate to it a cluster of impurities. The hoppings between the impurities as well the interaction on them are kept fixed at the lattice value, while the cluster embedding is defined self consistently. This approach is named **cellular DMFT** (CDMFT) [109, 114].

In the same direction goes the **variational cluster approach**² (VCA) [143]. In VCA the lattice is represented by a small cluster, but in this case, instead of treating the correlation beyond the cluster by embedding the cluster in a self-consistent bath (like in CDMFT), one deals with it by (i) attaching uncorrelated bath sites at the boundaries of the cluster; and by (ii) determining in variational way also the on-site energies and hoppings between the correlated cluster sites, to take effectively into account the correlations beyond the cluster size and to overcome the drawback of having a discrete embedding (bath sites) of the cluster instead of a continuous one.

An equivalent way to proceed consists in defining the cluster in momentum space: The

²Sometimes also called variational cluster perturbation theory [159].

Brillouin zone is divided in N_c patches, the self-energy being assumed constant in each patch:

$$\Sigma_{\mathbf{k}\sigma}(\omega) = \sum_i^{N_c} \Sigma_{i\sigma}(\omega) \zeta(\mathbf{k}, i). \quad (3.1)$$

Here $\zeta(\mathbf{k}, i)$ equals one if the momentum \mathbf{k} belongs to the patch i and zero otherwise. The self-energy of each patch is then computed solving self-consistently a cluster of N_c sites. This approach is known as **dynamical cluster approximation** (DCA) [64, 65, 122]. As cDMFT, DCA relies on the fact that, at least in systems of high dimensionality, the frequency dependence of the self-energy is supposed to be more important than the momentum one [64], and the latter can be therefore approximated well enough by an ansatz of the form of equation (3.1). For both (cDMFT and DCA) methods, it is also important to notice, that for small cluster sizes the geometry of the cluster (or, in other words, how the Brillouin zone is divided in patches) turns out to play an important role, with some geometries being more favorable than others [21].

An appealing feature of the cluster methods is that they provide an interpolation between the DMFT, corresponding to $N_c = 1$, and the exact solution, which is recovered in the limit of an infinite cluster size ($1/N_c \rightarrow 0$). Since the correlations inside the cluster are treated exactly, cluster methods, and DCA in particular, have been able to describe quite accurately short-range non-local correlations, and phenomena which are associated with them, like the opening of the pseudogap in the spectrum of the two-dimensional Hubbard model at half filling [87], as well as finite doping [51, 118]. Furthermore, it can also be seen that the Néel temperature for the antiferromagnetism at half filling is reduced with increasing cluster size [123], and that it is possible to find a divergent susceptibility associated with a $d_{x^2-y^2}$ pairing, for finite temperatures, compatible with a Kosterlitz and Thouless (KT) [4, 20, 105] transition [123]. However due to the space dependence of the order parameter the convergence with the cluster size is only very slow [122]. Moreover it is physically clear that whenever approaching a (second order) phase transition, which involves a divergent correlation length ξ the convergence of the results with the cluster size will become slower and slower, since the number of cluster sites required to reproduce the correlations will increase together with ξ . For the very same reason, the cluster methods are not able to give an accurate answer regarding the critical exponents at the transition.

In fact, the analysis of the critical exponents requires the study of the critical region, which, in temperature, corresponds to the immediate vicinity of the critical temperature $T - T_c \ll 1$. In this temperature regime a divergent length scale appears, since the correlation length diverges as $\propto (T - T_c)^{-\nu}$, that will soon exceed the length of the longest correlations that can be described exactly within a cluster, with scales with the number of cluster sites like $N_c^{(1/d)}$. All the correlations beyond this length will be captured only at the mean field level (in space), and hence the authors of reference Ref. [123] conclude that close enough to the transition the critical exponents reproduced in DCA reduce back to the mean-field ones, reflecting the mean field treatment of the correlations beyond the size of the cluster. Conversely, phenomena which arise from correlations related with a narrow region of reciprocal space, such as the vicinity of a Van Hove singularity [82], are very hard to describe [55] in cluster approaches.

It has also to be stressed that increasing the size of the cluster is computationally extremely challenging: Due to the increase of the size of the Hilbert space associated with the cluster the computational effort increases with the number of sites. This also limits the possibilities of the cluster calculations for multi orbital systems, which would require further computational effort. Besides this one should also consider that usually the cluster is solved using quantum Monte Carlo methods, and this might imply, away from half filling the emergence of the so-called sign problem, for large values of the Hubbard interaction [122].

The take home message from the discussion above is that the cluster methods are very powerful in dealing with the short-range correlations, which are treated very precisely, but might have to be supported with other methods for the analysis of the long range correlations arising in the proximity of (quantum) phase transitions and instabilities. To this aim, one such possibility is making use of the diagrammatic extensions of DMFT described below.

While the most powerful cluster techniques have been developed in Refs. [64, 109, 114], historically the idea of treating short range correlations using more than one impurity can be traced back to the work of Schiller and Ingersent [161]. In this paper the authors discuss about $1/d$ (d representing the number of dimensions) corrections to the infinite dimensional limit of DMFT: Due to the proper scaling of the hopping (sec. 1.5) the self-energy Σ_{ij} scales like $1/d^{\|i-j\|}$, $\|i-j\|$ being the Manhattan distance between the sites i and j , and therefore:

The [...] summation of all skeleton diagrams with no inter site distance greater than n constitutes a systematic approximation scheme correct to the order $1/d^n$.

In turns, the non-local Green's function between sites at a Manhattan distance smaller than n can be computed from the solution of an action of $n+1$ impurities. In other words, by defining a problem containing $n+1$ impurities we are able to describe (i) the Green's function G_{ij} for $\|i-j\| \leq n$ and (ii) the leading diagrams in $1/d$, up to the order $1/d^n$. Correspondingly, the Weiss field of $n+1$ impurities (which takes a matrix form) needs to be computed self-consistently.

Such so-called " $1/d$ **expansion**", however, is different from the other cluster expansions described below in some important aspects. First, the cluster which is solved in the $1/d$ approximation does not correspond to a small portion of the lattice (as in cDMFT or DCA), but is rather an auxiliary tool, defined to compute the local and non-local Green's function for distances inside the cluster size. Secondly, on the conceptual point of view, the $1/d$ expansions can be regarded as being at the border between diagrammatic and cluster extensions of DMFT: The parameter $1/d$ serves as "small" perturbative parameter, and the diagrammatic content of the approximation is controlled, in the sense that it is clear which diagrams can be attributed to the theory and which not. In this respect, the impurity clusters are introduced as an aid for the approximation, which is anyway derived diagrammatically. The first order correction $1/d$ was included for the Falicov-Kimball model in Ref. [161] by introducing an action involving two impurities. The correction obtained using the $1/d$ approach are very small and this approach has not been very successful, possibly also due to the very limited size of the cluster that one was able to solve exactly when the method was proposed. Thereafter not many studies have

been performed in this direction.

Diagrammatic extensions

The common idea behind the diagrammatic extensions of DMFT is assuming the DMFT as the zeroth order approximation, pinpointing a parameter that is supposed to be small and selecting a subclass of diagrams which corresponds to some form of perturbative expansion in the supposedly small parameter, while keeping the nonperturbative local physics of DMFT³ as starting point for the expansion.

Several approaches of this kind have been proposed. Historically, the first attempt to extend DMFT was the $1/d$ expansion [161], which shares aspects of the cluster and of the diagrammatic extensions of DMFT. In this case the perturbative parameter is given by $1/d$. The $1/d$ expansion allows for the inclusion of short range correlations only: At the order $1/d^n$ are exactly included only correlations extending to the first n neighbors, and increasing n involves the solution of a bigger auxiliary cluster of interacting impurities, therefore limiting the method to short length correlations.

A second attempt has been tried in Ref. [154], where the method used has been coined DMFT+ Σ_k . At odds with the previous one (and with the ones that we will describe below) this approach is mostly phenomenological: It is supposed that one can split the self-energy in a local part and a non local part, in an additive fashion. The local self-energy is then computed solving an appropriate AIM, while the non-local one is obtained using some other approximation scheme, taking into account, e.g., interactions with collective modes or order parameter fluctuations. It is clear that in this case the “small” perturbative parameter is given by the non-local self-energy itself. Of course the quality of the approximation depends on a number of factors, like the effective smallness of the non-local self-energy, the approximate way how this is computed, and the assumption of an additive form of the self-energy.

A third class of more “mature” diagrammatic methods⁴ has been developed starting from the second half of last decade, and includes dynamical vertex approximation (D Γ A) [147, 176], dual fermion (DF) [55, 151] and, more recently, the one particle irreducible approach (1PI) [146]. In these methods the idea is building subclasses of diagrams using “standard” perturbative approaches (e.g., n -order perturbation theory, ladder-like diagrams, parquet-like diagrams) but using “building blocks” (i.e., Green’s functions, two-particle interactions...) which already include all the local physics captured by DMFT.

Let us consider, as an example, a simple resummation of ladder diagrams. In standard perturbation theory these diagram are built up using as building block the bare Green’s function and the bare interaction vertex (i.e., U in the case of a single-band Hubbard model). Such ladder approximation is valid if U is small enough, i.e., in the perturbative regime. A possibility for

³Strictly speaking, in self-consistent schemes one takes the nonperturbative local physics of an auxiliary AIM as a starting problem. This AIM does not need to be the same as the one of DMFT.

⁴For completeness we also mention other diagrammatic methods: Ref [56] in which the short range correlation of DCA are supplemented with long range ones by means of a fluctuation exchange (FLEX) approximation, and so-called multiscale methods, like the one of Ref. [167].

accessing a non-perturbative regime of larger U consists in keeping fixed the topology of the subclass of diagrams (the ladder diagrams, for example, if they are well motivated physically) but using building blocks which are already nonperturbative, and include the strong correlation at best as we can do, i.e., at the DMFT level. In first approximation, this means that the ladder diagrams are to be built using a non-local Green's function (which already should keep into account the local self-energy of DMFT) in place of the full bare Green's function, and the local one particle irreducible vertex, fully irreducible in the ladder channel considered, of DMFT. In this way the building blocks of the perturbation theory already include nonperturbatively the effects of the interaction, at least at the local level, through the self-energy and the vertex. Since the DMFT is nonperturbative, and the DMFT diagrams are included in the theory from the beginning, also the resulting new theory will be nonperturbative in the purely local diagrams, i.e., no selection on the "topology" of the purely local diagrams is made. However, if the new theory will provide a good approximation for the problem considered essentially depends on how the non-local correlation effects can be captured by the diagrammatic selection done. In other words, the approximation will work only if a "perturbative" (i.e., Feynman diagrammatic) treatment of the non-local physics is possible. In this sense the discriminating criteria for the quality of the approximation is *not* the size of the ration U/D (D being the bandwidth), but rather how important are the non-local diagrams, neglected from the DMFT and not generated by the perturbative expansion. In this respect, for example, it is clear that the theories might work better for very large values of U , where the physics is closer to the atomic limit, than in the region of intermediate values of U [152]. For example, in the case of the half filled three dimensional Hubbard model the problematic region can be the one around the maximal Néel temperature for the antiferromagnetic transition [147], where a crossover between Slater and Mott antiferromagnetism is expected [171]. Furthermore the existence, or not, of a "*small parameter*" for non locality depends also on *how* the building blocks are defined, and different choices of the building blocks give rise to different approximations.

The D Γ A, for example, relies on the assumption that the two-particle fully irreducible vertex is purely local. This way, the locality condition of DMFT is raised from the one particle level of the self-energy to the two particle level of the two-particle irreducible (2PI) two particle vertex Λ_{irr} . The "control parameter" in this case would be the non-locality of the fully irreducible vertex Λ_{irr} : If the exact fully irreducible vertex is local enough, the D Γ A approximation is well justified. From the practical point of view, the condition of locality of Λ_{irr} should be translated in some diagram resummation, which can be carried out numerically. Keeping in mind that the solution of the parquet equations would formally allow to obtain the exact full 1PI vertex, when the exact frequency and momentum dependent 2PI vertex is used as input, it is clear that the best that one can do, is summing all the parquet diagrams after substituting the local 2PI vertex to the momentum dependent one. However the resummation of parquet diagrams (see also the section about the diagrammatics of DMF²RG) is a very difficult task, and, if allowed by the physics of the problem under consideration, one can rather restrict himself to ladder diagrams instead of parquet ones. In this case one does not need the fully irreducible local vertex, but rather the irreducible vertex in the one channel that is used in the ladder resummation. This

approximation is often referred to as *ladder-DΓA* [147].

A related approach is the dual fermion (DF) one [55, 151]. In this case one makes use of an Hubbard-Stratonovich transformation (HST) to introduce some new auxiliary (dual) fermionic degrees of freedom, which are noninteracting but couple to the original electrons. The transformation allows to formally integrate out the original degrees of freedom of the system. The price to pay for that is that in the action of the dual fermions appears a complicated interaction term, that, when the transformation is chosen properly, involves terms including the product of four and more fermionic fields, with coefficients related to the two- and more particle vertices of the local problem considered⁵. The first approximation in DF, considered that the Hubbard-Stratonovich transformation is obviously exact, is neglecting the terms with more than four fields, that would be not easy to treat numerically. This relies on the idea that the three- and more particle vertices⁶ are small and can be neglected. The problem now reduces to solving approximatively (here is the second approximation of DF) the problem in dual space, and then map the results back to evince the non-local vertex and self-energy of the original electrons. The advantage is that the HST was chosen from the beginning so that the local part of the interaction can be integrated out and the dual fermions have to account for the non-local effects only. Whenever the local part of the interaction is really the major one, then, it is reasonable to treat the DF action in a perturbative fashion. To this extent, one can then choose a subset of diagrams to construct using as building blocks the (two-particle) interaction and the Green's function of the dual fermions, which are respectively related with the local two particle vertex and with the non-local part of the self-energy [151]. To summarize the DF fermion approximation will be then successful if (i) the terms beyond the quartic one in the dual action which are neglected are small (in turns this means that the three particle local vertex must be small) and if (ii) the dual problem allows for a perturbative treatment. However, the choice of the diagram used in the perturbative treatment remains important, and also in this case the best that one can (and sometimes have to [188]) do is choosing a parquet-like approximation.

Finally, the recently introduced 1PI approach [146] presenting unifying aspects of both DΓA and DF. In this approach one tries to extract as much information as possible from a resummation of ladder-type diagrams. In fact, this resummation is performed in such a way to include, exploiting the introduction of further auxiliary fermionic fields, also diagrammatic contributions from the other channels, without making use of the parquet formalism.

It has to be stressed that DΓA, DF and 1PI, unlike the cluster methods, include correlations *at all length scales* although in an approximate way. It is in this respect that diagrammatic and cluster methods can be indeed considered **complementary**. A beautiful example of the capabilities of the diagrammatic methods is the accurate description of the critical properties, see, e.g., the calculation of the critical exponents, which has been performed in DΓA for the

⁵In first approximation the local problem can be the one of DMFT. However this is not necessary, and the proposed scheme [151] is self-consistent.

⁶Here we do not specify further *what* kind of vertex, since it depends on a non-unique choice of the Hubbard-Stratonovich transformation. With the choice of [151] the vertices to employ are the two and more particle Green's functions.

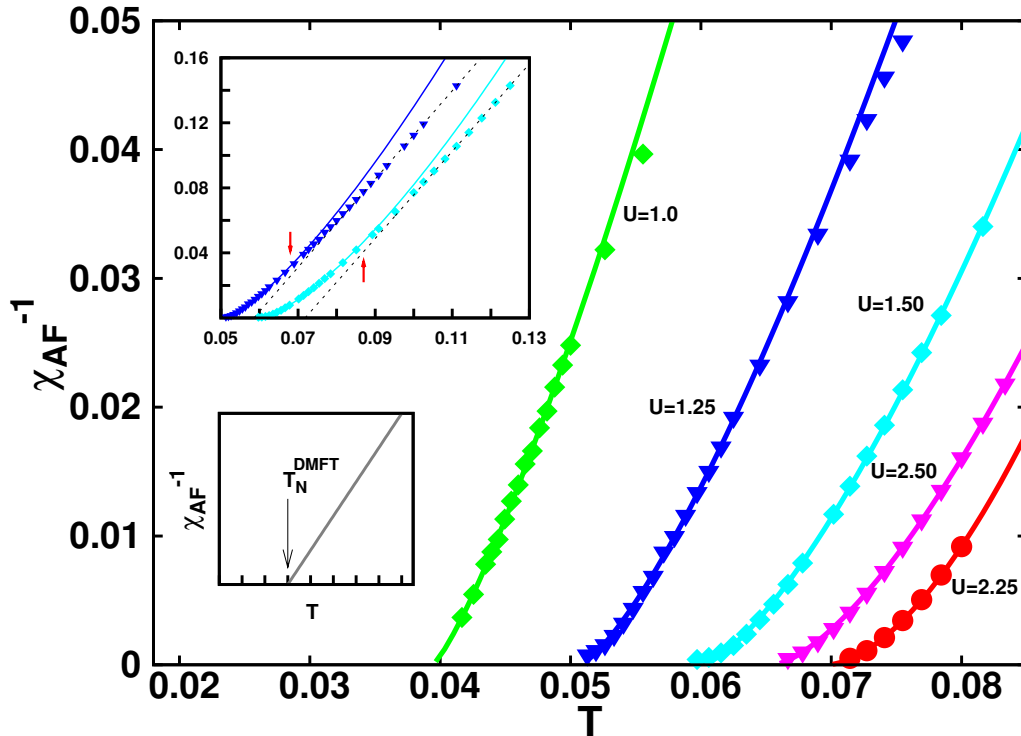


Figure 3.2: Inverse AF spin susceptibility as a function of T for different U values. Lower inset: Inverse DMFT susceptibility with a MF ($\gamma = 1$: linear behavior) critical exponent. Upper inset: larger T interval. Reproduced from Ref. [147].

case of the three-dimensional Hubbard model [147], see Fig. 3.2, and in DF for the two-, three- and four-dimensional Falicov-Kimball model [11].

However there is still a caveat: Even when it is possible to define a "small control parameter" for the physics beyond DMFT, it is still necessary to select and compute subclasses of diagrams that encode as *much as possible* the relevant non-local physics. In most cases, in fact, keeping only the lowest diagrams in perturbation theory does not allow for big improvements, and it is needed to use resummation of *infinite set of diagrams*, although, restricted to some specific topology, like in ladder or parquet approximation. If possible, the resummation of parquet diagrams is the best that one can do, and allows for the correct treatment of competing instabilities. However this is in general an extremely hard task, and in most cases one has to restrict himself to ladder diagrams. In specific cases, as those treated in Refs. [11, 147], this can be a good approximation, i.e., when there are reason to believe that one instability dominates over the others. However in more general situations, typically one does not know a priori whether a ladder channel dominates over the others or not, exactly as in the cuprate situation. In these cases a ladder approximation can produce rather biased results.

It is in this kind of situations that using DMF²RG may become appealing: As we have already discussed, thanks to fRG we have the possibility of computing parquet-like diagram (in the sense of Sec. 1.4.2), which we will use to obtain an *unbiased* treatment of the electronic correlations beyond DMFT in *all channels*. In the next section we will formalize the method and

we will see how these parquet-like diagrams are obtained using the non-perturbative building blocks of DMFT.

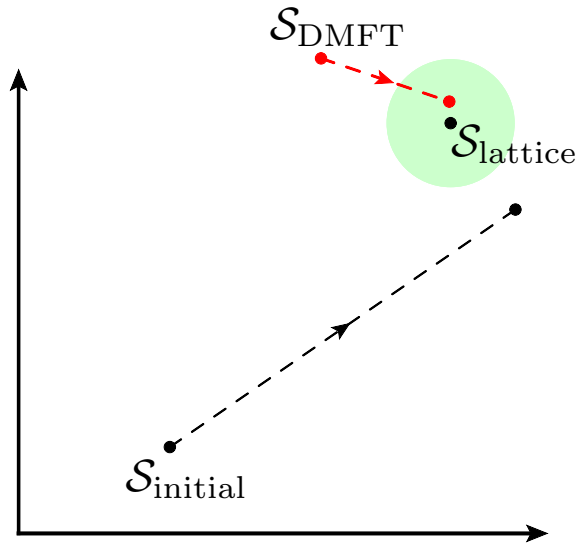


Figure 3.3: Sketchy representation of the difference between the standard fRG flow and the DMF²RG one. Each point of the “parameter space” corresponds to the action associated with a different gaussian propagator (but the same interaction term). The goal is computing field integrals relative to the action labelled $\mathcal{S}_{\text{lattice}}$, by performing a flow that starts from an action that we are able to solve ($\mathcal{S}_{\text{initial}}$). Choosing a cutoff corresponds in our sketchy representation to the selection of a path in the parameter space. Obviously if no approximation is done at the end of the flow one would end with the same result for the field integrals that one would have integrating $\mathcal{S}_{\text{lattice}}$. However, due to the truncation, we are not able to integrate exactly along the path, and therefore we might end quite off from the desired result, as represented in the figure. This makes the choice of the starting action very important. In a conventional fRG one usually starts from a problem in which all the fluctuations are suppressed: the propagator of the gaussian term is identically zero in the beginning of the flow. This corresponds to the case denoted $\mathcal{S}_{\text{initial}}$ in the figure. Increasing the value of the interaction U the full action contains gradually more correlations that are neglected in the initial one, and are only partially recovered during the flow. Therefore the result of the integration of the flow equations can be quite different from the exact result. In DMF²RG the starting point, $\mathcal{S}_{\text{DMFT}}$ corresponds to the action of the AIM associated with the DMFT solution of the lattice problem $\mathcal{S}_{\text{lattice}}$. Therefore it contains already a possibly big part of the correlations, i.e., the local ones. In the flow only a smaller part have to be built: The starting point of DMF²RG is “closer” to the final action than the starting point of fRG. As a consequence one can expect that the results obtained by integrating the flow equations of DMF²RG might be closer to the exact result.

3.0.3 From infinite to finite dimensions

The idea behind DMF²RG can be visualized pictorially as flowing from the solution of an infinite dimensional system to the solution of a finite dimensional one, as we represented schematically in Fig. 3.3.

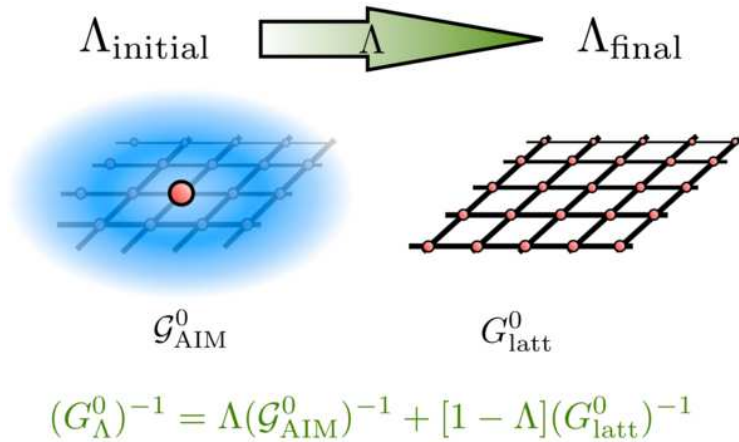


Figure 3.4: Schematic illustration of the DMF²RG approach, showing the evolution of the Gaussian part G_{Λ}^0 of the action from DMFT to its exact expression for a two-dimensional system. The (truncated) flow equations for the self-energy Σ^{Λ} and the two-particle vertex Γ^{Λ} are explicitly given in terms of Feynman diagrams.

The infinite dimensional system is introduced because it can be solved exactly, by means of DMFT, and therefore it can be taken as a starting point for fRG. As discussed in the chapter about DMFT, the solution of the infinite dimensional problem is obtained, in practice, from the one of an AIM embedded in a self-consistent bath, which accounts for the effects of the rest of the system, i.e., for the other sites of the lattice. In fact, in the single band case, the only lattice quantity entering in the DMFT self consistency equation (1.125) is the density of states $\rho(\epsilon)$, and a DMFT calculation for a finite and for an infinite dimensional lattice, will yield the same results⁷, provided that the density of states of the noninteracting systems are the same. However, only in the case of really infinite dimensional lattices the local physics will be described exactly by the AIM self-energy and Green's function, otherwise it will be an approximation. For this reason in Fig. 3.4 the "infinite dimensional" starting point has been sketched by an impurity site surrounded by a cloud, representing the effective bath of the self-consistent AIM that is replacing the hopping. As we flow towards the finite dimensional lattice of our interest the embedding cloud is supposed to fade out while the lattice hopping is gradually activated. This is the basic idea of DMF²RG that we are going to express more formally in the next paragraph.

⁷This is true if no symmetry breaking takes place [48].

Method

Let us start by briefly recapitulating the standard fRG technique, already discussed in the fRG chapter 1.4, which makes it easier, then, to clarify how the DMFT approximation can be combined with it.

We consider an interacting problem defined by the action:

$$\mathcal{S}_{\text{lattice}} = - \int_0^\beta d\tau d\tau' \sum_{\mathbf{k}\sigma} \bar{\psi}_{\mathbf{k}\sigma}(\tau) G_{\text{latt}}^0(\mathbf{k}, \tau - \tau')^{-1} \psi_{\mathbf{k}\sigma}(\tau') + \mathcal{S}_{\text{int}}. \quad (3.2)$$

Here, $\bar{\psi}_{\mathbf{k}\sigma}(\tau)$ ($\psi_{\mathbf{k}\sigma}(\tau)$) are the Grassmann variables [134] corresponding to the creation (annihilation) of a fermion with spin projection $\sigma = \uparrow, \downarrow$ of momentum \mathbf{k} at imaginary time τ . G_{latt}^0 is the free propagator of the finite dimensional system, which reads explicitly $G_{\text{latt}}^0(\mathbf{k}, i\omega_n) = (i\omega_n - \epsilon_{\mathbf{k}} + \mu)^{-1}$ in terms of the fermionic Matsubara frequencies $\omega_n = \pi/\beta(2n+1)$, the energy-momentum dispersion $\epsilon_{\mathbf{k}}$ and the chemical potential μ . All the terms beyond the Gaussian one are contained in \mathcal{S}_{int} . In the simplest case, for the interaction of a single band Hubbard model, this reads:

$$\mathcal{S}_{\text{int}} = U \int_0^\beta d\tau \bar{\psi}_{i\uparrow}(\tau) \psi_{i\uparrow}(\tau) \bar{\psi}_{i\downarrow}(\tau) \psi_{i\downarrow}(\tau). \quad (3.3)$$

The Grassman variables $\bar{\psi}_{i\sigma}$ ($\psi_{i\sigma}$) correspond to the creation (annihilation) of a fermion of spin projection σ on the lattice site i . The Grassman variables in real and momentum space are related by a Fourier transform:

$$\bar{\psi}_{j\sigma}(\tau) = \sum_{\mathbf{k}} e^{-i\mathbf{R}_j \mathbf{k}} \bar{\psi}_{\mathbf{k}\sigma}(\tau), \quad \psi_{j\sigma}(\tau) = \sum_{\mathbf{k}} e^{i\mathbf{R}_j \mathbf{k}} \psi_{\mathbf{k}\sigma}(\tau); \quad (3.4)$$

$$\bar{\psi}_{\mathbf{k}\sigma}(\tau) = \sum_i e^{i\mathbf{R}_j \mathbf{k}} \bar{\psi}_{i\sigma}(\tau), \quad \psi_{\mathbf{k}\sigma}(\tau) = \sum_j e^{-i\mathbf{R}_j \mathbf{k}} \psi_{i\sigma}(\tau). \quad (3.5)$$

Here \mathbf{R}_j is the lattice position of the site j . The summation $\sum_{\mathbf{k}}$ is intended over the first Brillouin zone. As usual Grassman fields can also be expressed in terms of the Matsubara frequencies:

$$\bar{\psi}_{\mathbf{k}\sigma}(\omega_n) = \int_0^\beta d\tau e^{-i\omega_n \tau} \bar{\psi}_{\mathbf{k}\sigma}(\tau), \quad \psi_{\mathbf{k}\sigma}(\omega_n) = \int_0^\beta d\tau e^{i\omega_n \tau} \psi_{\mathbf{k}\sigma}(\tau); \quad (3.6)$$

$$\bar{\psi}_{\mathbf{k}\sigma}(\tau) = \sum_n e^{i\omega_n \tau} \bar{\psi}_{\mathbf{k}\sigma}(\omega_n), \quad \psi_{\mathbf{k}\sigma}(\tau) = \sum_n e^{i\omega_n \tau} \psi_{\mathbf{k}\sigma}(\omega_n); \quad (3.7)$$

(the same transformation applies to the fields expressed in real space).

In general, the fRG procedure, described in Sec. 1.4 can be summarized conceptually in three steps [129, 141]:

1. First a ‘‘solvable’’ action (\mathcal{S}_{ini}) is introduced as initial starting point. Here, ‘‘solvable’’ means that at the beginning the ‘‘problematic’’ (i.e., non gaussian) parts of the original action are excluded (e.g., the degrees of freedom close to the Fermi level). Note that \mathcal{S}_{ini} differs from the original $\mathcal{S}_{\text{latt}}$ only in its Gaussian part.

2. A one-parameter family of actions \mathcal{S}^Λ is defined. These actions smoothly interpolate between the solvable action for the initial value of the parameter (i.e., if $\Lambda = \Lambda_{\text{ini}}$, $\mathcal{S}^{\Lambda_{\text{ini}}} \equiv \mathcal{S}_{\text{initial}}$) and the physical one at the end (for $\Lambda = \Lambda_{\text{fin}}$: $\mathcal{S}^{\Lambda_{\text{fin}}} \equiv \mathcal{S}_{\text{lattice}}$). This corresponds to a continuous change of the Gaussian propagator from $\mathcal{S}_{\text{initial}}$ to $\mathcal{S}_{\text{lattice}}$.
3. The evolution of all (1PI) m -particle vertex functions of the actions \mathcal{S}^Λ as a function of Λ is determined from a set of coupled differential equations, called ‘‘flow equations’’.

The formal derivation of this procedure, as well as of the flow equations for the vertex functions is presented exhaustively in the literature, see, e.g., the recent reviews Refs. [129, 141] as well in chapter 1.4. By integrating this set of differential equations, one can *in principle* evaluate exactly all 1PI m -particle vertex functions of the action \mathcal{S} of the problem of interest by computing the flow from the corresponding vertex functions of the solvable model, independently on which specific choice was made for it. However, in the presence of a two-particle interaction, the hierarchy of flow equations couples the m -particle vertex function Γ_m^Λ with the $(m + 1)$ -particle one, i.e., the set of flow equations is in general *infinite*. Hence, in practice one needs to truncate the equations: As an approximation, it is assumed that all the 1PI-vertex functions with m bigger than some value (typically $m_{\text{max}} = 2$) are neglected. Within this approximate treatment, the choice of the initial action becomes obviously important.

More specifically, by retaining only the one-particle vertex function (self-energy) and the two-particle vertex, and setting the three-particle vertex to zero, the truncated flow equations assume the form:

$$\partial_\Lambda \Sigma^\Lambda = \Gamma_2^\Lambda \circ S_\Lambda, \quad (3.8)$$

$$\partial_\Lambda \Gamma_2^\Lambda = \Gamma_2^\Lambda \circ (S_\Lambda \circ G_\Lambda) \circ \Gamma_2^\Lambda. \quad (3.9)$$

Here the symbol ‘‘ \circ ’’ stands for the standard summation over all internal variables, i.e., momentum integration as well as spin and Matsubara frequency summation. At each vertex, energy, spin, and momentum is conserved according to the conventional diagrammatic rules. The symbols Σ^Λ , Γ_2^Λ , G_Λ and S_Λ stand respectively for the self-energy, two-particle vertex, dressed Green’s function and single scale propagator, as defined in the main text. The initial condition for these differential equations, $\Sigma^{\Lambda_{\text{ini}}}$, $\Gamma_2^{\Lambda_{\text{ini}}}$ are obtained by solving the initial ‘‘solvable’’ action \mathcal{S}_{ini} .

Their explicit expression in terms of frequency, momenta and spin summations can be found, e.g., in Refs. [129] and in Chapter 1.4. The main difference from the conventional fRG approach, is that in DMF²RG we aim at including a major part of the correlated physics *already* at the level of the initial ‘‘solvable’’ action. This is certainly possible for the non-perturbative, but purely local, correlations of DMFT, because the DMFT solution of several models and realistic problems of solid state physics can be obtained both at the one and the two-particle level [54, 138, 149], providing the input for the truncated flow.

The formal implementation of this idea requires evidently to replace the initial action with a one describing the non-perturbative local physics of the DMFT solution and then to set up

the flow to the final action $\mathcal{S}_{\text{lattice}}$ of the desired problem (where *all* correlations, namely also those *beyond* DMFT, are eventually included). Due to the flexibility of the fRG scheme, there are several ways to realize this in practice. A first attempt can be obtained considering that, from a mathematical point of view, as DMFT corresponds to the exact solution of a quantum many body Hamiltonian in the limit of infinite dimensions ($d \rightarrow \infty$), the most intuitive way might be realized by building up a ‘‘dimensional’’ flow from $d = \infty$ to the actual dimensions (e.g., $d = 2$ or 3) of the problem of interest. In this case, one would start from the action of an infinite dimensional lattice (e.g., hypercubic) and the parameter Λ should gradually turn off the hopping in all directions, except the physical ones of the final problem.

This can be done considering the family of actions associated with the following Hamiltonians in the limit $d \rightarrow \infty$:

$$H^\Lambda = \sum_{\mathbf{k}\sigma} \left\{ \frac{1}{\sqrt{2d}} [f(\Lambda)\epsilon_{k_1 k_2} + \Lambda\epsilon_{k_3 \dots k_d}] - \mu \right\} c_{\mathbf{k}\sigma}^\dagger c_{\mathbf{k}\sigma} + U \sum_i n_{i\uparrow} n_{i\downarrow}, \quad (3.10)$$

with $n_{i\sigma} = c_{i\sigma}^\dagger c_{i\sigma}$.

Here the momenta in the first sum are d dimensional: $\mathbf{k} = (k_1, k_2, \dots, k_d)$ while the second sum extends over the lattice sites of a d dimensional lattice. The operators $c_{\mathbf{k}\sigma}^\dagger$ ($c_{\mathbf{k}\sigma}$) create (annihilate) a fermion of momentum \mathbf{k} and spin σ , $n_{i\sigma}$ is the number operator counting the fermions of spin σ at the lattice site i .

To be specific, let us assume that the energies $\epsilon_{k_1 k_2}$ refer to a two dimensional square lattice with nearest neighbors hopping t : $\epsilon_{k_1 k_2} = -2t(\cos k_1 + \cos k_2)$. The infinite dimensional limit of this lattice is obtained when $\Lambda = 1$ and $f(\Lambda) = 1$ taking $\epsilon_{k_3 \dots k_d} = -2t(\cos k_3 + \dots + \cos k_d)$. The factor $\frac{1}{\sqrt{2d}}$ accounts for the proper scaling: it guarantees that the kinetic energy does not diverge in the limit $d \rightarrow \infty$ (see sec. 1.5). The terms Λ and $f(\Lambda)$ are used to interpolate between the Hamiltonian in d and two dimensions. For example, assuming the following form for $f(\Lambda)$:

$$f(\Lambda) = 1 + (1 - \Lambda)(\sqrt{2d} - 1), \quad (3.11)$$

one recovers the $d \rightarrow \infty$ limit for $\Lambda = 1$, while for $\Lambda = 0$ one restores the two dimensional lattice Hamiltonian. To each Hamiltonian then, one can, in principle, associate an action \mathcal{S}^Λ . The most intuitive of doing this is just using the standard connection between the action and hamiltonian formulation:

$$\mathcal{S}^\Lambda = - \int_0^\tau \sum_{i\sigma} \bar{\psi}_{i\sigma} (-\partial_\tau + \mu) \psi_{i\sigma} - H^\Lambda[\psi, \bar{\psi}], \quad (3.12)$$

where $H^\Lambda[\psi, \bar{\psi}]$ is the Hamiltonian expressed in terms of the Grassman fields ψ and $\bar{\psi}$ instead of the usual creation and annihilation operators c and c^\dagger . It should be noted, however, that these actions are d dimensional: Formally even the final action should be written in terms of Grassman variables of a d dimensional lattice, and therefore it is not equal to the physical action

$\mathcal{S}_{\text{lattice}}$ (3.2), of the two dimensional lattice we are interested in. However, since at the end of the flow the hopping to the extra $d - 2$ dimensions is suppressed the corresponding Grassman variables are decoupled from the physical ones and can be integrated out.

A possible way of circumventing the problem is building “by hand” a family of action by defining an appropriate propagator for the gaussian part of the action that depends only on the two-dimensional physical momentum. This can be done rewriting the *interacting* Green’s function in the following way:

$$G^\Lambda(k_1, k_2; \omega_n) = \sum_{k_3, \dots, k_d} \frac{1}{i\omega_n - (1 - \Lambda)\epsilon_{k_1 k_2} - \Lambda \frac{\epsilon_{k_3 \dots k_d}}{\sqrt{2d}} + \mu - \Sigma^\Lambda(k_1, k_2, \omega_n)} \quad (3.13)$$

$$\stackrel{!}{=} \frac{1}{[\zeta^\Lambda(k_1, k_2, i\omega_n)]^{-1} - \Sigma^\Lambda(k_1, k_2, \omega_n)}. \quad (3.14)$$

This equation has to be seen as an implicit expression for the propagator ζ^Λ of the Gaussian part in the following action:

$$\mathcal{S}^\Lambda = \frac{1}{\beta} \sum_n \bar{c}_{k_1 k_2 \sigma}(\omega_n) [\zeta^\Lambda(k_1, k_2, i\omega_n)]^{-1} c_{k_1 k_2 \sigma}(\omega_n) + \mathcal{S}_{\text{int}}. \quad (3.15)$$

Equation (3.14) and (3.15) define a one parameter family of actions suited for a flow. In fact Eq. (3.13), in the beginning of the flow ($\Lambda = 1$) does not depend on k_1 and k_2 and reduces to the DMFT self consistency equation (1.125), which, is worth reminding, is exact in infinite dimensions. Therefore $\zeta^{\Lambda=1}(k_1, k_2, \omega_n) = \mathcal{G}_{\text{hyp}}(\omega_n)$, where $\mathcal{G}_{\text{hyp}}(\omega_n)$ is the gaussian propagator of the AIM which has the same local Green’s function of the infinite hypercubic lattice with rescaled hopping $t/\sqrt{2d}$, and the initial action \mathcal{S}_{hyp} would coincide with the solvable action of the AIM associated to the hypercubic lattice.

In spite of its rather intuitive picture, however, such “dimensional” flow equation scheme, is not the most suitable choice to be adopted in practice. The first reason is of practical nature: The gaussian propagator defined by Eq. (3.13) is extremely unpleasant, as it requires the inversion of an implicit equation that includes also the self-energy⁸. Since in the flow equation also the derivative of the propagator is required it is evident that a different definition of the propagator at intermediate scale Λ is required. The second, and most important, reason is of conceptual nature. In fact, one should consider that in most of its applications, and in particular in those aiming at the realistic description of materials, DMFT is employed as an *approximation* for describing the local physics of a given *finite*-dimensional system, and no limit of infinite dimensions is actually taken. Indeed, it would be rather cumbersome to define a rigorous and general procedure for connecting on a Hamiltonian level, case by case, a finite dimensional lattice with its infinite dimensional limit. In particular, the Hamiltonian for a real system involves complicated hopping amplitudes t_{ij} , which are not limited to the nearest neighbors and which are also often not isotropic. Therefore, even if it was the correct thing to do (and it is not, as

⁸Eq. (3.13) can actually be made explicit only in the case of a Lorentzian density of states, while it is well known that the density of states associated with the infinite dimensional hypercubic lattice is gaussian, see chapter about DMFT.

we discuss below), it would not be clear how to generalize the hoppings to those of an infinite dimensional lattice.

To understand why "generalizing the hopping" to $d = \infty$ is not the right thing to do, let us rethink of our goal, referring to the schematic representation of the flow of Fig. 3.3. We want to obtain the correlations in the action $\mathcal{S}_{\text{lattice}}$, which are difficult to access directly, because, in presence of \mathcal{S}_{int} , they have to be computed solving an integral over Grassman variables that go beyond the Gaussian term. fRG allows us to circumvent this integration. As discussed above, the first step is a different choice of the "solvable" action from $\mathcal{S}_{\text{initial}}$. This new action is represented by another point in the parameter space of Fig. 3.3. An usual choice in fRG would be an action \mathcal{S}_0 which is solvable because the fluctuations are completely suppressed by the choice of the Gaussian propagator, which often is assumed to completely vanish in the initial action. The choice of the explicit Λ -dependence of the propagator then singles out a path in the "action space". Integrating along this line we are able to obtain the correlations of $\mathcal{S}_{\text{lattice}}$. However, due to the truncation, some error is accumulated along the path. For this reason we want to start from an action which, besides being solvable, is also as close as possible, in some physical sense, to the final one. Therefore the question is: Which is the solvable action that, in a DMFT perspective, is closest to the lattice one? A possible choice is \mathcal{S}_{hyp} defined above. However a much better choice is given by the effective action of the DMFT solution ($\mathcal{S}_{\text{DMFT}}$), i.e., the action of the auxiliary AIM associated to the DMFT solution of the specific, finite dimensional problem of interest, i.e.:

$$\mathcal{S}_{\text{DMFT}} = - \int_0^\beta d\tau d\tau' \sum_{i\sigma} \bar{c}_{i\sigma}(\tau) \mathcal{G}_{\text{AIM}}^0(\tau - \tau')^{-1} c_{i\sigma}(\tau') + \mathcal{S}_{\text{int}}, \quad (3.16)$$

In fact we have seen in Sec. 1.5.2 that the action $\mathcal{S}_{\text{DMFT}}$ is the local action whose interacting Green's function equals the local Green's function of the problem of interest, under the DMFT approximation. It was also discussed that this action is obtained as the minimum of an appropriate functional of the local Green's function, which encourages our idea that it is closer to the final action.

The DMFT self consistency condition (1.125), which in the functional context arises naturally as a condition for the minimum of the functional, involves *only* the density of states of the lattice problem and no other details of the lattice, which in DMFT is the relevant quantity rather than the hopping itself. For example the density of states of the two dimensional lattice with nearest neighbors hopping:

$$\rho^{2D}(\epsilon) = \frac{1}{(2\pi)^2} \sum_{\mathbf{k}} \delta(\epsilon - \epsilon_{\mathbf{k}}), \quad (3.17)$$

is certainly different from the density of states of the initial Hamiltonian $H^{\Lambda=1}$, i.e., the density of states of the hypercubic lattice with nearest neighbors hopping, which is a Gaussian function. On the other hand it is possible, in principle, to find an *auxiliary* infinite dimensional Hamiltonian with hoppings \tilde{t}_{ij} so that its density of states equals $\rho^{2D}(\epsilon)$. For this auxiliary infinite dimensional Hamiltonian the DMFT solution is exact. Therefore we have two possible ways of looking at our starting point in DMF²RG:

- From an action perspective, we start our flow from the self-consistent action $\mathcal{S}_{\text{DMFT}}$ of the DMFT impurity problem that approximates the local physics of the lattice problem we want to study and we gradually attribute a momentum dependence to the gaussian propagator, until it equals G_{latt}^0 ;
- From an Hamiltonian perspective, we start our flow from an infinite dimensional auxiliary Hamiltonian with hopping amplitudes \tilde{t}_{ij} , and gradually change the hopping until the hoppings in $d - 2$ dimensions are suppressed and the Hamiltonian equals the two dimensional one.

This physically motivates our choice for the starting point of DMF²RG.

Now let us see how we can put in practice our intent of computing the correlation beyond DMFT, i.e. how do we single out a path in the parameter space, and perform the integration of the flow equations:

1. Find the impurity action $\mathcal{S}_{\text{DMFT}}$ whose self-energy and Weiss field fulfill the DMFT self consistency condition;
2. Solve the quantum many-body problem associated with this impurity action, extracting the 1PI one- $[\Sigma_{\text{DMFT}}(\omega_n)]$ and two-particle $[\Gamma_{\text{DMFT}}(\nu_1, \nu_2; \nu'_1, \nu'_2)]$ vertex functions;
3. Finally, use $\Sigma_{\text{DMFT}}(\omega_n)$ and $\Gamma_{\text{DMFT}}(\nu_1, \nu_2; \nu'_1, \nu'_2)$ as initial condition for the fRG flow-equations (3.8), (3.9) for the self-energy and the vertex functions.

This way the local correlated physics captured by DMFT will be present from the very beginning of the flow, and the local and non-local corrections to it will be generated unbiasedly in all channels by the fRG algorithm, via the numerical solution of the associated differential equations (see also section about the diagrams). The exact form of such equations is defined by the choice of \mathcal{S}^Λ (cutoff) and by the truncation scheme. While for the latter we have assumed the most simple truncation at the two-particle level, the cutoff choice will be discussed in the next subsection.

Cutoff scheme of DMF²RG

For DMF²RG, a quite natural cutoff choice is a linear interpolation of the Gaussian part ($G_\Lambda^0(\mathbf{k}, \omega_n)^{-1}$) of the action from $\mathcal{S}_{\text{initial}} = \mathcal{S}_{\text{DMFT}}$, where

$$\mathcal{S}_{\text{DMFT}} = - \int_0^\beta d\tau d\tau' \sum_{i\sigma} \bar{c}_{i\sigma}(\tau) \mathcal{G}_{\text{AIM}}^0(\tau - \tau')^{-1} c_{i\sigma}(\tau') + \mathcal{S}_{\text{int}}, \quad (3.18)$$

to $\mathcal{S}_{\text{fin}} = \mathcal{S}_{\text{lattice}}$. The interpolated Gaussian propagator reads explicitly:

$$G_\Lambda^0(\mathbf{k}, i\omega)^{-1} = f(\Lambda) \mathcal{G}_{\text{AIM}}^0(i\omega)^{-1} + [1 - f(\Lambda)] G_{\text{latt}}^0(\mathbf{k}, i\omega)^{-1}, \quad (3.19)$$

where $f(\Lambda)$ is an arbitrary smooth function of Λ such that $f(\Lambda_{\text{ini}}) = 1$ and $f(\Lambda_{\text{fin}}) = 0$. In practice without loss of generality one can take $f(\Lambda) = \Lambda$ with $\Lambda_{\text{ini}} = 1$ and $\Lambda_{\text{fin}} = 0$, as any

alternative choice of $f(\Lambda)$ can be reabsorbed in a change of variables in the integration of the flow equations.

We note that the cutoff scheme \mathcal{S}^Λ defined by Eq. (3.19) is similar to the ‘‘interaction cutoff’’ [72] in standard fRG, since it does not operate any selective cut on specific regions of the momentum and/or frequency space. The implementation of a cutoff analogous to the frequency cutoff in standard fRG, might read

$$G_\Lambda^0(\mathbf{k}, i\omega)^{-1} = [1 - \theta(|\omega| - \Lambda)]\mathcal{G}_{\text{AIM}}^0(i\omega)^{-1} + \theta(|\omega| - \Lambda)G_{\text{latt}}^0(i\omega, \mathbf{k})^{-1}, \quad (3.20)$$

where $\theta(x)$ is the Heavyside step function, or some smoothed version of it. Clearly, as long as the impurity problem $\mathcal{S}_{\text{DMFT}}$ does not show any infrared divergencies, this cutoff is regulating. Evidently all possible cutoff schemes are equivalent in the case of a non-truncated flow. In the actual implementation however, a frequency- or momentum-cutoff, which can regularize infrared divergences of the problem, might be more suited to study the regime in the proximity of (quantum) phase transitions. Its effective implementation, however, is numerically more involved than the simple cutoff of Eq. (3.19) and subject to future investigations.

3.0.4 Diagrammatic content

We will turn our attention now to the diagrammatic content of DMF²RG. The derivation of the diagrams included in DMF²RG follows directly from the diagrammatic analysis of fRG described in 1.4.2, and it will allow us to understand which diagrams are added to the standard diagrammatics of DMFT and fRG. This will allow us at the end of this section to compare the diagrammatic content of DMF²RG to the one of DΓA in its parquet and ladder implementations.

As we have discussed in 1.4.2, the diagrams generated by the integration of the flow equations can be written explicitly by formally solving the flow equations in an iterative fashion. The way this was done in Sec. 1.4.2 was quite general: We did not assume specifically any choice of the initial, condition, therefore what we have to do now is specializing to DMF²RG the results obtained there.

Let us first discuss the diagrammatic content of the DMFT initial condition and $\Sigma_{\text{DMFT}}(\nu)$ and $\Gamma_{\text{DMFT}}(\nu_1, \nu_2; \nu'_1, \nu'_2)$, trying to understand its relation with the standard fRG. The question can be posed in the following way: Let us suppose that we try to obtain the local (but nontrivial) initial condition of DMF²RG (i.e., the one- and two-particle 1PI vertices of $\mathcal{S}_{\text{DMFT}}$) using an fRG flow starting from an action \mathcal{S}_0 which suppresses all the fluctuations and flowing to the one of the auxiliary AIM. What diagrams would we lose compared to the initial condition obtained in DMFT? Of course if we were able to avoid the truncation of the flow equations we would obtain the same diagrams since both, fRG without truncation and the solution of the AIM in DMFT are exact. However in presence of a truncation, the fRG is not able to recover all the diagrams of the exact solution. In particular, with the usual truncation at the level of the three-particle vertex the fRG will reproduce only parquet-like diagrams (with the approximations already specified in Sec. 1.4.2). A typical diagram which is included in the DMFT solution of $\mathcal{S}_{\text{DMFT}}$ but not in the one of fRG, is the so-called ‘‘envelope diagram’’, shown in Fig. 3.5a).

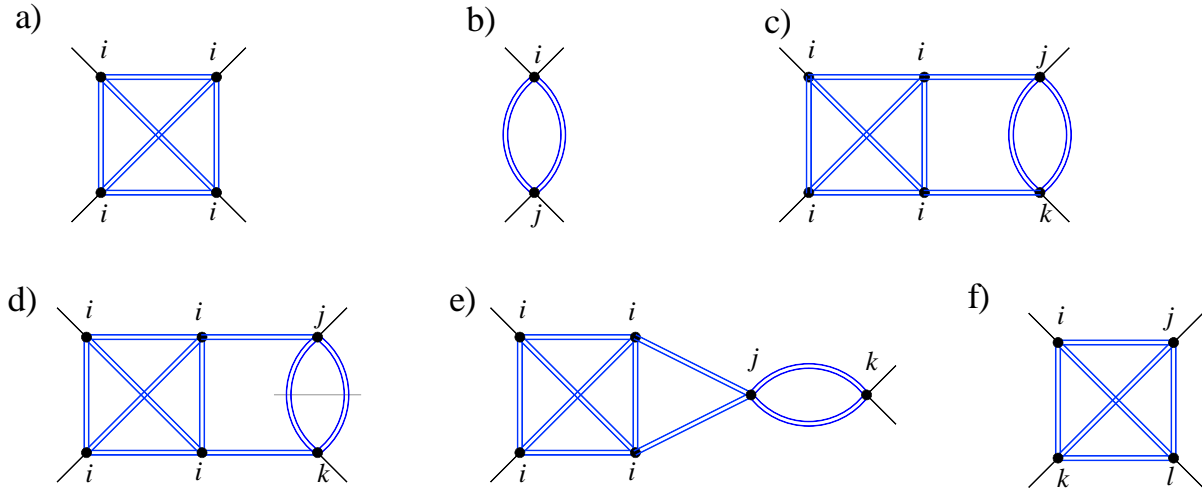


Figure 3.5: Examples of diagrams included in different theories. Diagram a) is included in DMFT, but not in fRG with truncation at the six point vertex; Diagram b) is included in fRG, but not in DMFT (as long as $i \neq j$); Diagram c) is included in D Γ A and, at a certain extent, also in DMF²RG. Diagram d) is the part of diagram c) which is neglected in DMF²RG; The line cutting the Green's function propagator stands for the fact that the integral over the derivative of the internal bubble is neglected. Diagram e) is included in DMF²RG, and in ladder-D Γ A, but only if $j = i$. Finally diagram f) is not included in any of the diagrammatic extensions of DMFT mentioned until now, unless all the site labels are equal (or if the distance between the sites is small, in the case of the $1/d$ expansion).

This diagram is the lowest order two-particle irreducible diagram, and can be generated in fRG only keeping vertices of an higher number of particles in the flow equations (see Sec. 1.4.2). More in general, the fRG truncated at the level of the three particle 1PI vertex will miss all the two particle irreducible diagrams contributing to the 1PI vertex Γ_{DMFT} . In turns, also the self-energy will be different. In truncated fRG, the self-energy is not related to the 1PI vertex by the equation of motion, but rather by perturbation theory-like equations and, together with the vertex, it does not fulfill exactly Ward identities [95]. On the other hand, this is not the case in DMFT: Since the self-energy and the vertex are obtained from the exact solution of the AIM, they are related by the equation of motion, and they respect the Ward identities.

Let us now focus on the diagrams that are generated along the flow. This can be understood specializing to the case of DMF²RG the discussion that was kept general in Sec. 1.4.2: The starting point of the flow is now constituted by Σ_{DMFT} and Γ_{DMFT} . All the *parquet-like* diagrams are now generated by building iteratively one-loop diagrams in all the channels with the 1PI two-particle vertex of DMFT, which, in this context, plays the role that is played by the bare interaction U in the diagrammatics of the parquet approximation (PA). To clarify this point, let us remind that the parquet equations form an exact set of equations [22] when the *fully-irreducible* two-particle vertex, momentum and frequency dependent, is known and used to build all the two-particle reducible diagrams (in all the channels). The simplest approximation, namely the parquet approximation, early introduced by the Soviet school [142], consists in

substituting the bare interaction U to the fully-irreducible two particle vertex, i.e., suppressing its frequency and momentum dependence and works only for small interaction values.

We should emphasize here that the term *parquet-like* diagrams is used in the same sense specified in Sec. 1.4.2 as opposed to the more standard diagrams of the PA. It is necessary to make this difference since in truncated fRG, and hence in DMF²RG, the diagrams generated by the flow have the topological structure of the PA diagrams, but are not computed exactly. In fact, the truncation has two consequences. The first one is that, instead of generating all the diagrams one is restricted to the PA ones. The fully irreducible diagrams, at the one-loop truncation level, are discarded. At higher truncation levels only the lowest order fully irreducible diagrams are generated, the maximum order of generated irreducible diagrams depending on the specific truncation level. The second consequence is that the diagrams are not computed exactly even within the PA. To understand what is the neglected contributions one can imagine a parquet diagram as a sequence of nested loops. In fRG, the Green's function lines that constitute these loops acquire a Λ -dependence. Any given diagram can be then formally obtained by an iterative integration of the flow equations as shown in Sec. 1.4.2. As discussed in Sec. 1.4.1, the derivative of the diagram is given by a sum of diagrams in which one Green's function line is substituted by its Λ -derivative represented by a smashed line, representing a Λ -derivative of the Green's function, see Eq. (1.63) and Fig. 1.14. Without truncation all these diagrams, with one smashed line substituting a propagator line are generated by the fRG flow equations. In presence of truncation, however, this is not the case. Truncating at the level of the n -particle vertex only diagrams in which the derivative acts on the $n-1$ outermost loop lines are generated, while the remaining contribution is neglected. This explains the nomenclature ‘‘parquet-like’’: The diagrams generated in truncated fRG share the same topology with the parquet diagrams, but reproduce them only partially. The definitive quality of this approximation crucially depends on a proper choice of the cutoff, that, as it is argued in Sec. 1.4.2, can be used to minimize the effects of the neglected contributions.

After this necessary remark we can go back, now, at the analysis of the DMF²RG diagrammatic content. A better approximation, compared to the PA, is obtained with D Γ A, by replacing the two-particle irreducible vertex in the parquet equations by the local fully irreducible vertex of DMFT⁹, i.e. its momentum dependence is suppressed while the frequency dependence is retained. Hence one includes all the local fully irreducible diagrams nonperturbatively, while the (mostly nonlocal) corrections to DMFT for the 1PI vertex and the self-energy are obtained through the parquet equations. An example of a diagram obtained in this way is shown in Fig. 3.5c): two non-local loops, involving the Green's function G_{ij} are built on the irreducible local ‘‘envelope’’ diagram. The diagrams of DMF²RG are topologically very close to the ones of D Γ A. In fact in both theories, all the local 1PI diagrams (two-particle reducible and irreducible) are included¹⁰, while all nonlocal diagrams are of the parquet type: Two particle reducible in

⁹In the full D Γ A treatment, the local vertex is not necessarily the one of DMFT, but can to be obtained in a self-consistent way, with the self-consistency being at the two-particle level rather than at the one-particle one [176].

¹⁰Let us stress again that when we refer to *local diagrams* strictly speaking we mean the diagrams of an auxiliary self-consistent AIM, where the self consistency is at the one-particle level (DMFT and DMF²RG) or at the two-

one channel. The main difference is that in DMF²RG the diagrams are do not coincide exactly with the ones generated by the parquet equations, as we discussed above: For example a diagram with the topological structure of the one in Fig. 3.5c) is clearly included in DMF²RG, since it consists of two non-local loops, built on a local fully irreducible vertex, but is not computed exactly. The neglected contribution equals the integral over Λ of the diagram shown in Fig. 3.5d), where each Green's function line has to be intended Λ -dependent, and the Λ -derivative acts on the two smashed lines.

At a first glance, moreover, one might be puzzled by yet another apparent difference: While in D Γ A the non-local parquet diagrams are built on the fully irreducible local vertex, in DMF²RG one builds them starting from the 1PI local vertex. In fact, trying to use the 1PI local vertex directly in the parquet equations of D Γ A would generate the local parquet diagrams twice, since they are already included in the 1PI local vertex $\Gamma_{\text{DMFT}}(\nu, \nu', \omega)$, with dramatic double counting issues. Consequently in D Γ A it is necessary to use the fully irreducible vertex $\Gamma_{\text{AIM}}^{\text{irr}}$, which is, however, a much more complicated object to deal with, as we explain below. It is important to stress here that, instead, there is no double counting of diagrams in DMF²RG. In fact (cf. Sec. 1.4.2) it is the fRG formalism itself that takes care of this double counting: In the formal iterative solution of the flow equations, the 1PI vertex at the iteration $n + 1$ can be obtained from an integral from Λ_{ini} to Λ_{fin} of Eq. (3.9), where the right hand side is computed from the vertex and the Green's function at the previous iteration n -th iteration. If one was able to integrate the flow equations without the truncation, one could perform the integral over Λ analytically and obtain, at this iteration step, a collection of diagrams, where the Green's function lines have to be computed at the boundaries of the integral, while the interaction vertex is held fixed at its initial value Γ_{DMFT} . Evaluating the upper boundary of the integral we generate the new diagrams which involve non-local lines with momentum dependent Green's function $G^{\Lambda=\Lambda_{\text{fin}}}(\mathbf{k}, \omega) = G_{\text{Latt}}^0(\mathbf{k}, \omega)$. The evaluation of the lower boundary gives topologically identical diagrams with opposite sign and with some of the Green's function lines evaluated at the beginning of the flow, i.e., in DMF²RG, local. This is the contribution that would otherwise be counted twice and, in this way, is removed completely. In presence of truncation the analytical integration is not possible anymore, or is possible only in the very first iteration steps. On the other hand the role of lower boundary of the integral remains the same, i.e., subtracting the 1PI parquet-like diagrams which fall apart cutting two *local* lines¹¹. In the D Γ A framework several results can be obtained using a ladder approximation, in a selected channel, instead of solving the parquet equations (ladder-D Γ A). In this way it is possible to include important non-local contributions which might be essential for the physics of the system, but the competition and the feedback between the channels is missed, so the applicability of this scheme crucially depends on the physical problem of interest. On a diagrammatic point of view, the diagram c) in Fig. 3.5 is not included in ladder-D Γ A, because it includes two bubbles that belong to ladders

particle level D Γ A. Hence, even with the same topology the local Green's function lines might not be the same.

¹¹Let us remark that this is possible only because in our approach we do not touch the interaction part of the action along the flow. If the interaction part of the action, instead, is changed one might need involved corrections to avoid double counting of diagrams [145].

in different direction. Diagram 3.5e) instead is included, but only provided that $j = i$.

From the discussion above we evince that the diagrammatic content of DMF²RG is topologically similar with the one of D Γ A, when the latter is solved in its parquet implementation. This implementation of D Γ A, to which we refer as *parquet*-D Γ A, however is extremely demanding numerically, and only recently it have started to be explored. There are two main difficulties in this implementation. The first one is, obviously, of technical nature, as the set of parquet equations are extremely difficult to solve [187]. The second issue is much deeper: The input of the parquet equations of D Γ A is the local two-particle irreducible two-particle vertex Λ_{irr} in DMFT. This quantity is neither directly accessible via a measuring process in QMC, nor can be computed in ED using a Lehmann representation. Rather it can be obtained starting from the two-particle Green's function and inverting a set of Bethe-Salpeter equations. Besides the technical complication of this operation, the second problem, is related to the strong-coupling divergencies of the irreducible vertex. In fact it has been reported [85, 160], that the fully irreducible vertex of DMFT diverges at low frequencies even well *before* the Mott transition takes place. This divergence is not connected with any symmetry breaking and does not cause any non-analytic behavior of the response functions. In fact, the physical origin of the divergence still remains elusive, although it has been argued that it represents a *precursor* of the Mott transition, as it should always take place at lower values of U than those of MIT (see Ref. [85, 160]). Independently of its physical interpretation, it is evident that in presence of this divergence, it is not possible to obtain the fully irreducible local vertex without running into this singularity problem, and as also stated in Ref. [85], it is preferable to reformulate the parquet equations in a way that they do not involve the 2PI vertex, but rather the 1PI, which is exactly what is done in DMF²RG.

3.1 Application to the 2D Hubbard model

As a first application of DMF²RG, we now show, results for a prototypical model of correlated fermions, the two-dimensional Hubbard model. We recall that many aspects of its physics, and especially the interplay of antiferromagnetism and superconductivity in this model have been studied by weak coupling truncations of different versions of the fRG already some time ago [57, 69, 91, 189]. More recently, these analysis have regained some attention in the context of fRG studies that include the frequency dependence of the interactions either fully on a smaller number of frequencies [178], or using a decomposition into fermionic bilinears [79]. In standard second-quantization notation, the Hubbard Hamiltonian with nearest-neighbors hopping, on which we are going to focus, reads [77]:

$$H = -t \sum_{\langle ij \rangle \sigma} c_{i\sigma}^\dagger c_{j\sigma} + U \sum_i n_{i\uparrow} n_{i\downarrow}, \quad (3.21)$$

where t denotes the nearest-neighbor hopping amplitude on a square lattice and U the local Coulomb repulsion. In the following, we will define our energies in terms of $4t \equiv 1$, and fix the average particle density to half filling $n = 1$. In this case, the momentum transfer of $(\pi, \pm\pi)$

corresponds to perfect (antiferromagnetic) nesting on the square shaped Fermi surface. As we have discussed in Sec. 3.0.1 the two dimensional Hubbard model is considered to be prototypical for the cuprates, and therefore it has been largely studied in that context. This applies, however, to cases with slightly different fillings and including also next nearest neighbors hopping, which show a rich phase diagram and different competing instabilities. As a test case for a new method, instead, we found more convenient to focus on a more simple situation, where the physics is largely dominated by the tendency towards antiferromagnetic fluctuations, due to the perfect nesting. Let us recall that, while the physics at weak coupling can be easily understood in terms of nesting of the Fermi surface. At stronger coupling other physical mechanism become more important. This has been analyzed systematically is the case for the Hubbard model in infinite dimensions, studied in Refs. [158] and [171], it is shown that even if at weak- and strong- coupling the ground state is antiferromagnetic, the physical mechanism that drives the symmetry breaking is very different: at weak-coupling the onset of long-range is stabilized by a gain in the potential energy, while at strong coupling by a gain in the kinetic energy.

In our DMF²RG study we integrated the truncated flow equations numerically, by means of a sixth order Runge-Kutta method. We have included the self-energy feedback in the equations for the self-energy Σ^Λ and for the vertex Γ^Λ . To keep the numerical effort under control we used a channel decomposition of the interaction vertex similar to the one of Ref. [94], while we decided to discretize the Brillouin zone in square patches, without making any further specific approximation, like those of [78, 79] where the momentum dependence is fixed to a specific choice of form factors. The details about the vertex parametrization are given below.

Parametrization of the two-particle vertex

Before describing our parametrization, let us focus on the 1PI vertex main features. The two-particle vertex is a difficult quantity to study numerically, since already in the one band translational invariant case, it depends on three momenta and three frequencies, making a numerical analysis quite demanding (even in simple terms of storage memory). In recent¹² years, however, also thanks to the increased computational power, the two-particle vertex has started to be investigated in its complexity. Most of the studies, however, focused only on some of the features of the vertex, and, even nowadays, a comprehensive and systematic knowledge of the frequency and momentum behavior of this object is partially missing. In fact, the momentum dependence of the vertex has been analyzed (at weak coupling) in several fRG studies while its frequency dependence has been explored in the DMFT framework. A simultaneous treatment of its frequency and spatial argument, instead, has been obtained within a DCA study of the dynamical susceptibilities (e.g., see Ref. [118]), and in a DCA approach based on fRG as cluster solver [100, 101].

More in detail, the momentum dependence of the vertex has been explored within the N -

¹²Some semi analytical studies of the vertex has been performed focusing on specific limits of the frequency arguments, with a more direct connection to physical properties of the system under consideration. For example the two particle vertex has been studied in relation to the Fermi liquid properties of a system in Refs. [39, 40].

patch renormalization group scheme [75, 157], in which one neglects the frequency of the vertex and divides the Brillouin zone into N patches. The momentum dependence of each patch is then projected onto the Fermi surface. This way it is possible to observe a nontrivial momentum dependence of the vertex arising along the flow, strictly related with the emergent leading instabilities of the system. A different approach to deal with the frequency dependence is the one first proposed by Husemann and Salmhofer [79], where the vertex is decomposed in three channels and for each channel the main momentum dependence is identified and treated with higher accuracy, while the dependence on the other two momenta is limited to a restricted set of basis functions.

A complementary line of investigation is the one followed in the DMFT framework [54, 110, 149]. In this case one focuses on the local two-particle vertex of the auxiliary AIM (by definition momentum independent) keeping fully the Matsubara frequency dependence. The calculation of the vertex can be then performed, numerically exactly, either using quantum Monte Carlo methods [54] or by means of exact diagonalization [148, 149]. In particular in ED, our method of choice in the calculation of the vertex that we are showing in the following, one can compute the two-particle Green's function using the Lehman representation, and from it one can extract the irreducible vertex, by amputating the external legs [134]. A drawback of the method is that the bath has to be discretized and described by a small number of bath sites, which in our case was five. This is, however, already enough to observe the nontrivial frequency structures of the vertex. We have also checked that the frequency structures that we observe are in good agreement with the ones computed in QMC using the vertex computed using the w2dynamics code [139] by M. Wallerberger.

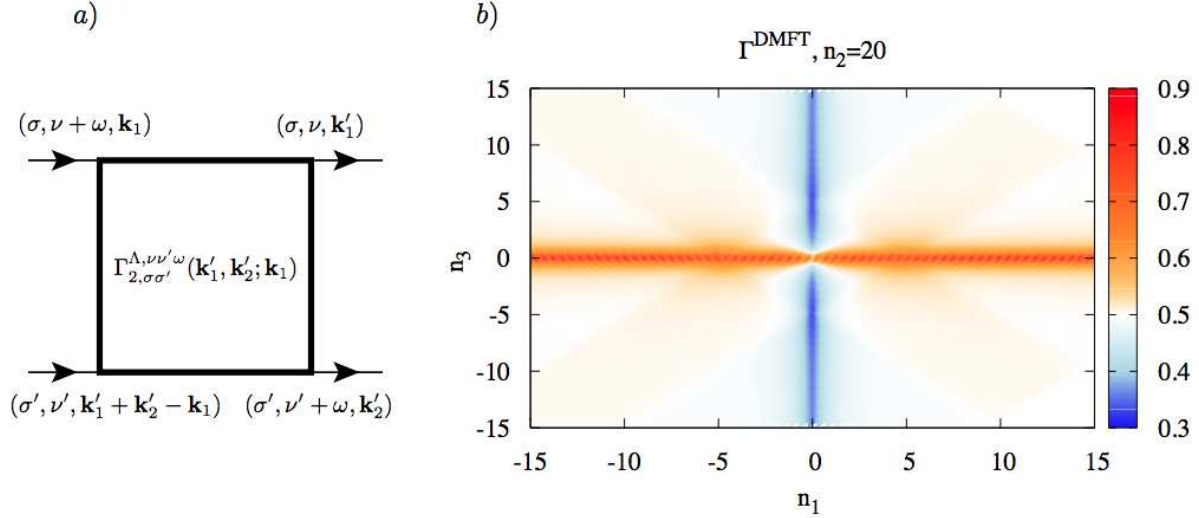


Figure 3.6: On the left, diagrammatic representation of the two-particle 1PI vertex function $\Gamma_{2,\sigma\sigma'}^{\Lambda,\nu\nu'\omega}(k'_1, k'_2; k_1)$; the arrows mark the position of the incoming and outgoing electrons. On the right, DMFT vertex function $\Gamma_{2,\uparrow\downarrow}^{\Pi\Delta X}$ as a function of Π and X at fixed Δ ($\Delta = 2\pi T n_2$; $n_2 = 20$) for the Hubbard model on a three dimensional cubic lattice with nearest neighbors hopping and $U = 0.5D$, $T = 0.038D$ (D measures the half bandwidth). The color coded values are measured in units of D . Please note that in DMFT the main features of the vertex *do not* depend significantly on the details of the lattice, but mostly on the bandwidth, or more precisely, on the second momentum of the density of states, therefore the following considerations apply in general, including the two dimensional case described in the main text. The white background color corresponds to the asymptotic value U reached by the vertex. On the top of this, one can recognize three structures: *i*) a vertical line at $\Pi = 0$, *ii*) a horizontal line at $X = 0$, and *iii*) a broader (hardly discernible at this U value) cross structure on the diagonals at $\Pi = \pm X$. The origin of the three structures has been analyzed in Ref. [149]. While the structures *i*) and *ii*) are well reproduced by the frequency dependence approximation described in the text, the cross structure is not captured by the approximation. Please notice that the white corners on the right of the density plot correspond to frequencies not included in the frequency window of our data set.

To show the frequency structures of the vertex, we use here the conventions¹³ and definitions of Ref. [149] (in particular in “*particle-hole notation*”). In general for an SU(2) symmetric interaction and for a single band translationally invariant system -- as we show in Fig. 3.6a)-- the vertex function depends on two spins, three frequencies, and three momenta variables, while the fourth frequency and momentum can be fixed requiring energy and momentum conservation:

¹³Please note, however, that there the two-particle 1PI vertex is labeled F and does not depend on the momenta, while here it is called Γ_2^{Λ} , and is in general momentum dependent.

$$\Gamma_{2,\sigma\sigma'}^{\Lambda,\nu\nu'\omega}(\mathbf{k}'_1, \mathbf{k}'_2; \mathbf{k}_1) := \Gamma_2^\Lambda \left(\underbrace{\nu\mathbf{k}'_1\sigma, (\nu' + \omega)\mathbf{k}'_2\sigma'}_{\text{outgoing electrons}} ; \underbrace{(\nu + \omega)\mathbf{k}_1\sigma, \nu'(\mathbf{k}'_1 + \mathbf{k}'_2 - \mathbf{k}_1)\sigma'}_{\text{incoming electrons}} \right). \quad (3.22)$$

Here ν and ν' are fermionic Matsubara frequencies, while ω is a bosonic Matsubara frequency. Physically this describes the scattering of a hole of energy $-\nu$ with an electron of energy $\nu + \omega$.

As we have discussed in Sec. 1.4.2 the most natural frequency parametrization for the weak coupling structure, that can be also used for the implementation of a frequency parametrization similar to the one of previous fRG studies [94] is a notation in terms of three *bosonic* Matsubara frequencies [94] defined as follows:

$$\Pi = \nu + \nu' + \omega, \quad (3.23)$$

$$\Delta = \nu - (\nu + \omega) = -\omega, \quad (3.24)$$

$$X = \nu' + \omega - (\nu + \omega) = \nu' - \nu. \quad (3.25)$$

As for the spin indexes by exploiting the SU(2) symmetry we have [100, 148]:

$$\Gamma_{2,\uparrow\uparrow}^{\Lambda,\Pi\Delta X}(\mathbf{k}'_1, \mathbf{k}'_2; \mathbf{k}_1) = \Gamma_{2,\uparrow\downarrow}^{\Lambda,\Pi\Delta X}(\mathbf{k}'_1, \mathbf{k}'_2; \mathbf{k}_1) - \Gamma_{2,\uparrow\downarrow}^{\Lambda,\Pi\Delta X}(\mathbf{k}'_2, \mathbf{k}'_1; \mathbf{k}_1). \quad (3.26)$$

Hence, we can concentrate on the vertex $\Gamma_{2,\uparrow\downarrow}^\Lambda$ only (all the other spin combinations can be obtained by symmetry) [93, 148].

Even by restricting ourselves to the $\uparrow\downarrow$ sector, the vertex function $\Gamma_{2,\uparrow\downarrow}^\Lambda$ displays, in general, a rather complicated structure in momentum and frequency space.

To keep under control the numerical effort required by our first DMF²RG calculations we decided to parametrize the frequency dependence of $\Gamma_{2,\uparrow\downarrow}^\Lambda$ following previous experience in fRG studies [94], as follows:

$$\Gamma_{2,\uparrow\downarrow}^{\Lambda\Pi\Delta X}(\mathbf{k}'_1, \mathbf{k}'_2; \mathbf{k}_1) \approx U + \tilde{\Gamma}_{2,\text{pp}}^{\Lambda,\Pi}(\mathbf{k}'_1, \mathbf{k}'_2; \mathbf{k}_1) + \tilde{\Gamma}_{2,\text{ph-d}}^{\Lambda,\Delta}(\mathbf{k}'_1, \mathbf{k}'_2; \mathbf{k}_1) + \tilde{\Gamma}_{2,\text{ph-c}}^{\Lambda,X}(\mathbf{k}'_1, \mathbf{k}'_2; \mathbf{k}_1). \quad (3.27)$$

This corresponds to approximating the complicated dependence of $\Gamma_{2,\uparrow\downarrow}^\Lambda$ on the three bosonic frequencies Π , Δ , X , assuming that the scattering amplitude among two particles can be completely decomposed in three different channels, particle-particle, particle-hole direct, and particle-hole crossed (pp, pp - d, ph - c). This assumption is not exact for a generic U , as one could immediately see already by looking at the DMFT vertex function, like the one shown in Fig. 3.6. Following Ref. [94], for the single impurity Anderson model, or Ref. [79], for a lattice system, one can derive the flow equations directly for the functions $\tilde{\Gamma}_{2,x=\text{pp,ph-d,ph-c}}^\Lambda$. This is possible because one can associate each function with a specific channel: particle-particle, particle-hole direct and particle-hole crossed, and attribute uniquely¹⁴ each diagram to a specific channel.

As described in detail in Refs. [94, 149], the bosonic frequency parametrization and decomposition of the vertex is consistent with the lowest-order perturbation theory for $\Gamma_{2,\uparrow\downarrow}^\Lambda$, see also

¹⁴At least at the truncation level of the three-particle vertex [41].

Sec. 1.4.2. In fact, each bosonic frequency correctly describes the frequency transfer associated with the lowest order [$\mathcal{O}(U^2)$] nontrivial¹⁵ diagrams contributing to the 1PI vertex. These diagrams are simply fermionic loops in the three channels, and with each of them is associated one of the three bosonic momentum transfers. This way, the bosonic frequency parametrization and vertex decomposition capture the main vertex structures up to $\mathcal{O}(U^3)$ and one expects them to be reliable for moderate values of U . The neglected structures appearing on the diagonals, instead, can be easily associated to processes in which one of the incoming or outgoing frequencies is small, and mainly arise from diagrams of third order in the interaction. Hence, at weak coupling, these structure will be suppressed compared to the vertical and horizontal ones. However, when the value of U is increased, the structure not captured by Eq. (3.27) will become gradually more important, making the vertex decomposition unreliable. This is one of the reason why we have hitherto restricted our numerical study to moderate U values in the following.

The last point left to be discussed is how to extract the initial condition for the three functions in Eq. (3.27) from the fully frequency dependent DMFT vertex $\Gamma_{\text{DMFT}}^{\Pi\Delta X}$ which contains more information than we need for the decomposed vertex. By looking at Fig. 3.6b), one sees that the problem consists in how to get rid of the cross structure (labeled *iii*) in the caption of Fig. 3.6 which depends on all the frequencies. However, the structure under consideration fades out becoming gradually broader and less intense as the third frequency is increased. Therefore to extract one of the three functions, say, e.g., $\tilde{\Gamma}_{2,\text{pp}}^{\Lambda_{\text{ini}},\Pi}$, it suffices to take a cut in Γ_{DMFT} keeping Δ and X fixed at some very large values $\bar{\Delta}$ and \bar{X} :

$$\tilde{\Gamma}_{2,\text{pp}}^{\Lambda_{\text{ini}},\Pi}(\mathbf{k}'_1, \mathbf{k}'_2; \mathbf{k}_1) = \Gamma_{\text{DMFT}}^{\Pi\bar{\Delta}\bar{X}}. \quad (3.28)$$

Even within this approximated scheme for the frequency dependence, to further speed up the calculations, we have found useful to consider only the Matsubara frequencies on a given grid, inspired to the logarithmic grid used in Ref. [94] for the $T = 0$ case. Practically, instead of taking all the (bosonic) Matsubara frequencies associated with any integer $n < N_{\text{max}}$, with N_{max} the number of frequency used in the calculation, we have considered only the (positive and negative) frequencies associated with the integers defined by:

$$n_i = \begin{cases} i, & \text{if } i \leq a; \\ a + 2(i - a) & \text{if } a < i \leq 2a; \\ 3a + 4(i - a) & \text{if } 2a < i \leq 3a; \\ \dots & \end{cases} \quad (3.29)$$

with a being some integer number, while whenever in the flow it was necessary to compute the vertex at a frequency not belonging to the grid we have used a linear interpolation. This choice is well motivated considering that the bosonic structures have only a rather small spread around zero frequency, and therefore the only thing that one has to check is that a is large enough to describe accurately these structures, while less accuracy is required by the large frequency tails.

¹⁵We do not consider here the trivial constant "background" of the vertex equal U .

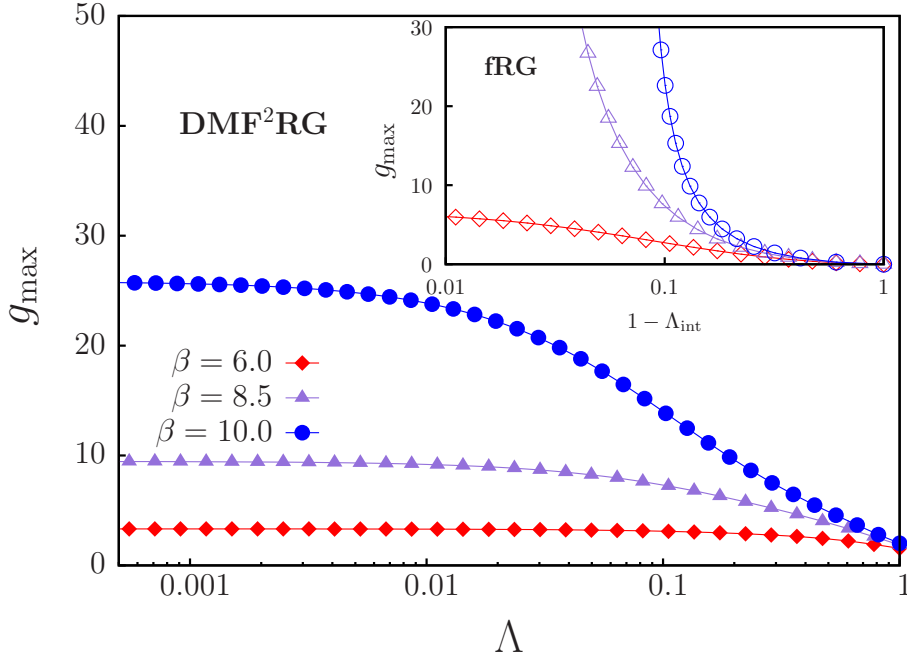


Figure 3.7: Flow of the largest component (g_{\max}) of the two-particle vertex function, i.e., in our case, Γ in the particle-hole crossed channel, for zero transfer frequency ($\nu_2 - \nu'_1 = 0$), antiferromagnetic momentum transfer ($\mathbf{k}_2 - \mathbf{k}'_1 = (\pi, \pi)$) and $\mathbf{k}_1 = (0, \pi)$, $\mathbf{k}_2 = (\pi, 0)$ computed by fRG, with interaction cutoff Λ_{int} [72] (inset) and DMF²RG (main panel) for the two-dimensional half-filled Hubbard model at $U = 1$, at different (inverse) temperatures.

On the other hand this choice of frequencies on a grid should not be expected to work well in the description of the full frequency dependent vertex, since it would fail in the description of the diagonal structures, which are not centered at small values of any of the bosonic frequencies.

Our momentum parametrization is a tradeoff between computational effort and accuracy of the description: The momentum-dependence is taken into account by discretizing the Brillouin zone into patches with constant coupling function. If fine enough, this discretization captures the angular variation of the coupling function along the Fermi surface with good precision. For simplicity, we restrict ourselves to 8 patches, which already includes important physical aspects of the $2D$ system [50]. We decided for this kind of parametrization to avoid the restriction of the momentum dependence to specific form factors, like in [79], and rather have a coarse, but general, description of the momentum dependence of the vertex. This is probably one of the parts of our calculation that can be most easily improved in a systematic way, in particular making use of some of the symmetries of the vertex in momentum space.

Numerical results

Our calculations for the two-particle vertex function and self-energy are reported in Figs. 3.7 and 3.8-3.9, respectively. In Fig. 3.7 we plot the largest component (g_{\max}) of the vertex function, which -- at half-filling -- is found in the particle-hole crossed channel for zero frequency and

antiferromagnetic momentum transfer: $\mathbf{k}'_2 - \mathbf{k}_1 = (\pi, \pi)$. This reflects the tendency of the system to antiferromagnetic ordering due to the perfect nesting of the Fermi surface.

The data, which refer to a weak-intermediate regime ($U = 1$), clearly show that the DMF²RG mitigates the fRG tendency to a low- T divergence of the flow: We still obtain a converged DMF²RG result for g_{\max} at $\beta = 1/T = 10$, whereas the fRG flow for the vertex is manifestly divergent. The fRG data presented in Fig. 3.7 have been obtained with the interaction cutoff, but we have verified that these results are robust with respect to the choice of the cutoff, by comparing the data also with those obtained with a sharp frequency cutoff, like the one of Ref. [94]. We also remind here that the interaction cutoff is not regularizing, but this problem is mitigated by the fact that we are working at finite temperature, and, on the other hand, this cutoff is the most similar to the simple cutoff that we have chosen for DMF²RG.

Quantitatively, by fixing an upper-bound for g_{\max} , we observe that the temperature at which it is reached is slightly decreased in DMF²RG compared to fRG for moderate values of the interaction (up to $U = 0.75$) while is significantly decreased from $T \sim 0.125$ (fRG) to ~ 0.085 (DMF²RG) at $U = 1$. This is attributed to the damping effect of the local correlations, captured from the very beginning in the flow of DMF²RG. In fact the DMFT self-energy is included in the propagators from the beginning of the flow, making them less metallic. We emphasize that this ‘‘divergence’’, observed also in DMF²RG, is *not* associated with a true onset of a long-range order. In principle, it is possible to adapt the fRG scheme to access also the disordered phase at lower T [17], though such an extension goes beyond the scope of the present thesis. The growth of the 1PI vertex, in fact, is associated, to a tendency of the system towards a strong coupling regime [157], where the form of the interaction is usually simplified, because some dominant term in the coupling appear, each corresponding to some emergent instability. However, extending the analysis about the ‘‘three regimes’’ of the flow defined in Ref. [157], i.e., a first regime associated with high energy scales, a second one in which the couplings grow, and a third one of strong coupling, to the case of DMF²RG, also depending on the specific choice of the cutoff, is a nontrivial task, considering that the initial condition, for larger values of the coupling, might already include nonperturbative effects from the three- and more particle vertex.

Let us also note here that the temperatures for which the leading coupling diverges are rather high. In particular these temperatures are higher than the Néel temperature of DMFT [99, 147] (which, in DMFT, is also finite, violating the Mermin-Wagner theorem [128]). With our present setup it is difficult to rationalize this empirical observation. On the one hand thinking of the ‘‘divergence temperatures’’ in terms of Néel temperature is somewhat misleading, as explained above. On the other hand, it cannot be excluded that this divergence temperatures in DMF²RG are artificially enhanced by our approximation to the vertex. In particular, while it is difficult to understand what might be the effect of using a fully frequency dependent vertex, one can expect that increasing the number of momentum patches will decrease the divergence temperature. In fact, the coarse discretization of the Brillouin zone might artificially enhance the feedback in the flow equation of combinations of momenta for which the vertex is particularly large. For example the vertex with momentum transfer (π, π) will represent several momentum transfers

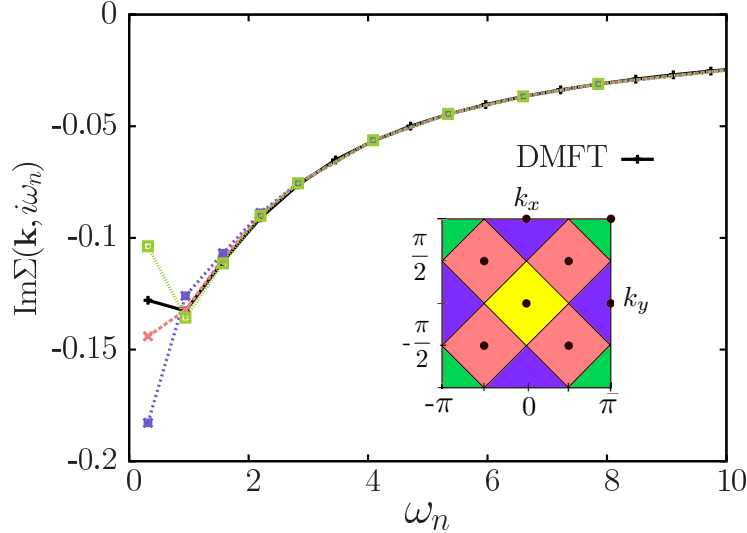


Figure 3.8: Comparison of the results for the imaginary part of the fermionic self-energy of the two-dimensional Hubbard model for $U = 1$, and $\beta = 10$, calculated within DMFT (\mathbf{k} -independent, in black) and DMF²RG, for different \mathbf{k} -vectors (the color coding of the different \mathbf{k} is defined in the inset, note that the values of $\text{Im}\Sigma(\mathbf{k}, i\omega_n)$ for $\mathbf{k} = (0, 0)$ and (π, π) coincide because of the particle-hole symmetry). *Inset:* Scheme of the 8-patches discretization used for the calculations.

within the discretized patches, on the right hand side of the flow equations. This is empirically confirmed by the fact that using a coarser discretization of the Brillouin zone, using only four patches, leads to much larger divergence temperatures. A definitive answer to this question, however, can only be given by comparing with further, improved, implementation of DMF²RG.

Self-energy We now turn to the analysis of the self-energy results obtained with the DMF²RG flow at the lowest temperature considered, i.e., $\beta = 10$. Here, the fRG flow diverges, and it is worth to compare the DMF²RG results with the original DMFT data, see Fig. 3.8. As expected in $2D$, the non-local correlations captured by the DMF²RG strongly modify the DMFT (\mathbf{k} -independent) results, determining a significant momentum dependence of the self-energy at low frequencies: While in DMFT a metallic solution, with a moderate Fermi-liquid renormalization of the quasi-particle mass, is obtained, in DMF²RG we observe a strong enhancement of the imaginary part of the self-energy at the Fermi surface. In fact, at the ‘‘antinodal’’ point $(\pi, 0)$, where the largest value of $-\text{Im}\Sigma$ is found, the low-frequency behavior is manifestly non quasi-particle-like, indicating the destruction of the Fermi surface in this region of the Brillouin zone. Deviations from the DMFT metallic results, albeit less marked, are found at the ‘‘nodal’’ point $(\frac{\pi}{2}, \frac{\pi}{2})$, for which one cannot exclude, at this temperature, a residual presence of strongly damped quasi-particle excitations. The significant reduction of $-\text{Im}\Sigma$ w.r.t. DMFT, observed

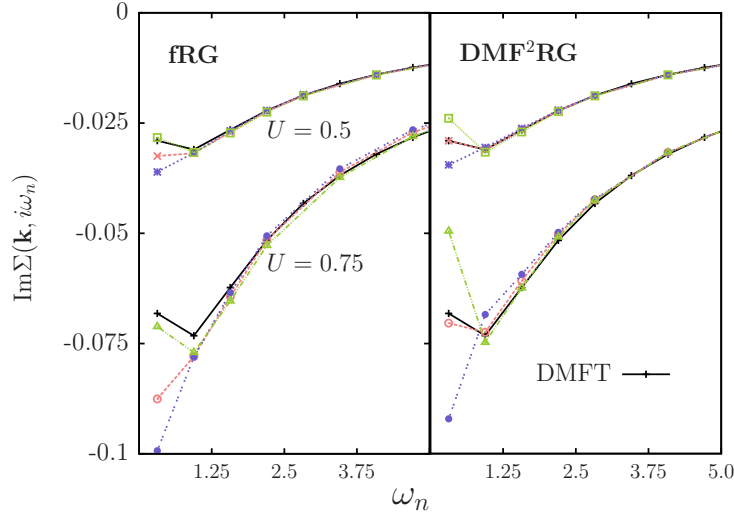


Figure 3.9: Comparison of the imaginary part of the self-energy for $U = 0.5, 0.75$, $n = 1$, and $\beta = 10$, calculated by fRG and DMF²RG, for different \mathbf{k} -vectors (color coding as in Fig. 3.8).

at $(0,0)$ or (π,π) , does not imply metallicity since these points are far away from the Fermi surface; and the real part of the self-energy is also strongly enhanced w.r.t. DMFT.

In Fig. 3.9, we compare the DMF²RG self-energy data with the fRG. The comparison can only be performed at weaker coupling and/or higher T than in Fig. 3.8, as the fRG flow needs to converge. Our numerical data of Fig. 3.9 indicate that in the considered parameter region (same T , but weaker interaction than in Fig. 3.8) the fRG and DMF²RG yield qualitatively similar results for the \mathbf{k} dependent self-energy. Considering that in DMF²RG *local* correlations have been included non-perturbatively via DMFT, this confirms the validity of previous fRG analysis of the Hubbard model at weak and moderate interaction. At the same time, the applicability of DMF²RG goes beyond the weak-to-intermediate coupling of the fRG, allowing for the study of parameter regions where the Mott-Hubbard physics “already” captured by DMFT becomes important.

As a further test, we have directly compared the self-energy of DMF²RG with the one of DCA. Unfortunately, in the DCA or cDMFT literature it is not usual to show the self-energy on the Matsubara axis, while usually the spectra, obtained via maximum entropy method for analytic continuation on the real axis, are shown. The latter quantity is not ideally suited for a methodological comparison, as it is affected by an additional uncertainty due to the ill-definiteness of any analytical continuation procedure. Hence, we have made a comparison with new (unpublished) DCA calculations, performed by Olle Gunnarsson for the specific set of data of Fig. 3.9, i.e., for $U = 3t$, $\beta = 10$.

As also recently reported for the case of DCA results in three dimensions [44], one observes a visible cluster dependence of the self-energy results for cluster-sizes as $N_c = 8, 16, \dots$ up to 100, especially at low energies. Hence, it is difficult to draw definitive and rigorous conclusions.

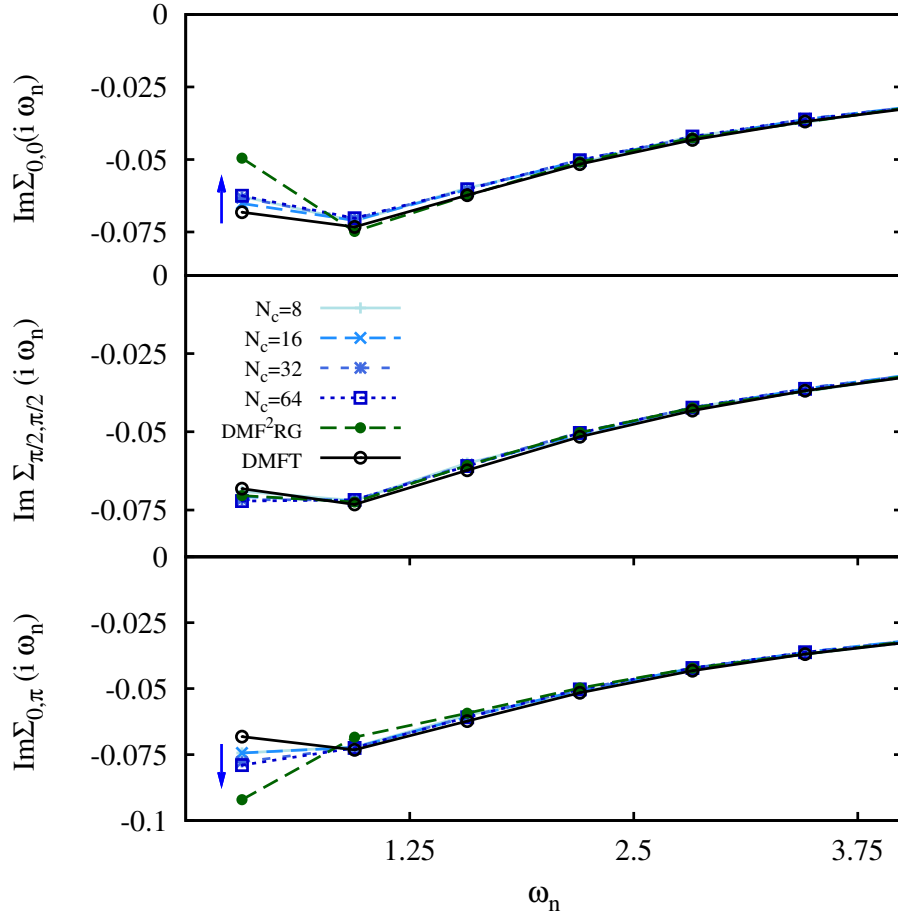


Figure 3.10: Comparison of the imaginary part of the self-energy as a function of the Matsubara frequency ($\text{Im} \Sigma(\mathbf{k}, i\omega_n)$) computed in DMFT (black empty circles), DMF²RG (green solid circles), with the (unpublished) DCA data (blue colored symbols, see legend) by Olle Gunnarsson for different cluster sizes N_c for the parameter set $U = 0.75, T = 0.1$. The blue arrows indicate the trend shown by the DCA data when the cluster size N_c is increased.

Nevertheless, looking at Fig. 3.10, we can clearly see that the results of DMF²RG do show a similar qualitative behavior as DCA. In particular, they reproduce well both the high-frequency tail of the self-energy and the trends of the (much more important) low-frequency corrections w.r.t. the DMFT self-energy for all \mathbf{k} -points. In this respect, both DCA and DMF²RG find that non-local correlations increase the incoherent part of the low-frequency self-energy mostly at the anti-nodal point $\mathbf{k} = (0, \pi)$, whereas $\text{Im} \Sigma$ at the nodal point $\mathbf{k} = (\pi/2, \pi/2)$ is less changed compared to DMFT. We also observe that the changes of the self-energy far from the Fermi Level present the same trend in DCA and DMF²RG, i.e., the reduction of $\text{Im} \Sigma$ is compensated by a corresponding enhancement of $\text{Re} \Sigma$ at $\mathbf{k} = (\pi, \pi)$ [or $(0, 0)$].

From a more quantitative viewpoint we found that, while the self-energy data at the smallest Matsubara frequency obtained with the conventional fRG displays a sort of systematic downwards shift for all \mathbf{k} -points w.r.t. the DCA data, such an ‘‘offset’’ is not present in the DMF²RG results. In the latter case, the most visible difference w.r.t. to DCA consists in a larger overall

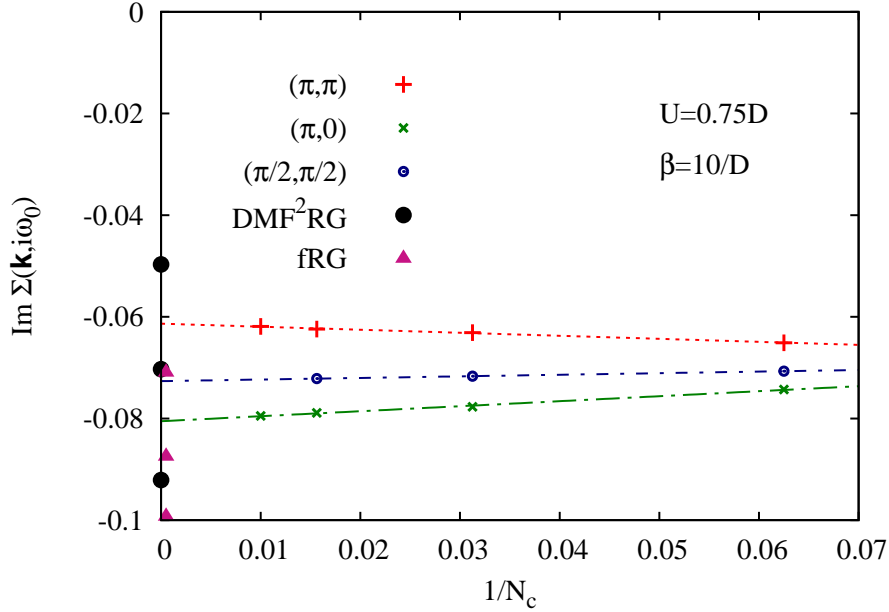


Figure 3.11: Comparison of the imaginary part of the self-energy at the lowest Matsubara frequency ($\text{Im } \Sigma(\mathbf{k}, i\omega_0)$), with $\omega_0 = \pi T$) computed in fRG (purple triangles) and DMF²RG (black circles), with the (unpublished) DCA data (colored symbols, see legend) by Olle Gunnarsson for different cluster sizes N_c for the parameter set $U = 3t$, $\beta t = 10$.

\mathbf{k} -dispersion (or spread) of $\text{Im } \Sigma$ at the smallest Matsubara frequency. In this respect, however, we should point out that for our parameter set ($U = 3t$, $\beta = 10$), the corresponding DCA results appears not fully converged yet w.r.t. the cluster size N_c . On the contrary, for cluster sizes bigger than $N_c = 16$, they display a net trend towards a *larger* \mathbf{k} -dispersion of $\text{Im } \Sigma$ by increasing N_c , i.e., in the direction of the results of DMF²RG. At the same time, increasing the number of patches used to discretize the Brillouin zone in DMF²RG we expect a trend towards a *smaller* \mathbf{k} -dispersion of $\text{Im } \Sigma$, i.e., in the direction of the DCA results. This expectation can be motivated by an argument similar to the one given above for the divergence temperature: A more refined description of the momenta should mitigate the influence of the largest components of the vertex in the flow equations. Also in this case, however, future studies will be needed for a more systematic benchmark of DMF²RG with respect to DCA (or other cluster methods). In this respect, the reduction of the \mathbf{k} -spread of the self-energy might be a good indicator for the specific choice of the cutoff more appropriate for a given implementation.

Spin-spin susceptibility

A further insight on the non-local correlations captured by the DMF²RG is given by the analysis of the momentum/frequency-dependent susceptibilities, which in DMF²RG can be extracted from the two-particle vertex. The frequency/momentum dependent susceptibility can be

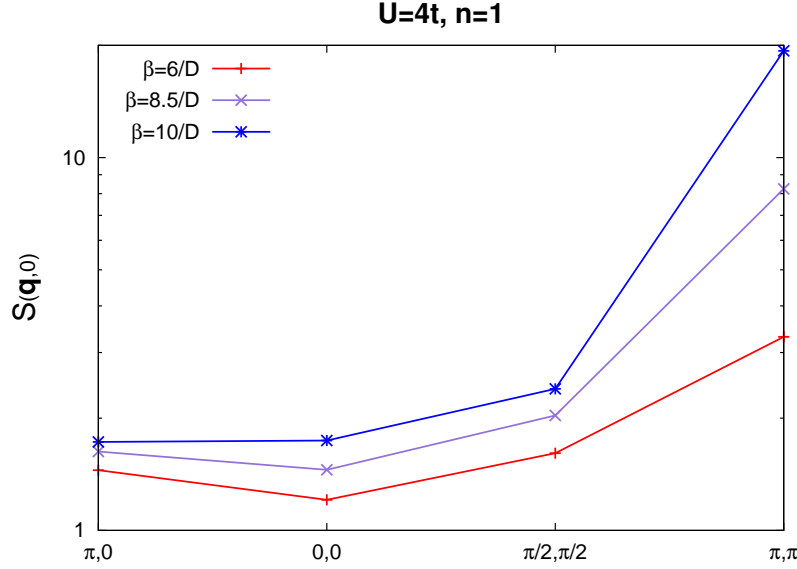


Figure 3.12: Temperature dependence of the momentum resolved static spin susceptibility $S(\mathbf{q}, i\Omega = 0) = \int_0^\beta d\tau \sum_{\mathbf{i}, \mathbf{j}} e^{i\mathbf{r}_{\mathbf{i}, \mathbf{j}} \cdot \mathbf{q}} C(\mathbf{r}_{\mathbf{i}, \mathbf{j}}, \tau)$, see text, computed with DMF²RG at $U = 1$ for different temperatures ($T = 1/\beta$).

computed as:

$$S(\mathbf{q}, \Omega) = \int_0^\beta d\tau \sum_{\mathbf{i}, \mathbf{j}} e^{i\mathbf{r}_{\mathbf{i}, \mathbf{j}} \cdot \mathbf{q}} e^{i\Omega\tau} C(\mathbf{r}_{\mathbf{i}, \mathbf{j}}, \tau), \quad (3.30)$$

where $C(\mathbf{r}_{\mathbf{i}, \mathbf{j}}, \tau)$ is the time dependent spin-spin correlation function:

$$\begin{aligned} C(\mathbf{r}_{\mathbf{i}, \mathbf{j}}, \tau) &= \frac{1}{N} \sum_{\mathbf{R}} \langle \hat{S}_z(\mathbf{R} + \mathbf{r}_{\mathbf{i}, \mathbf{j}}, \tau) S_z(\mathbf{R}, 0) \rangle \\ &= \frac{1}{N} \sum_{\mathbf{R}} \langle [\hat{n}_{\uparrow, \mathbf{R} + \mathbf{r}_{\mathbf{i}, \mathbf{j}}}(\tau) - \hat{n}_{\downarrow, \mathbf{R} + \mathbf{r}_{\mathbf{i}, \mathbf{j}}}(\tau)] [\hat{n}_{\uparrow, \mathbf{R}}(0) - \hat{n}_{\downarrow, \mathbf{R}}(0)] \rangle. \end{aligned} \quad (3.31)$$

where N is the number of lattice sites in the sum over \mathbf{R} , and $\hat{n}_{\uparrow, \mathbf{r}}$ the number operator for the spin projection \uparrow in the z direction at the lattice site \mathbf{r} . The spin susceptibility can be then expressed in terms of the two-particle Green's function that we can compute at the end of the flow. A similar definition of the susceptibility is adopted in Ref. [101], where it is also shown how to rewrite it explicitly in terms of the two-particle Green's functions for the $SU(2)$ symmetric case.

In Fig. 3.12, we show the DMF²RG results for the momentum-resolved spin-susceptibility at zero frequency $S(\mathbf{q}, i\Omega = 0)$. This quantity is most important at half-filling, where magnetic fluctuations predominate, and it is experimentally accessible, e.g., via neutron spectroscopy. Our results are in qualitative agreement with the QMC data of Refs. [23, 184] and show the major role played by antiferromagnetic fluctuations, with a pronounced peak at (π, π) , growing upon decreasing T . Furthermore, we also note that the evolution of the \mathbf{q} -dependence of $S(\mathbf{q}, i\Omega = 0)$ for decreasing temperatures is also consistent with the analysis of [112] and [29],

where numerical results obtained with diagrammatic extensions of DMFT were compared with QMC. At low T , the ferromagnetic fluctuations also get enhanced due to the van Hove singularity at the Fermi level, this explains the fact that the point $(0, 0)$ becomes a local maximum for $S(\mathbf{q}, i\Omega = 0)$ at low temperatures, here only visible as relative enhancement of $S(\mathbf{q} = (0, 0), i\Omega = 0)$ w.r.t $S(\mathbf{q} = (0, \Pi), i\Omega = 0)$. This behavior can be observed also in the bare bubble, i.e. without considering the vertex correction.

Frequency and momentum dependence of the vertex Let us now turn to a more quantitative analysis of the vertex, as obtained within our first implementation of DMF²RG. With our momentum parametrization we have 8^3 momenta combination for each of $\tilde{\Gamma}_{2,c}^{\Lambda,\Omega}$. This number can be reduced considering the symmetries in momentum space, but even so the number of functions to analyze remains quite large. Therefore we decided to focus on a particular subset of four combination of incoming and outgoing momenta of the vertex, labeled g_i , $i = a, b, c, d$, see Table 3.1.

	\mathbf{k}'_1	\mathbf{k}'_2	\mathbf{k}_1	$\mathbf{q}_{pp} = \mathbf{k}'_1 + \mathbf{k}'_2$	$\mathbf{q}_{ph-d} = \mathbf{k}'_1 - \mathbf{k}_1$	$\mathbf{q}_{ph-c} = \mathbf{k}'_2 - \mathbf{k}_1$
g_a	$(0, \pi)$	$(\pi, 0)$	$(0, \pi)$	(π, π)	$(0, 0)$	$(\pi, -\pi)$
g_b	$(0, \pi)$	$(\pi, 0)$	$(\pi, 0)$	(π, π)	$(-\pi, \pi)$	$(0, 0)$
g_c	$(0, \pi)$	$(0, \pi)$	$(\pi, 0)$	$(0, 0)$	$(-\pi, \pi)$	$(-\pi, \pi)$
g_d	$(0, \pi)$	$(0, \pi)$	$(0, \pi)$	$(0, 0)$	$(0, 0)$	$(0, 0)$

Table 3.1: Combinations of momenta shown for the analysis of the vertex. The columns from two to four refer to the incoming and outgoing momenta, while the last three columns refer to the momenta transfer in each channel, in analogy with the bosonic frequencies.

Our choice is the same of Ref. [97], and is well motivated considering that it allows for an "antiferromagnetic" momentum transfer of $(\pm\pi, \pm\pi)$ (marked in red in the table) or for a "ferromagnetic" momentum transfer of $(0, 0)$ (marked in blue) in each channel.

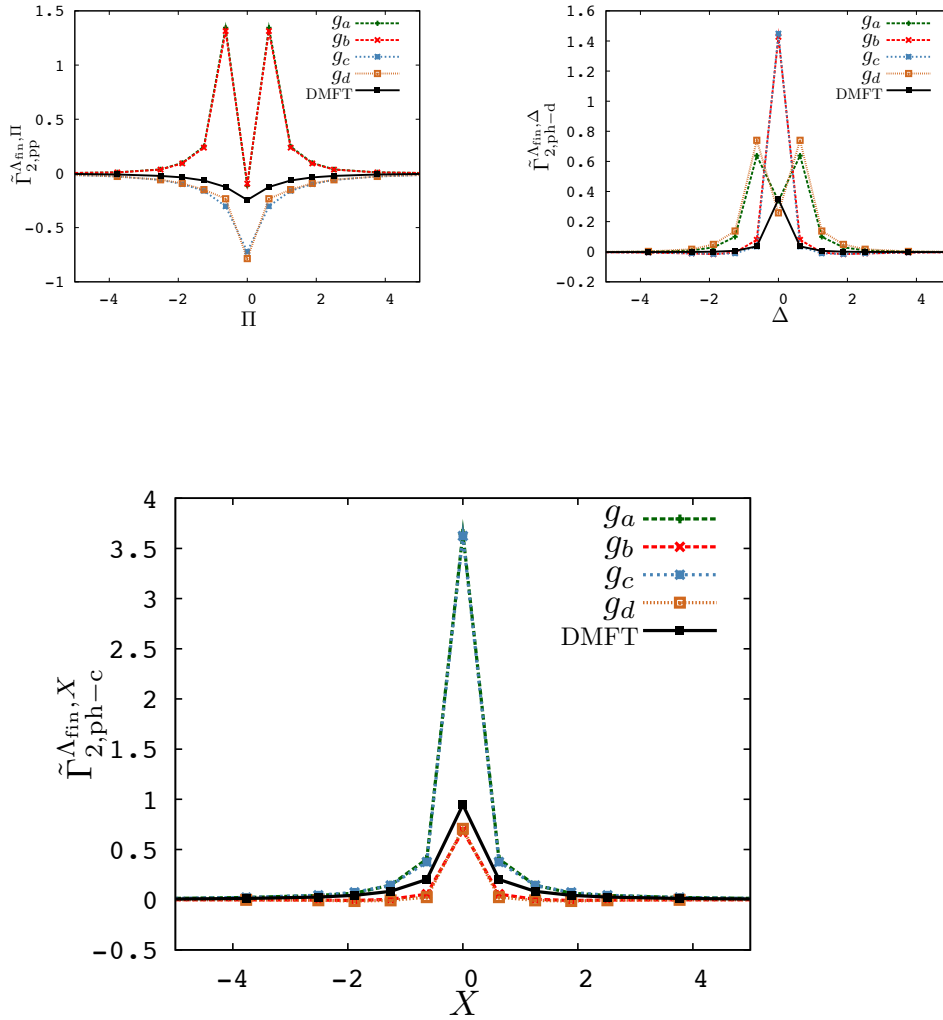


Figure 3.13: Frequency dependence of the real part of the three functions $\tilde{\Gamma}_{2,c}^{\Lambda,\Omega}$, with $c = \text{pp}, \text{ph} - \text{d}, \text{ph} - \text{c}$ and $\Omega = \Pi, \Delta, X$ respectively, at the end of the flow for a selected choice of the momentum arguments, see Table 3.1. The data refer to $U = 0.75$ and $T = 0.1$. Please note that the scale on the y -axis is different for the three channels. In all the three cases the enhancement compared to DMFT is noticeable and nontrivial. Furthermore for each channels the four curves are paired in two couples. By looking at the definition of the g_i 's, one can further see that the two curves of $\tilde{\Gamma}_{2,x}^{\Lambda,\Omega}$ which have a similar behavior are those which share the same momentum transfer in the x -channel, e.g., $\mathbf{k}'_1 + \mathbf{k}'_2$ for pp.

The results for the frequency dependent vertex functions are shown in Fig. 3.13, where is also shown, in black, the initial condition from DMFT. The data in the figure refer to the case of $U = 0.75$ and $T = 0.1$. Let us stress that in the discussion below we focus on the *real* part of the vertex, and that we will often refer to vertex *channels* to specify each of the terms in which the 1PI two particle vertex has been decomposed. It is evident that in all the three channels the frequency dependence induced by the flow is nontrivial, and, even within our simplified

frequency parametrization, it becomes richer than the one of DMFT. As a general trend, we observe that for each channel the four curves are arranged in two pairs, with the curves of each pair showing a very similar frequency dependence. This reflects the fact that there is a dominant momentum dependence associated with the momentum transfer in the channel considered. For example in the particle-hole crossed channel $\tilde{\Gamma}_{2,\text{ph-c}}$ the main momentum dependence is on the transfer frequency $\mathbf{q}_{\text{ph-c}} = \mathbf{k}'_2 - \mathbf{k}_1$, as one can see considering that the momenta combination are paired as g_a-g_c and g_b-g_d . As we have also anticipated at the beginning of the section, the maximum of the vertex function is reached in the particle-hole crossed channel for momentum transfer (π, π) , i.e., g_a and g_c . In this channel, due to the tendency of the system towards strongly enhanced antiferromagnetic fluctuations, the frequency structure is not particularly rich, being mostly affected by the strong increase (w.r.t DMFT) of the vertex corresponding to the antiferromagnetic momentum transfer and a slight suppression for the momentum transfer $(0, 0)$.

In the other two channels the situation is much more involved and the frequency dependence induced by the flow does not only change *quantitatively* the DMFT structure, but also alters it *qualitatively*. Let us focus in particular to the vertex function in the particle-particle channel. In this case, already the initial condition of DMFT has a different sign from the one of the particle-hole channels, i.e., charge fluctuations reduce the interaction. The effect of the flow for the two-momenta transfers $(0, 0)$ and $(\pm\pi, \pm\pi)$, corresponding respectively to g_c-g_d and g_a-g_b , is strikingly different. In fact, in the former case of $\mathbf{q}_{\text{pp}} = (0, 0)$ the flow leads to an enhancement of the (negative) corresponding initial vertex of DMFT.

On the other hand, the frequency dependence of $\tilde{\Gamma}_{2,\text{pp}}$ for the antiferromagnetic momentum transfer goes in the opposite direction and becomes *positive* (i.e., with the same sign of $\tilde{\Gamma}_{2,\text{ph-c}}$) apart for the single frequency $\Pi = 0$, for which it changes sign.

As a side remark, let us remind that not much is known about the frequency dependence of the vertex functions in fRG, and especially about the effect of the frequency decomposition of the vertex, equation (3.27), that we have employed here. A possibility to better understand the frequency dependence arising from the fRG flow, would be to comparing the 1PI vertex as obtained in a full treatment of the frequencies and in a channel decomposed approach, for a single impurity Anderson model. In this case, in fact, both the implementations have been achieved [94], also showing the efficiency of the channel decomposition, which, gives similar results to the full frequency implementation. For the specific case of the single impurity Anderson model one could also compare the vertex with those of QMC or ED (like the one that we are using as starting point in DMF²RG).

Despite these technicalities, which call for further investigations, it is clear that the 1PI vertex exhibits a very rich frequency and momentum dependence that will need to be analyzed and understood in future studies. Hence in future studies, it will be important to understand which are the main features of the vertex that are connected with the physical properties of the system. An important step in this direction is understanding how the vertex, computed numerically on the Matsubara frequency axis, can be connected with its frequency relevant limits on the real frequency axis [85], and in turns, with the Landau's parameters in Fermi

liquid theory [39, 40].

3.2 Summary, open questions ad outlook

In the course of the work that lead to the present thesis, we have introduced the new approach that we named DMF²RG, and that exploits the synergy of treating *local* DMFT correlations as well as *non-local* correlations generated by the fRG flow. To test the new method we have applied it to the 2D Hubbard model, finding that, due to the inclusion of all local correlations by the DMFT starting point, the divergence of the fRG-flow for the interaction vertex is pushed to lower temperatures, where significant non-local corrections to DMFT are found. At the same time, in the temperature interval where both fRG and DMF²RG converge, the self-energy results are qualitatively similar, supporting the results of previous fRG studies at weak-to-intermediate U . Quantitatively, the most visible effect of DMF²RG compared to fRG consists in a stronger k -dependence of the self energy for the considered parameters and a suppression of the “pseudocritical” temperature at which the vertex diverges. We consider these findings of our first implementation very promising.

At the same time, however, due to the novelty of the approach, we are aware that the issues to be addressed in the future are yet many more than those that have already been analyzed. Therefore, in this conclusive section, we would like to discuss in detail the several possible directions that, we believe, should be followed to bring DMF²RG at an equal or possibly superior level of applicability as other diagrammatic extensions of DMFT.

Practical improvement on the implementation From a practical point of view, it will be necessary to improve the present implementation of the method, in particular regarding the frequency and momenta parametrization. An improvement on the frequency parametrization is essential to capture the diagonal structure of the vertex, see Fig. 3.6, whose neglect can only be well justified at weak coupling. The improvement on the momentum parametrization, instead, might be important to reduce spurious effect of the course discretization of the Brillouin zone, like an artificial enhancement of the pseudocritical temperature, and of the overall low-frequency momentum spread of the electronic self energy.

Theoretical open issues Besides the problems connected with the practical implementation there are also some theoretical aspects that need to be investigated. These are related to two main interconnected issues: (i) the proper choice of a cutoff and (ii) the possibility of accessing the strong coupling, possibly Mott insulating, regime in presence of a truncation of the flow equations.

As for the choice of the cutoff, we have already noted that the cutoff employed in Sec. 3.1 is not regularizing. There we have already proposed a different choice of the cutoff, Eq. (3.20), that instead is regularizing. On a diagrammatic point of view, the choice of the cutoff also determines the part of parquet diagrams that is neglected due to the truncation, see Sec. 1.4.2.

There we have argued that, with a suitable choice of the cutoff, the retained contribution of the parquet diagrams is the dominant one [26]. However, the analysis of Ref. [26] applies well to "standard" regularizing cutoffs and is not easy to generalize to the cutoff of DMF²RG, even in the formulation of Eq. (3.20). Hence, a numerical analysis at the lowest perturbative order diagrams, as also suggested in section 1.4.2, might be the best solution to gain more insight in the search for future, better regularizing cutoffs in DMF²RG.

Furthermore the choice of the cutoff in DMF²RG is related to an additional problem to which we refer as the "*flow in infinite dimensions*". In fact, as we have extensively discussed in Sec. 1.5, in the limit $d \rightarrow \infty$ the DMFT solution becomes exact. Therefore it would be desirable that for any given density of states $\rho(\epsilon)$ considered as the density of states of an infinite dimensional problem and starting with the self-consistent self-energy of DMFT Σ_{DMFT} the integration of the flow equations maintains the DMFT results as a solution. As originally suggested by W. Metzner and A. A. Katanin, mathematically this corresponds to asking that for every value of Λ the local Green's function stays constant along the flow if the self-energy is kept at the DMFT value:

$$G_{\Lambda}^{\text{loc}}(\omega_n) = \int d\epsilon \frac{\rho(\epsilon)}{[G_{\Lambda}^0(\epsilon, i\omega_n)]^{-1} - \Sigma_{\text{DMFT}}(i\omega_n)} = G_{\text{DMFT}}(i\omega_n). \quad (3.32)$$

Where G_{DMFT} is the DMFT Green's function. Deriving with respect to Λ the above equation one can see that it also corresponds to the requirement that the local single scale propagator vanishes:

$$S_{\Lambda}^{\text{loc}}(\omega_n) = \left. \frac{dG_{\Lambda}^{\text{loc}}(\omega_n)}{d\Lambda} \right|_{\Sigma=\Sigma_{\text{DMFT}}} = 0. \quad (3.33)$$

As one can check from Eq. (3.32), at the beginning and at the end of the flow this condition coincides with the DMFT self-consistency condition, i.e., it is fulfilled if $G_{\text{DMFT}}(i\omega_n)$, Σ_{DMFT} and $G_{\Lambda_{\text{ini}}}^0$ are respectively the exact local Green's function, exact self-energy and Weiss field of the self-consistent AIM of the infinite dimensional problem with density of states $\rho(\epsilon)$. On the other hand, requiring that Eq. (3.32) is fulfilled for every value of Λ is more complicated, and it can be seen that our choice of the cutoff of Eq. (3.19) does not fulfill this condition, i.e., if we applied our flow in infinite dimensions we would incorrectly predict a flow away from the exact DMFT solution.

A possible condition for a choice of a cutoff that fulfills Eq. (3.32) is shown in the following. First let us rewrite a generalization Eq. (3.13) for a $D \rightarrow \infty$ dimensional problem with density $\rho(\epsilon)$:

$$G^{\Lambda}(k_1, k_2, \dots, k_D; \omega_n) = \sum_{k_{D+1}, \dots, k_d} \frac{1}{i\omega_n - (1 - \Lambda)\epsilon_{k_1, k_2, \dots, k_D} - \Lambda \frac{\tilde{\epsilon}_{k_{D+1} \dots k_d}}{\sqrt{2d}} + \mu - \Sigma_{\text{DMFT}}(\omega_n)}. \quad (3.34)$$

Σ_{DMFT} is the DMFT self-energy associated with a density of states $\rho(\epsilon)$. Here Λ acts as a multiplicative factor for the energies ϵ . We do not need to specify the energy dispersion in the extra $d - D$ dimensions $\tilde{\epsilon}_{k_{D+1} \dots k_d}$, we just assume that it is associated to a density of states $\tilde{\rho}(\epsilon)$.

Summing over k_1, \dots, k_D , and passing from the summations to the integral over the density of states, the Λ -dependent Green's function can be written as:

$$G_{\Lambda}^{\text{loc}}(\omega_n) = \int d\epsilon d\epsilon' \frac{\rho(\epsilon)\tilde{\rho}(\epsilon')}{i\omega_n - (1 - \Lambda)\epsilon - \Lambda\epsilon' + \mu - \Sigma_{\text{DMFT}}(\omega_n)}. \quad (3.35)$$

Requiring (3.32) at the beginning of the flow $\Lambda = 1$ and comparing with the definition of the DMFT self consistency:

$$G_{\text{DMFT}}(i\omega_n) = \int d\epsilon \frac{\rho(\epsilon)}{i\omega_n - \epsilon + \mu - \Sigma_{\text{DMFT}}(\omega_n)}, \quad (3.36)$$

one can see that $\tilde{\rho}(\epsilon) = \rho(\epsilon)$. Defining $\rho_x(\epsilon)$ the density of states of the energy dispersion $x\epsilon_{\mathbf{k}}$, i.e., $\rho_x(\epsilon) = \frac{\rho(\epsilon/x)}{|x|}$, we can rewrite Eq. (3.35) for a generic value of Λ :

$$G_{\Lambda}^{\text{loc}}(\omega_n) = \int d\epsilon d\epsilon' \frac{\rho_{(1-\Lambda)}(\epsilon)\rho_{\Lambda}(\epsilon - \epsilon')}{i\omega_n - \epsilon + \mu - \Sigma_{\text{DMFT}}(\omega_n)}. \quad (3.37)$$

Comparing with Eq. (3.36), we obtain:

$$\int d\epsilon' \rho_{(1-\Lambda)}(\epsilon)\rho_{\Lambda}(\epsilon - \epsilon') = \rho(\epsilon), \quad (3.38)$$

that should be fulfilled for every value of Λ . Taking a Fourier transform on both sides of the equations, one can get rid of the convolution, and obtain an equation in terms of the product of the Fourier transform of the density of states on the left hand side. It can be further seen that Eq. (3.38) has a simple solution if $\rho(\epsilon)$ is a gaussian density of states, i.e., the density of states of an hypercubic lattice in infinite dimensions. However for a general density of states, e.g., a two-dimensional one, solving Eq. (3.38) is more difficult. Clearly finding a solution to this problem for a general density of states would be very desirable because it would guarantee that the DMF²RG flow is exact in the limit of infinite dimensions. Obviously, in general in finite dimensions, the condition (3.32) should be fulfilled *only* for the initial value of the self-energy Σ_{DMFT} , and therefore it will *not* imply that the local single scale propagator vanishes along all of the flow. In fact, when the flow is applied to a finite dimensional problem, a nonlocal Λ -dependent self-energy will be generated and including its feedback in the single scale propagator it will also acquire a non vanishing local part.

Also connected to the choice of the cutoff in DMF²RG is the question about the regime of applicability of the method. In fact, in Ref. [157] arguments are presented that justify the use of a truncated equations.. These are based on phase space considerations, which are difficult to apply to the case of DMF²RG. Hence, one should think to a different analysis to better understand the regime of applicability of the method. Importantly, this question is related with the possibility of acceding to a strong coupling, possibly Mott insulating, regime within DMF²RG. This issue can be reformulated in terms of the existence of a small parameter associated with the non-locality of the problem¹⁶, and of the possibility to treat it in a perturbative way. Our physical understanding is that in the Mott insulating regime the physics becomes more localized

¹⁶More precisely on the non deviation from the purely local physics of DMFT

and therefore the local description provided by DMFT might represent a good starting point. When this is the case the 1PI two-particle vertex, might be described already quite well by the local DMFT picture, and the non-local corrections to it might be viewed as a sort of "small parameter". Then the fRG flow should only provide a smaller contribution to the final result. However one should be very careful in making these considerations. In fact, at strong coupling, the local vertex of DMFT is much enhanced compared to the already large, i.e., nonperturbative, interaction value. Therefore the feedback on the right hand side of the flow equations might be very large, leading very soon to a divergence of the interaction. At the same time, the insulating propagators, associated with a divergent self-energy, will moderate this feedback, possibly avoiding spurious divergences of the flow equations.¹⁷

The question about the existence of a small perturbative parameter can also be approached in a slightly different way, taking advantage of the studies of Refs. [100, 101]. There, the fRG was used as impurity solver for DMFT showing results consistent with previous studies, not only for the weak coupling regime but also for the Mott insulating one. More in detail the self-consistent AIM of DMFT was mapped on a model containing an interacting impurity attached to a chain of noninteracting sites. The problem was then approached using the hybridization cutoff introduced in Ref. [102]: First the chain is divided in a "core system", containing the interacting impurity and a small number of sites, and a "bath" containing the rest of the sites, see Fig. 3.14. Then, in the beginning of the flow, the hybridization between the core system and the bath is switched off, and therefore the core can be solved exactly. Afterwards the hybridization is gradually restored.

The important information, from our perspective, is the following: The attempt of a direct calculation of the vertex function of the interacting impurity was not always successful, since for larger couplings leads to a divergent flow. On the other hand the problem can be approached in a different way: First the interacting impurity (as well all the sites of the core but one¹⁸) can be formally integrated out. One therefore remains with a single interacting site. The interaction on this site can be treated by means of fRG, leading to non divergent results. The final step is tracing back the quantities obtained through the flow to the corresponding vertex of the impurity site, i.e., the one we were originally interested in. This way an essentially nonperturbative problem (the one of the impurity) is treated by solving, using fRG, a perturbative one (the one of the originally noninteracting site whose vertex are computed by the flow). In general, however we are interested in Hubbard models in which *each* site is interacting, and therefore

¹⁷We should also note here that, up to date, not many calculations in fRG have been performed in a gapped system, like it would be the Mott insulating one, and it is not completely clear what it can be expected performing the flow in a system not in the Fermi-liquid regime from the beginning. At the best of our knowledge, the only calculation in fRG starting from a gapped system is reported in a recent work from Eberlein and coworkers [41], where a small gap was assumed from the beginning of the calculation to describe the pairing in the attractive Hubbard model. The flow could the coupling associated with superconductive pairing would then grow during the flow and reach very large values, but the calculation could be anyway concluded.

¹⁸This site is usually the one at the end of the core system. Before the integration of the other degrees of freedom, in the action, the fields associated to this site appear only quadratically and linearly. After the integration there are also higher order terms corresponding to the remainder of the interaction on the impurity. More details are given in Ref. [102].

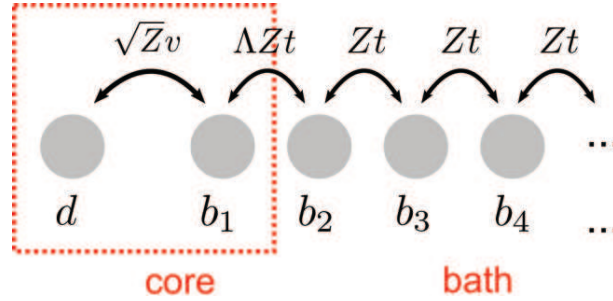


Figure 3.14: Schematic illustration of the subdivision of an infinite chain of sites into a "core" and a "bath" system. The core system is integrated exactly, while the interaction with the rest of the bath sites is restored with the cutoff Λ . The figure is reproduced from Ref. [102].

the application of this procedure will be more involved. For this goal, one can first make use of an Hubbard-Stratonovich transformation to introduce a new set of auxiliary (dual) fermions, like in the DF approach [55, 151]. As in the case of the chain described above, these fermions are interacting only through their hybridization to the "physical" fermions¹⁹. If the physics is local enough the auxiliary fermion problem can be approached perturbatively by means of fRG. Eventually, the solution of the auxiliary problem can be traced back to calculate the relevant quantities of the original one. At the moment this idea represents just one possibility, but we believe that it is an interesting direction to be explored in the near future for an efficient description of the whole phase diagram from weak to strong coupling.

Possible applications Clearly, after having tested our first implementation of DMF²RG on the two-dimensional Hubbard model at half filling, we would like to use the newborn method to approach more challenging problems. The *most* challenging problem is for sure the one of the Hubbard model in the regime of interactions, hoppings and filling relevant for the cuprates. Having access to this regime, we could not only test our new method against a large amount of data available in the literature, but we could also hope to gain new insight in the interesting physics associated with the opening of the pseudo-gap. Further technical improvements would be needed to also increase the number of bands that one can treat in DMF²RG. However, this should be possible considering the non exponential scaling of the method, and this would allow us to explore more realistic multi orbital situations [120, 121], as well the intriguing physics of system with multiple fermi surfaces pockets, like the iron pnictides [115].

A completely different line of investigation could be followed to treat an extended Hubbard model within DMF²RG. In fact, while DMFT is very effective in the treatment of the local interaction, the non local ones are only treated, as in the limit of infinite dimensions, at

¹⁹In this action there is no quartic term in the auxiliary fermions but only a linear coupling to the original ones.

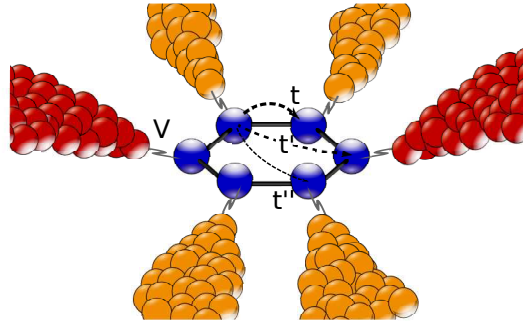


Figure 3.15: Schematic illustration of a benzene molecule (carbon atoms shown in blue) contacted to metallic environments (in red and orange). Also represented are the hopping channels t, t', t'' between the correlated sites, and the hybridization strength V . The figure is reproduced from Ref. [180].

the Hartree-Fock level, e.g., along the line of the *ab-initio* D Γ A [177]. Hence, improving this approximate treatment in finite dimensions using fRG is for sure appealing. Finally, the last application that we would like to mention, but probably the first that we are going to study, is represented by nanoscopic systems [179, 180]. In particular one could consider finite-size Hubbard clusters with periodic boundary conditions (which grant translational invariance). In fact, for systems involving only a few atoms, the Brillouin zone contains only a discrete number of k -points, and therefore several different approaches, including a numerically exact solution, become feasible. For example, for nanoscopic systems it is also possible to solve the the parquet equations with a relatively manageable computational effort (and without relying on any arbitrary sampling of the Brillouin zone). This offers a good chance to gain further insight on the physical content of different approximations, by critically comparing the fRG result against the ones obtained within the parquet approximation, as well as the DMF²RG and D Γ A ones. In this respect, nanoscopic systems represent an excellent playground for further testing our theory, and a comparison with existing results would be a very stringent test for the quality of our approximation.

Conclusion We emphasize, to conclude, the potential of the DMF²RG approach to extend the channel unbiased treatment of the fRG to the strong-coupling regime, where the Mott-Hubbard physics already captured by DMFT will play a more important role and qualitative changes in the self-energy and susceptibility results are expected. The flexibility of the DMF²RG scheme and its ability to avoid the sign-problem of a direct QMC treatment of non-local physics beyond DMFT look promising for future, unbiased studies of correlations in realistic multi-band models. We hope that DMF²RG may serve as a first bridge between two different methods (and the two related scientific communities), this way stimulating a stronger "hybridization" between the two approaches, that might lead, in the future, to yet better understanding of correlations in the

complicated regime that, up to now, DMFT and fRG alone are not able to correctly describe.

Chapter 4

Conclusions

Mastering the physics of strong electronic correlations represent a pivotal challenge for condensed matter physics as well as a prospective resource for future technological applications. In this thesis we have engaged this quest from a theoretical and computational point of view. The well established starting point for our investigation has been the state-of-the-art method for treating strongly correlated systems, namely dynamical mean-field theory (DMFT). Our strategy relies on combining the main strength of DMFT, i.e., its ability to treat nonperturbatively the local correlations, with the advantages of two different methods, namely the GW approximation and the functional renormalization group (fRG). These two approaches are the so-called GW +DMFT and the novel DMF²RG respectively. Both aim at overcoming some of the main limitations of DMFT.

Within GW +DMFT we addressed the problem of realistic calculation of material properties with *predictive power*. For this to be possible, it is essential to avoid any parameter fitting procedure and, instead, modeling the studied system from first principles, i.e., *ab-initio*. GW is capable of computing accurately nonlocal exchange correlations and, in a GW +DMFT framework, offers the chance to do so while accurately treating strong local electronic correlations at the local level of DMFT. Unfortunately, the practical implementation of this method has proven to be technically extremely involved, thus hampering its application to realistic calculations. In the course of this thesis we have shown how, making use of a "quasiparticle" approximation to the GW self energy, we can circumvent some of the most challenging steps of the full GW +DMFT, while still preserving, at least partially, its advantages. This way, our specific implementation, to which we refer as qp GW +DMFT, provides a valid alternative both to more standard combinations of density functional theory and DMFT (DFT+DMFT) and to more involved implementations of GW +DMFT. Compared to the former, it has the advantage of avoiding the introduction of fitting parameters, in particular for the Coulomb interaction, and of *ad hoc* double counting corrections. Compared to the latter, our quasiparticle implementation is more flexible and computationally cheaper.

We have tested the efficiency of qp GW +DMFT for the case of the correlated metal SrVO₃. Our results compare well with more demanding implementations of GW +DMFT as well with experimental results. Remarkably, we obtained improved results compared to DFT+DMFT at

a similar computational cost. Hence, while on the long run a full $GW+DMFT$ implementation definitively remains the final goal, the quasiparticle implementation proposed in this thesis deserves to be considered as an interesting option for the short-term future, and for the applications to particularly complex or large systems.

If within $qpGW+DMFT$ our main contribution was the implementation of an efficient algorithm in an already existing method, with DMF^2RG we undertook the more ambitious goal of combining, for the first time, two methods, i.e., $DMFT$ and fRG , in a novel approach. The purpose of the novel method is the treatment, at least at the model level, of the strong electronic correlations at all length scales. This scope is beyond the reach of both $DMFT$ and fRG taken separately, due to the local nature of the former and to the perturbative limit imposed to the latter by the truncation of the flow equations. On the other hand, exploiting the complementary strengths of the two methods, we have theoretically designed a new algorithm with high potential. This is because, ideally, the nonperturbative local physics of $DMFT$ is taken as a starting point for the fRG flow, which then treats the nonlocal correlations. Thanks to the fRG structure, these are unbiasedly generated in all the channels, allowing for a theoretical treatment of competing instabilities, which is not possible in schemes based on the summation of ladder-type diagrams, such as many of the state-of-the-art diagrammatic extensions of $DMFT$. To test the method we have accomplished the first implementation of DMF^2RG and we have applied it to a well studied case, i.e., the half-filled two-dimensional Hubbard model. In spite of the additional approximation required in our numerical implementation, we obtained results both for one and two-particle quantities in qualitative agreement with those of other well-established methods, such as cluster extensions of $DMFT$ or lattice quantum Monte Carlo. These first positive results pave the way for future progress in quantum many-body physics. From the methodological point of view, two questions stand out as prominent. The first is the one regarding the best choice of the cutoff, in particular regarding its regularizing nature and the properties of the "*flow in infinite dimensions*". The second is the applicability of DMF^2RG to describe nonlocal correlations in the strong coupling regime. The answer to these questions is beyond the scope of our first implementation, but motivates further studies, both from the point of view of the technical implementation as well from a purely theoretical perspective. Being able to provide a positive answer to these questions, we can be sure that DMF^2RG provides a great opportunity opening new ways towards the understanding of fascinating physics.

Bibliography

- [1] A. Abrikosov, L. Gorkov, and Dzyaloshinski. *Methods of Quantum Field Theory in Statistical Physics*. Dover, 1975.
- [2] Markus Aichhorn, Leonid Pourovskii, Veronica Vildosola, Michel Ferrero, Olivier Parcollet, Takashi Miyake, Antoine Georges, and Silke Biermann. Dynamical mean-field theory within an augmented plane-wave framework: Assessing electronic correlations in the iron pnictide LaFeAsO. *Phys. Rev. B*, 80:085101, Aug 2009.
- [3] C.O. Almbladh, U. von Barth, and R. van Leeuwen. Variational total energies from Φ - and Ψ - derivable theories. *International Journal of Modern Physics B*, 13(05n06):535--541, 1999.
- [4] A. Altland and B. Simons. *Condensed Matter Field Theory*. Cambridge University Press, 2008.
- [5] Sabine Andergassen, Tilman Enss, Christoph Karrasch, and Volker Meden. A Gentle Introduction to the Functional Renormalization Group: The Kondo Effect in Quantum Dots. In Bernard Barbara, Yosef Imry, G. Sawatzky, and P.C.E. Stamp, editors, *Quantum Magnetism*, NATO Science for Peace and Security Series, pages 1--17. Springer Netherlands, 2008.
- [6] O. Krogh Andersen. Linear methods in band theory. *Phys. Rev. B*, 12(8):3060--3083, Oct 1975.
- [7] O.K. Andersen, T.Saha-Dasgupta, S.Ezhov, L.Tsetseris, O.Jepsen, R.W. Tank, and C.A.G. Krier. Third-generation MTOs. *Ψ -k newsletter*, 45:86, 2001.
- [8] Philip Warren Anderson. *Basic notions of condensed matter physics*. Benjamin/Cummings Pub. Co., 1984.
- [9] V. I. Anisimov, D. E. Kondakov, A. V. Kozhevnikov, I. A. Nekrasov, Z. V. Pchelkina, J. W. Allen, S.-K. Mo, H.-D. Kim, P. Metcalf, S. Suga, A. Sekiyama, G. Keller, I. Leonov, X. Ren, and D. Vollhardt. Full orbital calculation scheme for materials with strongly correlated electrons. *Phys. Rev. B*, 71:125119, Mar 2005.

- [10] V I Anisimov, A I Poteryaev, M A Korotin, A O Anokhin, and G Kotliar. First-principles calculations of the electronic structure and spectra of strongly correlated systems: dynamical mean-field theory. *Journal of Physics: Condensed Matter*, 9:7359--7367, 1997.
- [11] A. E. Antipov, E. Gull, and S. Kirchner. Critical exponents of strongly correlated fermion systems from diagrammatic multi-scale methods. *arXiv:1309.5976*, 2013.
- [12] F. Aryasetiawan and O. Gunnarsson. The *GW* method. *Rep. Prog. Phys.*, 61:236, 1998.
- [13] F. Aryasetiawan, M. Imada, A. Georges, G. Kotliar, S. Biermann, and A. I. Lichtenstein. Frequency-dependent local interactions and low-energy effective models from electronic structure calculations. *Phys. Rev. B*, 70:195104, 2004.
- [14] N.W. Ashcroft and N.D. Mermin. *Solid State Physics*. Hartcourt College Publishers, New York, 1976.
- [15] T. Ayral, S. Biermann, and P. Werner. Screening and non-local correlations in the extended hubbard model from self-consistent combined *GW* and dynamical mean field theory. *Phys. Rev. B*, 87:125149, 2013.
- [16] T. Ayral, P. Werner, and S. Biermann. Spectral properties of correlated materials: Local vertex and nonlocal two-particle correlations from combined *GW* and dynamical mean-field theory. *Phys. Rev. Lett.*, 109:226401, 2012.
- [17] Tobias Baier, Eike Bick, and Christof Wetterich. Temperature dependence of antiferromagnetic order in the Hubbard model. *Phys. Rev. B*, 70:125111, Sep 2004.
- [18] D. N. Basov and Andrey V. Chubukov. Manifesto for a higher t_c . *Nat Phys*, 7(4):272--276, 04 2011.
- [19] Gordon Baym and Leo P. Kadanoff. Conservation laws and correlation functions. *Phys. Rev.*, 124:287--299, Oct 1961.
- [20] V.L. Berezinskii. Destruction of long-range order in one-dimensional and two-dimensional systems with a continuous symmetry group. ii. quantum systems. *Sov. Phys. JETP* 34(3), pages 610--616, 1972.
- [21] D. D. Betts, H. Q. Lin, and J. S. Flynn. Improved finite-lattice estimates of the properties of two quantum spin models on the infinite square lattice. *Can. J. Phys.*, 77:353, 1999.
- [22] N. E. Bickers. *Theoretical Methods for Strongly Correlated Electrons*, chapter 6, pages 237--296. Springer-Verlag New York Berlin Heidelberg, 2004.
- [23] N. E. Bickers and S. R. White. Conserving approximations for strongly fluctuating electron systems. ii. numerical results and parquet extension. *Phys. Rev. B*, 43:8044--8064, Apr 1991.

- [24] S. Biermann, F. Aryasetiawan, and A. Georges. First-principles approach to the electronic structure of strongly correlated systems: combining the GW approximation and dynamical mean-field theory. *Phys. Rev. Lett.*, 90:086402, 2003.
- [25] B. Binz, D. Baeriswyl, and B. Douçot. Wilson’s renormalization group applied to 2D lattice electrons in the presence of van Hove singularities. *Eur. Phys. J. B*, 25:69--87, 2002.
- [26] B. Binz, D. Baeriswyl, and B. Douçot. Weakly interacting electrons and the renormalization group. *Annalen der Physik*, 12(11-12):704--736, 2003.
- [27] N. Blümer. *Mott-Hubbard Metal-Insulator Transition and Optical Conductivity in High Dimensions*. PhD thesis, Universität Augsburg, 2002.
- [28] M. Born and R. Oppenheimer. Zur quantentheorie der molekeln. *Ann. Phys.*, 389:457--484, 1927.
- [29] S. Brener, H. Hafermann, A. N. Rubtsov, M. I. Katsnelson, and A. I. Lichtenstein. Dual fermion approach to susceptibility of correlated lattice fermions. *Phys. Rev. B*, 77:195105, 2008.
- [30] M. Casula, Ph. Werner, L. Vaugier, F. Aryasetiawan, T. Miyake, A. J. Millis, and S. Biermann. Low-energy models for correlated materials: Bandwidth renormalization from coulombic screening. *Phys. Rev. Lett.*, 109:126408, Sep 2012.
- [31] Michele Casula, Alexey Rubtsov, and Silke Biermann. Dynamical screening effects in correlated materials: Plasmon satellites and spectral weight transfers from a green’s function ansatz to extended dynamical mean field theory. *Phys. Rev. B*, 85:035115, Jan 2012.
- [32] D. M. Ceperley and B. J. Alder. Ground state of the electron gas by a stochastic method. *Phys. Rev. Lett.*, 45(7):566--569, Aug 1980.
- [33] Athanasios N. Chantis, Mark van Schilfgaarde, and Takao Kotani. *Ab Initio* prediction of conduction band spin splitting in zinc blende semiconductors. *Phys. Rev. Lett.*, 96:086405, Mar 2006.
- [34] R. Chitra and G. Kotliar. Dynamical mean-field theory and electronic structure calculations. *Phys. Rev. B*, 62:12715--12723, Nov 2000.
- [35] R. Chitra and Gabriel Kotliar. Effective-action approach to strongly correlated fermion systems. *Phys. Rev. B*, 63:115110, Mar 2001.
- [36] A. V. Chubukov, D. V. Efremov, and I. Eremin. Magnetism, superconductivity, and pairing symmetry in iron-based superconductors. *Phys. Rev. B*, 78:134512, Oct 2008.

- [37] P. H. Dederichs, S. Blügel, R. Zeller, and H. Akai. Ground states of constrained systems: Application to cerium impurities. *Phys. Rev. Lett.*, 53:2512--2515, Dec 1984.
- [38] P. A. M. Dirac. Note on exchange phenomena in the thomas atom. *Mathematical Proceedings of the Cambridge Philosophical Society*, 26:376--385, 7 1930.
- [39] N Dupuis. Fermi liquid theory: a renormalization group approach. *Eur. Phys. J. B*, 3:315, Jun 1998.
- [40] N. Dupuis and G. Y. Chitov. Renormalization-group approach to fermi-liquid theory. *Phys. Rev. B*, 54:3040--3043, Aug 1996.
- [41] A. Eberlein. *Functional renormalization group study of fluctuation effects in fermionic superfluids*. PhD thesis, University Stuttgart, 2013.
- [42] Sergey V. Faleev, Mark van Schilfgaarde, and Takao Kotani. All-electron self-consistent *GW* approximation: Application to Si, MnO, and NiO. *Phys. Rev. Lett.*, 93:126406, Sep 2004.
- [43] Alexander Fetter and John Dirk Walecka. *Quantum theory of many-particle systems*. 1971.
- [44] S. Fuchs, E. Gull, M. Troyer, M. Jarrell, and T. Pruschke. Spectral properties of the three-dimensional hubbard model. *Phys. Rev. B*, 83:235113, 2011.
- [45] A. Fujimori. Electronic structure of metallic oxides: Band-gap closure and valence control. *Journal of Physics and Chemistry of Solids*, 53:1595--1602, December 1992.
- [46] A. Georges. Lectures on the physics of highly correlated electron systems viii. *American Institute of Physics Conference Proceedings*, 715:3, 2004.
- [47] Antoine Georges and Gabriel Kotliar. Hubbard model in infinite dimensions. *Phys. Rev. B*, 45:6479--6483, Mar 1992.
- [48] Antoine Georges, Gabriel Kotliar, Werner Krauth, and Marcelo J. Rozenberg. Dynamical mean-field theory of strongly correlated fermion systems and the limit of infinite dimensions. *Rev. Mod. Phys.*, 68:13, Jan 1996.
- [49] Antoine Georges and Werner Krauth. Numerical solution of the $d = \infty$ hubbard model: Evidence for a mott transition. *Phys. Rev. Lett.*, 69(8):1240--1243, Aug 1992.
- [50] E. Gull, M. Ferrero, O. Parcollet, A. Georges, and A. J. Millis. Momentum-space anisotropy and pseudogaps: A comparative cluster dynamical mean-field analysis of the doping-driven metal-insulator transition in the two-dimensional Hubbard model. *Phys. Rev. B*, 82:155101, 2010.

- [51] Emanuel Gull, Olivier Parcollet, and Andrew J. Millis. Superconductivity and the Pseudogap in the Two-Dimensional Hubbard Model. *Phys. Rev. Lett.*, 110:216405, May 2013.
- [52] O. Gunnarsson, O. K. Andersen, O. Jepsen, and J. Zaanen. Density-functional calculation of the parameters in the Anderson model: Application to Mn in CdTe. *Phys. Rev. B*, 39:1708--1722, Jan 1989.
- [53] Martin C. Gutzwiller. Effect of correlation on the ferromagnetism of transition metals. *Phys. Rev. Lett.*, 10:159--162, Mar 1963.
- [54] H. Hafermann. Self-energy and vertex functions from hybridization expansion continuous-time quantum monte carlo for impurity models with retarded interaction. *arXiv*, 2013.
- [55] H. Hafermann, G. Li, A. N. Rubtsov, M. I. Katsnelson, A.I. Lichtenstein, and H. Monien. Efficient perturbation theory for quantum lattice models. *Phys. Rev. Lett.*, 102:206401, 2009.
- [56] J. P. Hauge, Mark Jarrell, and T. C. Schulthess. Fluctuation-exchange supplemented quantum Monte Carlo approach to the Hubbard model. *Phys. Rev. B*, 69:165113, Apr 2004.
- [57] Christoph J. Halboth and Walter Metzner. Renormalization-group analysis of the two-dimensional Hubbard model. *Phys. Rev. B*, 61:7364--7377, Mar 2000.
- [58] P. Hansmann, T. Ayrál, L. Vaugier, P. Werner, and S. Biermann. Long-Range Coulomb Interactions in Surface Systems: A First-Principle Description within Self-Consistently Combined *GW* and Dynamical Mean-Field Theory. *Phys. Rev. Lett.*, 110:166401, 2013.
- [59] L. Hedin. New Method for Calculating the One-Particle Green's Function with Application to the Electron-Gas Problem. *Phys. Rev.*, 139:A796, 1965.
- [60] K. Held. Electronic structure calculations using dynamical mean field theory. *Advances in Physics*, 56:829 -- 926, 2007.
- [61] K. Held, I. A. Nekrasov, G. Keller, V. Eyert, N. Blümer, A. K. McMahan, R. T. Scalettar, Th. Pruschke, V. I. Anisimov, and D. Vollhardt. Realistic investigations of correlated electron systems with LDA + DMFT. *physica status solidi (b)*, 243(11):2599--2631, 2006.
- [62] K. Held, R. Peters, and A. Toschi. Poor Man's Understanding of Kinks Originating from Strong Electronic Correlations. *Phys. Rev. Lett.*, 110:246402, Jun 2013.

- [63] K. Held, C. Taranto, G. Rohringer, and A. Toschi. Hedin Equations, GW, GW+DMFT, and All That. *Lecture Notes of the Autumn School 2011 Hands-on LDA+DMFT, Forschungszentrum Juelich GmbH (publisher)*, 2011.
- [64] M. H. Hettler, A. N. Tahvildar-Zadeh, M. Jarrell, T. Pruschke, and H. R. Krishnamurthy. Nonlocal dynamical correlations of strongly interacting electron systems. *Phys. Rev. B*, 58:R7479, 1998.
- [65] M.H. Hettler, M. Mukherjee, M. Jarrell, and H. R. Krishnamurthy. Dynamical cluster approximation: Nonlocal dynamics of correlated electron systems. *Phys. Rev. B*, 61:12739, 2000.
- [66] A.C. Hewson. *The Kondo Problem to Heavy Fermions*. Cambridge University Press, 1993.
- [67] P. Hohenberg and W. Kohn. Inhomogeneous electron gas. *Phys. Rev.*, 136(3B):B864--B871, Nov 1964.
- [68] B. Holm and U. von Barth. Fully self-consistent *GW* self-energy of the electron gas. *Phys. Rev. B*, 57:2108--2117, Jan 1998.
- [69] C. Honerkamp, M. Salmhofer, N. Furukawa, and T. M. Rice. Breakdown of the Landau-Fermi liquid in two dimensions due to umklapp scattering. *Phys. Rev. B*, 63:035109, Jan 2001.
- [70] Carsten Honerkamp. *Strongly correlated systems*, chapter 12, pages 373--408. Springer-Verlag New York Berlin Heidelberg, 2011.
- [71] Carsten Honerkamp. Effective interactions in multiband systems from constrained summations. *Phys. Rev. B*, 85:195129, May 2012.
- [72] Carsten Honerkamp, Daniel Rohe, Sabine Andergassen, and Tilman Enss. Interaction flow method for many-fermion systems. *Phys. Rev. B*, 70:235115, Dec 2004.
- [73] Carsten Honerkamp and Manfred Salmhofer. Magnetic and Superconducting Instabilities of the Hubbard Model at the Van Hove Filling. *Phys. Rev. Lett.*, 87:187004, Oct 2001.
- [74] Carsten Honerkamp and Manfred Salmhofer. Temperature-flow renormalization group and the competition between superconductivity and ferromagnetism. *Phys. Rev. B*, 64:184516, Oct 2001.
- [75] Carsten Honerkamp and Manfred Salmhofer. Flow of the quasiparticle weight in the N -patch renormalization group scheme. *Phys. Rev. B*, 67:174504, May 2003.

- [76] Li Huang, Thomas Ayrál, Silke Biermann, and Philipp Werner. Extended dynamical mean-field study of the hubbard model with long range interactions. *arXiv:1404.7047*, 2014.
- [77] J. Hubbard. Electron correlations in narrow energy bands. *Proceedings of the Royal Society of London. Series A, Mathematical and Physical Sciences*, 276:238--257, 1963.
- [78] C. Husemann, K.-U. Giering, and M. Salmhofer. Frequency-dependent vertex functions of the (t, t') Hubbard model at weak coupling. *Phys. Rev. B*, 85:075121, Feb 2012.
- [79] C. Husemann and M. Salmhofer. Efficient parametrization of the vertex function, Ω scheme, and the t, t' hubbard model at van hove filling. *Phys. Rev. B*, 79:195125, May 2009.
- [80] Mark S. Hybertsen and Steven G. Louie. Electron correlation in semiconductors and insulators: Band gaps and quasiparticle energies. *Phys. Rev. B*, 34:5390--5413, Oct 1986.
- [81] Masatoshi Imada, Atsushi Fujimori, and Yoshinori Tokura. Metal-insulator transitions. *Rev. Mod. Phys.*, 70:1039--1263, Oct 1998.
- [82] V. Yu. Irkhin, A. A. Katanin, and M. I. Katsnelson. Robustness of the Van Hove Scenario for High- T_c Superconductors. *Phys. Rev. Lett.*, 89:076401, Jul 2002.
- [83] Severin Jakobs. *Functional renormalization group studies of quantum transport through mesoscopic systems*. PhD thesis, RWTH Aachen, 2010.
- [84] Severin G. Jakobs, Volker Meden, and Herbert Schoeller. Nonequilibrium functional renormalization group for interacting quantum systems. *Phys. Rev. Lett.*, 99:150603, Oct 2007.
- [85] V. Janiš and V. Pokorný. Critical metal-insulator transition and divergence in a two-particle irreducible vertex in disordered and interacting electron systems. *arXiv:1403.2507*, 2014.
- [86] V. Janiš and D. Vollhardt. Comprehensive mean field theory of the Hubbard model. *International Journal of Modern Physics B*, 06(05n06):731--747, 1992.
- [87] M. Jarrell, T. Maier, C. Huscroft, and S. Moukouri. Quantum monte carlo algorithm for nonlocal corrections to the dynamical mean-field theory. *Phys. Rev. B*, 64:195130, 2001.
- [88] Mark Jarrell and J. E. Gubernatis. Bayesian inference and the analytic continuation of imaginary-time quantum monte carlo data. *Physics Reports*, 269(3):133 -- 195, 1996.
- [89] R. O. Jones and O. Gunnarsson. The density functional formalism: its applications and prospects. *Rev. Mod. Phys.*, 61:689, 1989.

- [90] Robert O. Jones. *Strongly correlated systems*, chapter 1, pages 1--28. Springer-Verlag New York Berlin Heidelberg, 2011.
- [91] A. P. Kampf and A. A. Katanin. Competing phases in the extended $U - V$ Hubbard model near the Van Hove fillings. *Phys. Rev. B*, 67:125104, Mar 2003.
- [92] Junjiro Kanamori. Electron correlation and ferromagnetism of transition metals. *Progress of Theoretical Physics*, 30(3):275--289, 1963.
- [93] C. Karrasch. *The Functional Renormalization Group for Zero-Dimensional Quantum Systems in and out of Equilibrium*. PhD thesis, RWTH Aachen, 2010.
- [94] C. Karrasch, R. Hedden, R. Peters, Th. Pruschke, K. Schönhammer, and V. Meden. A finite-frequency functional renormalization group approach to the single impurity Anderson model. *J. Phys.: Condens. Matter*, 20:345205, 2008.
- [95] A. A. Katanin. Fulfillment of Ward identities in the functional renormalization group approach. *Phys. Rev. B*, 70:115109, Sep 2004.
- [96] A. A. Katanin. Two-loop functional renormalization group approach to the one- and two-dimensional Hubbard model. *Phys. Rev. B*, 79:235119, Jun 2009.
- [97] A. A. Katanin and A. P. Kampf. Renormalization group analysis of magnetic and superconducting instabilities near van Hove band fillings. *Phys. Rev. B*, 68:195101, Nov 2003.
- [98] A. A. Katanin, A. Toschi, and K. Held. Comparing pertinent effects of antiferromagnetic fluctuations in the two- and three-dimensional Hubbard model. *Phys. Rev. B*, 80:075104, Aug 2009.
- [99] P. R. C. Kent, M. Jarrell, T. A. Maier, and Th. Pruschke. Efficient calculation of the antiferromagnetic phase diagram of the three-dimensional Hubbard model. *Phys. Rev. B*, 72:060411(R), 2005.
- [100] M. Kinza. *Single Impurity Anderson Model and Dynamical Mean Field Theory - A Functional Renormalization Group Study*. PhD thesis, RWTH Aachen, 2013.
- [101] M. Kinza and C. Honerkamp. Two-particle correlations in a functional renormalization group scheme using a dynamical mean-field theory. *Phys. Rev. B*, 88:195136, 2013.
- [102] M. Kinza, J. Ortloff, J. Bauer, and C. Honerkamp. Alternative functional renormalization group approach to the single impurity anderson model. *Phys. Rev. B*, 87:035111, 2013.
- [103] W. Kohn and L.J. Sham. Self-consistent equations including exchange and correlation effects. *Phys. Rev.*, 140:(4A) A1133, 1965.

- [104] Peter Kopietz, Lorenz Bartosch, and Florian Schütz. *Introduction to the functional renormalization group*. Springer-Verlag Berlin Heidelberg, 2010.
- [105] J. M. Kosterlitz and D J. Thouless. Ordering, metastability and phase transitions in two-dimensional systems. *Journal of Physics C: Solid State Physics*, 6(7):1181, 1973.
- [106] G. Kotliar. Landau theory of the Mott transition in the fully frustrated Hubbard model in infinite dimensions. *The European Physical Journal B - Condensed Matter and Complex Systems*, 11(1):27--39, 1999.
- [107] G. Kotliar, E. Lange, and M. J. Rozenberg. Landau Theory of the Finite Temperature Mott Transition. *Phys. Rev. Lett.*, 84:5180--5183, May 2000.
- [108] G. Kotliar, S. Y. Savrasov, K. Haule, V. S. Oudovenko, O. Parcollet, and C. A. Marianetti. Electronic structure calculations with dynamical mean-field theory. *Rev. Mod. Phys.*, 78:865, 2006.
- [109] Gabriel Kotliar, Sergey Savrasov, Gunnar Palsson, and Giulio Biroli. Cellular dynamical mean field approach to strongly correlated systems. *Phys. Rev. Lett.*, 87:186401, 2001.
- [110] J. Kuneš. Efficient treatment of two-particle vertices in dynamical mean-field theory. *Phys. Rev. B*, 83:085102, 2011.
- [111] Jan Kuneš, R. Arita, P. Wissgott, A. Toschi, Hiroaki Ikeda, and Karsten Held. Wien2wannier: From linearized augmented plane waves to maximally localized Wannier functions. *Computer Physics Communications*, 181:1888, 2010.
- [112] Gang Li, Hunpyo Lee, and Hartmut Monien. Determination of the lattice susceptibility within the dual fermion method. *Phys. Rev. B*, 78:195105, 2008.
- [113] A. I. Lichtenstein and M. I. Katsnelson. Ab initio calculations of quasiparticle band structure in correlated systems: LDA++ approach. *Phys. Rev. B*, 57:6884--6895, Mar 1998.
- [114] A. I. Lichtenstein and M. I. Katsnelson. Antiferromagnetism and d -wave superconductivity in cuprates: A cluster dynamical mean-field theory. *Phys. Rev. B*, 62:R9283, 2000.
- [115] J. Lichtenstein, S. A. Maier, C. Honerkamp, C. Platt, R. Thomale, O. K. Andersen, and L. Boeri. Functional renormalization group study of an eight-band model for the iron arsenides. *arXiv:1403.5487*, 2014.
- [116] A. Liebsch. Surface versus Bulk Coulomb Correlations in Photoemission Spectra of SrVO₃ and CaVO₃. *Phys. Rev. Lett.*, 90(9):096401, Mar 2003.
- [117] J. M. Luttinger and J. C. Ward. Ground-state energy of a many-fermion system. ii. *Phys. Rev.*, 118:1417--1427, Jun 1960.

- [118] Alexandru Macridin, M. Jarrell, Thomas Maier, P. R. C. Kent, and Eduardo D'Azevedo. Pseudogap and Antiferromagnetic Correlations in the Hubbard Model. *Phys. Rev. Lett.*, 97:036401, Jul 2006.
- [119] Gerald D. Mahan. *Many-Particle Physics*. Kluwer Academic/Plenum Publishers, New York, 2000.
- [120] Stefan A. Maier and Carsten Honerkamp. Effective three-particle interactions in low-energy models for multiband systems. *Phys. Rev. B*, 85:064520, Feb 2012.
- [121] Stefan A. Maier, Jutta Ortloff, and Carsten Honerkamp. Multiorbital effects in the functional renormalization group: A weak-coupling study of the Emery model. *Phys. Rev. B*, 88:235112, Dec 2013.
- [122] T. Maier, M. Jarrell, T. Pruschke, and M. H. Hettler. Quantum cluster theories. *Rev. Mod. Phys.*, 77:1027, 2005.
- [123] T. A. Maier, M. Jarrell, T. C. Schulthess, P. R. C. Kent, and J. B. White. Systematic Study of *d*-Wave Superconductivity in the 2D Repulsive Hubbard Model. *Phys. Rev. Lett.*, 95:237001, Nov 2005.
- [124] Kalobaran Maiti, U. Manju, Sugata Ray, Priya Mahadevan, I. H. Inoue, C. Carbone, and D. D. Sarma. Understanding the bulk electronic structure of $\text{Ca}_{1-x}\text{Sr}_x\text{VO}_3$. *Phys. Rev. B*, 73:052508, Feb 2006.
- [125] Nicola Marzari and David Vanderbilt. Maximally localized generalized Wannier functions for composite energy bands. *Phys. Rev. B*, 56:12847--12865, Nov 1997.
- [126] A. K. McMahan, Richard M. Martin, and S. Satpathy. Calculated effective Hamiltonian for La_2CuO_4 and solution in the impurity Anderson approximation. *Phys. Rev. B*, 38:6650--6666, Oct 1988.
- [127] A.K. McMahan, C. Huscroft, R.T. Scalettar, and E.L. Pollock. Volume-collapse transitions in the rare earth metals. *Journal of Computer-Aided Materials Design*, 5(2-3):131-162, 1998.
- [128] N.D. Mermin and H. Wagner. Absence of Ferromagnetism or Antiferromagnetism in One- or Two-Dimensional Isotropic Heisenberg Models. *Phys. Rev. Lett.*, 17:1133, 1966.
- [129] W. Metzner, M. Salmhofer, C. Honerkamp, V. Meden, and K. Schönhammer. Functional renormalization group approach to correlated fermion systems. *Rev. Mod. Phys.*, 84:299, 2012.
- [130] Walter Metzner and Dieter Vollhardt. Correlated lattice fermions in $d = \infty$ dimensions. *Phys. Rev. Lett.*, 62:324--327, Jan 1989.

- [131] Takashi Miyake, Ferdi Aryasetiawan, and Masatoshi Imada. *Ab initio* procedure for constructing effective models of correlated materials with entangled band structure. *Phys. Rev. B*, 80:155134, Oct 2009.
- [132] A. A. Mostofi, J. R. Yates, Y.-S. Lee, I. Souza, D. Vanderbilt, and N. Marzari. Wannier90: A tool for obtaining maximally-localised wannier functions. *Comput. Phys. Commun.*, 178:685, 2008.
- [133] E. Müller-Hartmann. Correlated fermions on a lattice in high dimensions. *Zeitschrift für Physik B Condensed Matter*, 74:507--512, 1988.
- [134] J. W. Negele and H. Orland. *Quantum Many-Particle Systems*. Westview Press, 1998.
- [135] I. A. Nekrasov, K. Held, G. Keller, D. E. Kondakov, Th. Pruschke, M. Kollar, O. K. Andersen, V. I. Anisimov, and D. Vollhardt. Momentum-resolved spectral functions of SrVO₃ calculated by LDA+DMFT. *Phys. Rev. B*, 73:155112, Apr 2006.
- [136] I. A. Nekrasov, G. Keller, D. E. Kondakov, A. V. Kozhevnikov, Th. Pruschke, K. Held, D. Vollhardt, and V. I. Anisimov. Comparative study of correlation effects in CaVO₃ and SrVO₃. *Phys. Rev. B*, 72:155106, Oct 2005.
- [137] Yusuke Nomura, Merzuk Kaltak, Kazuma Nakamura, Ciro Taranto, Shiro Sakai, Alessandro Toschi, Ryotaro Arita, Karsten Held, Georg Kresse, and Masatoshi Imada. Effective on-site interaction for dynamical mean-field theory. *Phys. Rev. B*, 86:085117, Aug 2012.
- [138] H. Park, K. Haule, and G. Kotliar. Magnetic Excitation Spectra in BaFe₂As₂: A Two-Particle Approach within a Combination of the Density Functional Theory and the Dynamical Mean-Field Theory Method. *Phys. Rev. Lett.*, 107:137007, 2011.
- [139] Nicolaus Parragh, Alessandro Toschi, Karsten Held, and Giorgio Sangiovanni. Conserved quantities of $SU(2)$ -invariant interactions for correlated fermions and the advantages for quantum Monte Carlo simulations. *Phys. Rev. B*, 86:155158, Oct 2012.
- [140] E. Pavarini, S. Biermann, A. Poteryaev, A. I. Lichtenstein, A. Georges, and O. K. Andersen. Mott Transition and Suppression of Orbital Fluctuations in Orthorhombic $3d^1$ Perovskites. *Phys. Rev. Lett.*, 92:176403, Apr 2004.
- [141] C. Platt, W. Hanke, and R. Thomale. Functional renormalization group for multi-orbital Fermi surface instabilities. *Advances in Physics*, 62(4-6):453--562, 2013.
- [142] I. Ya. Pomeranchuk, V. V. Sudakov, and K. A. Ter-Martirosyan. Vanishing of renormalized charges in field theories with point interaction. *Phys. Rev.*, 103:784--802, Aug 1956.

- [143] M. Potthoff, M. Aichhorn, and C. Dahnken. Variational cluster approach to correlated electron systems in low dimensions. *Phys. Rev. Lett.*, 91:206402, Nov 2003.
- [144] Lucia Reining, Giovanni Onida, and R. W. Godby. Elimination of unoccupied-state summations in *ab initio* self-energy calculations for large supercells. *Phys. Rev. B*, 56:R4301-R4304, Aug 1997.
- [145] Johannes Reuther and Ronny Thomale. Cluster functional renormalization group. *Phys. Rev. B*, 89:024412, Jan 2014.
- [146] G. Rohringer, A. Toschi, H. Hafermann, K. Held, V. I. Anisimov, and A. A. Katanin. One-particle irreducible functional approach: A route to diagrammatic extensions of the dynamical mean-field theory. *Phys. Rev. B*, 88:115112, 2013.
- [147] G. Rohringer, A. Toschi, A. A. Katanin, and K. Held. Critical Properties of the Half-Filled Hubbard Model in Three Dimensions. *Phys. Rev. Lett.*, 107:256402, 2011.
- [148] Georg Rohringer. *New routes towards a theoretical treatment of nonlocal electronic correlations*. PhD thesis, TU Wien, 2014.
- [149] Georg Rohringer, Angelo Valli, and Alessandro Toschi. Local electronic correlation at the two-particle level. *Phys. Rev. B*, 86:125114, 2012.
- [150] Marcelo J. Rozenberg, R. Chitra, and Gabriel Kotliar. Finite Temperature Mott Transition in the Hubbard Model in Infinite Dimensions. *Phys. Rev. Lett.*, 83(17):3498--3501, Oct 1999.
- [151] A. N. Rubtsov, M. I. Katsnelson, and A. I. Lichtenstein. Dual fermion approach to nonlocal correlations in the Hubbard model. *Phys. Rev. B*, 77:033101, Jan 2008.
- [152] A. N. Rubtsov, M. I. Katsnelson, A. I. Lichtenstein, and A. Georges. Dual fermion approach to the two-dimensional Hubbard model: Antiferromagnetic fluctuations and Fermi arcs. *Phys. Rev. B*, 79:045133, 2009.
- [153] A.N. Rubtsov and A.I. Lichtenstein. Continuous-time quantum Monte Carlo method for fermions: Beyond auxiliary field framework. *Journal of Experimental and Theoretical Physics Letters*, 80(1):61--65, 2004.
- [154] M. V. Sadovskii, I. A. Nekrasov, E. Z. Kuchinskii, Th. Pruschke, and V. I. Anisimov. Pseudogaps in strongly correlated metals: A generalized dynamical mean-field theory approach. *Phys. Rev. B*, 72:155105, 2005.
- [155] R. Sakuma, Ph. Werner, and F. Aryasetiawan. Electronic structure of SrVO₃ within *GW*+DMFT. *Phys. Rev. B*, 88:235110, Dec 2013.

- [156] M. Salmhofer. *Renormalization - An Introduction*. Springer-Verlag Berlin Heidelberg, 1999.
- [157] Manfred Salmhofer and Carsten Honerkamp. Fermionic renormalization group flows: Technique and theory. *Progress of Theoretical Physics*, 105(1):1--35, 2001.
- [158] G. Sangiovanni, A. Toschi, E. Koch, K. Held, M. Capone, C. Castellani, O. Gunnarsson, S.-K. Mo, J. W. Allen, H.-D. Kim, A. Sekiyama, A. Yamasaki, S. Suga, and P. Metcalf. Static versus dynamical mean-field theory of Mott antiferromagnets. *Phys. Rev. B*, 73:205121, 2006.
- [159] D. J. Scalapino. A common thread: The pairing interaction for unconventional superconductors. *Rev. Mod. Phys.*, 84:1383--1417, Oct 2012.
- [160] T. Schäfer, G. Rohringer, O. Gunnarsson, S. Ciuchi, G. Sangiovanni, and A. Toschi. Divergent Precursors of the Mott-Hubbard Transition at the Two-Particle Level. *Phys. Rev. Lett.*, 110:246405, 2013.
- [161] Avraham Schiller and Kevin Ingersent. Systematic $1/d$ corrections to the infinite-dimensional limit of correlated lattice electron models. *Phys. Rev. Lett.*, 75:113, 1995.
- [162] Wolf-Dieter Schöne and Adolfo G. Eguluz. Self-consistent calculations of quasiparticle states in metals and semiconductors. *Phys. Rev. Lett.*, 81:1662--1665, Aug 1998.
- [163] A. Sekiyama, H. Fujiwara, S. Imada, S. Suga, H. Eisaki, S. I. Uchida, K. Takegahara, H. Harima, Y. Saitoh, I. A. Nekrasov, G. Keller, D. E. Kondakov, A. V. Kozhevnikov, Th. Pruschke, K. Held, D. Vollhardt, and V. I. Anisimov. Mutual Experimental and Theoretical Validation of Bulk Photoemission Spectra of $\text{Sr}_{1-x}\text{Ca}_x\text{VO}_3$. *Phys. Rev. Lett.*, 93(15):156402, Oct 2004.
- [164] R. Shankar. Renormalization-group approach to interacting fermions. *Rev. Mod. Phys.*, 66:129, 1994.
- [165] M. Shishkin and G. Kresse. Implementation and performance of the frequency-dependent GW method within the PAW framework. *Phys. Rev. B*, 74:035101, Jul 2006.
- [166] M. Shishkin and G. Kresse. Self-consistent GW calculations for semiconductors and insulators. *Phys. Rev. B*, 75:235102, Jun 2007.
- [167] C. Slezak, Jarrell M., Th. Maier, and J. Deisz. Multi-scale extensions to quantum cluster methods for strongly correlated electron systems. *J. Phys.: Condens. Matter*, 21:435604, 2009.
- [168] M. Takizawa, M. Minohara, H. Kumigashira, D. Toyota, M. Oshima, H. Wadati, T. Yoshida, A. Fujimori, M. Lippmaa, M. Kawasaki, H. Koinuma, G. Sordi, and

- M. Rozenberg. Coherent and incoherent d band dispersion in SrVO_3 . *Phys. Rev. B*, 80:235104, Dec 2009.
- [169] C. Taranto, S. Andergassen, J. Bauer, K. Held, A. Katanin, W. Metzner, G. Rohringer, and A. Toschi. From infinite to two dimensions through the functional renormalization group. *Phys. Rev. Lett.*, 112:196402, May 2014.
- [170] C. Taranto, M. Kaltak, N. Parragh, G. Sangiovanni, G. Kresse, A. Toschi, and K. Held. Comparing quasiparticle gw +dmft and lda+dmft for the test bed material srvo_3 . *Phys. Rev. B*, 88:165119, 2013.
- [171] C. Taranto, G. Sangiovanni, K. Held, M. Capone, A. Georges, and A. Toschi. Signature of antiferromagnetic long-range order in the optical spectrum of strongly correlated electron systems. *Phys. Rev. B*, 85:085124, 2012.
- [172] T. Timusk and B.W. Statt. The pseudogap in high-temperature superconductors: an experimental survey. *Rep. Prog. Phys.*, 62:61, 1999.
- [173] J. M. Tomczak, M. Casula, T. Miyake, F. Aryasetiawan, and S. Biermann. Combined GW and dynamical mean-field theory: Dynamical screening effects in transition metal oxides. *EPL (Europhysics Letters)*, 100:67001, 2012.
- [174] Jan M. Tomczak, Michele Casula, Takashi Miyake, and Silke Biermann. Asymmetric band widening by screened exchange competing with local correlations in SrVO_3 : new surprises on an old compound from combined GW and dynamical mean field theory GW +DMFT. *arXiv:1312.7546*, 2013.
- [175] Jan M. Tomczak, M. van Schilfgaarde, and G. Kotliar. Many-Body Effects in Iron Pnictides and Chalcogenides: Nonlocal Versus Dynamic Origin of Effective Masses. *Phys. Rev. Lett.*, 109:237010, Dec 2012.
- [176] A. Toschi, A. A. Katanin, and K. Held. Dynamical vertex approximation: A step beyond dynamical mean-field theory. *Phys. Rev. B*, 75(4):045118, Jan 2007.
- [177] Alessandro Toschi, Georg Rohringer, Andrey Katanin, and Karsten Held. Ab initio calculations with the dynamical vertex approximation. *Annalen der Physik*, 523:698, 2011.
- [178] Stefan Uebelacker and Carsten Honerkamp. Self-energy feedback and frequency-dependent interactions in the functional renormalization group flow for the two-dimensional Hubbard model. *Phys. Rev. B*, 86:235140, Dec 2012.
- [179] A. Valli, G. Sangiovanni, A. Toschi, and K. Held. Correlation effects in transport properties of interacting nanostructures. *Phys. Rev. B*, 86:115418, 2012.

- [180] Angelo Valli, Giorgio Sangiovanni, Olle Gunnarsson, Alessandro Toschi, and Karsten Held. Dynamical vertex approximation for nanoscopic systems. *Phys. Rev. Lett.*, 104:246402, 2010.
- [181] J. C. Ward. An identity in quantum electrodynamics. *Phys. Rev.*, 78:182--182, Apr 1950.
- [182] Philipp Werner, Michele Casula, Takashi Miyake, Ferdi Aryasetiawan, Andrew J. Millis, and Silke Biermann. Satellites and large doping and temperature dependence of electronic properties in hole-doped BaFe₂As₂. *Nat Phys*, 8(4):331--337, 04 2012.
- [183] Philipp Werner, Armin Comanac, Luca de' Medici, Matthias Troyer, and Andrew J. Millis. Continuous-time solver for quantum impurity models. *Phys. Rev. Lett.*, 97:076405, Aug 2006.
- [184] S. R. White, D. J. Scalapino, R. L. Sugar, E. Y. Loh, J. E. Gubernatis, and R. T. Scalettar. Numerical study of the two-dimensional Hubbard model. *Phys. Rev. B*, 40:506--516, Jul 1989.
- [185] Kenneth G. Wilson. The renormalization group and critical phenomena. *Rev. Mod. Phys.*, 55:583--600, Jul 1983.
- [186] P. Wissgott, J. Kuneš, A. Toschi, and K. Held. Dipole matrix element approach versus peierls approximation for optical conductivity. *Phys. Rev. B*, 85:205133, 2012.
- [187] S.-X. Yang, H. Fotso, H. Hafermann, K. M. Tam, J. Moreno, T. Pruschke, and M. Jarrell. Parquet approximation for the 4×4 hubbard cluster. *Phys. Rev. E*, 80:046706, 2009.
- [188] S.-X. Yang, H. Fotso, H. Hafermann, K.-M. Tam, J. Moreno, T. Pruschke, and M. Jarrell. Dual fermion dynamical cluster approach for strongly correlated systems. *Phys. Rev. B*, 84:155106, Oct 2011.
- [189] D. Zanchi and H. J. Schulz. Weakly correlated electrons on a square lattice: Renormalization-group theory. *Phys. Rev. B*, 61:13609--13632, May 2000.
- [190] N. E. Zein, S. Y. Savrasov, and G. Kotliar. Local self-energy approach for electronic structure calculations. *Phys. Rev. Lett.*, 96:226403, Jun 2006.
- [191] Anatoleiy T. Zheleznyak, Victor M. Yakovenko, and Igor E. Dzyaloshinskii. Parquet solution for a flat Fermi surface. *Phys. Rev. B*, 55:3200--3215, Feb 1997.
- [192] Z. Zhong, M. Wallerberger, J. M. Tomczak, C. Taranto, N. Parragh, A. Toschi, G. Sangiovanni, and K. Held. Electronics with correlated oxides: SrVO₃/SrTiO₃ as a Mott transistor. *arXiv:1312.5989*, 2014.

